COMBUSTION QUALITY AND REGIMES FOR STANDARD AND ALTERNATIVE FUELS

BY

KARTHIK NITHYANANDAN

DISSERTATION

Submitted in partial fulfillment of the requirements
for the degree of Doctoral Philosophy in Mechanical Engineering
in the Graduate College of the
University of Illinois at Urbana Champaign, 2017

Urbana, Illinois

Doctoral Committee

Professor Chia-Fon F. Lee, Chair
Professor Alan C. Hansen
Professor Nick Glumac
Associate Professor Tonghun Lee

Abstract

Upcoming environmental constraints require the next generation internal combustion engine (ICE) to yield lower pollutant emissions and higher fuel efficiency. Various alternative fuels and combustion strategies and regimes have shown great potential in meeting these goals. The work done in this dissertation aims at exploring different alternative fuels and advanced combustion strategies through a combination of single-cylinder engine performance and emission tests, laser diagnostics in optical engines, and soot analysis using materials research techniques, in order to improve the combustion and emission performance of the modern ICE.

Alcohols, especially n-butanol, have been studied as potential fuels and have shown to be a possible alternative to pure gasoline. In this work, the intermediate product in bio-butanol production through acetone-butanol-ethanol (ABE) fermentation, ABE, was studied for the first time as a potential alternative fuel in spark ignition (SI) engines. Various blends of ABE and gasoline, with different ratios of acetone, n-butanol, and ethanol were studied under various engine operating conditions. The results obtained affirm ABE's potential as an alternative fuel and explain the effects of ABE components on the combustion process. This work also provides information regarding the optimum ABE ratio to be targeted in the ABE fermentation process. Finally, the datasets obtained are valuable for combustion mechanism and model validation.

Another promising and attractive alternative fuel is natural gas. Dual-fuel Compressed Natural Gas (CNG)/diesel combustion in compression ignition (CI) engines has shown the ability to substantially reduce the NO_x emission and at the same time produce very low particulate matter (PM) emissions. In this study, CNG/diesel dual-fuel combustion has been studied under various CNG substitution ratios and diesel injection strategies at a wide range of engine operating

conditions. The results show how an effective pilot diesel injection strategy in dual-fuel combustion could match the efficiency of diesel combustion (CDC). Furthermore, CNG/diesel dual-fuel combustion was also studied in an optical engine in order to understand the mechanism of dual-fuel combustion. Very few studies have performed visualization of this phenomenon. Exhaust particulate matter from CNG/diesel dual-fuel combustion was also studied and characterized for the first time using materials research techniques such as Transmission electron microscopy (TEM), Thermogravimetric analysis (TGA), CHN elemental analysis, Raman spectroscopy, and Diffuse Reflectance Infrared Fourier Transform (DRIFT) spectroscopy. The results would be invaluable for the design of exhaust after-treatment systems for vehicles using CNG/diesel combustion.

Gasoline direct injection (GDI) engines have shown improved efficiency and reduced fuel consumption, however, GDI combustion faces the serious issue of PM emissions. This study investigated lean-burn GDI combustion of ethanol-gasoline blends in an optical engine and tested a novel injector and combustion chamber design, in order to obtain better atomization and hence better air/fuel mixing, as well as an overall lean air/fuel mixture that would prevent rich zones and hence the formation of soot.

Through this work, a) ABE combustion was studied in gasoline engines for the first time and affirmed as an alternative fuel ; b) By developing improved pilot diesel injection strategies, CNG/diesel dual-fuel combustion was shown to obtain diesel-like efficiency; c) Exhaust particulate matter from CNG/diesel combustion was physically and chemically characterized for the first time using materials analysis techniques; d) CNG/diesel dual-fuel combustion was visualized using color high-speed imaging in an optical engine; e) Lean-burn combustion of ethanol-gasoline blends was investigated in an optical engine.

Acknowledgments

This work has only been possible by the extremely generous support of a number of people and organizations, and I will be forever be grateful for this.

First and foremost, I want to thank my guide and mentor, Professor Chia-fon F. Lee for supporting me every step of the way through my journey. He has not only guided me through research, but has shaped me into a better person. I applied to the U of I with the sole aim of working with him, and honestly, it has been the best decision I ever made. Your support, advice, criticism and encouragement has been instrumental in my research work. Secondly, I would like to sincerely thank Professor Alan Hansen, Professor Tonghun Lee and Professor Nick Glumac for devoting their invaluable time and interest in this research as my examination committee members.

I would also like to acknowledge the funding I received for my graduate education in pursuit of my doctoral degree. This includes the funding from the Department of Energy (DoE), the National Science Foundation (NSF), and First Auto Works (FAW). I would be remiss if I did not thank the Department of Mechanical Science and Engineering at the U of I for their generous financial assistance in the form of Teaching Assistantships. My time as a TA has been enriching and rewarding.

On a personal level, I want to convey my heartfelt thanks to the following friends and colleagues, without whom these last few years would have been dull, to say the least. First, I would like to thank Ming Huo for guiding me during my early years as a graduate student. Next, I want to thank Han Wu for being an excellent colleague and a great friend. I owe a lot to him. I want to thank Robert Donahue, Andy Yan, Yilu Lin, and Timothy Lee for their help and companionship

throughout my PhD. Having great friends in the workplace is a luxury I have enjoyed thanks to them.

I would also like to thank the machine shop in the MechSE department; your excellent machining has made my work so much easier. I also want to sincerely thank the unsung heroes of the MechSE department – Kathy Smith, Laurie MacAdam, Laura Reardon and Emily Lange. You ensured that things always ran smoothly.

There are also a huge number of friends, who I have had the pleasure of knowing and working with over the years: Bob, Andy, Yilu, Tim, Hari Raghavendra, Suya Gao, Haiqin Zhou, Yuanxu Li, Lei Meng, Yuqiang Li, Xiangyu Meng, Zhengxin Xu, Mianzhi Wang, Wayne Chang, and Cai Shen.

A very special and heartfelt thanks goes to my girlfriend, Manasa Harini, who has stood by me and supported me through all the difficult times in these past few years.

Last, but certainly not the least, I would like to thank my parents for always being there for me and supporting my dream of getting a PhD from a world-renowned institution. They are my constant source of support and inspiration. I'd also like to thank my sisters, Pallavi and Kavitha, and their families for all the emotional support. I owe everything to my family.

To My Parents

To My Family

Table of Contents

List of Figures

List of Tables

Abbreviations and Nomenclature

Abbreviations

ABDC	After Bottom Dead Center
ABE	Acetone-Butanol-Ethanol
AFR	Air/Fuel Ratio
ATDC	After Top Dead Center
BBDC	Before Bottom Dead Center
BMEP	Brake Mean Effective Pressure
BSFC	Brake Specific Fuel Consumption
BTDC	Before Top Dead Center
BTE	Brake Thermal Efficiency
CA	Crank Angle
CAD	Crank Angle Degree
CCD	Charge-Coupled Device
CFD	Computational Fluid Dynamics
CO	Carbon Monoxide
CHN	Carbon, Hydrogen, Nitrogen
CI	Compression Ignition
CMOS	Complementary Metal-Oxide-Semiconductor
CNG	Compressed Natural Gas
COV	Coefficient of Variation
CPO	Crude Palm Oil
CR	Compression Ratio

CVO	Crude Vegetable Oil
DDF	Diesel Dual-Fuel
DI	Direct Injection
DIATA	Direct
DISI	Direct Injection Spark Ignition
DOC	Diesel Oxidation Catalyst
DPF	Diesel Particulate Filter
DRIFT	Diffuse Reflectance Infrared Fourier Transform
ECU	Electronic Control Unit
EELS	Electron Energy Loss Spectroscopy
EGR	Exhaust Gas Recirculation
EGT	Exhaust Gas Temperature
EIA	Energy Information Administration
EMC	Embedded Micro Chamber
EOT	Extended Onset Temperature
EPA	Environmental Protection Agency
ETBE	Ethyl Tert-Butyl Ether
ETE	Engine Thermal Efficiency
EU	European Union
EVC	Exhaust Valve Close
EVO	Exhaust Valve Open
FID	Flame Ionization Detection
FSN	Filter Smoke Number

FT	Fischer Tropsch
FTIR	Fourier Transform Infrared
GDI	Gasoline Direct Injection
HACA	Hydrogen Abstraction Carbon Addition
HC	Hydrocarbons
HPDI	High Pressure Direct Injection
HRR	Heat Release Rate
HRTEM	High Resolution Transmission Electron Microscopy
IC	Internal Combustion
ICE	Internal Combustion Engine
IMEP	Indicated Mean Effective Pressure
ITE	Indicated Thermal Efficiency
IVC	Intake Valve Close
IVO	Intake Valve Open
LDV	Light Duty Vehicles
LFS	Laminar Flame Speed
LHV	Lower Heating Value
LLE	Liquid-Liquid Extraction
LNT	Lean NO_x Trap
LTC	Low Temperature Combustion
MAP	Manifold Air Pressure
MBT	Maximum Brake Torque
MFB	Mass Fraction Burned

MTBE	Methyl Tert-Butyl Ether
MJEI	Micro-Jet Enhanced Ignition
NDIR	Non-Dispersive Infrared
NL	Natural Luminosity
NO_x	Nitrogen Oxides
PAH	Poly-aromatic Hydrocarbons
PB	Paper Blackening
PDA	Phase Doppler Anemometry
PFI	Port Fuel Injection
PM	Particulate Matter
RON	Research Octane Number
RPM	Revolutions per minute
SCR	Selective Catalytic Reduction
SG	Spray-Guided
SG-DISI	Spray-Guided Direct Injection Spark Ignition
SI	Spark Ignition
SINL	Spatially Integrated Natural Luminosity
SNR	Signal to Noise Ratio
SMD	Sauter Mean Diameter
SOC	Start of Combustion
SOI	Start of Injection
TAEE	Tert-amyl Ethyl Ether
TEM	Transmission Electron Microscopy

TGA	Thermogravimetric Analysis
TDC	Top Dead Center
THC	Total Hydrocarbons
TINL	Temporally Integrated Natural Luminosity
TJI	Turbulent Jet Ignition
UHC	Unburned Hydrocarbons
ULSD	Ultra Low Sulfur Diesel
VOF	Volatile Organic Fractions
WOT	Wide Open Throttle
XPS	X-ray Photoelectron Spectroscopy
XRD	X-ray Diffraction

Nomenclature

C_1	First Planck's constant
C_2	First Planck's constant
$E_{b,\lambda}$	Monochromatic emissive power of a black body
F/A	Fuel /Air
I_D	Intensity of Raman D band
I_G	Intensity of Raman G band
$I_\lambda(T)$	Monochromatic emissive power of a non-black body
$I_{b,\lambda}(T)$	Monochromatic emissive power of a black body
L	Geometric thickness of flame along optical detection axis
R_f	Reflectometer value of un-blackened paper

R_p	Reflectometer value of sample
R_r	Relative brightness of the sample
T	Temperature
T_a	Brightness Temperature

Greek letters

α	Constant for KL factor
ε	Monochromatic emissivity of a non-black body
γ	Ratio of specific heats
λ	Wavelength
φ	Equivalence ratio

Subscript

b	Black body
λ	Wavelength
D	Raman D Band
G	Raman G Band
CH_4	Methane

Chapter 1 Introduction

1.1 Background

Internal combustion (IC) engines are, and will continue to be the primary mode of power generation for ground transportation. Conventional internal combustion engine powered vehicles are projected to decrease at an annual rate of 0.5% over the next 25 years in the US, with gasoline internal combustion engines decreasing at an annual rate of 0.7%, whereas diesel combustion engines actually increasing at an annual rate of 4.7% in the U.S. for light-duty vehicles used in personal transportation [1]. Meanwhile, alternative fuel-vehicles, including flex-fuel, hybrids, natural gas, electric, liquefied petroleum gas and fuel cells are expected to grow at an annual rate of 7.3% over the next 25 years [1]. According to this projection, the internal combustion engine (ICE) is still going to play an important role in power generation and ground transportation in the foreseeable future.

The growing concerns over global warming and depletion of fossil fuel resources have been associated with the boom of IC engines for decades. Meanwhile, driven by the increasingly stringent emission regulations, significant improvement in emission levels in both spark ignition (SI) engine and compression ignition (CI) has been achieved, with minimum penalty on engine power and performance. As illustrated in Table 1.1, the fuel efficiency has increased by 126% and 77% for cars and trucks respectively from 1975 to 2010. The increase will continue as reflected in the forecast by the Energy Information Administration (EIA) annual energy outlook shown in Table 1.1. The fuel economy for light duty trucks, for example, is projected to further increase from 28.8 miles per gallon (MPG) to 40.3 MPG by 2025.

To achieve the projected fuel economy, various vehicle types that do not solely rely on the gasoline IC engine for power have been developed (summarized in Table 1.2). Although hybrid- and electric- type vehicles have been considered attractive for ground transportation in the future due to their remarkable fuel efficiency, the battery capacity and life (typically made of lithium-ion) currently remain a major hindrance for their widespread use in the current automotive market. On the other hand, CI engines have the advantages of no throttling losses, high compression ratio and overall lean operation compared to SI engines, and are a proven short-to-medium-term solution to the problem of reducing fossil-fuel consumption and minimizing greenhouse gas emissions. As a result, the diesel engine has been long established as the principal power-plant for heavy-duty trucks, buses, and off-road vehicles and machinery.

Conventional diesel combustion, however, results in higher emissions of nitrogen oxides (NO_x) and particulate matter (PM), consequently exhaust after-treatment is necessary to meet the increasingly stringent government emission regulations. Figure 1.2 illustrates Environmental Protection Agency (EPA) and European Union (EU) non-road emission regulations from Tier1 to Tier4. Note that the PM and NO_x has reduced by 90% and 50% respectively from Tier3 to Tier4 interim and another 80% NO_x reduction will be enforced from Tier4 interim to Tier4 final [4]. The current strategy for heavy-duty diesel after-treatment includes a diesel particulate filter (DPF) to capture PM, a selective catalytic reduction (SCR) or lean-NO_x trap (LNT) system to control NO_x, and a diesel oxidation catalyst (DOC) to oxidize Unburned hydrocarbon (UHC) and carbon monoxide (CO) emissions [5,6,7]. The potential cost, weight, package-volume, complexity, and fuel-consumption penalties associated with these after-treatment devices makes them an unwanted necessity and thereby impeding the market penetration and subsequent impact of the conventional diesel combustion engine.

To meet these efficiency and emission targets, and to reduce the cost, complexity and fuel economy penalty of after-treatment devices, alternative fuels and advanced combustion strategies are being intensively studied in recent years. Alcohols, especially n-butanol, have been studied as potential fuels and have shown to be a possible alternative to pure gasoline. N-butanol has properties that closely resemble those of gasoline, and when used as a transportation fuel, can save 39–56% fossil energy while reducing greenhouse gas emissions by up to 48% on a lifecycle basis [8]. Biologically produced butanol is popularly known as 'biobutanol'. The most widely used production route of biobutanol is acetone–butanol–ethanol (ABE) fermentation. However, this process suffers from high substrate costs as well as high recovery costs. If the intermediate product of fermentation, the ABE mixture, could be used for clean combustion, the separation costs would be mitigated. This would save time and money in the production chain of bio-butanol [9].

Another promising and attractive alternative fuel is natural gas. The advantages of natural gas include its widespread availability; its reduced environmental burden relative to conventional fuels (cleaner combustion) and its applicability in conventional diesel and gasoline engines. Dual-fuel Compressed Natural Gas (CNG)/diesel combustion in CI engines has shown the ability to substantially reduce the NO_x emission and at the same time produce very low PM emissions; which is extremely difficult to achieve in conventional diesel engines [10]. Although natural gas/diesel dual-fuel combustion has been studied widely, there is still room for improvement in the quality of dual-fuel combustion, specifically with respect to efficiency. Another area that needs further investigation is the combustion mechanism of dual fuel combustion, i.e., premixed methane/air combustion initiated by a pilot diesel injection. Very few studies have performed visualization of this phenomenon.

As mentioned earlier, conventional diesel engines suffer from high pollutant emissions such as NO_x and PM. PM has been a serious concern for human health due to its direct and broad impact on the respiratory organs, as well as contributing to the global warming issue [11]. As such, PM emission standards are continually evolving and becoming more stringent globally. The most common after-treatment method for soot reduction is to employ a DPF to trap soot particles. However, the design and effectiveness of these filters depend on soot properties. Characterizing the physico-chemical properties of soot is important and can provide crucial information to improve the design and operation of after-treatment systems. Although soot morphology and nanostructure have been widely studied for other alternative fuels such as crude vegetable oil and biodiesels, there have been no studies that compared PM from diesel combustion and that from diesel/CNG dual-fuel combustion.

Vehicles powered by gasoline direct injection (GDI) engines aiming to improve engine efficiency and reduce fuel consumption have entered the car market since the late 1990s. In addition, the global volume of GDI engines is expected to overtake that of port fuel injection (PFI) engines by 2020. Historically, particulate emissions have been related to diesel engines. However, in recent years, particulate emissions from GDI engines, especially the emission of ultrafine particulates, have become a subject of concern [12]. Stratified charge lean-burn GDI combustion is a promising combustion regime that can alleviate PM emissions. This strategy needs to be further investigated and improved. Novel injector and combustion chamber designs need to be developed to obtain better atomization and hence better air/fuel mixing, as well as an overall lean air/fuel mixture that would prevent rich zones and hence the formation of soot.

1.2 Problem Statement

These alternative fuels and combustion strategies have enabled improved efficiency and significant reduction of in-cylinder soot and NO_x emissions. However, there remain several challenges and unanswered questions as mentioned above. Further research is required to meet efficiency and emission targets using these new solutions and to understand the combustion mechanisms behind these strategies. Under the scope of investigating the combustion characteristics of these alternative fuels and combustion strategies, the following issues will be addressed in this thesis work.

- The performance and emission characteristics of various ABE blends will be studied for the first time in spark ignition engines to evaluate the applicability of ABE as an alternative fuel
- The performance and emission characteristics of CNG/diesel dual-fuel combustion will be investigated with an aim to maximize efficiency at high CNG substitution ratios
- Physico-chemical characterization of exhaust soot from CNG/Diesel dual-fuel combustion will be performed for the first time
- Combustion visualization of alternative combustion regimes such as dual-fuel combustion and stratified lean GDI combustion will be performed with an aim to understand the combustion and sooting mechanisms.

1.3 Thesis Overview

The remainder of the thesis is organized as follows: Chapter 2 presents the study of ABE as an alternative fuel in spark ignition engines. Various blends of ABE and gasoline, with different ratios of acetone, n-butanol, and ethanol were studied under various engine operating conditions. Chapter

3 discusses CNG/diesel dual-fuel combustion in compression ignition engines. CNG/diesel dual-fuel combustion has been studied under various CNG substitution ratios and diesel injection strategies at a wide range of engine operating conditions.

Chapter 4 studies exhaust particulate matter from CNG/diesel dual-fuel using materials research techniques such as Transmission electron microscopy (TEM), Thermogravimetric analysis (TGA), Carbon, Hydrogen, Nitrogen (CHN) elemental analysis, Raman spectroscopy, and Diffuse Reflectance Infrared Fourier Transform (DRIFT) spectroscopy.

Chapter 5 investigates CNG/diesel dual-fuel combustion was also studied in an optical engine in order to understand the mechanism of dual-fuel combustion. Color high-speed imaging was used to visualize the combustion process and the 2-color method was used to obtain soot temperature and soot volume fraction information.

Chapter 6 studies stratified charge lean-burn GDI combustion of alcohol-gasoline blends in an optical engine using a novel injector and combustion chamber design. The fuel injector spray was characterized using high-speed imaging and Phase Doppler Anemometry (PDA) and the combustion process was visualized using high-speed natural flame luminosity imaging.

Chapter 7 summarizes the results and recommends directions for future research.

Table 1.1 Estimated average fuel economy and greenhouse gas emissions standards proposed for light-duty vehicles (LDV), model years 2017-2025 [2]

	2016	2017	2018	2019	2020	2021	2022	2023	2024	2025
	Fuel Economy only (miles per gallon)									
Passenger cars	37.8	40.0	41.4	43.0	44.7	46.6	48.8	51.0	53.5	56.0
Light-duty trucks	28.8	29.4	30.0	30.6	31.2	33.3	34.9	36.6	38.5	40.3
All light duty	34.1	35.3	36.4	37.5	38.8	40.9	42.9	45.0	47.3	49.6

[a] Based on Projected mix of LDV sales

Table 1.2 Vehicle types that do not rely solely on a gasoline internal combustion engine for motive and accessory power [2]

Vehicle Type	Description
Diesel	Vehicles that use diesel fuel in a compression-ignition internal combustion engine
Micro hybrid	Vehicles with gasoline engines, larger batteries, and electrically powered auxiliary systems that allow the engine to be turned off when the vehicle is coasting or idling and then quickly restarted. Regenerative braking recharges the batteries but does not provide power to the
Hybrid electric (gasoline or diesel)	Vehicles that combine internal combustion and electric propulsion engines but have limited all-electric range and batteries that cannot be recharged with grid power.
Plug-in hybrid electric	Vehicles that use battery power for driving some distance, until a minimum level of battery power is reached, at which point they operate on a mixture of battery and internal combustion power. Plug-in hybrids also can be engineered to run in a “blended mode,” where an onboard computer determines the most efficient use of battery and internal combustion power. The batteries can be recharged from the

Electric	Vehicles that operate by electric propulsion from batteries that are recharged exclusively by electricity from the grid or through
Flex-fuel	Vehicles that can run on gasoline or any gasoline-ethanol blend up to 85 percent ethanol.

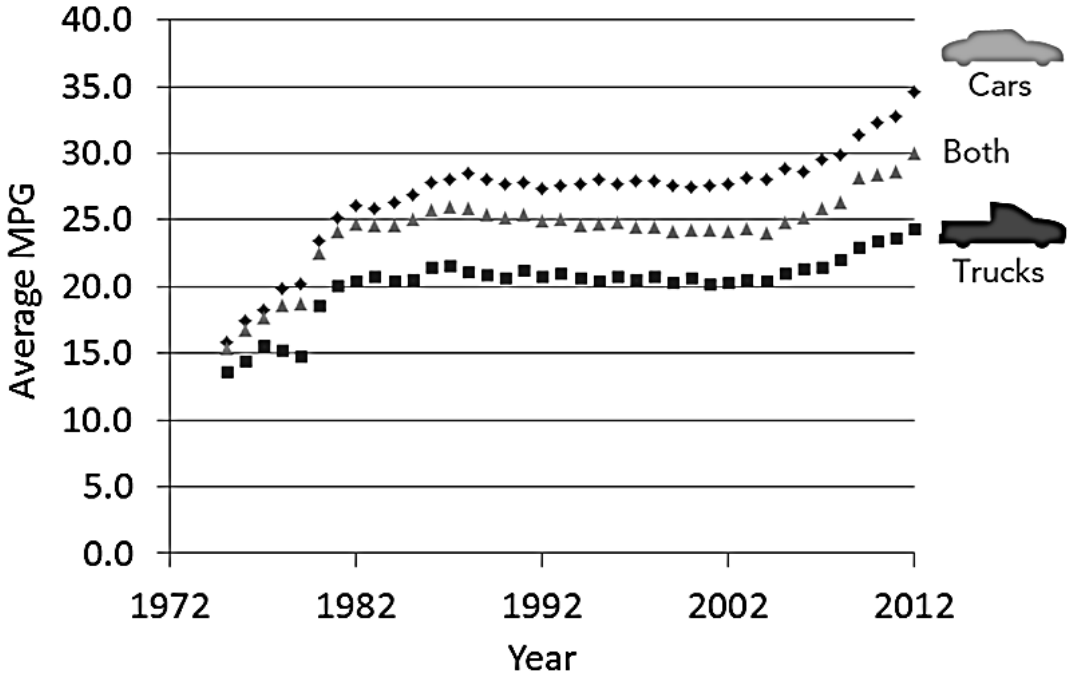

Figure 1.1 Average estimated fuel economy by model year [3]

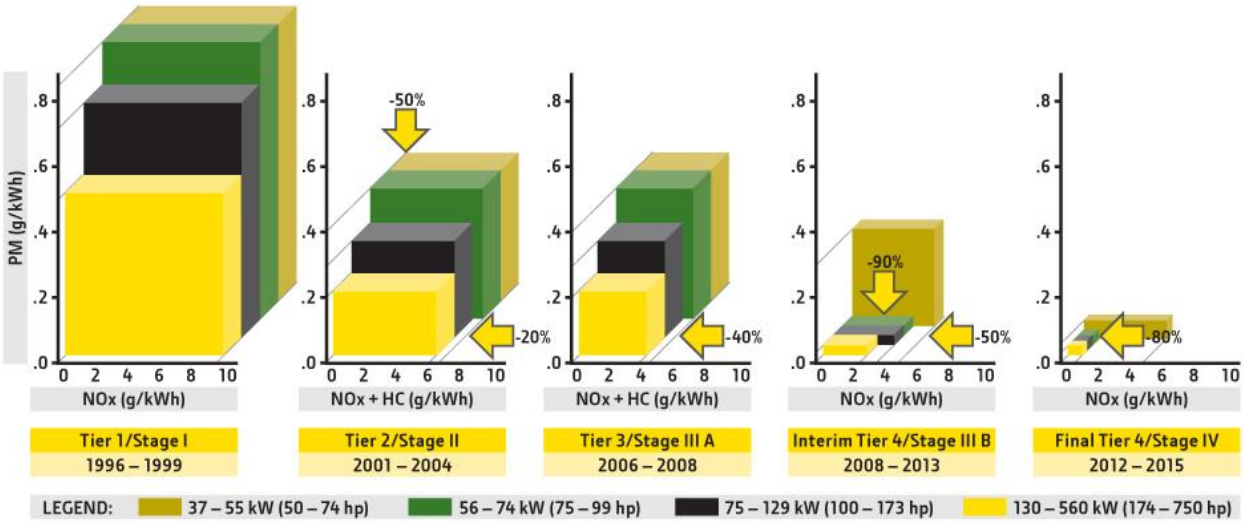

Figure 1.2 EPA and EU non-road emissions regulations [4]

Chapter 2 ABE Combustion in SI Engines

Many studies on n-butanol have been conducted due to its properties that closely resemble those of gasoline. These properties include ease of transportation through pipelines due to its hydrophobic nature; a stoichiometric air/fuel ratio that closely resembles that of gasoline allowing for greater percentages of butanol to be mixed with gasoline without heavy engine modification; and an energy content that is 30% more than ethanol, providing higher energy density than the widely used E85 fuel. ABE fermentation primarily involves bacterial fermentation of biomass feedstock to produce acetone, n-butanol and ethanol at volume percentages of approximately 22–33%, 62–74%, and 1–6% respectively (roughly a 3:6:1 ratio). Due to the depletion of fossil fuels and subsequent rise in oil prices, interest in ABE as a viable alternative to the petroleum process has been renewed. In this study, the potential of the intermediate fermentation product, ABE, as an alternative fuel is investigated in a single-cylinder SI engine by combusting various ABE blends and acquiring and analyzing in-cylinder pressure, performance and emission data. The chapter starts with the literature review on ABE fermentation and previous relevant studies. The experimental setup will be detailed next followed by the results and discussion. Several key topics regarding ABE combustion will be addressed:

- A comprehensive literature review on the ABE fermentation process
- Performance and emission tests of ABE-gasoline blends with varying ABE content
- Performance and emission tests of neat ABE with varying A:B:E ratios.

2.1 Literature Review

2.1.1 Introduction

Over the past decades, the biofuel industry has grown significantly due to increasing interest in renewable energy sources. It is highly desirable to progressively move away from petroleum-based energy sources to satisfy increasing global energy demands, partly alleviate the production of greenhouse gases, and reduce the dependence on imported oil. Ethanol and biodiesel have been the main focus of development for the biofuel industry. However, more recently, due to advances in biotechnology and separation sciences, bio-butanol is starting to emerge as a viable biofuel. Butanol is considered a better biofuel than ethanol because its properties are similar to conventional fuels such as diesel and gasoline. Additionally, butanol has higher energy density and lower volatility than ethanol, is less hygroscopic, and is less corrosive to the existing infrastructure [13].

The conventional chemical manufacturing process for butanol is the oxo process (hydroformylation), in which synthesis gas (a mixture of CO and H_2) first reacts with propylene to yield buteraldehyde, which is subsequently hydrogenated to butanol. Another chemical process for butanol synthesis is through crotonaldehyde, in which two molecules of acetaldehyde undergo aldol condensation to yield the intermediate crotonaldehyde, which is then dehydrated and hydrogenated to give butanol. Butanol also can be produced from various biological substrates such as sugars, starch, and biomass through various different routes. Biologically produced butanol is popularly known as ‘biobutanol’. The most popular and historical route to biobutanol has been ABE fermentation by means of solvent-producing strains of Clostridium sp. including Clostridium

acetobutylicum and Clostridium beijerinckii. The conventional substrates for ABE fermentation have been corn or molasses; however, several alternative substrates have been considered [21].

The current international price of bulk grade butanol is approximately $4 per gallon (liquid fuels) with a worldwide market of 350 million gallons per year [21]. Since 2005, a North American-based company DuPont and a UK-based company British Petroleum have declared their intent to restart butanol production by ABE fermentation on an industrial scale [23]. According to data presented by the U.S. EIA, total World biofuels production in 2001 was equal to 54,511 m^3/ day, whereas in 2011 production of biofuels reached a value of 304,587 m^3/day and 302,290 m^3/day in 2012.This means that production of biofuels increased during 10 years by more than five times. Bio-butanol production plants have been recently built in China, Russia, Saudi Arabia, Brazil, Belgium etc. [25].

However, there are some problems in a typical batch ABE fermentation process that constrict the application of butanol industrially as an alternative to fossil fuels: (1) relatively high substrate costs and negative effect on food and feed markets due to the usage of edible biomass, (2) low final butanol concentrations (ca. <20 g/L; roughly 20-25%) due to butanol feedback inhibition, (3) low butanol yields (ca. <0.35 g/g) due to heterofermentation, (4) low volumetric butanol productivity (ca. <0.5 g/L/h) due to low cell concentration, (5) high cost of butanol recovery (conventional distillation is energy intensive) [23]

If the intermediate product of fermentation, the ABE mixture, could be used for clean combustion, the separation costs would be mitigated. This would save time and money in the production chain of bio-butanol [13, 20, 21, 23].

2.1.2 ABE Fermentation

2.1.2.1 Substrates

The most commonly considered substrates for clostridial cultures include fibrous biomass containing hemicellulose and cellulose (e.g., wheat straw, rice straw); starchy biomass (such as ground corn and whey permeate); and fruits and vegetables containing fructose, glucose, xylose, and so on as basic components [21]. Other substrates include agriculture wastes (directly from plant) like barley straw, corn stover, corn fibers, bagasse, and switchgrass, potatoes, rice, jawari, bajra, apple pomace, cheese whey, and Jerusalem artichokes [21], which are readily available in agriculture based countries. Therefore, the availability and low cost of these raw materials aid in establishing industrial level plants [14].

Substrate cost is a major factor affecting the economics of butanol production. Spray-dried soy molasses have also been used to produce ABE by C. beijerinckii BA101 in batch cultures. Butanol has also been produced from low cost waste products such as starch-based waste packing peanuts and agricultural waste, highlighting the versatility of C. beijerinckii BA101. Low-grade glycerol and low cost substrates like corn fiber has also been used to produce butanol. Using maltodextrins, soy molasses, agricultural waste, and packaging peanuts as carbon sources, C. beijerinckii BA101 was able to produce 18.6 g/L (26.1%), 18.3 g/L (22.8%), 9.8 g/L (14.8%), and 15.7 g/L (21.7%) of butanol (total solvent), respectively [15].

2.1.2.2 Genetic Engineering of Bacteria

A large variety of clostridial cultures capable of producing acetone, butanol, isopropanol, and ethanol, with varying yield and proportions have been known for more than half a century. As

many as 34 strains representing 15 species of clostridia have been studied for production of acetone, butanol, isopropanol, and ethanol [21]. Currently, the butanol:acetone:ethanol mass fraction ratio in a typical fermentation broth is approximately 6:3:1 and butanol concentration in the product varies between 1 and 2 wt. %. From the metabolic engineering aspect, it would be ideal if a microorganism could be genetically modified to increase the concentration of butanol while reducing or eliminating the formation of other co-products such as acetone and ethanol [20]. Several examples of metabolic engineering of Clostridium sp. have been reported over the years [15]. ABE fuel properties can be adjusted to suit internal combustion engine requirements, by changing the ratio of the ABE components through fermentation. As mentioned earlier, the typical ratio of acetone, butanol and ethanol is 3:6:1 during the formation process, but this is adjustable. Modification of bacterial strains at the genetic level is the common method for researchers to optimize production components. At the same time, fermentation products and the ratio of their formation also vary with the fermentation conditions (pH, temperature, nutrients) [15, 20, 21]. Table 2.1 shows a summary of various bacterial species (some genetically modified) that produce various ratios of acetone, butanol and ethanol as well as varying overall productivity.

2.1.2.3 Recovery

To increase butanol productivity and to partly alleviate the problem of butanol toxicity, various separation techniques have been suggested. Solvent recovery is not the most significant factor affecting the production costs in a conventional ABE plant, but its energy intensity is one reason which affects the economic feasibility of the ABE process. Because of this, literature covers a wide range of energy-efficient alternatives for butanol recovery [24]. These in-situ butanol recovery techniques include vacuum adsorption, gas stripping, liquid-liquid extraction (LLE), reverse

osmosis, pervaporation, membrane solvent extraction (pertraction), freeze crystallization, membrane distillation, thermos pervaporation, sweeping gas pervaporation and vacuum pervaporation. All these techniques have advantages and disadvantages in terms of capacity, selectivity, energy requirements, and most importantly the cost. [13, 21, 25]

Of these, LLE is particularly relevant to using ABE directly, as it could result in fuel blends that could be directly applicable as fuels. LLE is a method used to extract a dissolved substance from liquid mixture in a certain solvent, by another solvent. However, the market value of the extractant and the subsequent cost of extractant recycling have prevented their being applied on a large scale. An ideal in-situ extractant would be one that has a direct end-use as a fuel, which would then eliminate the need for expensive butanol recovery and extractant recycling procedures.

Butanol is suitable for blending with biodiesel, and biodiesel has been used as the extractant in the liquid-liquid extraction method to recover ABE solvents. This would eliminate the need for separating the butanol after extraction. Additionally, biodiesel is much less costly than the traditionally used oleyl alcohol. If biodiesel-derived glycerol is used as the feedstock for butanol production, and biodiesel is used as the extractant to recover butanol from the fermentation broth, production of a biodiesel/butanol fuel blend could be a fully integrated process within a biodiesel facility.

The bacterium Clostridium pasteurianum has been shown to produce significant amounts of butanol, 1, 3-propanediol, and ethanol using both purified and crude glycerol as the sole carbon source. C. pasteurianum is capable generating butanol yields up to 30 wt. % using biodiesel-derived crude glycerol as the sole carbon source. This is notably higher than the 15–20 wt. % butanol yields that are typically obtained using C. acetobutylicum or C. beijerinckii. Additionally, glycerol fermentation does not produce acetone and produces much less ethanol. This process

could ultimately help reduce the cost of butanol separation and ultimately help improve the overall economics of butanol fermentation using renewable feedstocks. Adhani et al. [16] showed that soybean-derived biodiesel is an effective extractant for butanol from fermentation mixtures containing butanol, ethanol, and 1, 3-propanediol. Single-stage extraction using a biodiesel:aqueous phase volume ratio of 1:1 can remove up to 50% of the butanol when the initial concentration is comparable to that produced during anaerobic fermentation, while two stages could remove up to 71% of the butanol. This work also showed that biodiesel is highly selective for butanol and removes very little ethanol and essentially no 1, 3-propanediol. Therefore, if biodiesel were used as an extractant, subsequent separation could produce a very pure butanol product. However, since butanol is a suitable fuel for blending with biodiesel, recovery of the butanol may not be necessary.

The fuel properties of the biodiesel–ABE mixture are comparable to that of No. 2 diesel, but with higher cetane numbers; therefore, it could serve as an efficient No. 2 diesel substitute [18]. Blending butanol with biodiesel effected an improvement in the flow properties of butanol-enriched biodiesel. Ethanol is generally used to blend in diesohol; however, butanol is an alcohol, which has higher solubility in diesel than ethanol and can improve the fuel properties of the blends [26]. To this end, microbial-produced butanol is the best choice for enriching and improving the fuel properties of biodiesel. The biodiesel preferentially extracted butanol, minimized product inhibition, and increased both the production of butanol (from 11.6 to 16.5 g/L) and the total solvents (from 20.0 to 29.9 g/L) by 42% and 50%, respectively. The fuel properties of the ABE-enriched biodiesel obtained by means of extractive fermentation were also analyzed. The key quality indicators of diesel fuel, such as the cetane number (which increased from 48 to 54) and the cold filter plugging point (which decreased from 5.8 to 0.2 °C), were significantly improved

in ABE-enriched biodiesel. Thus, the application of biodiesel as the extractant for ABE fermentation would increase ABE production, bypass the energy intensive butanol recovery process and result in an ABE-enriched biodiesel with improved fuel properties [27]. Yen et al. [22] also found that adding biodiesel at the beginning at a ratio of 1:1 successfully enhanced butanol production. The fed-batch operation with in-situ butanol removal, accomplished by adding biodiesel, greatly enhanced butanol productivity as compared to that of a simple batch. Other extractants which could produce directly usable fuel blends include methylated crude palm oil (CPO) and oleyl alcohol [17, 18], and biodiesel produced from sunflower oil [19].

Kurkijärvi and Lehtonen [24] described a dual-extraction method utilizing iso-octane and petrol components such as: 2-methoxy-2-methylpropane (methyl tert-butyl ether, MTBE), 2-ethoxy-2-methylpropane (ethyl tert-butyl ether, ETBE), 2-methoxy-2-methylbutane (tert-amyl methyl ether, TAME), and 2-ethoxy-2-methylbutane (tert-amyl ethyl ether, TAEE). The ethers made from ethanol, namely ETBE and TAEE, offer the additional benefit that the ethanol used in their production could be bio-based. These extraction solvents had not been used traditionally as they are most likely toxic to the microbes used in the ABE process. If the dual extraction method is used, this toxicity aspect can be ignored. This dual extraction method contains two extraction columns. In the first column, non-biocompatible solvents were utilized to extract effectively ABE products, whereas in the second column traces of the toxic solvent were removed from the broth to make it bio-compatible. After the extraction, the fermentation broth is recycled back to the reactor, and as such, the unfermented nutrients, reaction intermediates, and remaining products could be reutilized. The authors claimed that the product mixture from this process (ABE removed from broth and extractants) could be utilized as a petrol additive without purification steps. Simulations performed in this study showed that ETBE and MTBE were the most effective

solvents for butanol recovery, followed by TAME and TAEE. However, ABE concentration in the end product was low (7.6 kg of butanol in 477.4 kg total amount of product, i.e., less than 16 g/kg). Table 2.2 provides a summary of various fuels used as extractants for in-situ solvent recovery.

2.1.2.4 Economics

Principal factors governing economics of butanol are mode of fermentation, solvent recovery, and substrates. The first two factors govern the total fixed capital investment of the process, whereas the third factor governs the total production cost [21]

Kumar et al. performed an economic assessment of ABE fermentation based on cellulosic and non-cellulosic feedstock and found that the recovery costs contributed to about 5% of the fixed capital cost, and would likely be much higher if operation costs were taken into account. They also found that the total capital investment of the process based on glucose as substrate is 37% lesser than the other cellulosic and non-cellulosic materials. However, unitary production cost based on glucose is fourfold higher than sugarcane and cellulosic materials due to its higher cost ($1.11 per kg). [14]

2.1.3 Previous work

Butanol has been widely investigated as an alternative fuel for both gasoline and diesel engines. Zheng et al. investigated the effects of n-butanol and its isomers on combustion and emissions of a diesel engine, and found that the alcohol blends showed retarded combustion phasing, higher combustion efficiency and lower soot emissions. However, gaseous emissions were not affected obviously [28]. They also studied combustion and emission of blends of diesel, gasoline and n-butanol, and found that the indicated thermal efficiency (ITE) was slightly increased with the

blended fuels [29]. Liu et al. studied the combustion of neat n-butanol and soybean biodiesel in a constant volume chamber and found that n-butanol was more effective in soot suppression relative to biodiesel [30]. They also studied n-butanol and biodiesel dual-fuel combustion in a diesel engine. A slightly higher ITE and significantly reduced NO_x, soot emissions were observed [31]. Liu et al. also investigated the effect of adding various oxygenated fuels (20% by volume) to diesel fuel and found that among n-heptane, iso-octane, n-butanol and methyl octynoate, n-butanol showed the largest soot reduction, however, they found that fuel properties and oxygenated structures had minor effects on gaseous emissions and ITE [32].

As for SI engines, Masum et al. [33] studied the combustion and emissions of methanol, ethanol, butanol and pentanol blended with 80 vol.% gasoline. They found that all alcohol blends displayed better engine torque and lowered emissions relative to gasoline. Costagliola et al. [34] studied performance and emissions of various gasoline/alcohol blends. They found an increase in global efficiency and a reduction in emissions using the blends. Alasfour [35, 36] studied the butanol/gasoline blends and showed a reduction in engine thermal efficiency (ETE) during the whole fuel/air equivalence. He also found NO_x emissions to be lower for the blends than those for pure gasoline. Williams et al. [37] investigated a series of conventional and alcohol fuels and concluded that thermal efficiency, combustion, and emissions were not adversely affected because of adding any butanol to gasoline. Dernotte et al. [38] evaluated the combustion and emissions characteristics of butanol–gasoline blends in a port fuel injection (PFI) SI engine. The results demonstrated that a 40% butanol/60% gasoline blend by volume minimized HC emissions and no significant change in NO_x emissions were observed with the exception of the 80% butanol/20% gasoline blend. The addition of butanol improved combustion stability and reduced ignition delay (0–10% mass fraction burned (MFB)). The change of specific fuel consumption of B40 blend was

within 10% of that of pure gasoline for stoichiometric mixture. Wigg et al. [39] showed that blends containing below 40% volume of butanol offered similar unburned hydrocarbon (UHC) emissions to gasoline, but higher hydrocarbons (HC) levels than pure gasoline at higher butanol concentrations. The results also indicated a slight increase in brake specific fuel consumption (BSFC) with the butanol addition. Venugopal and Ramesh [40] studied engine performance with simultaneous injection of butanol and gasoline, as well as blended fuels. On the whole, at all operating conditions, simultaneous injection results in reduced HC levels and improved or similar performance as compared with B50. Gu et al. [41] studied combustion in a spark-ignition engine fueled with gasoline–n-butanol blends. It was found that, HC, carbon monoxide (CO) and NO_x emissions fueled with gasoline and n-butanol blends are lower than those of gasoline. Pure n-butanol increased the HC and CO while decreased the NO_x; these tendencies were similar to [36]. Yacoub et al. [42] performed several studies on application of straight chain alcohols C1–C5 (methanol to pentanol) as fuels blended with gasoline. The study showed that all alcohol–gasoline blends showed reduction in CO emissions, and total hydrocarbons (THC) emissions were also reduced at optimized operating conditions. However, all blends had a higher unburned alcohol emission than gasoline, with the highest emissions coming from those with the highest alcohol content. Aldehyde emissions were higher for all blends with formaldehyde as the main constituent and the NO_x emissions may increase or decrease depending on different operating conditions. Szwaja and Naber [43] investigated the combustion characteristics of n-butanol in a single cylinder engine and results indicated that the highest peak pressure advanced with the increase of n-butanol ratio due to a faster combustion and the crank angle degree (CAD) of 50% mass fraction burn (MFB) from n-butanol was approximately 2° earlier when compared to gasoline. Wallner et al. [44] investigated the combustion, performance, and emissions of pure gasoline, 10% ethanol (E10)

and 10% butanol (Bu10) blends in a direct-injection (DI) four-cylinder SI engine. Results showed that the burning velocity of the Bu10 was higher than those of both E10 and gasoline. Their further study [45] demonstrated that addition of alcohol to the fuel blend results in a consistent reduction in NO_x emissions regardless of operating point. Both formaldehyde and acetaldehyde emissions increased with the addition of butanol, whereas formaldehyde did not increase significantly with addition of ethanol. Propene, 1, 3-butadiene, and acetylene emissions, which are required for carbon growth processes leading to benzene, also increased only with the addition of butanol.

Recent studies on ABE include ABE–diesel blends combustion in diesel engines (showing simultaneous reductions in PM and NO_x emissions) [46] and kinetic modeling of ABE combustion [47]. Wu et al. [48, 49, 50, 51, 52, 53] performed various optical studies on combustion characteristics of ABE and ABE–diesel blends in a combustion chamber, and found that ABE provides simultaneous soot and NO_x reduction capabilities. It was also found that ABE(6:3:1) showed the highest combustion efficiency, while maintaining phasing close to that of pure diesel. However, to date, combustion characteristics of ABE fuels in SI engines have not been investigated. This is the primary motivation for this study.

2.2 Experimental Setup

2.2.1 Engine Setup

Experiments were conducted using a single cylinder engine with identical cylinder geometry to the V8 engine used in a 2000 Ford Mustang Cobra [39]. The peak power output of the original V8 engine was 239 kW (329 HP) and 407 N m (300 lb-ft) of torque resulting in a peak output for the single cylinder engine of slightly less than 30 kW (40 HP) and 52 N m (38 lb-ft) as a result of increased frictional losses. The bottom end is composed of two iron castings produced by Ford.

The lower casting houses the crankshaft bearings and the upper casting consists of a single cylinder bore, which aligns with cylinder two on the head. The cylinder head is from the left bank of the production V8 engine featuring double overhead camshafts and four valves per cylinder with a centrally located spark plug. In order to reduce frictional losses, the rocker arms were removed from cylinders one, three and four. The engine is coupled to a GE type TLC-15 class 4-35-1700 dynamometer capable of delivering up to 14.9 kW (20 HP) and absorbing up to 26.1 kW (35 HP) at a maximum rotational speed of 4500 RPM. The dynamometer is controlled using a DyneSystems DYN-LOC IV controller and a DyneSystems DTC-1 digital throttle controller. In-cylinder pressure is measured using a Kistler type 6125B pressure transducer and an AVL 3057-AO1 charge amplifier and indexed against a crankshaft position signal from a BEI XH25D shaft encoder. The engine is controlled through the use of a Megasquirt II V3.0 Engine Control Unit (ECU) which allows the adjustment of fuel through volumetric efficiency tables and adjustment of ignition timing (spark advance) as functions of engine speed (RPM) and engine load (manifold air pressure, (MAP)). The fuel injector used was a Bosch injector # 0 280 150 558 rated at 440 cm3/min at a fuel pressure of 3 bar. A schematic of the engine layout is shown in Figure 2.1, and engine specifications are listed in Table 2.3.

2.2.2 Exhaust gas Analyzers

NO_x and λ (and Φ) measurements were conducted using a Horiba MEXA-720 NO_x non-sampling type meter in the exhaust manifold of the engine. The measurement range for NO_x is 0–3000 ppm with ±30 ppm accuracy for 0–1000 ppm, ±3% accuracy for 1000–2000 ppm, and ±5% accuracy for 2000–3000 ppm. The measurement of range for lambda is 0.65–13.7. To enhance accuracy and ensure reliable data, a LabVIEW code was written to collect and average

NO_x and lambda measurements over a 60 s period at 10 samples per second (600 samples total). Measurements of unburned hydrocarbons and carbon monoxide were made using a Horiba MEXA-554JU sampling type meter. A probe was fabricated to fit in the exhaust manifold of the engine that allowed the sampling tube to transport the exhaust gases to the meter.

The measurement range is 0–10,000 ppm for unburned hydrocarbons, 0.00–20.00% by volume for carbon dioxide, and 0.00–10.00% by volume for carbon monoxide. Exhaust gas temperature measurements were made using a type-K thermocouple located in the exhaust manifold. It should be noted that the analyzer used to measure emissions of unburned hydrocarbons uses a nondispersive infrared (NDIR) analyzer. Both NDIR and flame ionization detection (FID) measurements of emissions exhibit low responses to oxygenated hydrocarbons. Engine tests in [45] examined the differences between a Horiba FIA-23A FID analyzer and an MKS 2030 Fourier Transform Infrared (FTIR) analyzer, which can speciate hydrocarbons and more accurately measure oxygenated hydrocarbons. Comparisons between FID and FTIR showed that, for oxygenated fuels, FID consistently underestimated the amount of unburned hydrocarbons although the observed trends were preserved between the two analyzers. However, for the NDIR measurements reported here, using an alcohol fuel does not alter the substance of the results.

2.2.3 Test Fuels

Ethanol-free Gasoline (Research Octane Number (RON) = 90) was selected as the baseline fuel in this study. The ABE solution was first prepared at a volumetric ratio of A:B:E = 3:6:1 using analytical grade acetone (99.5%), butanol (99.5%) and ethanol (99.8%). The n-butanol was supplied by Fisher Scientific while acetone and ethanol meeting USP specs were supplied by Decon Laboratories, Inc. Using an A:B:E ratio of 3:6:1, using splash blending, blends containing

ABE from 0 to 80% vol. were first created to study the impact of increasing ABE content in ABE-gasoline blends. The ABE-gasoline blends with 20% vol. ABE will be referred to as ABE20 and those with 40% vol. ABE will be referred to as ABE40 and so on, in the remainder of the text. A gravitational test for stability was carried out as samples of the prepared blends were deposited in a test tube at 25 °C and 1 atm for 90 days. The blends displayed a clear single phase after the stability test.

Further, neat ABE blends at volume ratios of A:B:E = 3:6:1, 6:3:1 and 5:14:1 were created. The ABE blend with ABE ratio of 3:6:1 will be referred to as ABE(3:6:1); that with ABE ratio of 6:3:1 will be referred to as ABE(6:3:1), and so on, in the remainder of the text. Pure gasoline will be referred to as ABE0. The ABE ratio of 3:6:1 is studied because it is the most commonly produced in the fermentation product [54, 55]. The ratio of 6:3:1 is used as it helps in understanding the effect of increasing acetone and decreasing butanol. It has also been found in [50] that ABE (6:3:1) showed great potential for improving combustion efficiency. ABE(5:14:1) is investigated as it was studied in [46] and showed promising results in diesel engine combustion. Finally, pure n-butanol is studied for comparison purposes and to further understand the effects of different components. The properties of individual fuels are listed in Table 2.4. The difference in the latent heats of vaporization between the fuels is worth noting, as are the different laminar flame speeds (LFS). Note that the latent heat of vaporization of acetone is slightly higher than that of gasoline; however, those of ethanol and butanol are nearly 50–75% higher than that of gasoline. As far as the LFS is concerned, gasoline has the lowest value among the individual fuels. The LFS plays an important role in the early phase of combustion [43]. The LFS for the components is as follows: Butanol > Ethanol > Acetone > Gasoline (Table 2.4). The LFS of ABE (3:6:1) was predicted by Van Geem et al. to be 37 cm/s (298 K, Stoichiometric) [47]. This is about 3 cm/s higher than gasoline. It is

expected that the LFS of the fuels would increase with increasing n-butanol content. However, it is to be noted that a small addition of a component with higher LFS does not show any major effects on the LFS of the blend [56, 57]. Another parameter of importance is the latent heat of vaporization, which would cause a charge cooling effect. Alcohol fuels have been shown to have higher charge-cooling relative to that with gasoline [58]. The LFS strongly depends on temperature. It was shown that the effect of temperature on LFS dominated over the effect of 50 vol. % addition of ethanol to iso-octane [57]. Therefore, it is expected that the combustion phasing of ABE blends would be determined by the balance between the increase in LFS due to the addition n-butanol, and the decrease in LFS due to the reduction in temperature at ignition by charge-cooling. Finally, acetone with a boiling point of 56 °C could help the blend's spray collapse significantly, as a small portion of a low boiling point substance within a fuel may be the catalyst to spray collapse, even if the majority constituent of the fuel is not in the region of flash boiling in terms of temperature [59]. Table 2.5 shows properties of the ABE-gasoline blends, and Table 2.6 shows properties of neat ABE blends calculated using simple mixing rules.

2.2.4 Test Conditions

For the ABE-gasoline blends study, the engine load was fixed at 375 kPa (BMEP) (medium load) and the speed at 1200 RPM, similar to cruising conditions. The throttle plate was fully opened (100%) and the intake manifold pressure was fixed (75 kPa) by regulating supply air from the building. Ignition timing was set to 20° Before Top Dead Center (BTDC), the default value for gasoline at these engine conditions, to perform an analysis of ABE use in SI engines without any modifications.

For the neat ABE blend study, the engine load was set to 3 bar and 5 bar (BMEP) and the speed at 1200 RPM. The throttle plate was fully opened (Wide Open Throttle (WOT)). The fuels were first tested under stoichiometric conditions with the same ignition timing as gasoline's maximum brake torque (MBT) timing (18° Before Top Dead Center (BTDC) at 3 bar and 24° BTDC at 5 bar BMEP, the default values for gasoline at these conditions), to perform an analysis of ABE use in SI engines without any modifications. Next, each fuel was tested at its own MBT timing (Table 2.8) and an air/fuel ratio sweep was performed. It should be noted that the engine started up immediately using all fuels except n-butanol, for which the engine had to be warmed up beforehand. This is likely due to the enhanced volatility of ABE fuels due to the presence of acetone. Measurements of brake torque, lambda, and NO_x were averaged of a 60-s period while UHC, CO and exhaust gas temperature (EGT) measurements were recorded directly from the emissions analyzer. In the figures, error bars represent the variability in the data in terms of standard deviation between runs. In addition, in-cylinder pressure traces were taken for all fuels to examine the differences in peak cylinder pressure. The experiments were performed 3 times and these datasets were then averaged. The tests were performed in a temperature-controlled laboratory; so the effects of humidity were assumed to be negligible. The intake air pressure was controlled using an electronic regulator, which provides precise control (Accuracy: ±0.1 kPa). Furthermore, the engine was allowed to run at every operating condition for an extended period to ensure steady state measurements. The conditions used in this test are summarized in Table 2.7.

2.3 Results and Discussion

2.3.1 ABE-Gasoline Blends

The following figures present performance and emissions measurements for all the fuels under the testing conditions described previously. The results under stoichiometric conditions are first presented and discussed in detail, after which, results over the range of equivalence ratios tested are presented for completeness and briefly discussed. The in-cylinder pressure traces are first presented to compare differences in peak cylinder pressure between the fuels. Next, emissions measurements are presented starting with UHC. UHC emissions are presented first since they provide insight into how well the fuel mixes with the air and is consumed during the combustion process. Emissions of carbon monoxide are then shown to estimate the completion of combustion, followed by NO_x emissions to analyze the effect of ABE's lower energy content on NO_x production.

2.3.1.1 In-Cylinder Pressure Traces

Figure 2.2 shows the pressure traces of all tested fuels under stoichiometric conditions, i.e. an equivalence ratio of unity ($\Phi = 1$). The traces shown are the mean trace of several 25 consecutive engine cycle samples recorded over a 60 second period. The peak cylinder pressure of ABE80 is higher compared to ABE0. The CA50 (50% MFB location) (Figure 2.3(b)) is also advanced with respect to ABE0. ABE has a higher latent heat of vaporization and a higher LFS relative to ABE0. For the blends with gasoline as the major component (<50% vol.), the LFS decrease due to charge cooling dominates over the LFS increase due to the addition of ABE. From the pressure trace, it appears that ABE20 and ABE40 show similar combustion characteristics; however, their peak

pressure is reduced due to the charge-cooling effect. For ABE80, the higher flame speeds of ABE have the dominant impact, causing the combustion to initiate faster and approach completion, leading to a higher combustion peak and advanced CAD position with respect to ABE0.

2.3.1.2 Mass Fraction Burned (MFB) Profiles

Normalized MFB plots, which can express heat release from combustion, were determined from each of the pressure traces and illustrated in Figure 2.3(a). In this analysis the heat transfer to walls and fuel flow into crevices were neglected. Therefore, the apparent HRR was calculated from the pressure trace using the first law of thermodynamics as expressed in Equation (2.1).

$$\frac{dQ_n}{dt} = \frac{\gamma}{\gamma - 1} p \frac{dV}{dt} + \frac{1}{\gamma - 1} V \frac{dp}{dt} \qquad \ldots (2.1)$$

where, γ is the specific heat ratio, p is the in-cylinder pressure, V is the cylinder volume, and Qn is apparent heat release.

From Figure 2.3(a), quantities such as 10% MFB, 50% MFB and 90% MFB can be determined. These values correspond to 0.1, 0.5 and 0.9 of normalized MFB, respectively. Figure 2.3(b) shows the CA50 location for the different fuels at Φ = 1. ABE0 and ABE80 have very similar combustion phasing. This is reflected in the CA50 location in Figure 2.3(b). The difference in 50% MFB location between ABE0 and ABE20 (and ABE40) is about 1.4° (retarded), and that between ABE80 and ABE0 is about 0.3° (advanced). The 50% MFB represents the center of combustion, and it has been shown that the engine torque strongly depends on the location of 50% MFB.

The ignition delay shown in Figure 2.4(a) is calculated as the difference between the spark timing and 0.1 MFB timing; combustion duration presented in Figure 2.4(b) is calculated as a difference between 0.9 MFB and 0.1 MFB. They are expressed in degrees of crankshaft angle. As plotted in

Figure 2.4(a), the ignition delay increases with addition of ABE up to ABE40, and then decreases. During this period of early combustion, the combustion rate is impacted by the laminar flame speed of the fuel–air mixture. At later times which are in the fully developed bulk burn, the combustion is dominated by turbulent flame propagation [43].

As seen in Figure 2.4(b), the combustion duration decreases for ABE20 and ABE40 relative to ABE0, and then increases for ABE80. Figure 2.4(c) shows a combustion duration split and it is observed that for all fuels, the 10%-50% MFB period remains almost the same and the differences arise from the latter half of the combustion process. Although the ignition delay and 50% MFB duration changed for the blends, the relative change in the rate of combustion was small. In summary, as shown under this condition, the normalized MFB does not change significantly with ABE fraction. For optimal combustion phasing the spark timing should be adjusted or controlled as a function of the ABE fraction. The trends observed are different from [37, 38] and [42, 43] which showed a steady advancement of combustion phasing (CA50) with butanol addition. However, with ABE, it is seen that phasing is slightly retarded for blends with lower ABE content and advanced for those with higher ABE content. This is explained by the impact of LFS and charge-cooling. Also, the LFS of ABE is ~37 cm/s, which is lower than that of n-butanol (46 cm/s). So the increase in LFS due to addition of ABE would be much lower relative to that due to addition of butanol.

Figure 2.5 (a) shows the ignition delay of different fuels at varying equivalence ratios. It is apparent that the fuels behave most similarly near stoichiometric conditions. At leaner and richer equivalence ratios, the combustion behavior is more widely separated. A shorter ignition delay is observed at richer equivalence ratios. This is due to the fact that flame development is slower at

leaner equivalence ratios [58]. It appears that fuels with higher ABE content show combustion behavior that is less sensitive to the equivalence ratio.

Figure 2.5 (b) shows a plot of the main combustion duration against the CA50 location for different fuels at varying equivalence ratios. The five markers for each equivalence ratio indicate the different fuels. This plot gives an idea about the degree of variation in combustion phasing among the fuels at different air/fuel ratios. Overall, the center of combustion is progressively retarded as the mixture gets leaner. It is also apparent that the main combustion duration for all fuels is the longest at stoichiometric conditions. As mentioned earlier, it appears that combustion phasing of the fuels seems to be closer at richer equivalence ratios and start spreading apart as the mixture gets leaner. Therefore, the spark timing should be adjusted at leaner operating conditions to match combustion phasing.

2.3.1.3 Brake Thermal Efficiency and Brake Specific Fuel Consumption

Figure 2.6 shows the Brake Thermal Efficiency (BTE) of different fuels. It is seen that ABE20 and ABE40 show an increase in BTE, whereas ABE60 shows a decrease in BTE, and the BTE of ABE80 is similar to that of ABE0. The BTE represents the fuel conversion efficiency as a ratio of engine power output versus fuel energy input. However, the fuel energy input changes with the fuel properties, mainly based on the ratio of lower heating value to stoichiometric air demand. To ensure an unbiased comparison in fuel consumption, the brake specific fuel consumption (BSFC) was calculated, which represents the fuel consumption as a function of engine power. The results are shown in Figure 2.7. It is apparent that the BSFC was lowest for ABE0, 303 g/kWh versus 318.5 g/kWh for ABE20 and 338.5 g/kWh for ABE40. The increase in BSFC was approximately 5% for ABE20 and 11.5% for ABE40 and about 25% for ABE80 compared to ABE0. The

differences result from the lower volumetric energy density (see Table 2.5) as well as the reduced stoichiometric air/fuel ratio. The increased efficiency shown by ABE20 is likely due to the shorter main combustion duration. The decreased efficiency of ABE60 is due to a combination of lower input energy, higher latent heat of vaporization, and improper combustion phasing leading to incomplete combustion – this is supported by the high CO emissions for ABE60, as seen in the later section. However, ABE80 shows an increase in efficiency as its phasing is advanced and closer to that of ABE0, due to the LFS increase due to ABE addition.

2.3.1.4 Exhaust Gas Temperature

EGT provides insight into the combustion process by measuring the temperature of the burned gases directly after they exit the engine. With ignition timing fixed, the differences in EGT should be proportional to the combustion temperature of the fuels. Figure 2.8 shows the effect of different fuel blends on EGT at stoichiometric air/fuel ratio. The EGT is seen to drop slightly, with increase in ABE content. ABE0 has the highest EGT (392 °C) and ABE80 the lowest (385 °C) suggesting that gasoline is releasing the most heat and ABE80 the lowest. The reduction in EGT for ABE20 and ABE40 may also be partially caused by the more rapid burn (shorter combustion duration) of ABE20 and ABE40 as indicated by Figure 2.4, resulting in more power extraction from the gas and thus a lower exhaust temperature. ABE60 shows a slight increase in EGT, however, it is within the error range. Similar results showing a decrease in EGT were observed in [35] for a 30% butanol-gasoline blend due to the fact that the alcohol fuel has a higher latent heat of vaporization and a lower heating value than gasoline.

2.3.1.5 Emission Behavior

All reported emissions are raw emissions without the use of a catalytic converter. UHC emissions provide direct insight into the combustion process by measuring how much fuel is left over after the combustion of the fuel-air mixture. Engine-out THC emissions are primarily a result of engine configuration, fuel structure, oxygen availability, and residence time. It might be hypothesized that the addition of an alcohol such as ethanol or butanol to gasoline would improve THC oxidation due to the higher oxygen content in the cylinder and exhaust. However, note that the engine is operated at the stoichiometric air fuel ratio for each specific fuel blend, and thus excess oxygen is not available [44].

Figure 2.9(a) and Figure 2.10(a) show the UHC and CO emissions respectively, under stoichiometric conditions. These emission measurements are shown and discussed together as they give us an idea of combustion completion. The UHC emissions for ABE20 and ABE40 are seen to increase, possibly due to decreased HC oxidation during expansion and exhaust processes (shorter main combustion duration), while those for ABE60 and ABE80 decrease to values slightly lower than that obtained from ABE0.

The CO emissions show the opposite trend. ABE20 and ABE40 show lower CO emissions compared to that of ABE0. This is also reflected in the increased BTE exhibited by ABE20 and ABE40 (Figure 2.6). However, ABE80 gives higher CO emissions. Decreasing in both CO post-flame oxidation and engine power output is responsible for this. Overall, all blends show reduced CO emissions relative to ABE0. These trends are consistent with those of [38] and [41].

CO production is primarily controlled by the air/fuel ratio in the cylinder. Mixtures richer than stoichiometric produce high levels of CO and are sensitive to small changes in air/fuel ratio.

Mixtures at stoichiometric and leaner produce little CO emissions and are relatively insensitive to air/fuel ratio changes [44]. Figure 2.9(b) and Figure 2.10(b) show UHC and CO emissions respectively for the different fuels at varying equivalence ratios

All the fuels behave similarly for the most part, and trends observed for the stoichiometric case are repeated at all equivalence ratios. It is worth noting that CO emissions for the blends are lowered across the board relative to ABE0. This is likely due to the enhanced spray collapse and mixing due to the presence of acetone, as mentioned earlier [52].

It appears that adding a small amount of ABE can improve both power output and emissions behavior. Also, ABE20 and ABE40 show similar emissions behavior while ABE0 and ABE80 also behave quite similarly. This makes sense, as fuels with similar CA50 for a given spark timing, are known to show similar emissions behavior [61].

Figure 2.11(a) shows the NO_x emissions for the different fuels tested under stoichiometric conditions. No major changes are seen in NO_x emissions. NO_x slightly decreases for ABE20 and ABE40 however, those of ABE60 and ABE80 are almost similar to that from ABE0. All the variations were found to be within the error range. This agrees with the results in [38, 41], where no major changes in NO_x emissions were observed for blends of gasoline and n-butanol, and only observed for pure butanol. Similar behavior is observed across the equivalence ratio range tested, as shown in Figure 2.11(b). Combustion approaches close to completion under stoichiometric conditions, which leads to higher peak combustion temperatures, and hence the highest NO_x emissions are seen at stoichiometric conditions with a decrease as the equivalence ratio gets relatively richer or leaner.

2.3.2 Neat ABE Blends

2.3.2.1 In-Cylinder Pressure Traces

Figure 2.12(a) shows the pressure traces of all tested neat ABE fuels at 3 bar BMEP and gasoline MBT at $\Phi = 1$. The traces shown are the mean traces of several 25 consecutive engine cycle samples recorded over a 60 second period. The peak cylinder pressures of all ABE fuels except ABE(6:3:1) are higher compared to that of gasoline. ABE(6:3:1) shows the most retarded phasing due to it having the lowest LFS. ABE(3:6:1) shows a slightly advanced peak pressure because its' higher flame speed which causes the combustion to initiate faster and approach completion, leading to a higher combustion peak and advanced CAD position with respect to gasoline. Figure 2.12(b) shows the pressure traces of all tested fuels at 3 bar BMEP and each fuel's own MBT timing(shown in Table 2.8), under stoichiometric conditions. It appears that at their MBTs, ABE(3:6:1), ABE(5:14:1) and n-butanol show similar combustion phasing, whereas, ABE(6:3:1) and gasoline behave similarly. However, ABE(6:3:1) has a marginally retarded phasing.

2.3.2.2 Mass Fraction Burned (MFB) Profiles

Normalized MFB plots, which can express heat release from combustion, were determined from each of the pressure traces and illustrated in Figure 2.13. Figure 2.14(a) shows the ignition delay for the different fuels at both 3 and 5 bar BMEP, at gasoline MBT at $\Phi = 1$. During this period of early combustion, the combustion rate is impacted by the laminar flame speed of the fuel–air mixture. At later times which are in the fully developed bulk burn, the combustion is dominated by turbulent flame propagation [43]. ABE(3:6:1), ABE(5:14:1) and n-butanol show similar, relatively shorter ignition delays, followed by gasoline, and ABE(6:3:1) having the longest ignition

delay. This trend is in accordance with the LFS of the fuels, and this effect is further pronounced at 5 bar BMEP. Figure 2.14(b) shows the CA50 location for the different fuels under the same conditions. The CA50 trends are similar to those seen for ignition delay. Under 5 bar, the difference in CA50 between ABE0 and ABE(3:6:1), ABE(5:14:1) is about 1.2° (advanced), and that between ABE0 and ABE(6:3:1) is about 1° (retarded). The 50% MFB represents the center of combustion and it has been shown that the engine torque strongly depends on the location of 50% MFB. From Figure 2.14(c), we can see that the combustion duration trends at 3 bar BMEP are similar to those observed for CA50. At 5 bar BMEP, it appears that all ABE fuels show slightly longer combustion duration than that of pure gasoline.

Figure 2.15 shows the ignition delay (top), CA50 (middle) and combustion duration for the different fuels at 3 bar BMEP, at the fuels' MBT at varying equivalence ratios. It is apparent that the fuels behave most similarly near stoichiometric and richer conditions. At leaner equivalence ratios, the combustion behavior is more widely separated. A shorter ignition delay is observed at richer equivalence ratios. This is due to the fact that flame development is slower at leaner equivalence ratios [60]. It can be seen that throughout the equivalence ratio range tested, combustion phasing is consistent with the amount of butanol in the fuel. As butanol content increases, phasing gets advanced. ABE(3:6:1), ABE(5:14:1) and n-butanol behave quite similarly, whereas gasoline and ABE(6:3:1) have similar phasing. Fuels with higher n-butanol show shorter ignition delays and combustion durations due to higher LFS. ABE (6:3:1) behaves similar to ABE0 for the most part, likely because these two fuels would have almost similar LFSs. As such, the trends observed are similar to those in [37, 38, 42, 43] where the addition of butanol advanced combustion phasing. In summary, ABE(6:3:1) does not cause an appreciable change in phasing, however, ABE(3:6:1) and ABE(5:14:1) advance combustion phasing.

2.3.2.3 Brake Thermal Efficiency and Brake Specific Fuel Consumption

Figure 2.16 shows the BSFC of different fuels. The BSFC represents the fuel consumption as a function of engine power. All test blends have higher BSFC than gasoline because of their lower lower heating value (LHV) (seen in Table 2.6). ABE(6:3:1) has the lowest LHV among the fuels, so its BSFC is the highest at the same output torque. At Φ=1, the BSFC of the blends was roughly 10-30% higher than that of ABE0.

The fuel energy input changes with the fuel properties, mainly based on the ratio of lower heating value to stoichiometric air demand. To ensure an unbiased comparison and to better evaluate the fuel economy of alternative fuels, Figure 2.17 shows the BTE of the fuels. The differences in BTE among all test fuels are much less compared to those in BSFC. ABE(6:3:1) shows relatively higher efficiency than all other fuels at stoichiometric and richer air/fuel ratios, whereas butanol shows highest efficiency at leaner air/fuel ratios. The other fuels show slightly higher efficiency relative to that of gasoline. For instance, at Φ=1, the BTE of ABE(6:3:1) is 1.6% higher than that of ABE0, whereas n-butanol shows an increase of 1% relative to ABE0. The relatively lower efficiency of the blends with higher butanol content is likely due to their retarded spark timing and incomplete combustion as seen by a spike in HC and CO emissions (shown later).

The higher thermal efficiency of ABE(6:3:1) can be attributed to the fact that blends with low carbon numbers contain more oxygen than those with high carbon numbers. As a result, combustion is improved, thereby enhancing thermal efficiency. Secondly, from Figure 2.12(b), it can be seen that ABE(6:3:1)'s compression work is quite reduced compared to the other fuels. From Figure 2.15, it can be observed that ABE(6:3:1) shows relatively similar CA50 as that of gasoline, however, it has a longer combustion duration. This reduced compression work increases

the net work output, and the slower rate of combustion leads to comparatively lower heat losses, and better post-flame HC and CO oxidation, which ultimately leads to a higher thermal efficiency. Acetone's higher volatility is likely to make it easier to burn thus approaching complete combustion, as indicated by ABE(6:3:1)'s reduced HC and CO emissions (shown later). In DI engines, fuel is vaporized in the compression stroke when latent heat of vaporization is high. Given that fuel absorbs heat from the cylinder during vaporization, the air–fuel mixture is compressed more easily, thus improving thermal efficiency [33]. This indicates the potential for consumption reductions in DI spark ignition engines. The higher acetone content would also enhance spray collapse and mixing and make the fuel much more volatile. Therefore, acetone addition could improve combustion quality significantly. In summary, the typically produced fermentation product, i.e., ABE(3:6:1) may not be ideal for engine combustion. In terms of efficiency, fermentation products with higher acetone content, such as ABE(6:3:1) would be much better suited as alternative fuels for SI engines.

2.3.2.4 Exhaust Gas Temperature

EGT provides insight into the combustion process by measuring the temperature of the burned gases directly after they exit the engine. With ignition timing fixed, the differences in EGT should be proportional to the combustion temperature of the fuels. Figure 2.18 shows the EGT of different at Φ=1. It can be seen that there is no real change in the exhaust temperature. Even though the blends have a higher latent heat of vaporization and a lower heating value than gasoline, their pressure traces and combustion phasing were relatively similar, and hence the EGTs are not affected significantly.

2.3.2.5 Emission Behavior

Figure 2.19(a) and Figure 2.19(b) show the UHC emissions at gasoline MBT (Φ=1) and fuels' MBT, respectively. The HC emissions are reduced with the use of ABE(6:3:1), which shows the lowest HC emissions. This is due to higher oxygen content, higher volatility and better post-flame oxidation of the fuel, likely due to the impact of acetone. However, with higher butanol content, the HC emissions rise steeply, as shown by ABE(5:14:1) and n-butanol. From Figure 2.19(b), it is seen that similar behavior is observed at all equivalence ratios under the fuels' MBT. The increase of HC with increasing butanol addition is consistent with the literature [34, 38]. This is due to butanol's high latent heat of vaporization, which could reduce the combustion temperature and lead to unburnt fuel.

CO production is primarily controlled by the air/fuel ratio in the cylinder. Mixtures richer than stoichiometric produce high levels of CO and are sensitive to small changes in air/fuel ratio. Mixtures at stoichiometric and leaner produce little CO emissions and are relatively insensitive to air/fuel ratio changes [44]. Figure 2.20(a) and Figure 2.20(b) show the CO emissions at gasoline MBT (Φ=1) and fuels' MBT, respectively. From Figure 2.20(a), it is observed that CO emissions for the alcohol fuels are consistently higher than that for gasoline. ABE(3:6:1) has the highest CO emissions, while that for ABE(6:3:1) is very close to that of ABE0. This is also reflected in the increased BTE exhibited by ABE(6:3:1) and the reduced BTE of ABE(3:6:1). ABE(3:6:1), ABE(5:14:1) and n-butanol show relatively similar CO emissions. From Figure 2.20(b), it is seen that the CO emissions are slightly improved at the fuels' MBTs; however, increasing butanol content results in increasing CO emissions at Φ=1. Decreases in both CO post-flame oxidation and engine power output are responsible for this.

It appears that ABE(6:3:1) can improve both power output and emissions behavior. Also, ABE(6:3:1) and gasoline show roughly similar emissions behavior. This makes sense as fuels with similar CA50 for a given spark timing are known to show similar emissions behavior [61]. The effect of acetone is to keep ABE(6:3:1)'s phasing close to that of gasoline, while improving efficiency and reducing emissions.

Figure 2.21(a) and Figure 2.21(b) show the NO_x emissions at gasoline MBT (Φ=1) and fuels' MBT, respectively. From Figure 2.21(a), no major changes are seen in NO_x emissions between gasoline, ABE(6:3:1) and ABE(3:6:1). With increasing butanol content, NO_x decreases slightly for ABE(5:14:1) and n-butanol. This agrees with the results in [34, 38, 41] where no major changes in NO_x emissions were observed for blends of gasoline and n-butanol (i.e., relatively lower butanol content). Similar behavior is observed across the equivalence ratio range tested, as shown in Figure 2.21(b), where n-butanol consistently shows lowest NO_x emissions. Combustion approaches close to completion under stoichiometric conditions, which leads to higher peak combustion temperatures, and hence the highest NO_x emissions are seen at stoichiometric conditions with a decrease as the equivalence ratio gets relatively richer or leaner. The lower NO_x measured with increasing butanol is in accordance with higher vaporization heat, typical of oxygenated compounds, giving lower air/fuel mixture temperature at intake and, consequently, lower peak temperatures in the combustion chamber. The mixture temperature at intake valve, measured during experiments, is progressively lower with alcohol increasing in blends [38].

2.4 Conclusions

Blends of pure ethanol-free gasoline and ABE (3:6:1 vol. % ratio), as well as neat ABE blends with varying A,B,E content were combusted in a PFI SI engine in addition to pure ethanol-free

gasoline as a baseline for comparison, and the combustion performance and emission behavior were analyzed. The fuels were combusted at 1200 RPM, and 3 bar and 5 bar BMEP and measurements such as brake torque and emissions were made along with in-cylinder pressure data. Each fuel was tested across a range of equivalence ratios, from lean to rich.

In-cylinder pressure data showed that the peak pressure of all the blends was slightly lower than that of gasoline, except for ABE80 which showed a slightly higher and advanced peak relative to gasoline. Blends with lower ABE content featured a slightly longer ignition delay and retarded 50% MFB location, which is attributed to the reduction in laminar flame speed due to ABE's charge cooling effect. Regarding the neat ABE tests, under gasoline MBT, the peak pressure of the ABE blends was slightly higher than that of gasoline, while ABE(3:6:1) also showed an advanced peak relative to gasoline. Under their MBTs, ABE(3:6:1), ABE(5:14:1) and n-butanol showed similar phasing, whereas ABE(6:3:1) and gasoline behaved similarly. Increasing n-butanol showed advanced combustion phasing (CA50) which is attributed to the increase in laminar flame speed due to butanol's higher flame speed.

The BSFC increased steadily with increasing ABE fraction, due to the lower energy content of the blends and thus more fuel was required to match the power output of gasoline. However, ABE20's BSFC was within 5% of that of ABE0's. When using neat ABE blends, the BTE of ABE(6:3:1) was higher than that of ABE0, whereas other fuels showed similar or slightly higher efficiency relative to ABE0.

Emission data showed that CO decreased and UHC initially increased then decreased for all the blends, showing slightly enhanced air/fuel mixing and more fuel being partly oxidized, due to better spray collapse and mixing due to the presence of acetone (low boiling point). With respect to NO_x, no major changes were observed between gasoline and ABE, which was supported by the

minor variations in exhaust gas temperature. With neat ABE blends, increasing n-butanol showed increased HC emissions and increased CO emissions, due to incomplete combustion. On the other hand, ABE(6:3:1) showed reduced HC emissions. CO for ABE(6:3:1) was roughly the same as that of ABE0. With respect to NO_x, no major changes were observed between gasoline and ABE(6:3:1), ABE(3:6:1), which was supported by the minor variations in exhaust gas temperature. However, further increase in butanol content steadily decreased NO_x emissions.

Based on these tests, a small amount of ABE(3:6:1) addition (<40%) can enhance thermal efficiency and reduce emissions. In the neat form, however, acetone addition could improve combustion quality significantly. This study affirms the potential of ABE to be used as an alternative fuel in SI engines.

Table 2.1 List of clostridia microorganisms with corresponding typical fermentation broth ABE concentrations [20, 21]

Microorganism	Acetone (g/L)	Butanol (g/L)	Ethanol (g/L)	Total solvent production (g/L)
Clostridium acetobutylicum (JB200)	1	19.2	1.7	21.9
Clostridium acetobutylicum (CGMCC 5234)	5.9	12.3	1.6	19.8
Clostridium acetobutylicum (ATCC824)	5	11	1	17
Clostridium acetobutylicum (BKM19)	4.4	17.6	10.5	32.5
Clostridium acetobutylicum (260)	6.3	13.2	0.8	20.3
Clostridium saccharobutylicum (DSM 3864)	4.6	10.1	1.4	16.1
Clostridium saccharobutylicum (262)	3.2	10.4	0.7	14.3
Clostridium butylicum (NRRL 502)	6.7	12.5	0.5	19.7
Clostridium beijerinckii (8032)	3.4	10.5	0.7	14.6
Clostridium beijerinckii (BA101)	3.5	13.9	0.5	18

Table 2.2 Summary of LLE using fuels as extractants

Extractant	Reference
Soybean-derived biodiesel	Adhami et al. 2009 [16]
Crude palm oil	Ishizaki et al. 1999 [17], Crabbe et al. 2001 [18]
Biodiesel	Li et al. 2010 [27], Yen et al. 2013 [22]
Sunflower oil biodiesel	Grobben et al. 1993 [19]
Gasoline components (MTBE, ETBE, TAME, TAFE)	Kurkijärvi et al. 2014 [24]

Table 2.3 Engine Specifications

Displaced volume	575 cc
Stroke	90.1 mm
Bore	90.3 mm
Connecting Rod	150.7 mm
Compression ratio	9.6:1
Number of Valves	4
Fuel Injection	PFI

Table 2.4 Properties of Individual Fuels [44, 60]

Parameter	Gasoline	Ethanol	Butanol	Acetone
Chemical Formula	C_4-C_{12}	C_2H_5OH	C_4H_9OH	C_3H_6O
Composition (C,H,O) (Mass %)	86, 14, 0	52, 13, 35	65, 13.5, 21.5	62, 10.5, 27.5
Lower Heating Value (MJ/kg)	43.4	26.8	33.1	29.6
Density (kg/m^3)	715-765	790	810	790
Energy Density (MJ/l)	32.20	21.17	26.81	23.38
Octane Number ((R+M)/2)	90	100	87	-
Boiling Temperature (°C)	25-215	78	118	56.2
Latent Heat of Vaporization (25°C) (kJ/kg)	380-500	904	716	518
Self-Ignition Temperature (°C)	~300	420	343	465
Stoichiometric Air/Fuel Ratio	14.7	9.0	11.2	9.5
Laminar Flame Speed (LFS) (cm/s)	~33[a]	~39[a]	~48[b]	~34[c]
Mixture Calorific Value (MJ/m^3)	3.72	3.85	3.82	4.04
Ignition Limits in Air (vol. %) [Lower-Upper]	0.6 - 8	3.5 - 15	1.4 - 11.2	2.6 - 12.8
Solubility in Water at 20°C (ml/100 ml H_2O)	<0.1	Fully Miscible	7.7	Fully Miscible

[a] p = 1 atm, T = 325 K [44]; [b] p = 1 atm, T = 343 K [60] ; [c] p = 1 atm, T = 298 K [60]

Table 2.5 Properties of ABE-gasoline blends tested (calculated)

Fuel Type	Specific Gravity	Lower Heating Value (LHV) (MJ/kg)	Energy Density of Stoichiometric Air-Fuel Mixture (MJ/l)	Stoichiometric Air/Fuel Ratio
ABE0	0.739	43.44	31.78	14.7
ABE20	0.751	41.05	30.85	13.84
ABE40	0.763	38.74	29.60	12.98
ABE60	0.776	36.50	28.32	12.13
ABE80	0.788	34.33	27.05	11.27

Table 2.6 Properties of neat ABE Blends (Calculated)

Fuel Type	Specific Gravity	Lower Heating Value (LHV) (MJ/kg)	Energy Density (MJ/l)	Stoichiometric Air/Fuel Ratio	Butanol Vol. %	Acetone Vol. %
Gasoline	0.739	43.44	31.68	14.65	0	0
ABE(6:3:1)	0.796	30.3	24.1	9.94	30	60
ABE(3:6:1)	0.802	31.45	25.22	10.36	60	30
ABE(5:14:1)	0.804	31.93	25.67	10.64	70	25
n-Butanol	0.810	33.1	26.81	11.06	100	0

Table 2.7 Test conditions

Engine Speed	1200 RPM
Load (BMEP)	3 bar, 3.75 bar, 5 bar
Equivalence Ratio	0.83 – 1.2
Spark Timing	Default Gasoline Timing, MBT Timings
Fuel Pressure	3 bar

Table 2.8 Neat ABE Fuel MBT Timings

Fuel	MBT @ 3 bar BMEP	MBT @ 5 bar
Gasoline	18° BTDC	24° BTDC
ABE(6:3:1)	17.7	23.6
ABE(3:6:1)	17.6	23.5
ABE(5:14:1)	17.5	23.4
n-Butanol	17.4	23.3

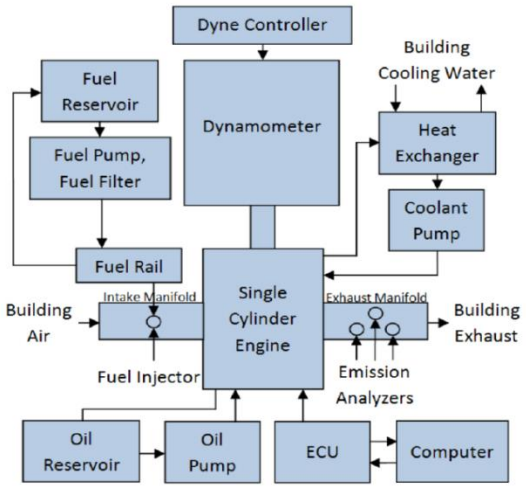

Figure 2.1 Single cylinder engine layout [39]

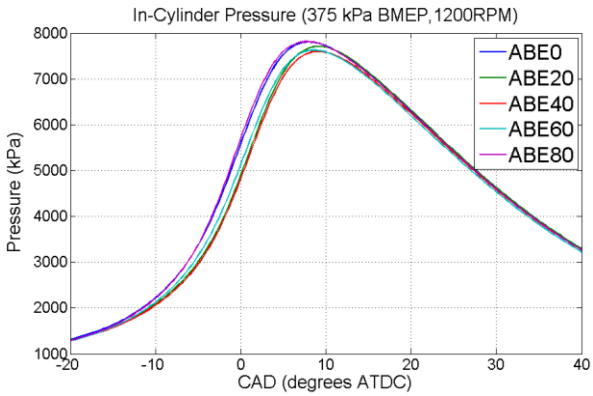

Figure 2.2 Pressure traces of different fuels

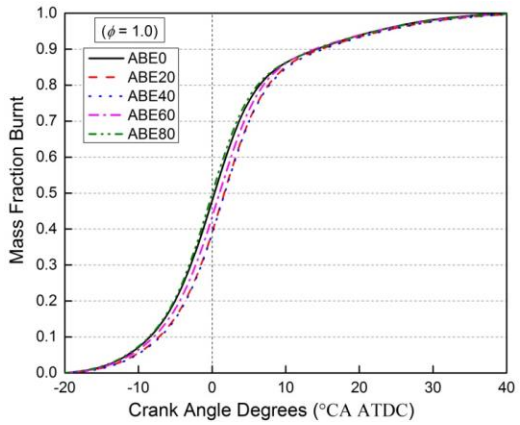

(a)

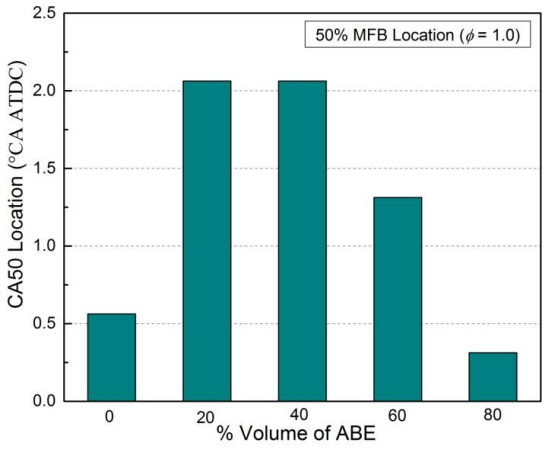

(b)

Figure 2.3 (a) MFB profiles for tested fuels (φ = 1), (b) CA50 location (φ = 1)

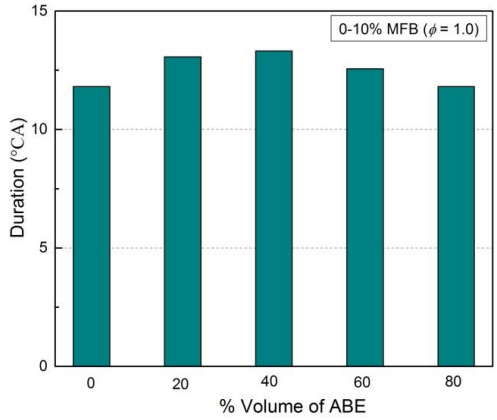

(a)

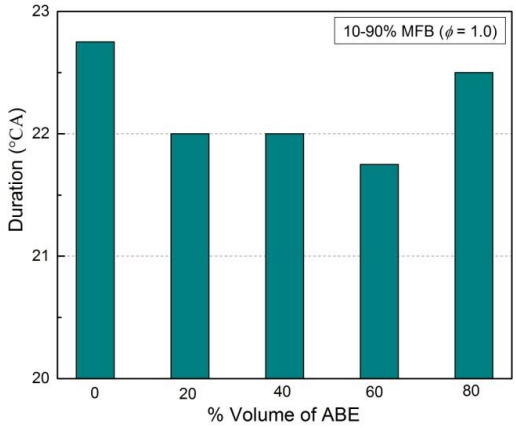

(b)

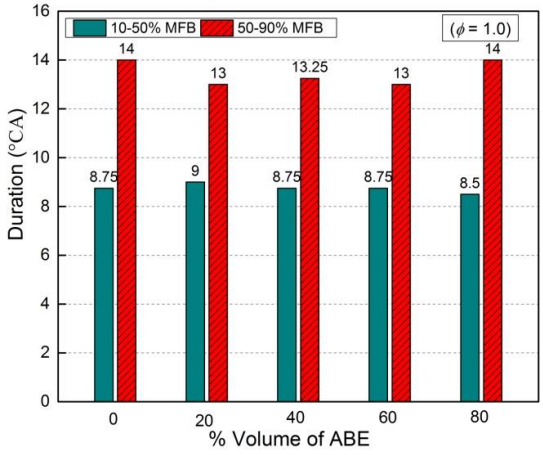

(c)

Figure 2.4 (a) 0-10% MFB, (b) 10-90% MFB, (c) combustion duration split (φ = 1)

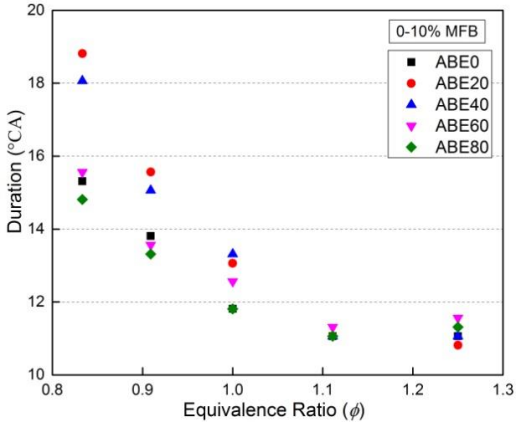

(a)

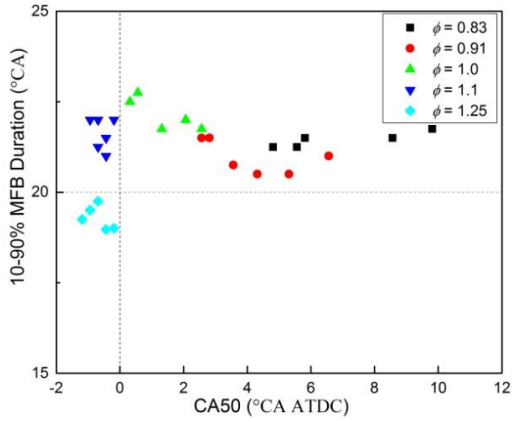

(b)

Figure 2.5 (a) 0-10% MFB, (b) 10-90% MFB vs CA50 (varying equivalence ratios)

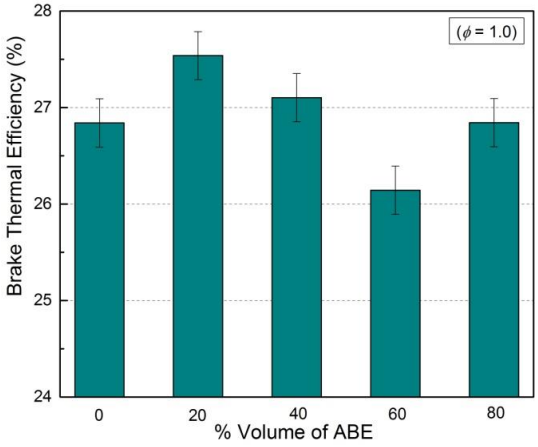

Figure 2.6 BTE of different fuels (φ = 1)

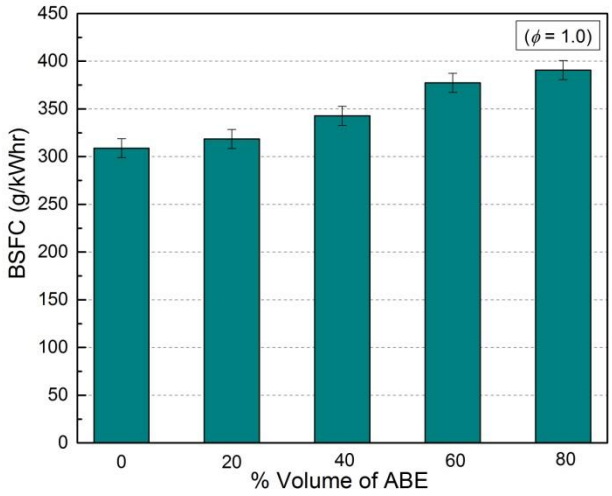

Figure 2.7 BSFC of different fuels (φ = 1)

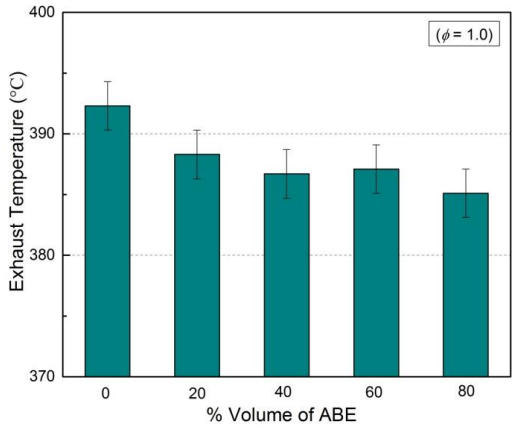

Figure 2.8 EGT of different fuels (φ = 1)

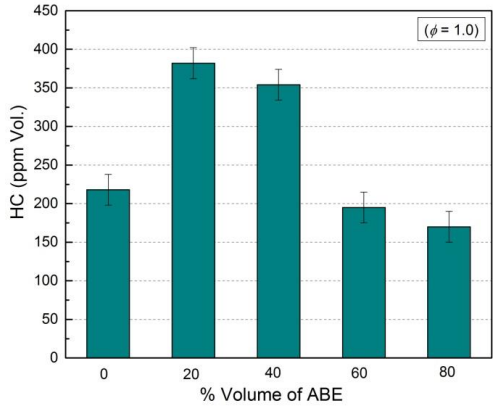

(a)

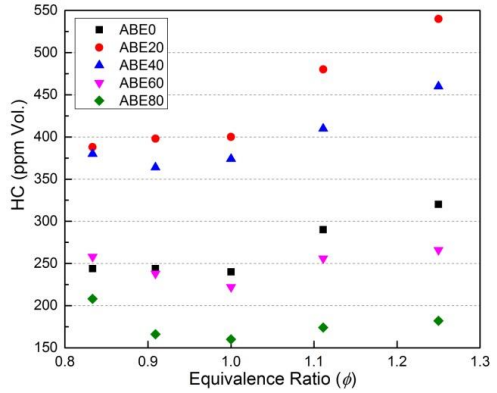

(b)

Figure 2.9 UHC emissions of different fuels (a) φ = 1 (b) varying equivalence ratio

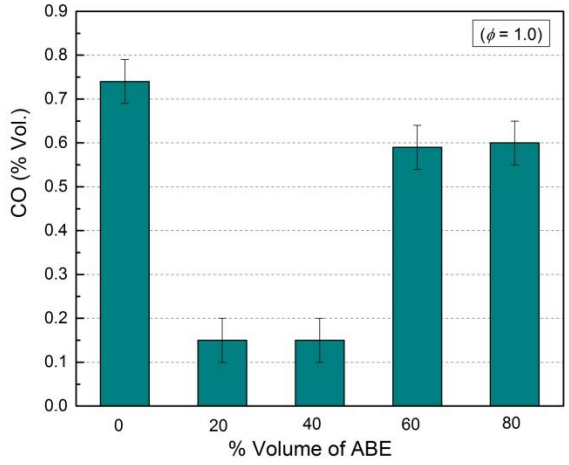

(a)

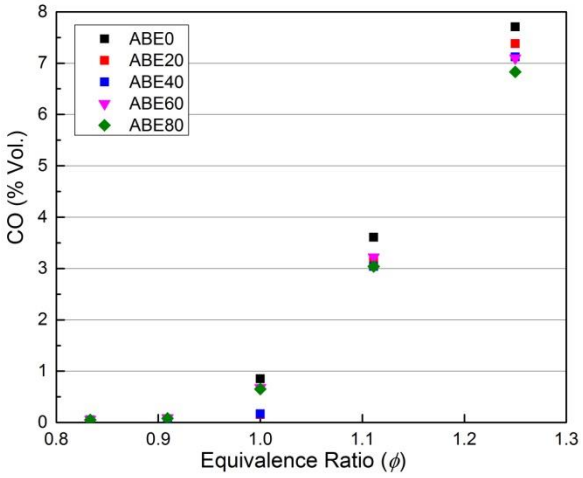

(b)

Figure 2.10 CO emissions of different fuels (a) φ = 1 (b) varying equivalence ratio

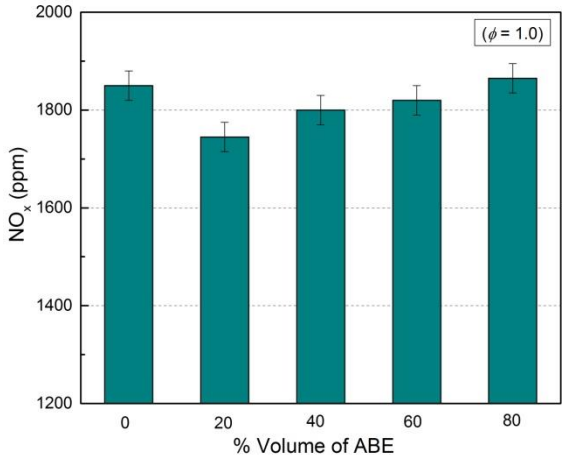

(a)

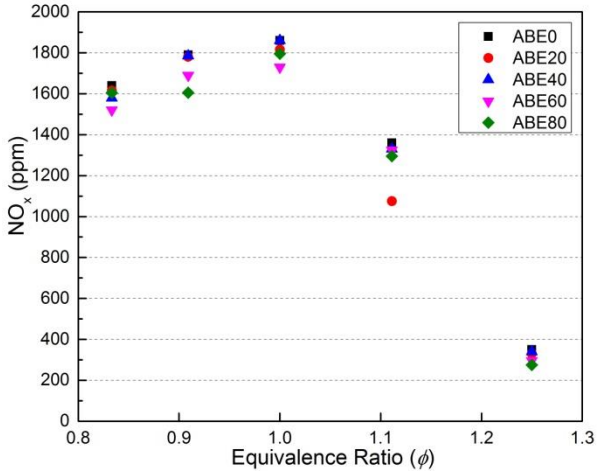

(b)

Figure 2.11 NO_x emissions of different fuels (a) φ = 1 (b) varying equivalence ratio

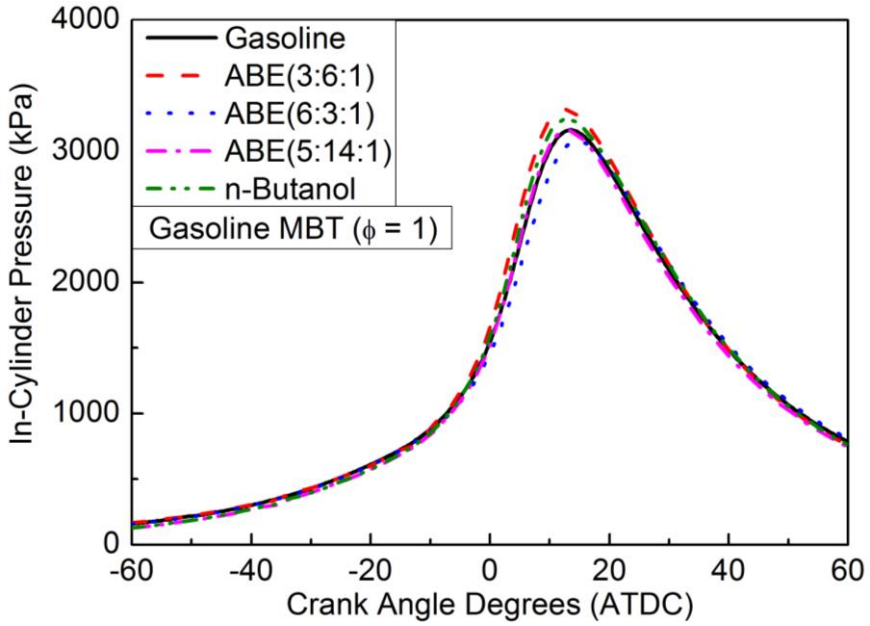

(a)

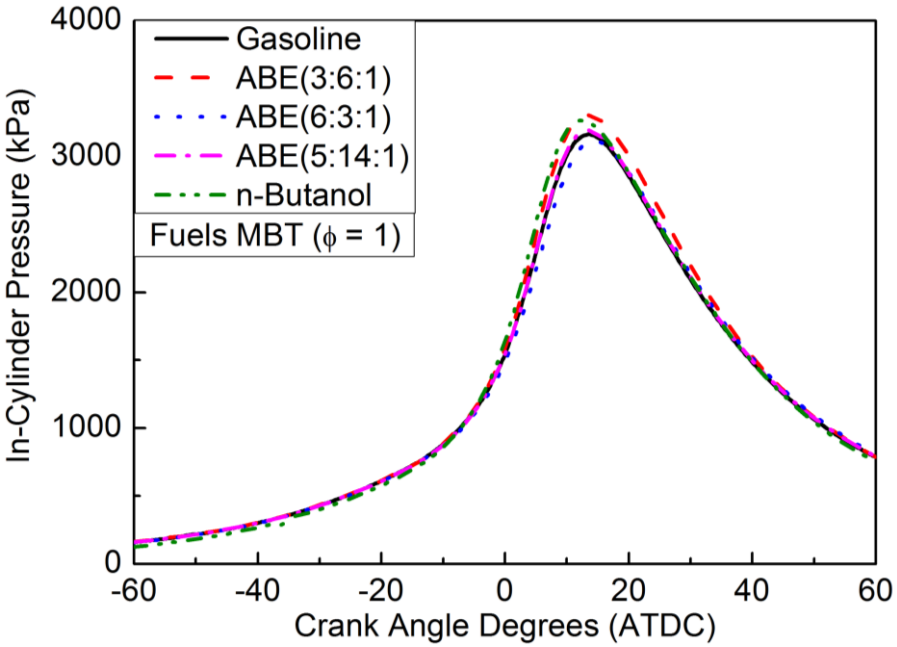

(b)

Figure 2.12 In-Cylinder Pressure at 3 bar, 1200 RPM (a) Gasoline MBT (b) Fuels MBT

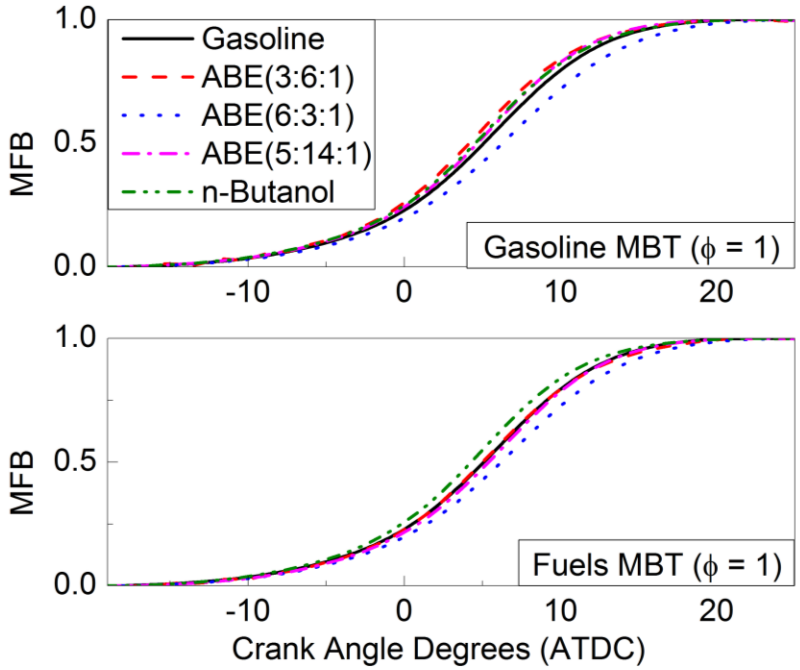

Figure 2.13 MFB profiles – 3 bar, 1200 RPM, Φ = 1 at Gasoline MBT (top) and Fuels MBT (bottom)

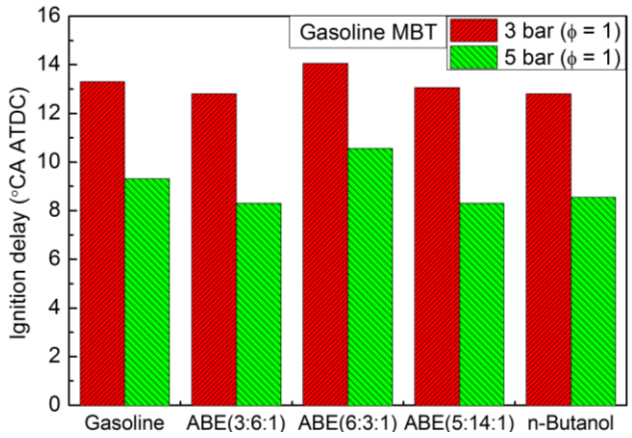

(a)

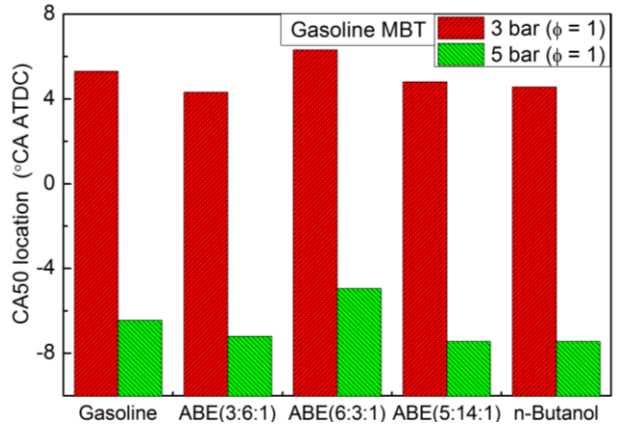

(b)

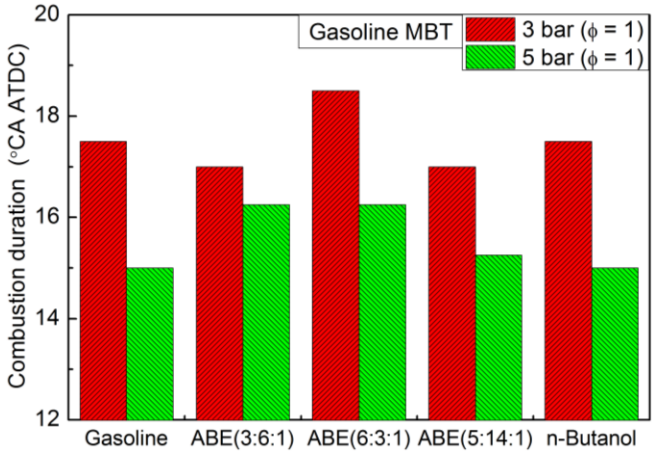

(c)

Figure 2.14 (a) 0-10% MFB Duration, (b) CA50 Location, (c) 10-90% MFB Duration

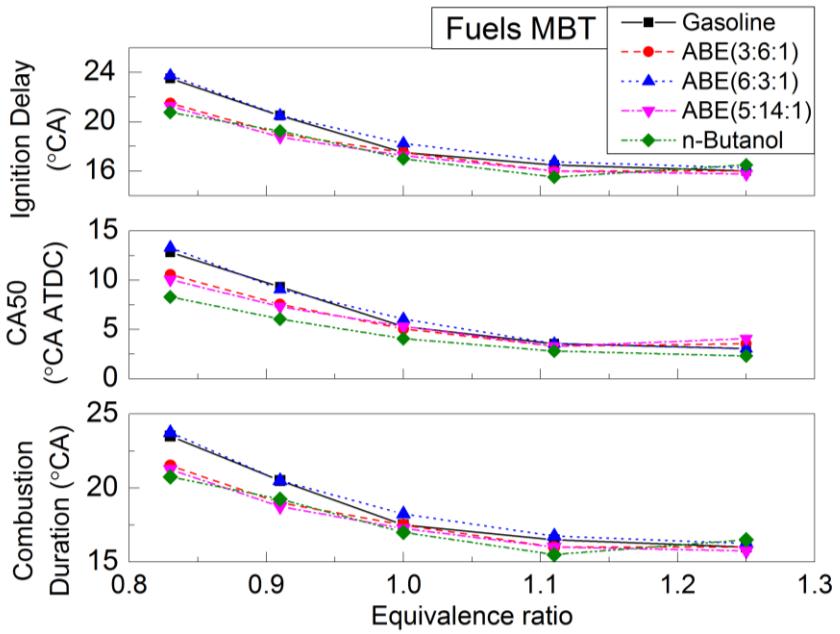

Figure 2.15 (a) 0-10% MFB Duration (top), CA50 Location (middle), 10-90% MFB Duration (bottom) at 1200 RPM, 3 bar BMEP

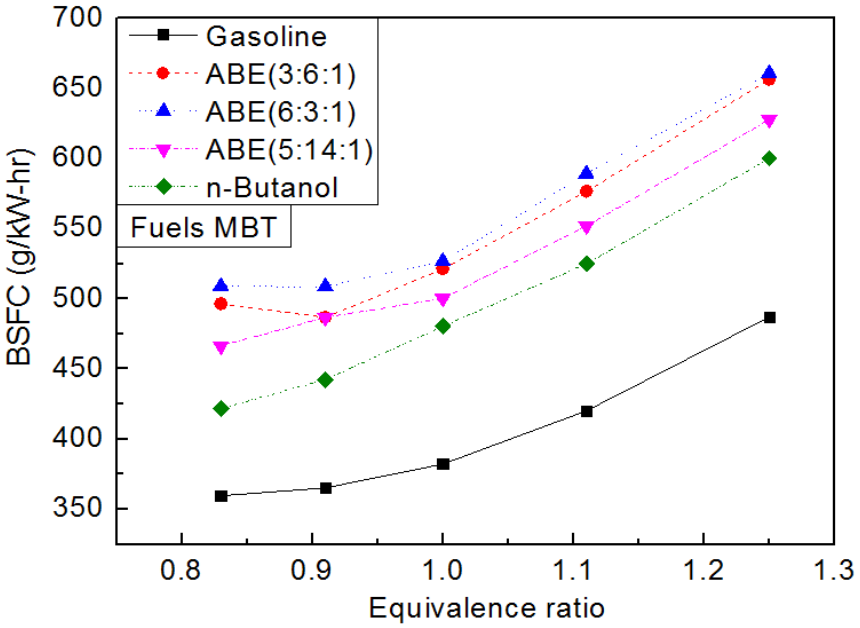

Figure 2.16 BSFC at 1200 RPM, 3 bar BMEP

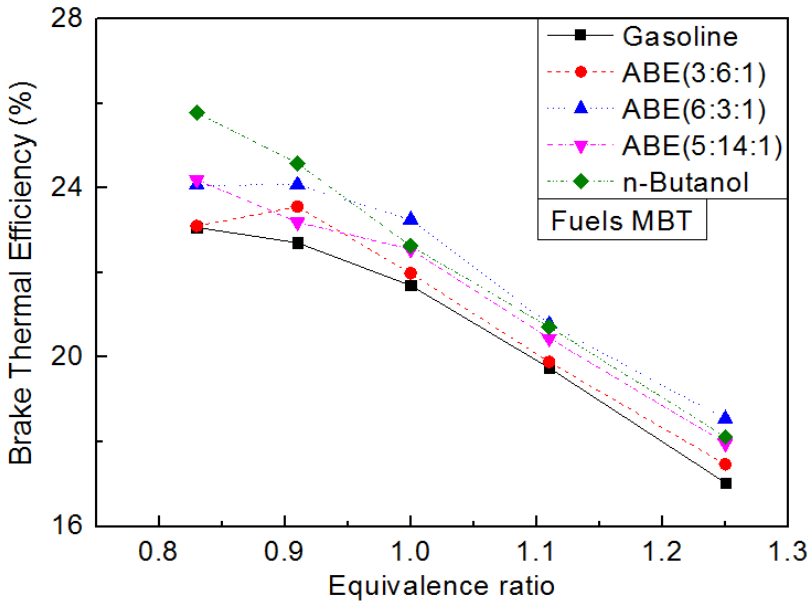

Figure 2.17 BTE at 1200 RPM 3 bar BMEP

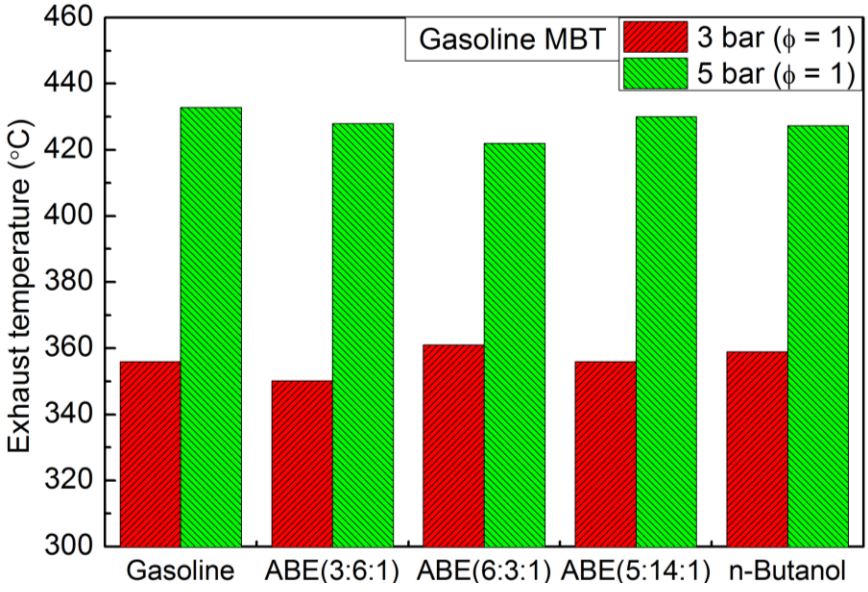

Figure 2.18 EGT at Φ=1, at 3 and 5 bar BMEP.

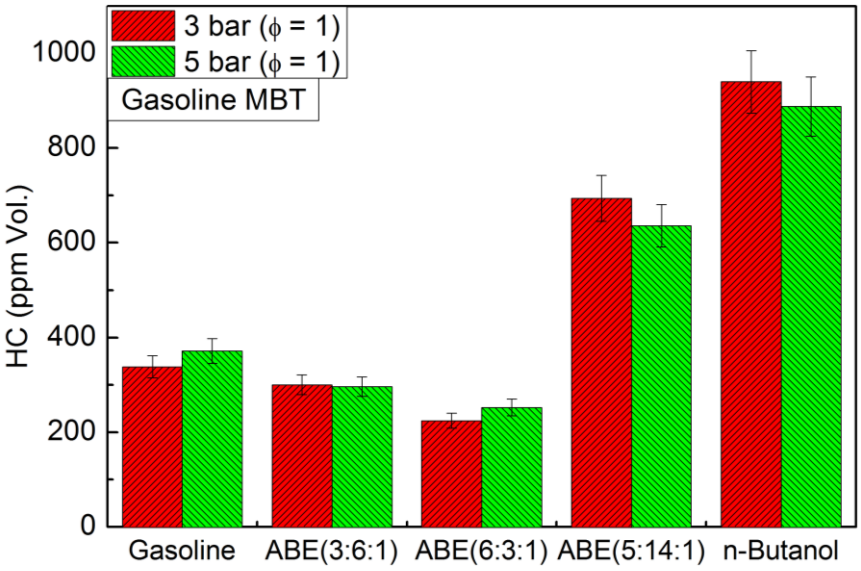

(a)

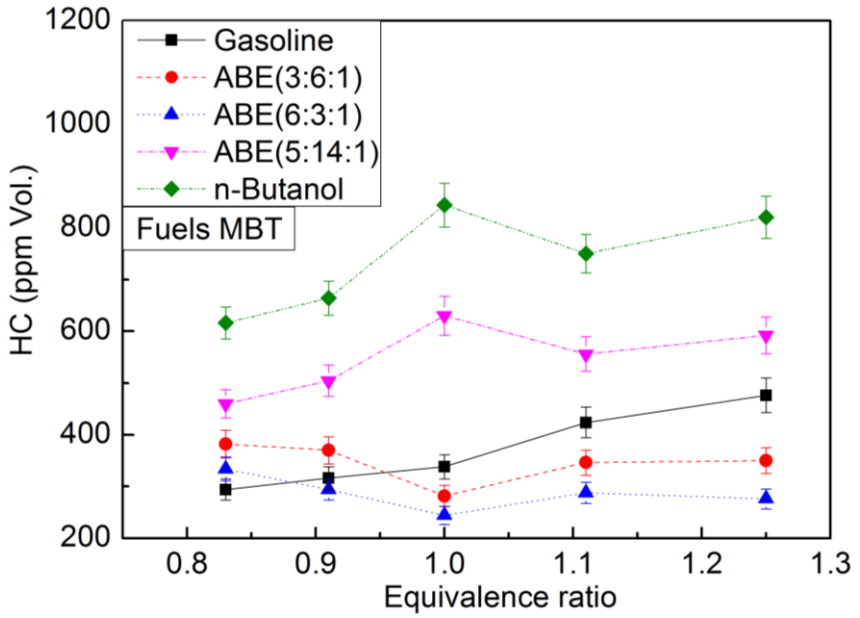

(b)

Figure 2.19 UHC emissions at (a) gasoline MBT, Φ=1; (b) fuels MBT, 3 bar BMEP (bottom)

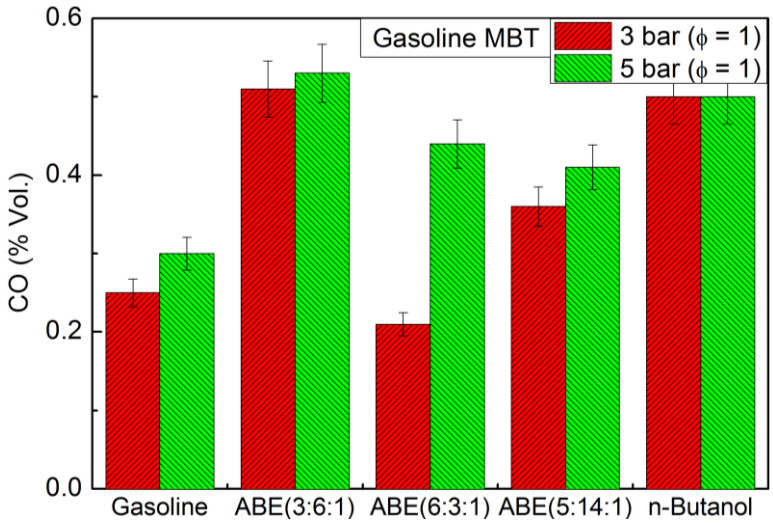

(a)

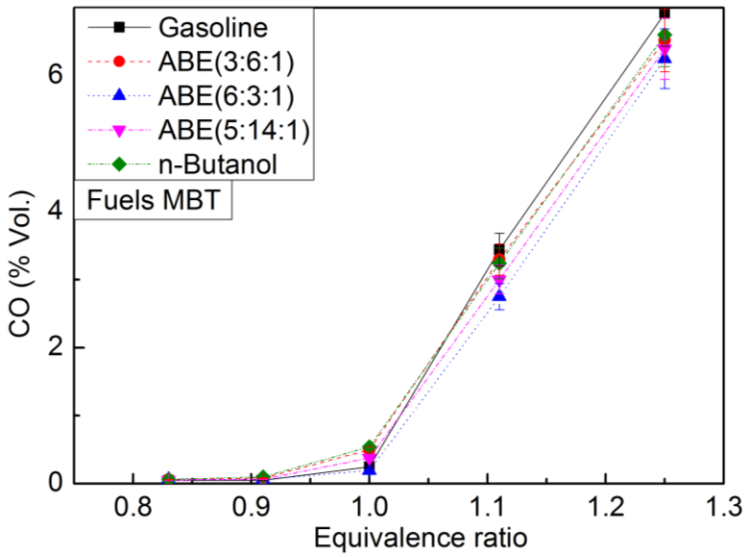

(b)

Figure 2.20 CO emissions at (a) gasoline MBT, Φ=1; (b) fuels MBT, 3 bar BMEP (bottom)

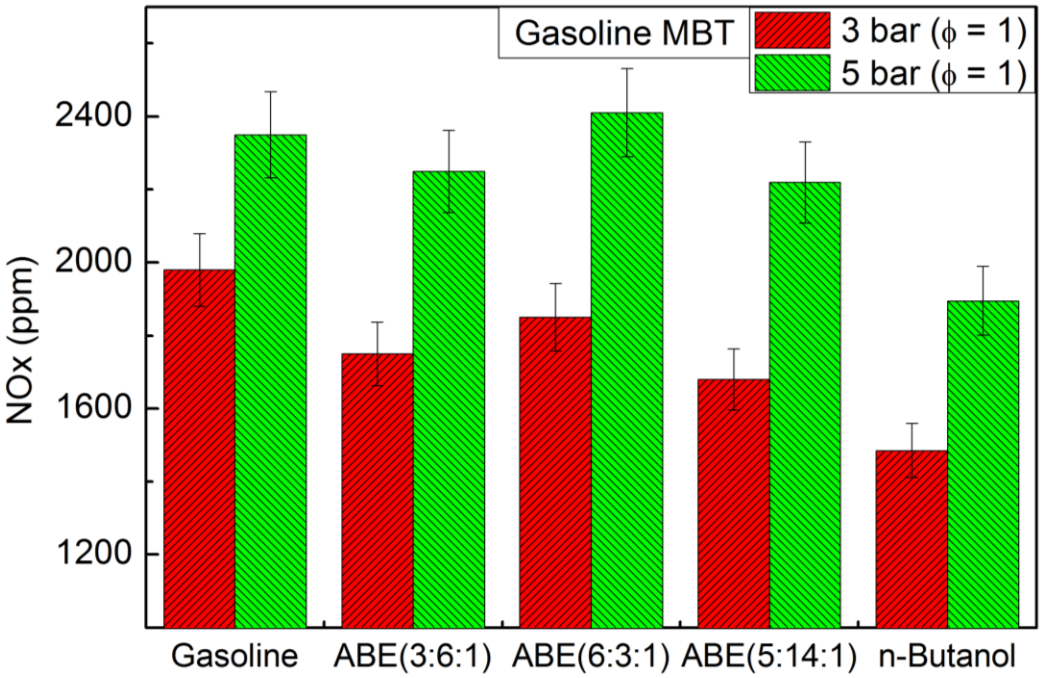

(a)

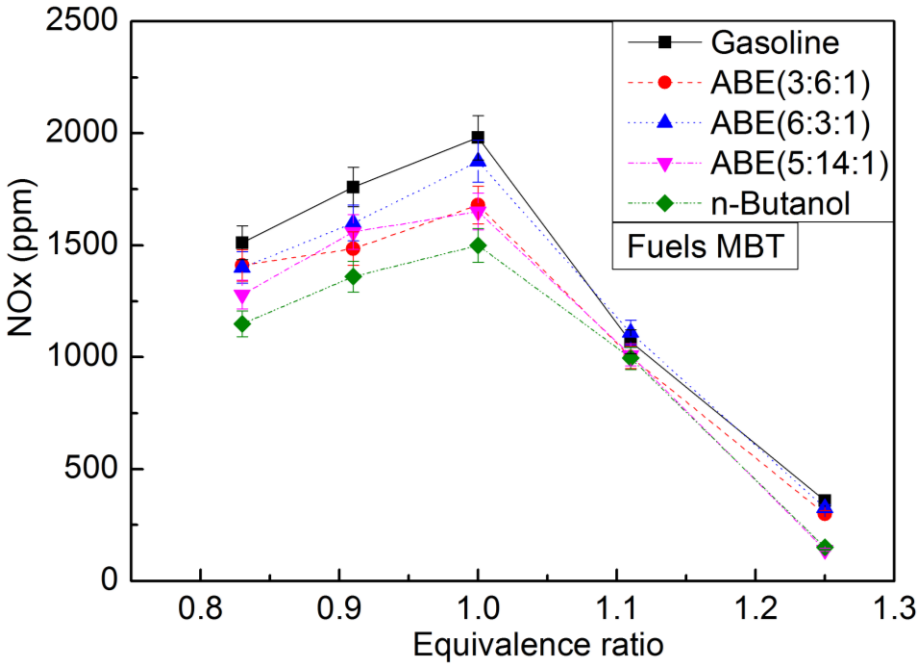

(b)

Figure 2.21 NO_x emissions at (a) gasoline MBT, Φ=1; (b) fuels MBT, 3 bar BMEP (bottom)

Chapter 3 Diesel/CNG Dual-Fuel Combustion

A dual fuel engine (as referred to in this study) is an internal combustion engine in which the primary fuel (in this case, natural gas) is premixed with air or directly injected into combustion chamber, and ignited by injecting a small amount of pilot fuel (which is diesel in this case) as the piston approaches top dead center (TDC). Natural gas is a clean, low CO_2 emitting fuel with superior resource availability. The advantages of natural gas include its widespread availability, its reduced environmental burden relative to conventional fuels (cleaner combustion) and its applicability in conventional diesel and gasoline engines. Dual-fuel CNG/diesel combustion in CI engines has shown the ability to substantially reduce the NO_x emission and at the same time produce very low PM emissions; which is extremely difficult to achieve in conventional diesel engines. Although natural gas/diesel dual-fuel combustion has been studied widely, there is still room for improvement in the quality of dual-fuel combustion, specifically with respect to efficiency. In this study, CNG/diesel dual-fuel combustion has been studied in a single-cylinder CI engine under various CNG substitution ratios and diesel injection strategies at a wide range of engine operating conditions and acquiring and analyzing in-cylinder pressure, performance and emission data. The chapter starts with the literature review on natural gas and previous relevant studies. The experimental setup will be detailed next, followed by the results and discussion. The following topics will be addressed:

- Performance and emission tests of CNG/diesel dual-fuel combustion under various CNG substitution ratios
- Diesel injection strategy optimization for optimum dual-fuel combustion

3.1 Literature Review

3.1.1 Natural Gas

Among the various alternative fuels, natural gas is very promising and highly attractive in the transportation sector. Firstly, natural gas is available in several areas worldwide at encouraging prices. Beside the oil fields and natural gas fields, the natural gas industry is producing gas from increasingly more challenging resource types: sour gas, tight gas, shale gas, coal-bed methane, and methane gas hydrate [62]. Secondly, although the main component of natural gas, namely methane, is a greenhouse gas, natural gas still is an eco-friendly fuel. It can contribute to the reduction of CO_2 emission because it exhibits the lowest carbon-to-hydrogen ratio of all the fossil fuels. Natural gas can also substantially reduce the NO_x emission and at the same time produce almost zero smoke and PM; which is extremely difficult to achieve in conventional diesel engines. On the other hand, in order to avoid its own environmental pollution, it is important to reduce the leakage of natural gas. Thirdly, natural gas is not prone to knock due to its high methane number under normal circumstances. Therefore, it can be used in engines with relatively high compression ratio and obtain a higher thermal efficiency compared with that of normal gasoline engines [63].

Natural gas is produced from gas wells or tied in with crude oil production [64]. The main component of natural gas is methane, which is the simplest hydrocarbon. Natural gas is a mixture of a variety of gases. It contains some kinds of lightweight alkanes, such as methane, ethane, propane, n-butane and isobutane, and pentanes. It may also contain carbon dioxide, nitrogen and trace amounts of water vapor. The composition and content of natural gas varies slightly depending on the source and the production process. Normally, methane accounts for 87–96% of natural gas. Therefore, the physicochemical properties of natural gas are very similar to methane. Natural gas

is an environmentally friendly alternative fuel for transportation because it contains less carbon per unit of energy than any other fossil fuel and thus produces lower CO_2 emission per vehicle mile traveled. However, it is a little difficult for natural gas to be used in compression ignition engine due to its high auto-ignition temperature. However, natural gas is very suitable for spark ignition engine due to its excellent anti-knock quality and it does not require any modification to the engine. [63, 64, 66].

CNG has long been used in stationary engines, but the application of CNG as a transport engine fuel has been considerably advanced over the last decade due to several reasons. The first reason is availability, the second is its environmental compatibility and the third is that it can be used in conventional diesel and gasoline engines. According to [65], operating costs are another reason, where natural gas powered vehicles theoretically have a significant advantage over petroleum-powered vehicles; the basis for this argument is the lower cost per energy unit of natural gas compared to that of petroleum. There are also several problems associated with compressed natural gas applications such as onboard storage due to low energy volume ratio, knock at high loads and high emission of methane and carbon monoxide at light loads. However, proper design, fuel management and exhaust treatment techniques can overcome these issues.

The octane rating of natural gas is about 130, meaning that engines could operate at compression ratios of up to 16:1 without “knock” or detonation. The means of natural gas used in spark ignition engine are already well established, whereas its use in compression ignition engine is still under development. The usage of natural gas in diesel engines suffers from poor ignition characteristics due to its high auto-ignition temperature and low cetane number compared to that of diesel fuel [66]. Therefore, an ignition source is always needed to ignite the natural gas in the cylinder.

According to the way of inducting natural gas into the cylinder and the ignition source, there are two primary methods for applying natural gas in diesel engines. They are:

(a) Dual fuel — in this mode, natural gas is inducted or injected in the intake manifold to mix uniformly with air and then is introduced to the cylinder and ignited by the direct injected pilot fuel with high cetane number [71 - 75].

(b) High pressure direct injection (HPDI) — in this mode, a small amount of pilot diesel is firstly injected late in the compression stroke and then natural gas is directly injected. At some point during the time interval between the two injections or early in the natural gas injection, the diesel fuel auto-ignites, providing the ignition source to initiate natural gas combustion [67, 68, 70].

3.1.2 Previous work

Dual-fuel diesel engines using natural gas are an attractive low polluting option for diesel engines, because natural gas is a clean, low CO_2 emitting fuel with superior resource availability. Natural gas is a very cheap fuel, which has low greenhouse gas emissions due to its low C/H ratio, as well as low NO_x and soot emissions [68, 68, 70]. Dual fuel operation with port injection of natural gas and direct pilot injection of diesel fuel has been widely investigated in recent years. Natural gas/diesel dual-fuel combustion has been proved to be one of the most effective methods to improve fuel economy and emissions compared to conventional CI engines [71, 72, 73, 74].

Previous studies on natural gas/diesel dual-fuel combustion have shown that there is a slight reduction of BTE in comparison with pure diesel combustion [71, 72, 73]; however, it could be improved at high loads [74]. It has been reported that NO_x concentration under dual-fuel combustion is much lower than that of pure diesel combustion due to the decreased local

temperatures. Significantly decreased soot emissions were also reported [75]. On the other hand, THC and CO emissions have been demonstrated to be much higher than that of pure diesel operation [76, 77, 78]. Yang et al. [79, 80] studied the effects of diesel pilot injection timings with different natural gas injection timings under low load conditions and found that an advanced pilot injection timing obtained better BTE and emissions except NO_x due to the premixed combustion of pilot fuel.

Papagiannakis et al. [81] found that the increase of natural gas proportion resulted in lower NO_x emissions compared to that under normal diesel operation, especially at high load, but led to higher CO and UHC emissions at low and intermediate loads. Liu et al. [82] studied the effects of pilot fuel quantity with optimized pilot injection timing. In their results, dual fuel mode decreased NO_x emissions by 30% on average compared to the pure diesel mode. The THC emissions were much higher than that of pure diesel mode, where around 90% of it was unburned methane. However, it was reduced significantly with the decrease of natural gas quantity. Cheenkachorn et al. [83] conducted dual-fuel experiments on a heavy-duty turbocharged diesel engine. In order to avoid knocking, the proportion of natural gas was decreased with increasing engine speed, and the maximum portion was 77.90% at 1300 rpm. They also concluded that the BTE was on average 3.5% less than that of pure diesel operation. The dual fuel operation showed lower volumetric efficiency than diesel fuel operation. Imran et al. [84] investigated emissions of natural gas/diesel dual-fuel operation speed and load sweeps. The THC emissions were significantly higher in all cases at low load conditions across all engine speeds compared to that of pure diesel operation. However, decreased THC emissions were reported with increasing load at constant speed. Yoshimoto et al. [85, 86, 87] investigated natural gas dual-fuel combustion using different pilot fuels. It was found that for CNG substitution under 75%, the efficiency was similar to that of pure

diesel. UHC and CO emissions increased with increasing CNG substitution, while soot emissions were significantly decreased. They also found that NO_x emissions increased with increasing CNG% due to more premixed combustion.

Although natural gas/diesel dual-fuel combustion has been studied widely, there is still room for improvement in the quality of dual-fuel combustion, specifically with respect to efficiency. The goal of this study is to maximize dual-fuel efficiency by studying engine performance and emissions under various CNG substitution ratios, multiple pilot fuel injection timings as well as different load and speed conditions.

3.2 Experimental Setup

Experiments in this study were carried out in an AVL 5402 single-cylinder diesel engine. Table 3.1 shows some key engine specifications. External fuel, lubrication, and cooling systems are used as shown in the engine schematic. The engine was modified to run diesel/CNG dual-fuel mode by adding a SOLARIS CNG injection system (Fuel Injection System + ECU). The engine is coupled to a GE type TLC-15 class 4-35-1700 dynamometer capable of delivering up to 14.9 kW (20 HP) and absorbing up to 26.1 kW (35 HP) at a maximum rotational speed of 4500 RPM. The dynamometer is controlled by a DyneSystems DYN-LOC IV controller. In-cylinder pressure is measured using a Kistler type 6125B pressure transducer and an AVL 3057-AO1 charge amplifier and indexed against a crankshaft position signal from a BEI XH25D shaft encoder.

A schematic of the engine setup is shown in Figure 3.1. To establish full communication with the engine ECU (AVL RPEMS), ETAS INCA is used for the development and calibration of the control and diagnostic parameters in the engine ECU. With INCA, data acquisition and real-time recording of many engine operating conditions present in the ECU can be realized. The hardware

connection between the program and ECU is made possible with the ETAS ES580 interface card. The decompressed CNG from the CNG tank is injected to the intake manifold by the SOLARIS CNG injection system. By using a computer-based control program (Solaris Diesel V4), the CNG amount under different speed and load can be adjusted. A mass flow meter (Omega) between the CNG tank and CNG injector monitors the CNG flow rate. The diesel fuel flow rate was measured using a specific fuel consumption device built in-house (time taken to consume a certain volume of diesel is measured 5 times and averaged).

The CNG substitution (%) was defined as the percentage of heat energy from CNG, in the total heat energy available in the cylinder (based on load). Under a load of 20 mg/cycle (medium load), a CNG flow rate of 15 L/min is equivalent to 70% CNG substitution ($\Phi = 0.68$). When substituting for diesel, the total combined energy input was kept the same. For example, 70% CNG indicates that 70% of the energy input at that condition was provided by CNG.

In-cylinder pressure traces shown are the average of 25 combustion cycle pressure traces. NO_x and λ (and Φ) measurements were conducted using a Horiba MEXA-720 NO_x non-sampling type meter in the exhaust manifold of the engine. The measurement range for NO_x is 0-3000 ppm with ±30 ppm accuracy for 0-1000 ppm, ±3% accuracy for 1000-2000 ppm, and ±5% accuracy for 2000-3000 ppm. Measurements of unburned hydrocarbons and carbon monoxide were made using a Horiba MEXA-554JU sampling type meter. A probe was fabricated to fit in the exhaust manifold of the engine that allowed the sampling tube to transport the exhaust gases to the meter. The measurement range is 0-10,000 ppm for unburned hydrocarbons, 0.00-20.00% by volume for carbon dioxide, and 0.00-10.00% by volume for carbon monoxide. Exhaust gas temperature measurements were made using a type-K thermocouple located in the exhaust manifold.

Soot measurement is performed using a standard filter paper method. Samples of raw exhaust gas are drawn through a 7/8″ round filter paper using -vacuum pump. The filter paper discs are cut from rectangular strips of filter paper supplied by Grainger Industrial Supply (#6T167) and the filter holder is taken from a Bacharach True-Spot smoke meter adapted to the new setup. Condensed water or oil is removed from the sampling line by a line filter installed after the vacuum pump. After sample collection, the filter blackening is to be measured with a digital scanner. The paper blackening (PB) is defined in Eqn. (3.1):

$$PB = (100 - R_R)/10 \quad \ldots (3.1)\text{ , where}$$

$$R_R = \left(\frac{R_p}{R_f}\right) \times 100\ \% \quad \ldots (3.2)$$

R_p = reflectometer value of sample

R_f = reflectometer value of un-blackened paper

R_R = relative brightness of the sample (relative radiance factor)

A flow meter is used to monitor the sampling flow rate, which is controlled by a needle valve on the inlet of the vacuum pump. Based on the expected soot content, the flow rate and sampling duration are selected to achieve an effective sampling length of 405 mm. With the sampled volume at 298 K and 1 bar, the paper blackening value can be considered as the filter smoke number (FSN). More details can be found in [88].

Measurements of brake torque, lambda, and NO_x were averaged of a 60-second period while UHC, CO and EGT measurements were recorded directly from the emissions analyzer. In the figures, error bars represent the variability in the data in terms of standard deviation between runs. In addition, in-cylinder pressure traces were taken for all fuels to examine the combustion characteristics. The experiments were performed 3 times and these datasets were then averaged.

The tests were performed in a temperature-controlled laboratory; so the effects of humidity were assumed to be negligible. The engine was allowed to run at every operating condition for an extended period to ensure steady state measurements

3.3 Results and Discussion

The dual-fuel experiments were performed using Ultra low sulfur diesel (ULSD) and CNG. 99% Methane (CH_4) gas was used to emulate CNG. The CNG was injected into the intake manifold, and gets inducted into the combustion chamber along with the air. The goal of these experiments was to maximize the efficiency. This was done as follows – the CNG substitution rate (based on energy) was increased from 40% to 90% at fixed engine operating conditions, to identify the optimum CNG substitution rate. After that, using that rate, a main injection timing sweep was performed. Then holding the CNG rate and the optimum main timing constant, a pilot timing sweep was performed. The combustion behavior was also compared between single, double and triple diesel injections. Finally, a load and speed sweep at the optimum CNG rate and timings were performed.

3.3.1 CNG Substitution Rate Sweep

Figure 3.2(a) shows combustion pressure and heat release rate (HRR) for different CNG substitution rates. These tests were performed at 1200 RPM, using a 20 mg/cycle baseline, at an injection timing of 4^0 BTDC. It is observed that the combustion phasing progressively gets retarded with increasing CNG substitution rate. As far as the peak pressure is concerned, it increases with increasing CNG up to 70% substitution, after which it starts decreasing. Figure 3.2(b) shows the ignition delay and combustion duration under different substitution rates. The

ignition delay gets progressively larger, whereas the combustion duration gets shorter up to 70% CNG, but starts increasing with further CNG substitution. The difference in ignition delay between 0% CNG and 40% CNG is nearly 1.5 degrees; however, further increasing the CNG substitution increases the ignition delay marginally. As CNG substitution is increased from 40% to 90%, the overall change in ignition delay is about 1.2 degrees. Combustion appears to be deteriorated for 90% CNG substitution, likely due to amount of diesel injected not being enough for igniting the entire CNG/air mixture.

Figure 3.3 shows the performance and emissions under different CNG substitution rates. With respect to efficiency, it can be seen that the ITE decreases first (relative to diesel (single injection)) then increases with increasing CNG substitution up to 70% then decreases further with 80 and 90% CNG substitution, with the ITE being maximum for 70% CNG substitution. Figure 3.2(b), it can be observed that 70% CNG has the smallest combustion duration, which could explain the higher ITE (approaching constant volume combustion).

The NO_x emissions increase progressively with increasing CNG substitution until it becomes lower again at 90% CNG substitution. This is possibly due to deteriorated combustion at 90% substitution, as seen from the reduced HRR curve for this case. This NO_x trend follows the peak pressure trend fairly. The literature suggests that NO_x steadily decreases with Diesel/CNG dual-fuel combustion; however, in this experiment the CNG% is increased at a constant load. Therefore, higher CNG substitution effectively means a higher CNG flow rate (while air flow remains constant) which steadily increases the global fuel equivalence ratio and further enhances premixed combustion. From the HRR curves, it can be observed that dual fuel operation results in longer ignition delays (Figure 3.2(b)) and the promotion of premixed combustion. Then the amount of heat released during the premixed combustion (combustion of the CNG-air pre-mixture) increases.

As a result, the local gas temperatures would rise and this results in an increase in NO_x concentrations [85, 86, 87].

The UHC emissions increase steadily with CNG substitution. With dual fuel operation, unburned mixture easily enters quenching regions such as the cylinder wall and piston top clearance, and this may be a reason for the HC emission increases. Moreover, a further reason for the increase in HC emissions may be that there are parts of the CNG-air mixture that are not entrained into the spray flux of the ignition fuel. As the mixture is very lean and outside the flammable range, the flames do not propagate here and this mixture may remain in the cylinder without burning. This would result in higher HC emissions.

The CO emissions increase as CNG% increases as long as diesel is the major component, but with further increase in CNG%, CO decreases steadily. For conditions below 50% substitution, as the ignition fuel quantity decreases, the spray combustion region decreases with increasing CNG supply because of the lower equivalence ratio in the CNG-air premixed mixture. This suggests that the quenching region (being outside of the spray combustion) expands, and the CO emissions (in-complete combustion products) increase. For the cases with CNG substitution above 50%, the equivalence ratios increase with increasing CNG supply (because air flow is constant). It is considered that the temperature in the regions of flame propagation combustion rise and the result is a decrease in CO concentration with the combustion improvements in these regions.

Soot emissions are also shown in Figure 3.3 in the form of the FSN. It can be seen that the soot gets drastically reduced as CNG% is increased, due to enhanced premixed combustion. 40% CNG provides a 46% reduction in the FSN, whereas CNG70 and CNG90 show an 86% and a 92% reduction, respectively.

3.3.2 CNG Main Timing Sweep

Figure 3.4 shows the pressure and HRR curves for a main injection timing sweep performed for 70% CNG substitution, at an engine speed of 1200 RPM, under a load of 20 mg/cycle (diesel equivalent). As expected, the combustion phasing gets progressively advanced as the main injection timing is advanced. It can be observed that as the injection timing is advanced, the HRR peak gets higher and the overall combustion process (in the HRR curve) becomes narrower (faster). Figure 3.5 shows the performance and emissions for 70% CNG at 1200 RPM under different main injection timings. The ITE progressively increases as injection timing is retarded, reaches a maximum value at 4^0 BTDC, and then decreases again upon retarding it further to 0^0 BTDC. It should also be noted that further retardation of the injection timing caused the engine to misfire. It appears that at a diesel injection timing of 4^0 BTDC is optimum for 70% CNG at 1200 RPM. This is due to optimum combustion phasing. As the main injection timing is retarded, the diesel fuel is injected later into the compression stroke, i.e., into higher temperature and pressure, which helps in achieving complete combustion. Secondly, the duration of combustion is optimum such that the combustion does not extend too late into the expansion stroke, which might cause quenching. This is also the reason why the timing of 0^0 BTDC has a lower ITE. Again, since the CNG-air mixture is already mixed, advancing the injection timing does not enhance mixing any further. In this way, it seems that the combustion has an MBT diesel injection timing for efficient CNG-air combustion. The NO_x emissions progressively gets lowered with retarding injection timing (similar to pure diesel combustion); meanwhile, the HC and CO emissions do not change significantly with retardation of injection timing.

Under pure diesel combustion, soot emissions increase with retarded injection timing (less mixing); however, under dual-fuel combustion, it is observed that soot emissions remain roughly unchanged when the injection timing is retarded.

3.3.3 Pilot Timing Sweep

Figure 3.6 show the pressure and HRR curves for a pilot timing sweep performed with 70% CNG, at 1200 RPM and at a diesel equivalent load of 20 mg/cycle; the pilot contains 33% of the total diesel injection. The main injection timing was fixed at 4^0 BTDC. The combustion phasing gets advanced with advancing pilot timing injection. The case of 12^0 BTDC pilot shows the highest peak heat release rate. It was also found that adding a post injection does not affect combustion much relative to the double injection case.

Figure 3.7 shows the performance and emissions for a pilot timing sweep performed with 70% CNG, at 1200 RPM and at a diesel equivalent load of 20 mg/cycle. The pilot contains 33% of the total diesel injection. NO_x increases with advancing pilot injection timing. The 33% injection (2 mg) provides a higher spray area of the ignition fuel for the CNG-air mixture to entrain. The ITE reaches a maximum of 43% for the case of pilot injection at 12^0 BTDC, and main injection timing of 4° BTDC. This gap between the pilot and the main provides the optimum combustion efficiency. It should also be noted that these timings also provide a high ITE for pure diesel combustion. This makes sense because the better the diesel fuel burns, the better the CNG-air mixture will burn. We can conclude that for a given engine operating condition, injection parameters that are optimum for diesel, will provide optimum combustion for CNG as well, because the diesel flame is the ignition source for the CNG mixture.

3.3.4 Diesel/CNG – Multiple Injection Comparison

Figure 3.8 shows the performance and emissions using multiple diesel injections for 70% CNG. It can be seen that the ITE is lowest for single diesel injection, highest for double diesel injection, and is the same for the triple injection case. As mentioned earlier, since the double injection improves diesel combustion, it improves the CNG combustion as well. The triple diesel injection does not increase the diesel/CNG ITE further. This is likely due to the reduced main injection quantity which reduces the entrainment area for CNG combustion.

The figure also provides pure diesel triple injection data for the purpose of a fair comparison. The ITE of pure diesel with triple injection results in an ITE of 42.98%, whereas 70% CNG shows an efficiency of 43.05%. This shows that diesel-CNG combustion can be as efficient as that of pure diesel with proper optimization. Meanwhile, the NO_x is seen to be slightly higher for diesel-CNG combustion. Soot emissions from dual-fuel combustion are considerably lower than that from pure diesel combustion. However, soot emissions increase under dual-fuel mode, with the number of diesel injections. The soot is highest for the triple diesel injection case because of less mixing time for the diesel droplets. The HC emissions are higher for diesel-CNG combustion due to leaner combustion of CNG, whereas the CO emissions are reduced relative to that with pure diesel combustion.

3.3.5 Diesel/CNG – Load and Speed Sweep

For further optimization and completeness, load and speed sweeps were performed for 70% CNG combustion. Figure 3.9 shows the pressure and HRR curves for a load (diesel equivalent) sweep performed at 1200 RPM. We can see that the peak pressure and HRR are higher for higher loads, due to the higher energy input. Figure 3.10 shows the performance and emissions for the load

sweep at 1200 RPM at 4^0 BTDC main injection timing. The efficiency decreases quite drastically, indicating that the injection timing needs to be optimized for different loads. NO_x emissions increase steadily, as do the soot emissions (richer equivalence ratio at higher loads) and the CO emissions.

Figure 3.11 shows the pressure and HRR curves for a speed sweep performed at 20 mg load and 4^0 BTDC injection timing. We can see that the peak pressure and HRR are lower for higher speeds, similar to pure diesel combustion. Higher speed also retards the combustion phasing. Figure 3.12 shows the performance and emissions for the speed sweep at 20 mg load and 4^0 BTDC main injection timing. The ITE is highest for 1500 RPM. Again, the ITE could be improved for the higher speeds by advancing the injection timing, thus providing more time for CNG combustion and providing optimum combustion phasing. The NO_x emissions decrease with increasing engine speed and the soot emissions increase (less mixing time); this behavior is similar to that of pure diesel combustion with varying engine speeds. Figure 3.13 shows the performance and emissions for the speed sweep at 20 mg load and 10^0 BTDC main injection timing. It can be observed that advancing the injection timing under higher speeds improves the overall combustion process as indicated by an increased ITE. For example, for CNG70 at 2000 RPM, advancing the injection timing from 4 to 10 degrees BTDC improves the ITE by 2 percentage points.

3.4 Conclusions

Pure diesel combustion and Diesel-CNG dual-fuel combustion were tested in a single-cylinder diesel research engine under different operating conditions.

1. Based on the CNG substitution rate sweep, it was found that at 1200 RPM, and a 20 mg/cycle diesel equivalent load, 70 % CNG substitution provided the optimum combustion, with the highest indicated thermal efficiency. Increasing the CNG % further deteriorated combustion quality.

2. Based on the main injection timing sweep for 70% CNG at 1200 RPM and a 20 mg/cycle diesel equivalent load, 4^0 BTDC provided the highest indicated thermal efficiency. This is due to optimum combustion phasing. It appears that diesel-CNG dual-fuel combustion has an MBT diesel injection timing for different conditions which provides the highest torque.

3. The pilot timing sweep for 70% CNG at 1200 RPM and a 20 mg/cycle diesel equivalent load shows that a 33% pilot split improved combustion, relative to a single diesel injection. This is because a higher spray area for CNG entrainment with a pilot fuel injection. Secondly, it was found that a pilot timing of 12^0 BTDC and main timing of 4^0 BTDC provided the highest dual-fuel combustion efficiency. The conditions that favor pure diesel combustion, also favor dual-fuel combustion because better diesel combustion provides better ignition and combustion for the CNG-air mixture.

4. Based on multiple injection comparison, for 70% CNG dual-fuel combustion, the double diesel injection and triple diesel injection showed similar efficiencies – this is due to the fact that the triple diesel injection reduces the main injection quantity which reduces the spray area for proper CNG entrainment, and also affects combustion phasing.

5. For higher speeds and diesel equivalent loads, the injection timings must be advanced appropriately to maintain optimum combustion phasing.

Based on the experiments conducted, diesel-CNG dual-fuel combustion is able to achieve similar efficiency relative to pure diesel combustion. As such, CNG can be effectively used to substitute for diesel fuel in CI engines.

Table 3.1 Engine Specifications

Engine	AVL 5402 Diesel engine
Number of cylinders	1
Bore	85 mm
Stroke	90 mm
Displaced volume	510.7 cm^3
Number of valves	4
Compression ratio	17.1:1
Diesel injection	Direct injection
Diesel Injection system	BOSCH common rail CP3
Number of injection holes	5
Diameter of injection holes	0.18 mm
CNG injection	Port injection
CNG injection	SOLARIS CNG injection system

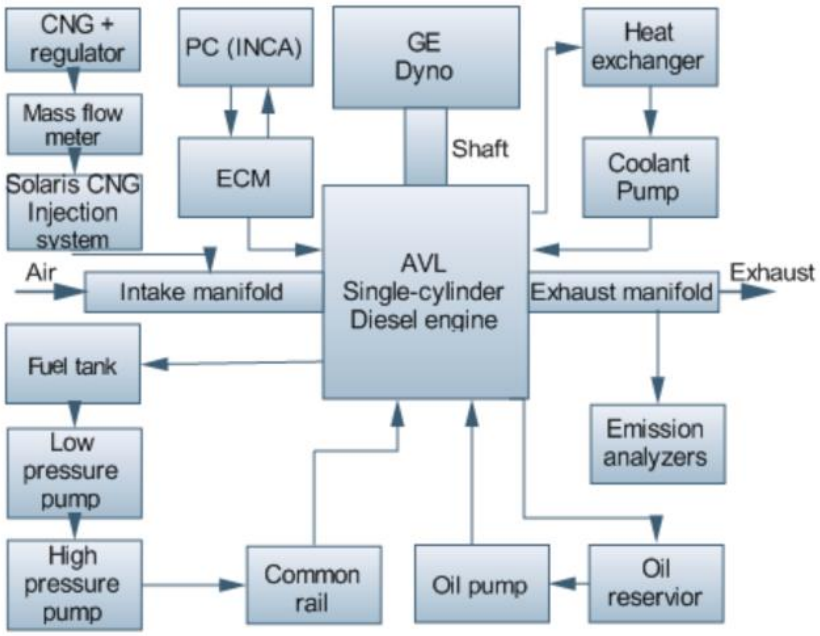

Figure 3.1 Experimental setup

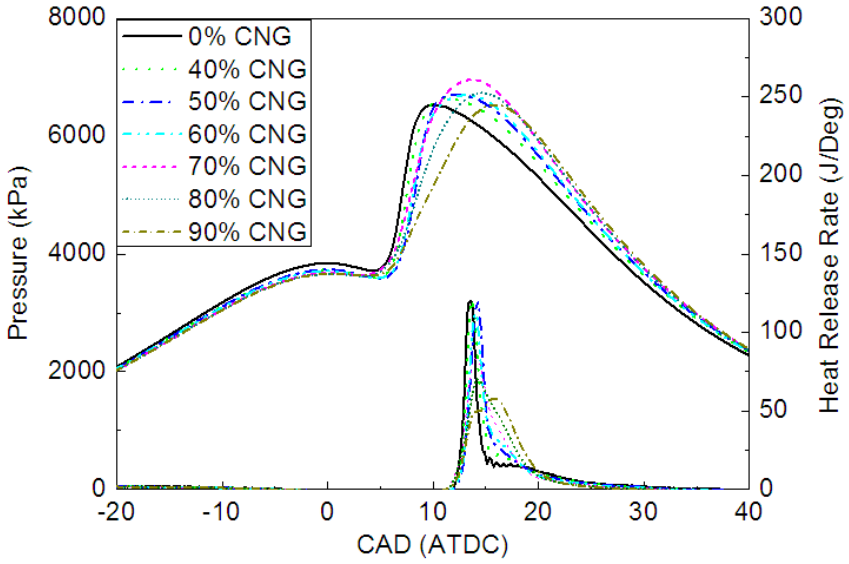

(a)

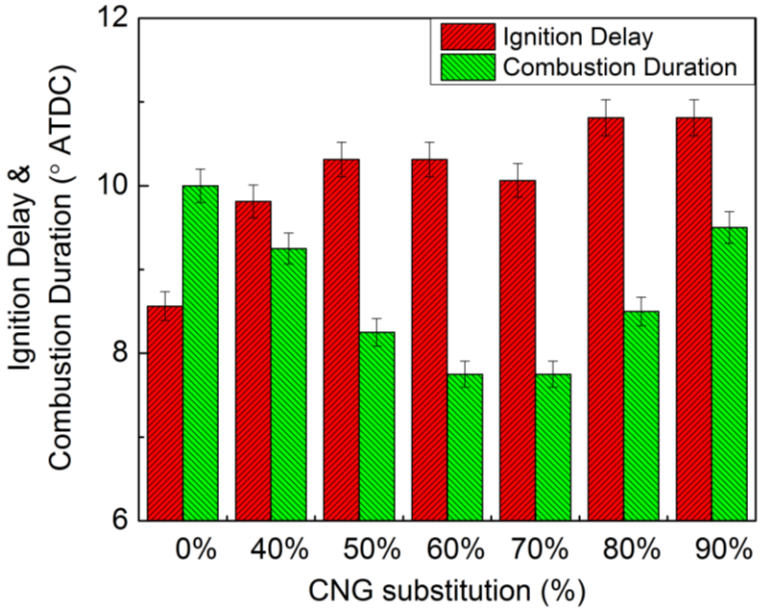

(b)

Figure 3.2 CNG substitution sweep – 1200 RPM, 20 mg/cycle baseline@ 4° BTDC inj. Timing: (a) Pressure and HRR (b) Combustion characteristics

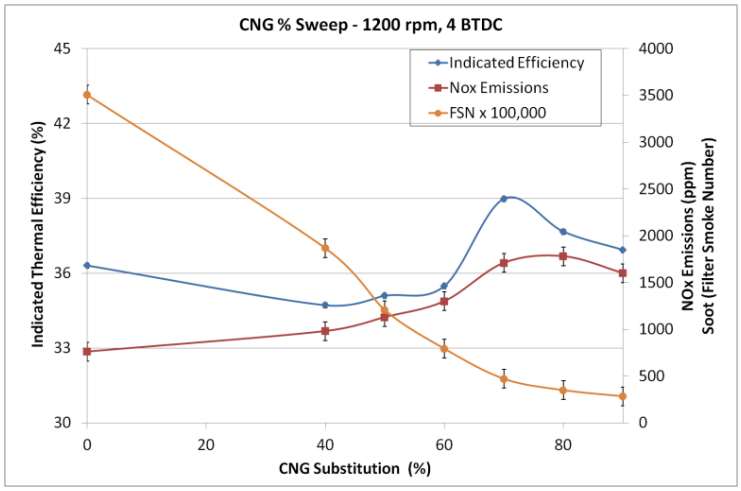

(a)

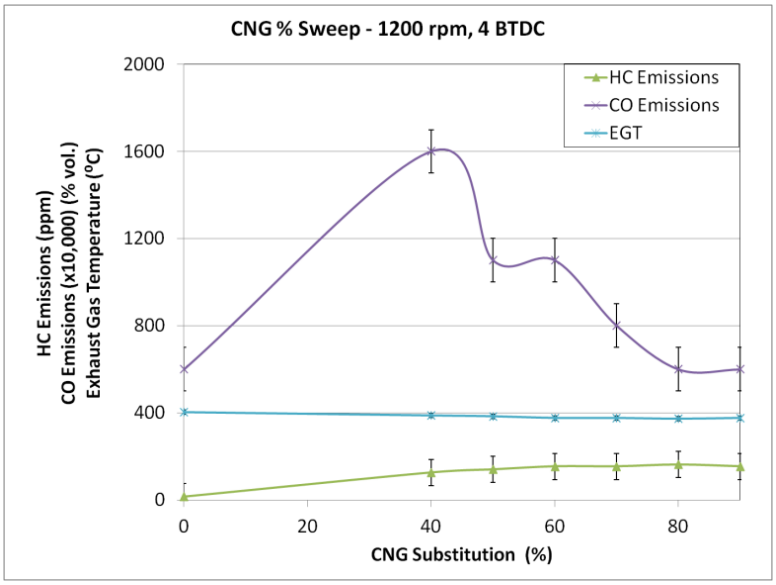

(b)

Figure 3.3 CNG substitution sweep – 1200 RPM, 20 mg/cycle baseline @ 4° BTDC inj. Timing – (a) ITE, NO_x and FSN; (b) HC, CO, EGT

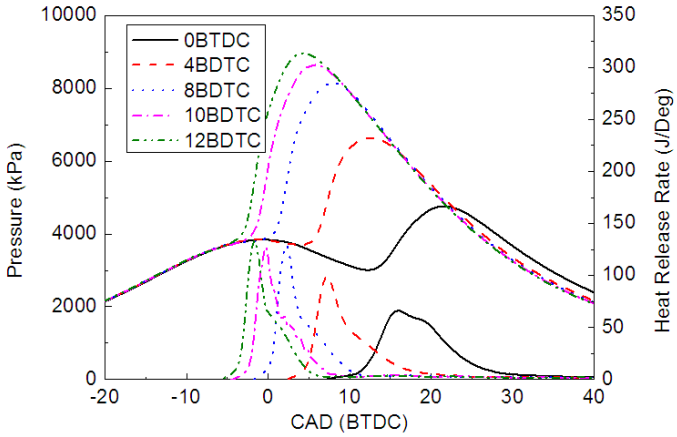

Figure 3.4 CNG70 main timing sweep – 1200 RPM, 20 mg/cycle baseline

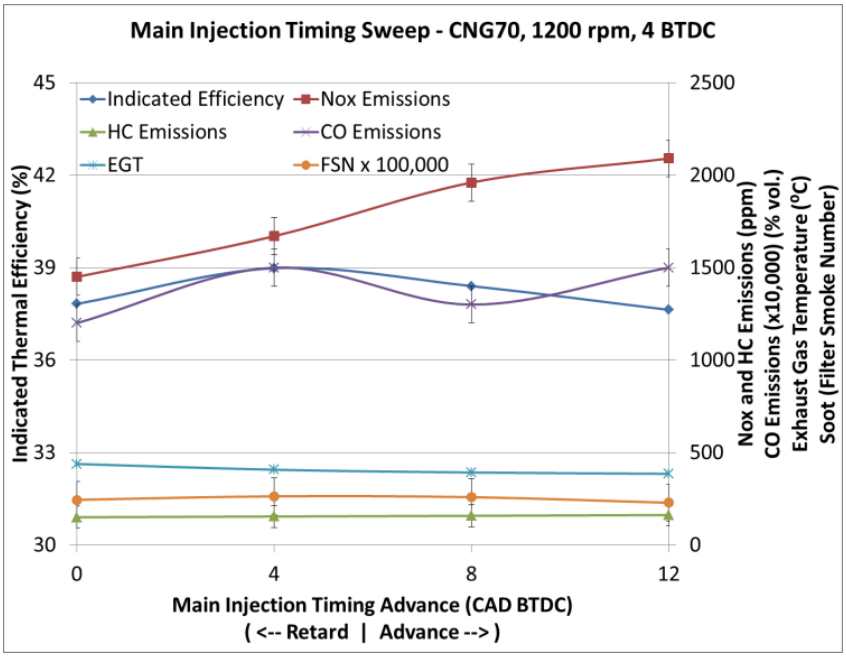

Figure 3.5 CNG 70 – 1200 RPM, 20 mg/cycle baseline - performance and emissions

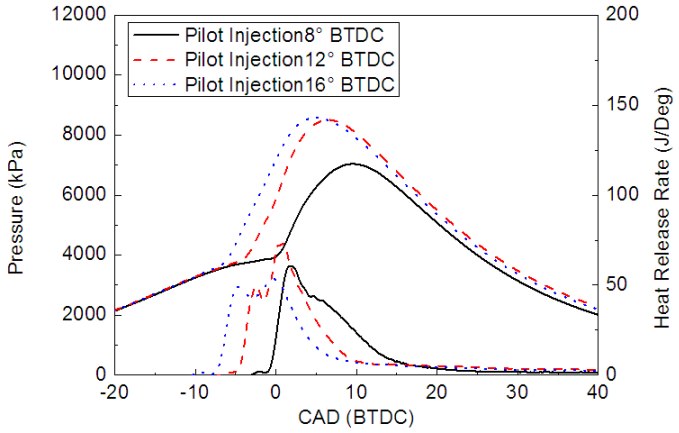

Figure 3.6 CNG70 pilot timing sweep (pilot 33%) – 1200 RPM, 20 mg/cycle baseline, 4° BTDC main injection

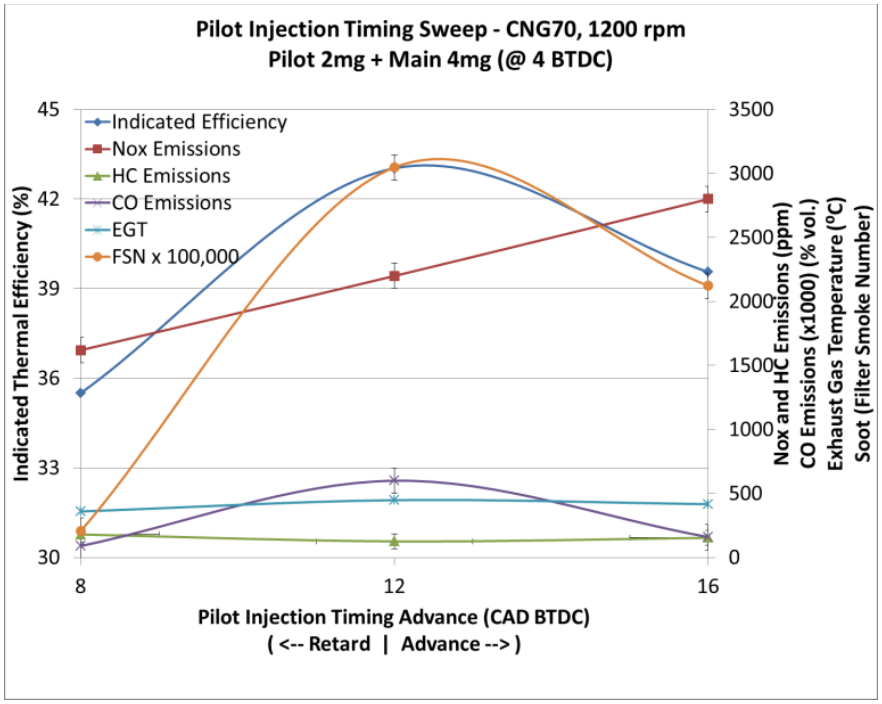

Figure 3.7 CNG 70 – pilot (33%) sweep - 1200 RPM, 20 mg/cycle baseline - performance and emissions

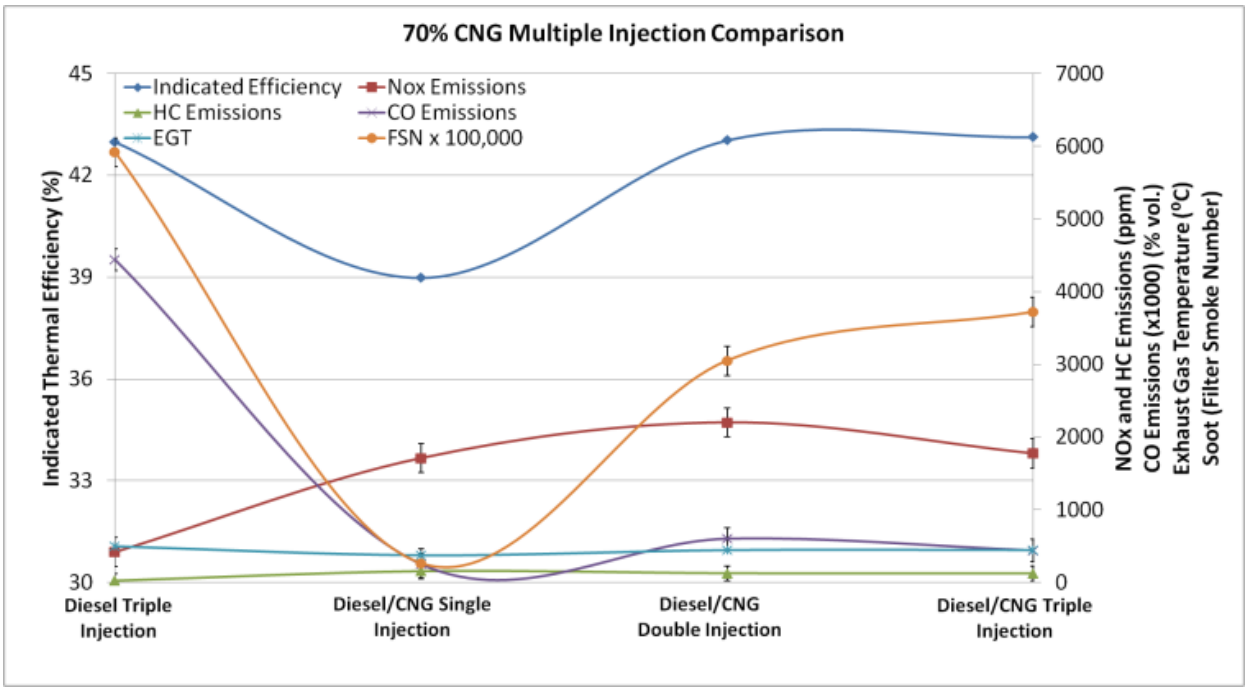

Figure 3.8 70% CNG – multiple injection comparison – performance and emissions

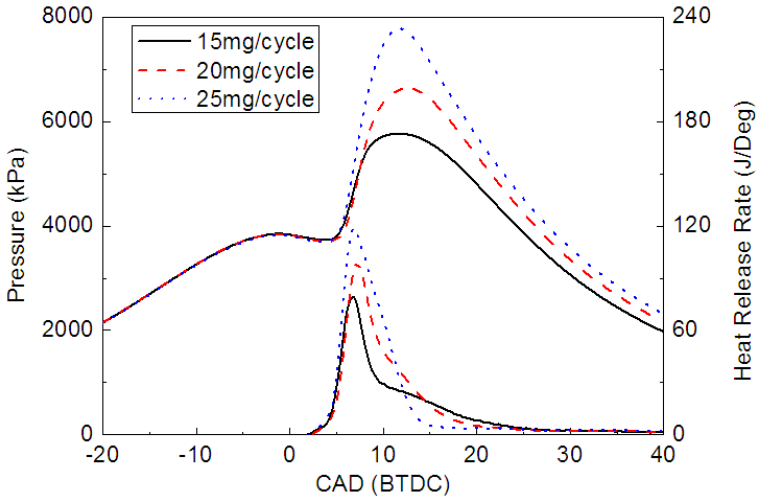

Figure 3.9 CNG70 load sweep – 1200 RPM, 4° BTDC main injection

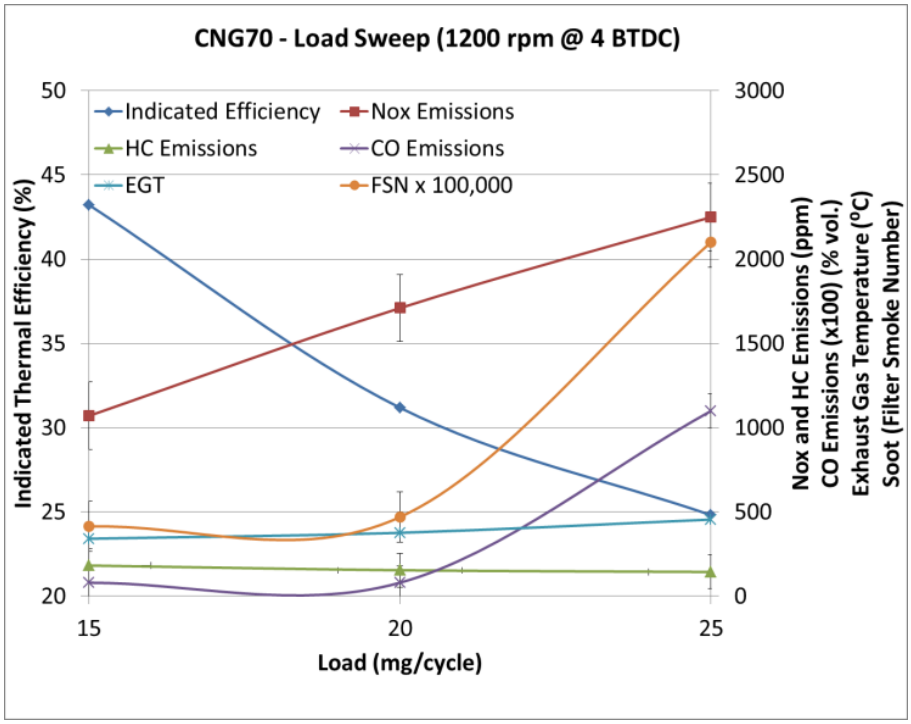

Figure 3.10 CNG70 load sweep – performance and emissions

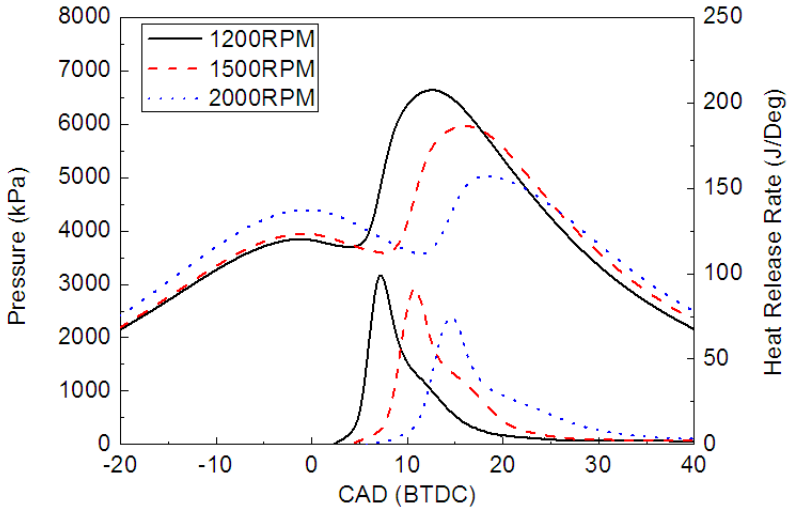

Figure 3.11 CNG70 speed sweep – 20 mg/cycle, 4° BTDC main injection

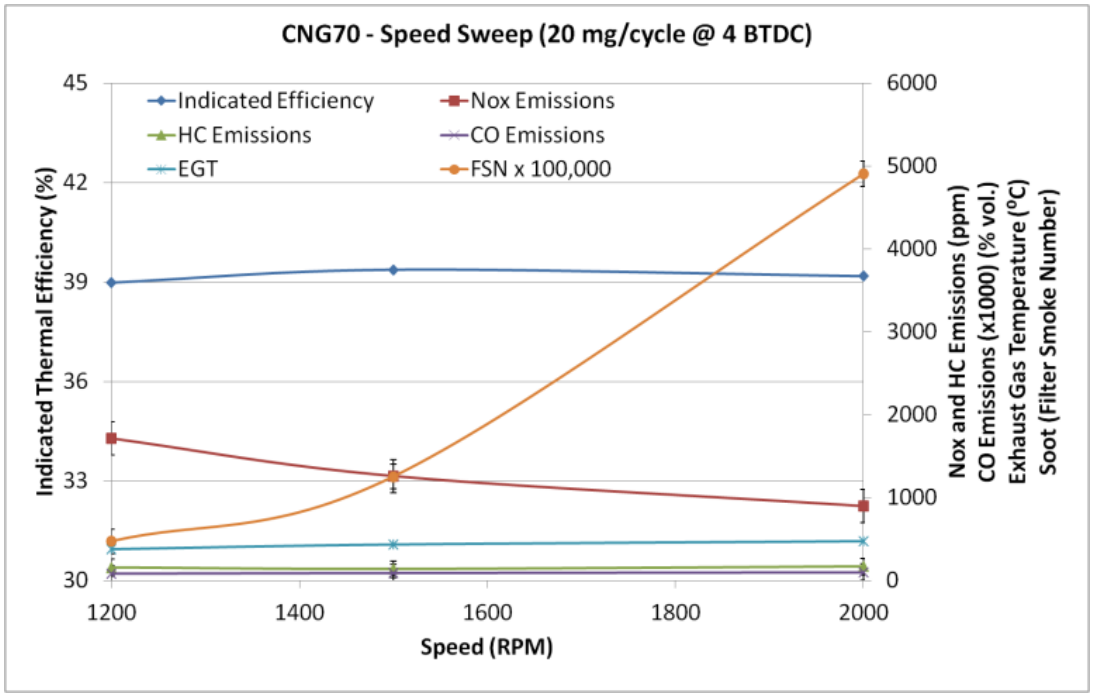

Figure 3.12 CNG70 speed sweep (@ 4° BTDC) – performance and emissions

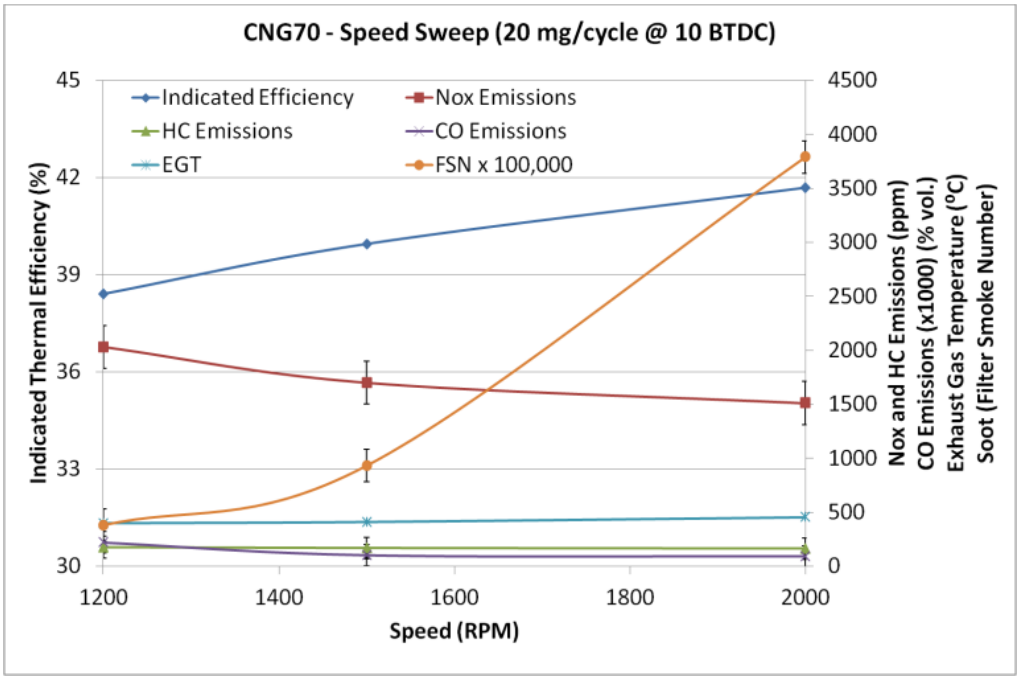

Figure 3.13 CNG70 speed sweep (@ 10° BTDC) – performance and emissions

Chapter 4 Exhaust Soot Characterization

Diesel exhaust gas is a major contributor to combustion-derived particulate-matter air pollution. As such, PM emission standards are continually evolving and becoming more stringent globally. The most common after-treatment method for soot reduction is to employ a DPF to trap soot particles. However, the design and effectiveness of these filters depend on soot properties. Thus, soot characterization has been the subject of several recent studies. The nanostructure of soot depends strongly on the initial fuel identity and synthesis conditions, such as burning temperature, residence time, fuel properties, and fuel/oxygen ratio; the nanostructure in turn affects the oxidation reactivity of the soot. Therefore, the physico-chemical characteristics of soot are important and can provide crucial information to improve the design and operation of after-treatment systems. Given that CNG/diesel combustion fundamentally differs from the conventional diesel combustion process, it is expected that the nature and properties of exhaust soot would be quite different between the two. CNG consumption has risen since 1995 due to tax incentives, increased CNG supply, and falling prices. As such, it is essential to characterize exhaust soot from dual-fuel combustion to appropriately modify the after-treatment systems. In this study, soot samples were collected for both conventional diesel combustion as well as CNG/diesel dual-fuel combustion (CNG40 and CNG70) from the exhaust pipe, and soot properties were examined and compared using materials analysis techniques such as High Resolution Transmission Electron Microscopy (HRTEM), TGA, CHN Elemental Analysis, Raman Spectroscopy and DRIFT spectroscopy. The chapter starts with the literature review on previous relevant studies. The experimental setup will be detailed next, followed by the results and discussion.

4.1 Literature Review

4.1.1 Introduction

Particulate emissions from diesel engines have negative impacts on human health and environment. Health studies have shown that diesel PM can accumulate in the respiratory system and cause various health problems. Since the introduction of Clean Air Act in 1970s, there has been great progress in the development of particulate emission control technologies [92]. Particulate matter emissions may be collected with a post-treatment system in the exhaust (particulate filter). These particulate filters (the DPF) trap the soot (main component of particulate matter), which is later eliminated in a regeneration process once a sufficient amount of soot has been accumulated. The study of the chemical composition, nanostructure and oxidation reactivity of PM may contribute to the knowledge of design parameters of diesel particulate filters, and to determine its potential as a human health hazard. Generally, the nanostructure of soot depends strongly on the initial fuel identity and synthesis conditions, such as burning temperature, residence time, fuel properties and fuel/oxygen ratio, and the nanostructure in turn affects the oxidation reactivity of the soot. The term “reactivity” is used hereinafter to refer to the soot ability to be oxidized at higher rates and/or under a lower temperature environment, which leads to a more efficient regeneration process. In other words, if trapped soot is highly reactive, lower fuel consumption is needed during engine post-injections to reach the soot oxidation temperature [93, 100]. PM nanostructure is closely related to oxidation reactivity and they are governed by the fuel properties and combustion process under which the PM is formed. High temperature, long residence time and rich local fuel environment, promote pyrolysis kinetics leading to polyaromatic hydrocarbons (PAHs), which are the main constituents of the graphene layers. During PM

formation, oxygenated functional groups, like C-OH and C=O, aliphatic C-H groups and several impurities that affect soot reactivity, are attached to non-six membered PAHs rings. Although the relation between carbon structure and reactivity has been widely studied and is well known for carbon science, it remains unclear for diesel combustion soot [100].

4.1.2 Previous work

Lu et al. [94] investigated the oxidation of particulate emitted by a DI diesel engine fueled with three fuels, including neat biodiesel produced from waste cooking oil, under different engine loads. Song et al. [95] studied the oxidation behavior of biodiesel soot using TGA and electron energy loss spectra (EELS), using a soybean biodiesel and a blended fuel containing 20% biodiesel mixed with 80% diesel fuel. Biodiesel (B100) soot was found to be far more reactive than diesel soot, and it underwent a unique oxidation process leading to capsule-type oxidation and eventual formation of graphene ribbon structures. Initially, it was suggested that oxidation reactivity of the soot was more dependent on the relative amount of initial surface oxygen groups than on its initial structure properties. However, they reported later in a separate work, that those groups, as determined by X-ray Photoelectron Spectroscopy (XPS), did not dominate the soot oxidation reactivity and that even under matched combustion phasing, fuel formulation such as oxygen and aromatics content, had a definitive influence on soot reactivity and nanostructure. They also found that NSB exhibited faster oxidation than low sulfur diesel (BP15) and Fischer-Tropsch (FT) soot [99]. Salamanca et al. [96] investigated the variations in the chemical composition and morphology of soot induced by two neat biodiesel fuels, palm oil biodiesel and linseed biodiesel, and their 50% blends, with various techniques, including TGA, Raman spectroscopy analysis, and energy dispersive X-ray analysis. From a morphological point of view, all the results showed that neat

biodiesel does not affect significantly the size of the particulate matter emitted. However, soot particles produced by neat biodiesel are more carbonized or have a graphite-like (less amorphous) structure than diesel particles. Salamanca et al. [97] also studied the influence on the chemical composition of the particulate matter produced in an automotive diesel engine operated with palm oil biodiesel and its blend with diesel fuel. Lapuerta et al. [98] used an automotive diesel engine to compare the effect of diesel fuel and an animal fat-derived biodiesel on the soot nanostructure and on loading and regeneration of diesel particulate filters. TEM analysis of the agglomerates showed that soot primary particles obtained with biodiesel fuel were significantly smaller and had a higher specific active surface than those of diesel soot. Yehliu et al. [99] focused on the impact of fuel on soot reactivity and nanostructure, using ultra-low sulfur diesel (ULSD), soybean biodiesel, and synthetic FT fuel, and applied TGA, XPS, and X-ray diffraction (XRD) techniques in the investigation. They concluded that the soot oxidative reactivity is dominated by the degree of disorder of the carbonaceous nanostructure, not by the abundance of surface oxygen content. Agudelo et al. [100] used TEM, TGA, Raman spectroscopy and FTIR spectroscopy to study the impact of crude vegetable oils (CVO) on the oxidation reactivity and nanostructure of PM. It was found that the CVOs soot was more reactive to oxidation, and its graphite-like nanostructure was more ordered than diesel soot. Additionally, it was found that the more unsaturated the CVO (jatropha) is, the more reactive – at low temperature – and more ordered its nanostructure is, in comparison with the saturated one (palm). Man et al. [101] investigated the effect of waste cooking oil biodiesel on the physico-chemical properties of particulates from a DI diesel engine. They observed that more primary particles with smaller size were generated under higher engine speed or lower engine load or when biodiesel was added. Biodiesel and lower engine load favored the formation of immature primary particles while engine speed had less influence on the

nanostructure of the primary particles. With regard to the oxidative reactivity, they concluded that the impact of engine load at constant engine speed was more pronounced than the impact of engine speed. Biodiesel has the lowest activation energy at all operating conditions. The soot oxidative reactivity is closely related to the nanostructure properties, volatiles, and the oxygen content in fuel. Moreover, soot with amorphous nanostructure has faster rate of mass loss than soot with typical core–shell nanostructure. They concluded that biodiesel blending alters nanostructure of the primary soot particles and reduces the temperature required to initiate regeneration of the diesel particulate filter.

The influence of engine operating conditions on the physico-chemical properties of particulates emitted by a diesel engine has also been investigated by several studies. Lee et al. [102] collected PM from a 2.4 L single-cylinder supercharged direct injection diesel engine. They found that the engine load (in-cylinder pressure and temperature) was more important for the formation of particulates agglomerates than the engine speed (characteristic time). The primary particulate size decreased with the engine load and speed, and the particulates turned more ordered and partially oxidized due to the high in-cylinder temperature. Neer and Koylu [103] observed, by using a 5.9 L, 6-cylinder medium-duty diesel engine, an increase in soot spherule and aggregate size with the engine load. The contradiction with the study conducted by Lee et al. [102] could be attributed to differences in engine technology and experimental conditions. Zhu et al. [92] observed that the degree of order of the soot structure increased with the engine load, and that soot particulate size decreased due to the faster oxidation of the particulate at high in-cylinder temperature. Al-Qurashi and Boehman [104] using a 2.5 L, 4-cyllinder, turbocharged, common rail direct injection diesel engine, found that soot generated under 20% of exhaust gas recirculation (EGR) was more reactive due to slow external burning and rapid internal burning as compared to non-EGR soot, which

burned from outside in. Chien et al. [105] used FTIR spectroscopy to determine the composition of the PM produced by a non-road diesel generator. They found that chemical structures of PM were closely related to the fuel and engine oil properties, and that engine load had not a significant effect on the PM composition. Li et al. [106] used a 5.79 L, 6-cylinder, common rail, direct injection, heavy-duty diesel engine modified to develop a total cylinder sampling system to collect in-cylinder soot generated during combustion process. They found that both fringe tortuosity and separation distance decreased as combustion proceeds, indicating that the soot evolved towards a more graphitic structure during the combustion process. Wang et al. [107] used the same experimental set-up that the one used by Li et al. [106] and found that independently of the equivalence ratio, the relative amount of aliphatic C-H groups present in the diesel soot surface was more important in governing soot oxidation reactivity than C-OH and C=O groups. Lu et al. [94] using a naturally aspirated, 4-cylinder, direct injection diesel engine found that primary particle size was not affected by the engine operating conditions. However, they reported that particles exhibit a disordered structure at low engine load and high engine speed due to lower in-cylinder gas temperatures and shorter combustion duration. They also observed that graphitization of primary particles was affected by the engine torque, but not by the engine speed. In contrast, Yehliu et al. [108] showed that the impact of the engine speed (characteristic time) was more pronounced than the impact of the engine torque (equivalence ratio), with regards to soot oxidation reactivity and nanostructure. Jung et al. [109] showed that exhaust soot from low temperature combustion (LTC) was ‘immature’, i.e., not completely developed, and thus more reactive relative to soot from conventional diesel combustion. They attributed the higher reactivity to the LTC soot being more amorphous, and porous due to a higher presence of volatile organic fraction (VOF).

4.1.3 Factors affecting soot particle size

Soot particles are normally aggregates of primary particles. Soot radiative and transport properties are influenced by its morphology. As discussed above, TEM is the most common method used for direct characterization of the morphology of soot aggregates [110, 111, 112]. Diesel soot is known to be agglomerates consisting principally of spherical primary particles with diameters of 15–70 nm and possessing characteristic structural properties. The primary particle size and fractal dimension are two important structural parameters for understanding of diesel soot growth processes [113]. The sizes of both primary and aggregate particles need to be measured, because the growth of individual primary particles is responsible for the total mass of particulate emissions, while the aggregate particles formed through agglomeration of primary and smaller aggregates, which are emitted to the environment, are more closely related to human health [92]. Significant experimental research has been conducted to characterize and explain the size of soot aggregates and the primary particles of which they are comprised. Explanations for primary particle sizing are quite varied.

According to multiple studies, primary particle size increases with equivalence ratio. Increasing equivalence ratio creates locally rich regions that promote particle nucleation and suppress particle oxidation [103]. In addition, less excess oxygen, accompanied by higher temperatures and pressures promote growth of existing soot nuclei [114]. According to Gaddam et al. [110], no change in primary particle sizing was observed with changing fuel-to-air ratio, however increasing fuel quantity at higher load had the same effect in creating locally rich regions and promoting primary particle growth. Li et al. studied the differences in primary particle size when employing pilot and post injections. The pilot-main injection case produced the largest soot particles because

there is less premixed combustion and more diffusion combustion, creating more soot nuclei and promoting larger particle mass. The main-post injection yielded the smallest particles because the enhanced mixing and increased temperature later in the combustion due to post injection improved soot oxidation [115]. In a study by Zhu et al., it was found that particle size decreases as exhaust temperature (proportional to combustion temperature) increases, due to increased oxidation at high temperatures. However, it was also observed that at the lowest temperatures, primary particles slightly increased with temperature increase because particle nucleation and growth dominated the oxidation effects [92]. Another study by Jung et al. shows that in the LTC regime, primary particles are smaller than in the conventional mode. Using elemental analysis, it was determined that in the C/H ratio was lower for LTC, demonstrating immaturity of LTC soot particles [109]. Several other studies make observations pertaining to particle size. Two studies showed that the presence of biodiesel decreased the size of primary soot particles compared to diesel soot [98]. In a study by Z. Li et al., soot particles were sampled from the cylinder at different crank angles. It was observed that primary particles start small and over time reach a maximum size, and then decrease in size. During the early combustion phase, particle size increases as temperature and pressure rapidly increase. As combustion proceeds, soot formation decreases and the high oxidation rate causes the soot particles to decrease in size [106]. In several previous studies, a decrease in primary particle size is observed as engine speed increases. This trend is simply attributed to shorter residence times in high temperatures [109, 101, 106, 116].

4.1.4 Soot from Natural Gas combustion

Increased natural gas energy substitution has been found to be very effective in reducing NO_x and PM emissions while maintaining acceptable engine performance [84, 89]. Particulate matter (PM)

mass emissions are significantly reduced with natural gas fuels, since natural gas does not contain aromatic and polyaromatic compounds and contains less dissolved sulfur compounds than petroleum fuels [68]. Thus, the contribution of natural gas vehicles to smog formation can be less than that of comparable gasoline- and diesel-powered vehicles. Since methane does not have carbon–carbon molecular bonds, natural gas combustion results in a substantially lower probability of benzene ring formation, which in turn means a reduction in formation of carcinogenic PAHs and soot [90]. While the soot emissions are substantially lower using HPDI of natural gas in comparison with conventional diesel engines, natural gas has been found to be the main contributor of these (reduced) soot emissions. Natural gas contributes to soot formation at high engine load conditions and is in fact the main contributor to soot emissions at high engine load with EGR by far [91].

Although soot morphology and nanostructure have been widely studied for other alternative fuels such as crude vegetable oils and biodiesels as discussed above, there are no studies that have compared PM from diesel and diesel/CNG dual-fuel combustion. With increasing natural gas-fueled vehicles, such a study is necessary to appropriately modify and design exhaust after-treatment systems for these vehicles. In this study, we compare soot samples from pure diesel, 40% CNG, and 70% CNG (energy based substitution rate) collected from the exhaust pipe. First, soot oxidation reactivity was characterized using TGA. TEM was then used to determine the diameter of the spherules and the morphology of agglomerates. Raman spectroscopy was employed to determine the graphitic nature of the soot, Carbon, hydrogen, and nitrogen weight fractions were obtained using elemental analysis estimate soot aging, and finally, DRIFTS was used to identify surface functional groups of soot samples.

4.2 Experimental Setup

Experiments were carried out in the AVL 5402 single-cylinder diesel engine described in the previous chapter (displacement = 0.5 L; compression ratio = 17.1). The engine was modified to run diesel/CNG dual-fuel mode by adding a Solaris CNG injection system, which was used to inject CNG into the intake manifold (port injection). Experiments were performed using No. 2 diesel and chemically pure methane was used to emulate CNG. The Solaris Diesel V4 control program was used to adjust the mass of CNG injected. ETAS INCA v7 was used to control the electronic control module. In-cylinder pressure was measured using a Kistler pressure transducer, and NO_x, UHC, CO, and FSN were measured using Horiba emissions analyzers. More details can be found in [117].

The CNG substitution was defined as the percentage of heat energy from CNG available in the cylinder. For example, 70% CNG indicates that 70% of the energy input for the given engine condition was provided by CNG. Under a load equivalent to 20 mg/cycle diesel (medium load), a CNG flow rate of 15 L/min is equivalent to 70% CNG substitution. Test conditions are summarized in Table 4.1.

4.2.1 PM Sampling

The PM sampling system was designed to allow simultaneous collection of raw PM on TEM grids, quartz fiber filter papers, and on stainless steel filters. PM was collected on TEM grids based on the thermophoretic principle [95]. A fast-acting solenoid valve system controlled by LabVIEW allowed sampling times of the order of milliseconds. The TEM grids (400 mesh Au) were inserted into the manifold through a Swagelok tee. A brass rod, ½-inch diameter and approximately one foot long was machined to create a TEM grid mount. The TEM grid is held at the end of the rod

by two miniature hex bolts (see Figure 4.1). Insertion of the post through a 1/2 in. Swagelok Tee-fitting provided a method for plumbing into sample lines with easy interchange of the held grid. Commercial grade cleaning alcohol was used to periodically clean the sample holders. The key advantage is that soot is directly collected in the aerosol phase onto TEM grids, bypassing filter collection and re-dispersal upon a TEM grid. Such processes cause agglomeration of soot aggregates and obscure aggregate recognition. For better HRTEM analysis, sampling was done on lacey carbon grids [110]. PM was simultaneously collected on quartz (Pall Tissuquartz filters) and stainless steel filters using a vacuum pump system. PM collected on TEM grids was subjected to TEM, the quartz filters were used for Raman spectroscopy, and the PM was carefully scraped from the stainless steel filters for DRIFTS and TGA analysis.

4.2.2 Diagnostic Techniques

4.2.2.1 TGA

A TA Instruments Q50 was used to perform TGA. The sample was loaded in an alumina crucible and placed inside a furnace, where the temperature was increased following a user-defined program (Table 4.2) and the weight loss was continuously recorded. A sample mass of 3 mg was used in all tests. This value was selected based on repeatability.

4.2.2.2 TEM

To perform different levels of image analysis that include macro- (aggregate), micro- (spherule) and nano-scale (nanostructure), a 200-kV field emission TEM (JEOL 2100 CRYO TEM) was used to take high-resolution bright field images. Depending on the soot samples, the applied magnifications varied between 40,000x and 500,000x. For every sample, images of soot

aggregates at more than forty locations were recorded. Digital images were acquired by Gatan image software.

Photographs were taken at various locations across the grid surface due to the insensitivity of soot concentration to grid position in the exhaust stream. For image comparison between samples, images were taken at similar magnification, while the sampling times were also identical. During the present sampling, no dilution or impaction was used, preventing condensation/nucleation of new particles or aggregate breakup upon deposition. Measurements were usually repeatable within the experimental uncertainties, which were dominated by the consideration of a finite number of particulates, the dependence of sampling on size and morphology, and image analysis biases [103].

4.2.2.3 Raman Spectroscopy

Raman spectra were acquired with a laser Raman confocal microscope (Nanophoton RAMAN-11). The excitation wavelength of the Nd:YAG laser was 532 nm; the sample was illuminated through an objective lens (10x, Numerical aperture (NA) = 1.2). The profile of the laser was shaped into a line using a cylindrical lens. Raman scattered light from the illuminated line was collected with the same objective lens and guided to the confocal slit of a spectrograph (Czerny–Turner type, f = 500 mm). The slit width was fixed at 60 μm. The scattered light was dispersed by a 1200-groove mm^{-1} grating, and the spectra were recorded by a thermoelectrically cooled CCD camera (−70° C, 1340 × 400 pixels). Spectra of the samples were in the range of 100 – 3600 cm^{-1}. A 120 second exposition time and a source power of 0.2 mW were used to avoid altering or burning the sample. Interference from fluorescence was detected in the Raman spectra of all PM samples. This can be produced by the presence of polycyclic aromatic hydrocarbons (PAHs) [100]. Three Lorentzian functions (3L) for G band (1580 cm^{-1}), D1 band (1360 cm^{-1}), D4 band (1180 cm^{-1}) and

one Gaussian function (1G) for D3 band (1500 cm^{-1}) were used [100]. Several different spots were analyzed and averaged for each sample to improve the statistical significance.

4.2.2.4 DRIFTS

Surface functional groups of the samples were analyzed using DRIFTS. A Thermo Nicolet Nexus 670 spectrometer with a MCT detector and a Spectratech diffuse reflectance accessory were used. Spectra were recorded from 4000 to 800 cm^{-1} by collection of 60 scans at 1 cm^{-1} resolution. Raw soot was dispersed on a gold mirror, and subjected to DRIFTS. DRIFT spectra of both the background (clean gold mirror) and the loaded mirror were acquired. DRIFTS was initially attempted directly on TEM grids containing soot, however, this did not yield a sufficiently strong signal and hence soot particles were directly dispersed on gold mirrors.

4.2.2.5 CHN Elemental Analysis

An elemental analyzer (Exeter Analytical - Model CE 440 CHN Analyzer) was employed to classify each species, including carbon, hydrogen, and nitrogen, by weight fraction. For C, H, and N, the amounts of CO_2, H_2O, N_2, and N_xO_y, which undergo dynamic flash combustion and reduction, were quantified by the thermal conductivity detector (TCD) after classification in a chromatographic column.

4.3 Results and Discussion

4.3.1 Combustion Characteristics and Emissions

Figure 4.2 shows combustion pressure and heat release rate curves for the cases tested. It is observed that the combustion phasing progressively gets advanced with increasing CNG

substitution, and the peak pressure steadily increases. The CA50 of diesel, CNG40 and CNG70 are 6.0625°, 5.5625° and 2.5625° CAD (ATDC), respectively. Table 4.3 shows various combustion characteristics for different substitution rates. The ignition delay increases, while the combustion duration decreases with increasing CNG. The difference in ignition delay and combustion duration between diesel and CNG70 is 0.7 and 6 degrees, respectively. The equivalence ratio (Φ) increases with increasing CNG substitution because the increased CNG displaces air. The longer ignition delay results in a higher peak pressure, which subsequently increases the NO_x emissions. The decreased FSN and increased HC and CO emissions with increasing CNG content is consistent with the literature [75, 76, 80, 117].

4.3.2 Thermogravimetric Analysis (TGA)

Figure 4.3 shows the thermogravimetric profiles for the soot samples. Mass reduction started at lower temperature for both CNG soot samples, indicating higher oxidation reactivity with respect to diesel soot. The drop in mass observed at 400° C is due to the devolatilization process, wherein VOF are removed. In order to further examine the differences in reactivity, two parameters were calculated: (i) the extrapolated onset temperature (EOT), calculated as it is indicated in Figure 4.3 and (ii) $T_{50\%}$, the temperature at which the 50% of carbon was converted [118]. This information has been provided in Figure 4.3 (inset). Both CNG soot samples showed an earlier onset temperature as well as a lower $T_{50\%}$. These temperatures were significantly lower for CNG70, indicating that a higher CNG content increases reactivity of the soot. This implies that after-treatment systems could be designed to operate at lower temperatures with the use of diesel/CNG dual-fuel combustion.

The higher reactivity of CNG soot samples after 500 °C, in comparison with diesel soot, could be due to a higher content of aliphatic and oxygen functional groups (discussed further in section 4.3.7). It could also be attributed to more active surface sites that enable chemical reactions [119]. Moreover, the drop in soot mass due to devolatilization is higher for CNG70. It has been reported that the specific area of the soot particles can increase during VOF desorption [109]. Thus, the increased surface area due to VOF removal could also enhance soot oxidation. Although speculative, it is possible that CNG soot leads to capsule-type oxidization (faster than surface burning), as observed for biodiesel soot [100].

4.3.3 CHN Elemental Analysis

The atomic ratio of carbon to hydrogen (C/H ratio) is a good measure to assess soot maturity because the soot particles attain a higher degree of carbonization, along with dehydrogenation, throughout their growth. The weight fractions of species based on elemental analysis are listed in Table 4.4. The rest of the elements include Oxygen, Sulfur and other trace elements such as Phosphorus, Calcium, Zinc etc. It is quite apparent that the weight fraction of carbon decreases and that of hydrogen increases as CNG content increases. This indicates that CNG soot is less "aged" relative to diesel soot, and as such, is expected to have a higher reactivity, which agrees with the TGA results observed.

4.3.4 Transmission Electron Microscopy (TEM)

4.3.4.1 TEM Macrostructure Observations

Figure 4.4 shows TEM images of the three soot samples; the lacey carbon mesh is visible in figures (c) ~ (f). Many spherules agglomerated to form aggregates of fractal-like geometry. From Figure

4.4(a) and (b), some familiar features of diesel soot can be observed. First, there was significant variation in overall aggregate sizes. Secondly, particulates had different shapes with grape-like structures [114]. For diesel soot, spherules had nearly uniform diameters. In addition, the boundaries between spherules were unclear. In comparison, Figure 4.4(c), (d) and (e), (f) show typical soot macrostructures observed in CNG40 and CNG70 samples, respectively. CNG soot is less clumped due to decreased loading; note that the sampling times were similar. CNG soot is long, highly curved, and has more complex chains compared to diesel soot. CNG chains are looser and more open-looped, containing a single chain of particles, whereas diesel soot is more tightly packed. Another notable feature of CNG70 soot is that the spherules are less circular and show irregular, distorted shapes; these are signs of immature soot [109].

4.3.4.2 Soot Aggregate Characteristics

The curves in Figure 4.5 indicate that diesel soot aggregates contain the largest number of spherules compared to CNG soot aggregates of similar size. The size of soot aggregates depends on the rate of two reaction mechanisms: surface growth and collisional aggregation [120]. In the collisional aggregation pathway, the frequency of collisions between primary soot particles in CNG cases is lower than that of diesel. Methane, the main component of CNG, does not contain carbon-carbon bonds, substantially lowering the probability of benzene ring formation and thus the formation of aromatic hydrocarbons and PAHs [90]. Fewer precursors generated during combustion will lead to less frequent collisions among particles, leading to fewer soot particles within aggregates.

4.3.4.3 Primary Soot Particle Diameter Distributions

Spherule diameter was measured manually using ImageJ software. The diameter was determined by fitting circles to each spherule. Figure 4.6 shows the distribution of spherule sizes; the distribution functions were normalized for an even comparison. For each of the cases, more than 1000 particles from roughly 50 images were counted and measured.

Figure 4.6 shows that CNG soot has significantly higher variation in spherule size distributions, showing a wider distribution curve. Diesel has the greatest population for particle sizes smaller than 25nm. For particles greater than 25nm, diesel has the lowest population. This indicates that the distribution of CNG cases shifts toward larger spherule sizes with increasing CNG.

Statistical comparisons were made between soot spherule diameter data between samples from D100 versus samples from CNG40 and CNG70, as shown in Table 4.5. Two-sided Student's t-test with $p=0.05$ was used to test for significant differences between sample set means. It was found that the differences between spherule particle diameters were statistically significant at the 95% confidence level. This result further concluded that the addition of CNG increased the mean diameter of soot spherule size.

The particle size is due to the competing result of surface growth and soot oxidation processes. Increasing CNG substitution results in an increased Φ, which promotes particle nucleation and growth, while suppressing particle oxidation [103]. In the model proposed by Frenklach et al. [119], the reaction rate of surface growth and the oxidation reaction is proportional to the number density of active sites. CNG soot likely contains more active sites and thus grows faster, resulting in larger particle sizes. This argument can be further supported by the enhanced reactivity observed using TGA. On the other hand, the oxidation process during combustion and post-combustion

decreases the particle size. It can be seen from Figure 4.2 that the bulk-averaged combustion temperature is higher for CNG cases (higher peak pressure), implying an enhanced oxidation reaction rate. However, another key parameter is the residence time allowed for oxidation reaction. From Table 4.3, dual-fuel combustion shows significantly shorter combustion durations, i.e., a shorter residence time, which limits the advancement of oxidation reactions in CNG cases. Therefore, it seems that the residence time may have a larger impact on soot oxidation (and thus particle size) than the combustion temperature.

4.3.5 HRTEM Nanostructure

HRTEM images were studied to examine the nanostructure of spherules. On a nanometric scale, a diesel spherule presents two distinct parts: an inner core and an outer shell, each with different structures. In the characteristic shell/core nanostructure, graphene layers are parallel to the external surfaces in the outer shell, but are randomly arranged in a turbostratic (not well aligned) state in the central core region [106]. A particle with a slightly aggregated structure, called an immature particle, generally exhibits an irregular shape and is not fully developed. It is formed from the coalescence of a number of pre-formed particles. A particle with a typical inner core–outer shell structure, called a mature particle, contains one or several nucleation sites. The inner core is surrounded by concentrically ordered graphene layers (outer shell) [101].

Figure 4.7 shows a comparison between HRTEM images of the three soot samples. The nanostructure observed for diesel soot is in agreement with the literature. Diesel and CNG40 soot seem to be more ordered, i.e., displaying clear concentric graphitic layers. They also exhibit signs of a mature soot particle. On the other hand, CNG70 soot has a relatively random, incoherent arrangement of lamellae without a clear center. It was also observed in Figure 4.4 that CNG70 soot

exhibited irregular shaped spherules. Therefore, it can be concluded that CNG70 soot is immature. This can be attributed to two factors during the combustion process: first, CNG addition reduces formation of soot precursors and hence favors the formation of particles with aggregated structures, rather than mature particles; second, as mentioned earlier, the shorter residence time is insufficient for the soot to develop an inner core and outer shell structure. The HRTEM images of CNG70 soot also seem comparable to those obtained for immature soot from premixed methane flames in a burner, in that they are comprised of disordered carbon without a clear structural order [116]. Given that immature soot is more susceptible to oxidation [109, 116], it is expected that it would be more reactive, which agrees with TGA results.

4.3.6 Raman Spectroscopy

Raman spectroscopy provides information about the graphitic nature of carbonaceous material. The D3 band (~1500 cm^{-1}) represents impurities of the graphene lattice, due to interstitials defects or amorphous carbon, such as that associated with organic molecules, fragments or functional groups; the D1 (~1350 cm^{-1}) band has been related to the degree of order (edge sites and basal defects) of the graphene lattice. A higher intensity in these bands relative to the G band indicates a larger amount of impurities and a less ordered nanostructure, which could lead to higher reactivity. Although there exist several criteria to describe carbon structural information based on Raman spectra, in this work the criterion of I_D/I_G intensity ratio has been adopted [100]. The uncertainties in I_D/I_G values were ±0.03.

Differences were observed among the Raman spectra of all soot samples. Figure 4.8 shows that both CNG soot samples exhibited similar spectra, but they differ from diesel soot as follows: (i) CNG soot had slightly lower width in the diesel D1 band (~1350 cm^{-1}) and (ii) the G band (1580

cm^{-1}) of CNG soot had a slightly lower intensity. Figure 4.8 (inset) shows I_{D1}/I_G, I_{D3}/I_G intensity ratios for all soot samples. No significant differences were observed between CNG soot samples. Diesel soot exhibited more nanostructural irregularities. Therefore, although CNG soot is more reactive, the initial structure and orderliness does not directly affect soot reactivity. Similar results were observed in [95].

4.3.7 DRIFTS

Figure 4.9 shows the DRIFT spectra of the three soot samples. The most prominent absorption bands are observed in the range 1400–1700 cm^{-1} and in the range 1100–1200 cm^{-1}. These two bands correspond to C=O (1660–1750 cm^{-1}) and C–O (1120–1220 cm^{-1}) stretching of carboxylic acids [110, 118, 95]. The increasing sharpness of the peak at ~1740 cm^{-1} as CNG content increases, suggests a higher degree of oxygen functionality for CNG soot [93, 95].

The peaks at 2850 – 2960 cm^{-1} (aliphatic C-H symmetric and asymmetric stretches) are present but not significant in the spectra. The presence of aliphatic groups is further suggested by the peaks in the range of ~1460 and ~1370 cm^{-1} (in-plane deformation of aliphatic C-H bonds) [110]. CNG40 shows a peak at 1370 cm^{-1}, which is absent in the other samples; meanwhile, CNG70 shows a sharp peak at 1460 and another at ~1590 cm^{-1} (aromatic C=C enhanced by C=O conjugation), which are not present in the others. The concentration of hydroxyl groups (peaks at ~3100-3500 cm^{-1}) [93] is also more apparent for the CNG70 case. The peak at ~2909 cm^{-1} is characteristic of the C–H vibrations of saturated hydrocarbons, indicating the presence of sp^3 hybridized carbon, which is related to the graphitic structure of soot [100, 118]. This peak is similar for the three samples; this agrees with the results obtained from the Raman spectra, which showed no major differences in the I_D/I_G ratios.

High content of aliphatic hydrocarbons (C-H groups) are more important in governing soot oxidation reactivity than other oxygenated surface functional groups, and their higher H/C ratio and reactivity compared with aromatics, enhances the soot reactivity [100, 121]. Moreover, initial oxygen groups have a definite correlation with the rate constant, implying a strong influence on oxidation behavior [95]. Finally, it has been suggested that higher soot reactivity is related to the concentration of hydroxyl groups [93]. As such, CNG soot satisfies all the above criteria, which explains its higher reactivity. The higher presence of aliphatic groups in CNG soot could be explained by the effect of methane, which does not contain C=C bonds, thus lowering the formation of aromatic hydrocarbons. The DRIFT spectrum recorded in the present work fails to detect any significant peak around 3050 cm^{-1} (aromatic C-H stretch) [100], which further supports this theory.

4.3.8 Further Discussions on Sizing, Reactivity and Aging

Although the detailed mechanisms of soot formation during combustion have not been fully understood, one of the most accepted concepts in soot surface growth is the hydrogen abstraction carbon addition (HACA) process [122], where active sites are generated and exposed by the removal of the H atom in a C-H bond, followed by a reaction with a hydrocarbon that propagates the growth. The HACA concept is being widely applied in many models for predicting soot mass growth. Frenklach [123] assumed the first step in soot formation to be the formation and growth of PAHs. In this model, the particles grow via surface reactions whose reaction rate is mainly governed by the HACA mechanism. In parallel with surface growth is the aromatic oxidation, where active sites react with oxidizing agents and remove carbon. The HACA-based model indicates that during the lifetime of soot particles, hydrogen atoms are constantly being removed

and thus carbon are being concentrated. So, the C/H elemental ratio can be seen as an indicator of residence time of soot particles in a flame. The HACA-based mechanism also suggests that the reaction rate of surface growth and oxidation reactions are both dependent on the number of active sites. Given that the C/H ratio decreases as CNG content increases, the residence time is lower (further supported by the reduced combustion duration), and the soot is therefore less 'mature', which also agrees with the HRTEM images. The results obtained from the TGA and CHN elemental analysis agree well with the HACA concept.

Harris et al. measured the soot formation in premixed flames and inferred from experimental observations that the surface growth rate of soot particles decreases with increasing residence time [124]. Singh et al. [125] performed numerical simulations on various hydrocarbon flames and concluded that the fraction of active sites is a function of soot age and exponentially decays with residence time. It is also suggested that the decay function of the fraction of active sites will vary with specific flame and fuel. Khosousi et al. [126] proposed a model that describes soot surface reactivity that accounts for surface growth and oxidation simultaneously. In this model, the number of available active sites is defined as a function of temperature and residence time. The surface reactivity increases, peaks, and then decreases during its lifetime. Li et al. [106] found that primary particles are initially small, then enlarge to a maximum size during the early diffusion combustion phase, and subsequently become smaller as the combustion proceeds.

The higher reactivity of CNG soot, which is likely enhanced by its higher number of active sites (less soot aging), causes it to grow in size early on in the combustion process, but because of CNG's shorter combustion duration, it does not complete oxidation and thus its size is not reduced further. This is the reason why CNG soot particles have a higher size although their residence times are shorter relative to diesel. If sizing differences were analyzed only on the basis of

residence times, then it would be expected that CNG soot particles would have smaller sizes due to the reduced combustion duration. However, given that it has a higher reactivity and a lower C/H ratio relative to diesel, a shorter residence time leads to a higher particle size. Therefore, when explaining primary particle size trends for soot samples obtained using the same fuel, the residence time (aging) of soot in the flame is of more importance. However, when comparing particle sizes among different fuels, residence time alone does not provide enough information. It is essential to include reactivity in the discussion as well.

4.4 Conclusions

Physicochemical characterization of soot from diesel/CNG dual-fuel combustion was performed using TGA, elemental analysis and HRTEM. Based on the observations, the following conclusions can be made:

- Soot oxidation reactivity increased significantly with increasing CNG content. Both the onset and the T50% temperatures were considerably lower for CNG soot.
- Elemental analysis showed that CNG soot was less “aged” relative to diesel soot.
- TEM results showed that number of particles in an aggregate decreases, as well as aggregate size, with increasing CNG due to less collisional aggregation. CNG soot has a larger distribution of particle sizes and the distribution shifts towards larger particle size with increasing CNG due to higher surface growth rate.
- HRTEM images showed that CNG70 soot appears to be immature due to shorter residence times (in spite of higher combustion temperature).

- Raman spectra showed no differences between the soot samples, indicating that initial nanostructure and orderliness of graphene layers does not affect reactivity. Therefore, Raman spectroscopy might not be a reliable method to assess reactivity for the cases tested.
- DRIFTS showed that CNG soot had markedly higher concentration of aliphatic groups and oxygen functional groups, which explains the high oxidation reactivity.
- When comparing particle sizes among different fuels, residence time alone does not provide enough information. It is essential to include reactivity in the discussion as well.

This is the first study of its kind for diesel/CNG soot characterization. With increase in CNG consumption as well as dual-fuel engines, it is necessary to understand how CNG soot differs from conventional diesel soot. Under the tested condition, it can be concluded that the use of CNG affects the morphology, structure, chemical composition, and hence the reactivity of soot, which is relevant for design and operation of after-treatment devices.

Table 4.1 Test conditions (1200 RPM, 20 mg/cycle load)

Fuel	Diesel Injection Strategy
#2 Diesel	5 mg @ 12 BTDC; 15 mg @ 4 BTDC
CNG40	3 mg @ 12 BTDC; 9 mg @ 4 BTDC
CNG70	2 mg @ 12 BTDC; 4 mg @ 4 BTDC

Table 4.2 TGA heating program

1. Initial atmosphere: N_2
2. Ramp 3°C/min to 45°C
3. Ramp 10°C/min to 400°C
4. Isothermal for 30 minutes
5. Changing atmosphere: air
6. Ramp 10°C/min to 850°C
7. Isothermal for 10 minutes

Table 4.3 Combustion characteristics and emission of tested fuels

Fuel	Equivalence ratio (Φ)	Ignition Delay (CAD)	Combustion Duration (CAD)	NO_x (ppm)	HC (ppm)	CO (% vol.)	FSN
No. 2 Diesel	0.66	9.125	23	680	26	0.04	0.03509
CNG40	0.98	9.3125	21.5	850	148	1.09	0.01868
CNG70	1.11	9.8125	17	1020	164	2.21	0.00470

Table 4.4 Weight fraction of C, H, N in soot samples using elemental analysis

Element	Diesel	CNG40	CNG70
C	90.6	84.69	81.08
H	0.14	0.24	0.3
N	0.46	0.6	0.6

Table 4.5 Statistics of Spherule Diameter from Tested Fuels (Unit: nm)

	D100	CNG40	CNG70
Mean	21.19	22.15	25.63
S.D.	8.03	9.10	9.49

Figure 4.1 TEM grid mount

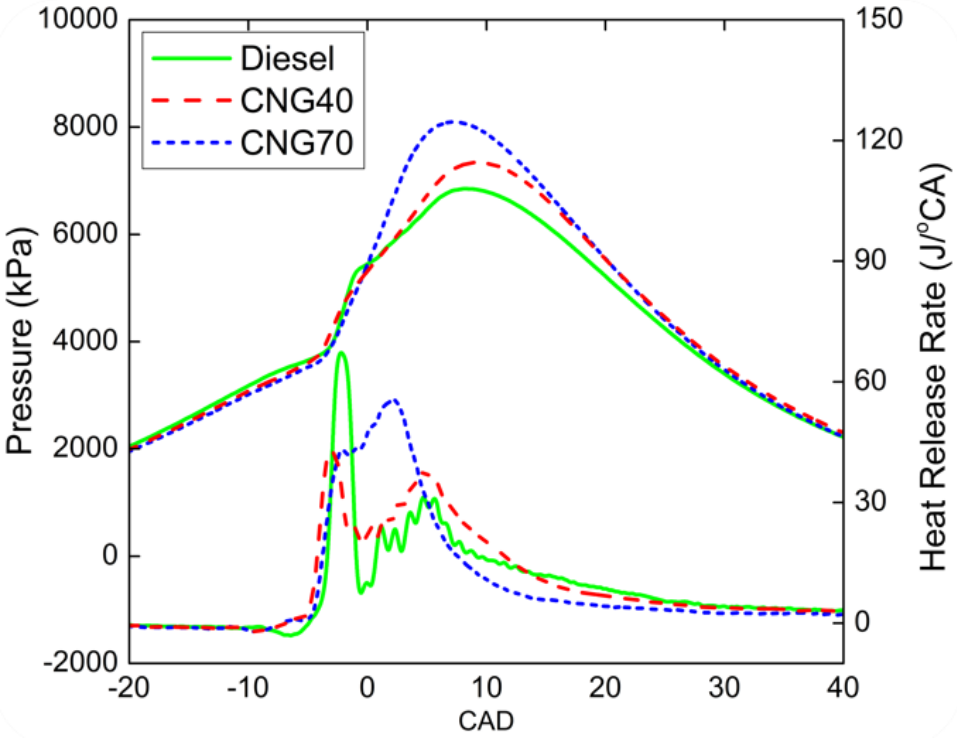

Figure 4.2 In-cylinder pressure of soot samples

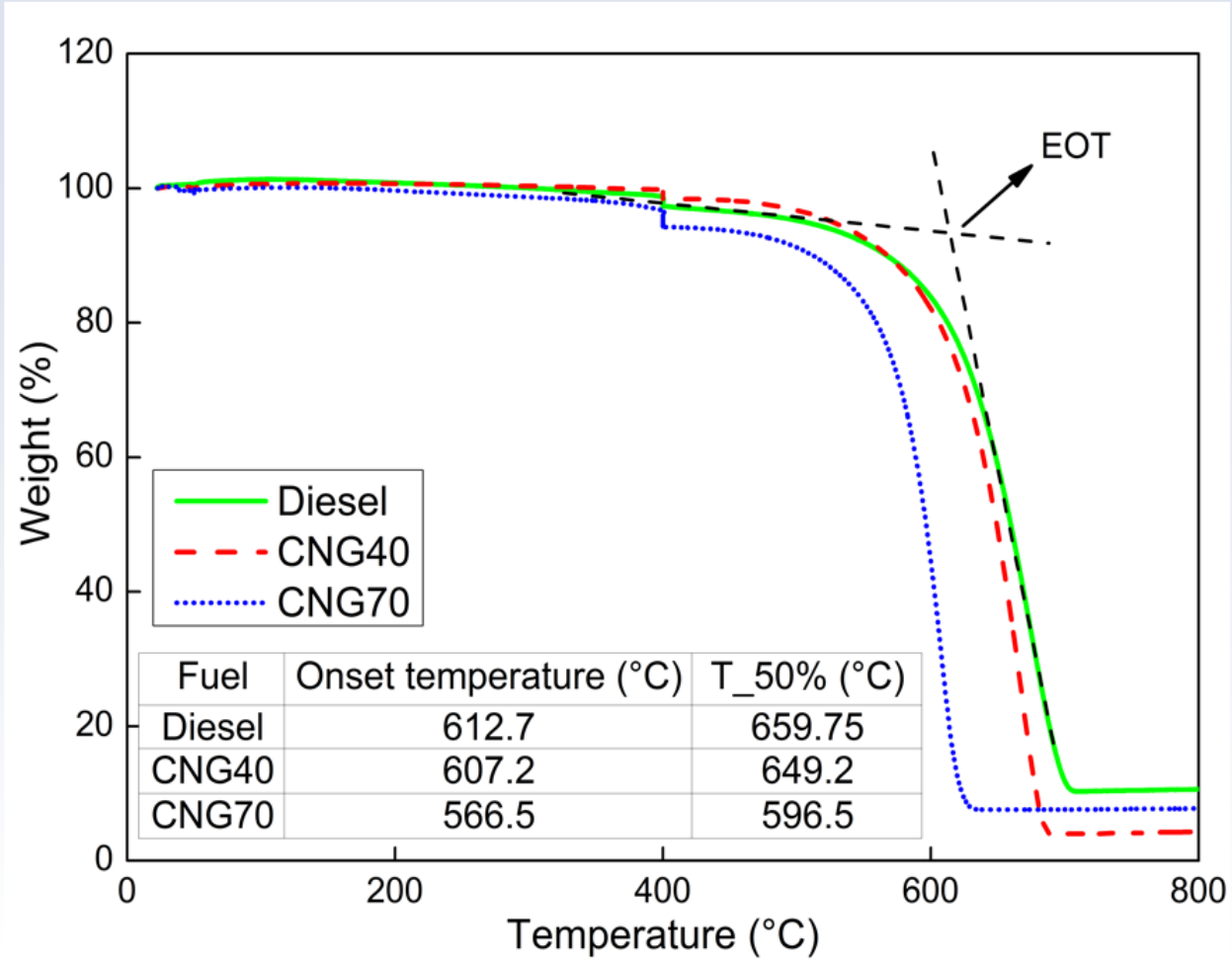

Figure 4.3 TGA profiles (mass % lost) of soot samples

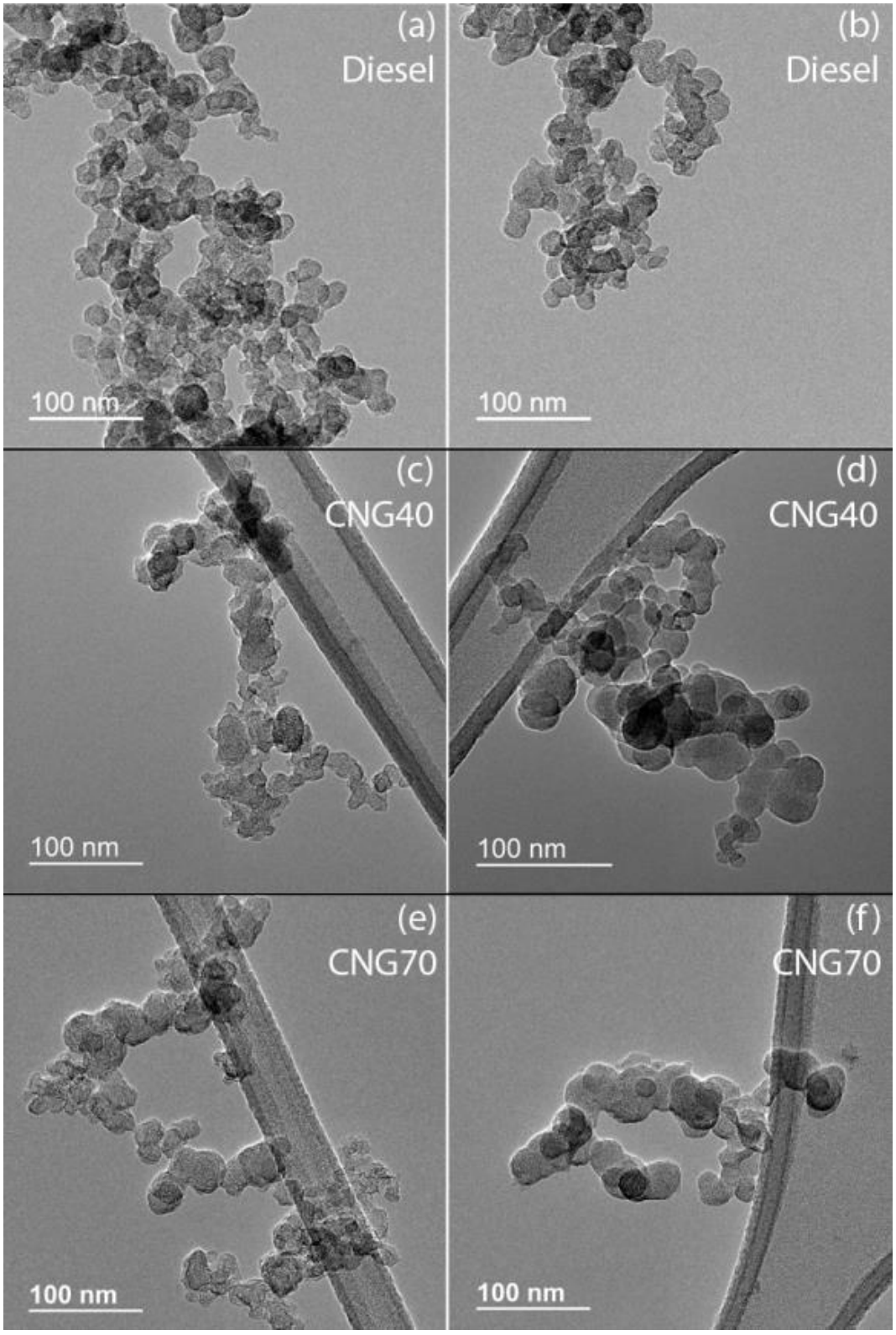

Figure 4.4 Typical TEM images of soot samples

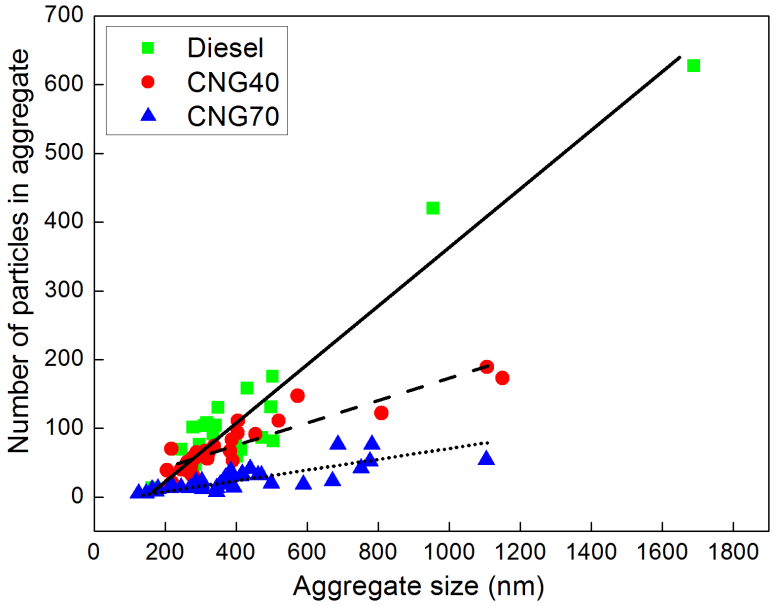

Figure 4.5 Relationship between spherules per aggregate and aggregate size

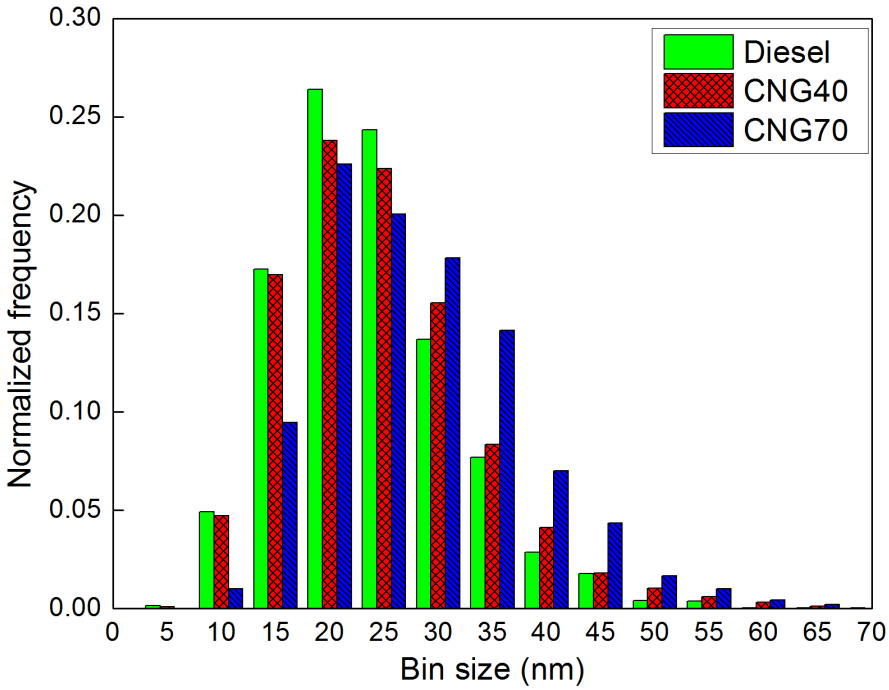

Figure 4.6 Normalized spherule size distributions

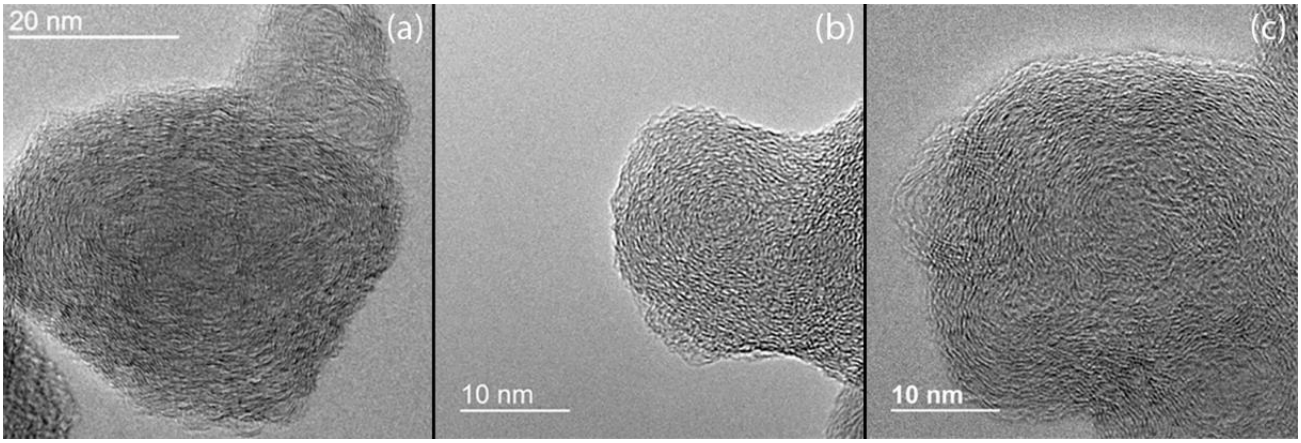

Figure 4.7 Typical HRTEM images of (a) diesel (b) CNG40 (c) CNG70

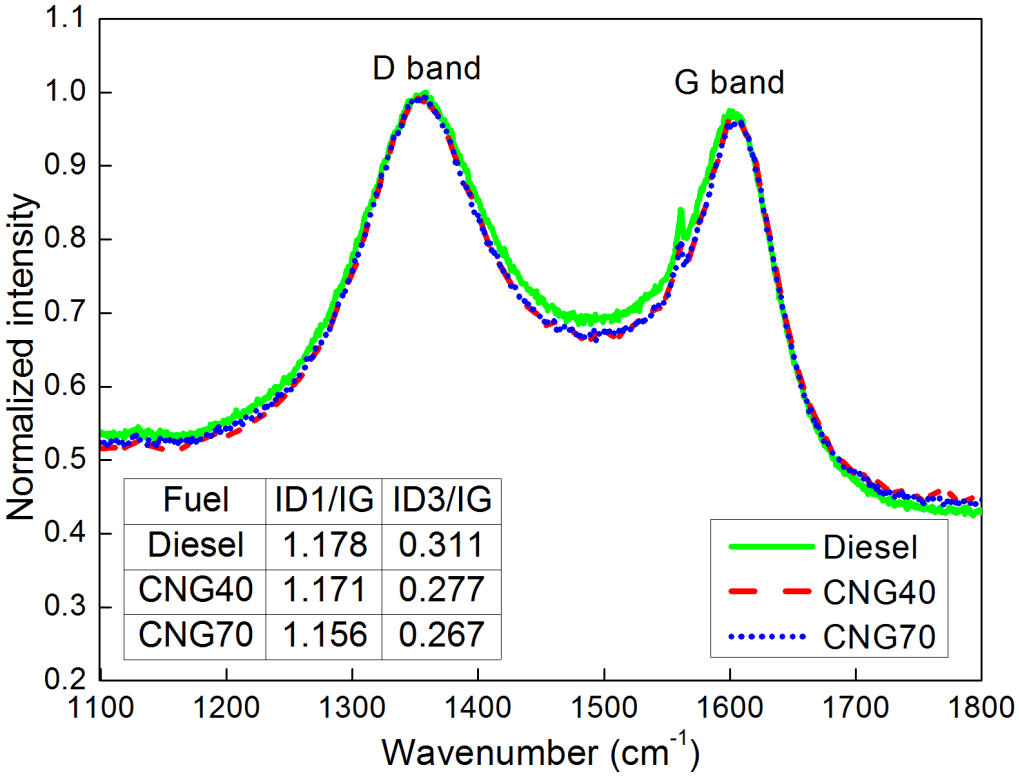

Figure 4.8 Raman spectra of soot samples

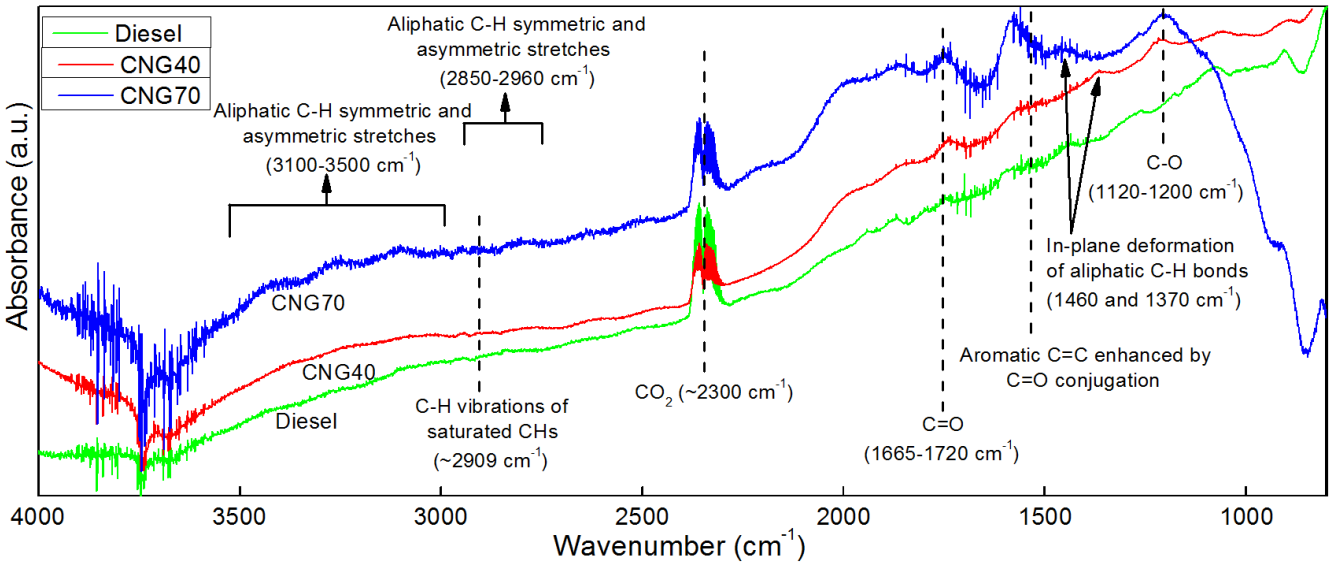

Figure 4.9 DRIFT spectra of soot samples

Chapter 5 Optical Investigation of Diesel/CNG Combustion

Dual-fuel combustion combining a premixed charge of compressed natural gas (CNG) and a pilot injection of diesel fuel offer the potential to reduce diesel fuel consumption and drastically reduce soot emissions. Despite the increasing popularity of the dual-fuel NG combustion, studies focusing on visualization of CNG/diesel combustion are quite rare and a deeper understanding of the dual-fuel combustion mechanism is required, specifically the differences between the dual-fuel combustion regime and the conventional diesel diffusion combustion regime. In addition, understanding of the impact of the fundamental combustion process and fueling parameters such as multiple pilot injections is still incomplete.

In this study, dual-fuel combustion using methane ignited with a pilot injection of No. 2 diesel fuel, was studied in a single cylinder diesel engine with optical access. Experiments were performed at various CNG substitution rates over a wide range of equivalence ratios of the premixed charge, as well as different diesel injection strategies (single and double injection). A color high-speed camera was used to perform temporally resolved natural luminosity imaging. From the color images, soot temperature and soot volume fraction (KL factor) information was also obtained. Corresponding cylinder pressure and heat release rate data was also acquired. The chapter starts with the literature review on previous diesel/CNG optical studies. The experimental setup will be detailed next, followed by the results and discussion. The following topics will be addressed:

- Visualization of CNG/Diesel dual-fuel combustion using multiple pilot diesel injections through time-resolved natural flame luminosity imaging
- Soot temperature and soot volume fraction (KL factor) imaging using Two-Color method.

5.1 Literature Review

As mentioned earlier, studies investigating diesel/CNG combustion in an optical engine are very rare. However, in order to understand the combustion and emission formation mechanisms for diesel dual-fuel (DDF) combustion, a few optical investigations have been performed. Carlucci et al. [127] looked into the effect of inlet bulk flow, port-fuel injector positions, pressure and quantity of the diesel pilot injection on dual-fuel combustion at light load using single-shot endoscope natural luminosity imaging, and found that the pilot injection quantity and the methane injector position in the intake had significant impacts on the combustion process. Schlatter et al. [128] studied diesel pilot ignited dual-fuel in a rapid compression and expansion machine by looking at spatially resolved OH*, and integrated OH*, CH*, C2. They observed increased ignition delays, as indicated by first measurable OH* signal, with increasing amounts of premixed methane. Dronniou et al. [129] performed a detailed optical study on the effect of the premixed charge equivalence ratio using time-resolved natural luminosity (NL) and single-shot OH* chemiluminescence imaging. They observed that the reaction zone propagated from the bowl perimeter to the center of the combustion chamber. Evidence of flame propagation at higher premixed equivalence ratios ($\Phi>0.8$) was also observed. Finally, they found that at low equivalence ratios ($\Phi<0.6$), consumption of methane was a major challenge which could be the potential cause of high methane emissions at low loads [130].

5.2 Experimental Setup

5.2.1 Engine Setup

Tests were conducted on a Jiangling Motors R425 four-cylinder diesel engine, modified to run on only one cylinder. The cylinder was lengthened and a quartz window was installed in the piston head so that the cylinder combustion process could be visualized through a 45° mirror below the quartz window. The engine specifications are shown in Table 5.1. Figure 5.1 shows the schematic diagram of the experimental system. In order to stimulate the real engine working conditions, circulating water at the temperature of 363K was used to heat the engine. Cylinder pressure was measured using a Kistler pressure transducer which was mounted through an opening in the cylinder head. More details can be found in [131].

The high speed camera was a PHANTOM v7.3 Complementary Metal-Oxide-Semiconductor (CMOS) color camera with broad-band Bayer filters. The camera was synchronized with the engine crank so as to enable the crank angle at which the images were captured to be chosen. Exposure time was set to 98 μs in order to observe the lean premixed methane flames. As a result, some of the images were found to be saturated. The aperture was set to f/16.0. Furthermore, the resolution was 512×512 pixels, and the recording speed was 10000 frames per second. Images obtained were further enhanced using MATLAB and this will be discussed further in the following sections. Specifications of the imaging system are shown in Table 5.2.

The pilot fuel used was commercial ULSD. CNG containing 99% CH_4 was injected into the intake manifold and the flow rate was controlled using the pulse width sent to the CNG injectors. The required calibration for these injectors was performed beforehand. Fuel properties are shown in Table 5.3.

5.2.2 Image Enhancement

In order to clearly identify and distinguish between the premixed flame zones and the diffusing flame regions, a high exposure of 98 μs was used. However, the boundaries of the blue premixed flame in the images was still not clearly observed. A MATLAB code was developed to enhance the image. Figure 5.2 shows a comparison between an original image obtained and an enhanced image. In the example below, the image is too dark to reveal any detail. The code maps the pixel range [0, 26] in the original image to [0, 255] in the output image. This brightens the image considerably, and widens the dynamic range of the dark portions of the original image, making it much easier to see the details in the image, including the blue premixed flame propagation. Note, however, that because all values above 26 in the original image are mapped to 255 (white) in the adjusted image, the adjusted image appears saturated in some regions, as can be seen near the center of the image.

5.2.3 Two-Color Method

Usage of the PHANTOM v7.3 CMOS color camera with broadband Bayer filters allowed for applying the classic two-color method [132]. Soot concentration can be quantified by the KL factor, where K is an absorption coefficient and is proportional to the number density of soot particles, and L is the geometric thickness of the flame along the optical detection axis. A larger value of the KL factor in a specific area means a higher soot concentration in the specified area. Through two-color method, two-dimensional false-color maps of soot temperature and soot concentration were calculated based on the flame images. The two-color system was calibrated using a blackbody calibration furnace. The principle of the two-color method has been presented here for completeness [132-135].

During diesel combustion, both solid soot particles and gaseous combustion products are present. However, diesel combustion is dominated by the intense radiation from the soot particles. Since the two-color method utilizes the thermal radiation from soot particles, it directly measures their temperature. The temperature of the combustion gases is not directly measured. However, it can be shown that the temperature difference between the two temperatures is negligible (< 1 K) when the ambient gas and soot particles have attained thermal equilibrium, which can be attained in about 10^{-50}-10^{-6} s within the cylinder. In the absence of surface reaction on the soot particles, it can also be proven that the soot particles can faithfully follow the surrounding gases' temperature when the temperature of the surrounding gases changes with time. From the above discussion, it may be assumed that the soot particle and combustion gas temperatures are approximately the same [133]. In the rest of this text, therefore, the flame temperature refers to the soot particle temperature.

In the two-color method, the thermal radiation at two different wavelengths is detected and the flame temperature is then determined from their ratio by eliminating an unknown factor. The introduction to the two-color method therefore starts with the theory of thermal radiation. The intensity of radiation from a black body varies with wavelength and it also depends on the temperature of the black body. This is described mathematically by Planck's equation:

$$E_{b,\lambda}(T) = \frac{C_1}{\lambda^5[e^{(C_2/\lambda T)} - 1]} \quad \ldots(5.1)$$

Where,

$E_{b,\lambda}$ = monochromatic emissive power of a black body at temperature T (W m^{-3});

λ = wavelength (μm);

T = temperature (K);

C_1 = first Planck's constant = 3.7418 E-16 W m^2;

C_2 = second Planck's constant = 1.4388 E-2 m K.

The monochromatic emissivity of a non-black body is defined as

$$\varepsilon_\lambda = \frac{I_\lambda(T)}{I_{b,\lambda}(T)} \quad \ldots (5.2)$$

Where $I_\lambda(T)$ and $I_{b,\lambda}(T)$ are the monochromatic emissive power of a non-black body and a black body respectively, at the same temperature T and wavelength λ. In other words, ε_λ is the fraction of the black body radiation emitted by a surface at wavelength λ.

In the two-color method, an apparent temperature T_a is introduced and defined as the temperature of a black body that will emit the same radiation intensity as a non-black body at temperature T. T_a is also known as the brightness temperature. From this definition of T_a it follows that

$$I_{b,\lambda}(T_a) = I_\lambda(T)$$

Then equation (5.2) becomes

$$\varepsilon_\lambda = \frac{I_{b,\lambda}(T_a)}{I_{b,\lambda}(T)} \quad \ldots (5.3)$$

Combining equations (5.1) and (5.3), the monochromatic emissivity is given theoretically by

$$\varepsilon_\lambda = \frac{e^{(C_2/\lambda T)} - 1}{e^{(C_2/\lambda T_a)} - 1} \quad \ldots (5.4)$$

In practice, ε_λ has been estimated for soot particles by the widely used empirical correlation of Hottel et al. [132],

$$\varepsilon_\lambda = 1 - e^{(-KL/\lambda^\alpha)} \quad \ldots (5.5)$$

where,

K = an absorption coefficient, proportional to the number density of soot particles;

L = geometric thickness of the flame along the optical axis of the detection system.

The value of the parameter α depends on the physical and optical properties of the soot in the flame. According to Zhao et al. [133], two-color results are less dependent on α if visible wavelengths are selected. In this range of the spectrum, a fixed value of 1.39 is recommended [132, 134, 135] for most fuels.

Combining equations (5.4) and (5.5) gives

$$KL = -\lambda^{\alpha} \ln\left[1-\left(\frac{e^{(C_2/\lambda T)}-1}{e^{(C_2/\lambda T_a)}-1}\right)\right] \quad \ldots (5.6)$$

The unknown product KL can be eliminated by rewriting the above equation for two specific wavelengths, λ_1 and λ_2:

$$\left[1-\left(\frac{e^{(C_2/\lambda_1 T)}-1}{e^{(C_2/\lambda_1 T_{a1})}-1}\right)\right]\lambda_1^{\alpha_1} = \left[1-\left(\frac{e^{(C_2/\lambda_2 T)}-1}{e^{(C_2/\lambda_2 T_{a2})}-1}\right)\right]\lambda_2^{\alpha_2} \quad \ldots (5.7)$$

It can be seen that this equation can be solved for the flame temperature T, provided the apparent temperature T_{a1} and T_{a2} for the flame are known at the two wavelengths, λ_1 and λ_2; i.e., the two-color method is based on the measurement of the radiation at two different wavelength values, $I_1 = I_{soot}(\lambda_1, T, KL)$ and $I_2 = I_{soot}(\lambda_2, T, KL)$, from which the temperature T and the soot amount in terms of KL can be obtained [134]. An accurate calibration for the optical system is a critical step in the two-color measurement, which has a great effect on the data process. In this study, the two-color system was calibrated using a blackbody calibration furnace, and camera linearity was verified within the experimental exposure time range; λ_1 and λ_2 were chosen to be 546.1 nm and 435.8 nm, respectively. The raw color image was processed to obtain intensity values with equivalent dimensional information corresponding to the two wavelengths. The calculation of soot

temperature and KL factor was then conducted pixel-by-pixel on the two processed wavelength intensities.

There are three main sources of inaccuracy when using the 2-color method: (i) it is assumed that soot particle and combustion gas temperatures are approximately the same – this is relatively accurate as explained above; (ii) the entirety of the green and blue segments of the color image are represented by the respective calibration wavelengths (i.e., 546.1 nm (green) and 435.8 nm (blue); (iii) The color images obtained are broadband line-of-sight averaged – as such, given that emissivity is proportional to the fourth power of temperature, the broadband signal obtained is heavily favored towards the hotter particles along the line-of-sight. This is where the majority of the inaccuracy would arise. As such, in the future, spectral measurements of temperature would complement and validate results obtained from the 2-color method.

The accuracy of the two-color method can be affected by several aspects, such as soot deposition on windows, wall reflections, and non-uniform distribution of temperature and soot. The effect of soot deposition can be ignored by using two visible wavelengths as reference. The error for KL factor is at most 10% at very low soot concentration and decreases to 2% at high soot loading, and the effect on the estimation of temperature is very small (of the order of 2 K or 3 K). Non-uniformity of temperature has a larger effect on the calculation of KL factor, while uneven soot concentration has a smaller effect on the calculation of temperature. For high-temperature combustion, the two-color temperature is 200K higher than soot-mass averaged temperature and KL factor is 50% below the area-averaged KL factor; for LTC, error values decrease to 100 K and 25% for temperature and KL factor, respectively. Despite its large uncertainty of KL factor, the two-color method is still valid for a semi-quantitative comparison [135]. However, methods to address the uncertainties and inaccuracies mentioned above need further exploration.

5.3 Results and Discussion

The goal of this study was to optically investigate diesel/CNG dual-fuel combustion at various CNG substitution ratios and explore the potential of having two diesel pilot injections to improve the combustion process. This results section is organized as follows. First, various CNG substitution ratios were compared at the same load using two diesel injections. Next, the dual diesel injection strategy is compared with the single pilot diesel injection strategy. Then an equivalence ratio sweep was performed by varying load at substitution ratios of 30%, 50% and 70%. Finally, the dual diesel injection strategy is further explored at 70% CNG substitution by performing a main timing sweep, a pilot timing sweep and a pilot/main injection mass split sweep.

5.3.1 CNG Substitution ratio Comparison

5.3.1.1 Combustion Characteristics

In this test, the pilot diesel injection strategy was tested using two diesel injections at different substitution ratios of 30%, 50%, 70% and 85%. Table 5.4 shows the experimental conditions used for this comparison. The dwell between the two diesel injections was maintained at 10 degrees. The injection timings for the two diesel injections was constant while changing the main injection quantity with increasing substitution (increasing CNG flow rate). Figure 5.3 and Figure 5.4 shows the pressure and HRR curves and quantitative combustion characteristics such as ignition delay (gap between SOI of main injection and CA at which 5% of total heat was released), initial combustion duration (gap between CA at which 50% of total heat was released and CA at which 5% of total heat was released), and main combustion duration (gap between CA at which 90% of

total heat was released and CA at which 50% of total heat was released) in terms of crank angle degrees under the different substitution ratios, respectively.

It can be observed that combustion phasing gets progressively retarded as CNG substitution and thus, premixed CNG/air equivalence ratio increases, which is consistent with the literature. From the HRR curves, it can be observed that as CNG content increases, the combustion mode becomes increasingly diffusion-dominant and the long tail near the end of combustion is extended further indicating a prolonged diffusion combustion. This can be clearly seen in Figure 5.3 and Figure 5.4. At higher substitution, the reactivity of the air-CNG-diesel mixture is low and ignition is delayed since the diesel concentration (ignition source) is low; thus the combustion duration becomes longer. The mixing and ignition mechanisms between the hot burned gases and fresh unburned fuel tend to progress from richer to leaner regions and are slowed down as a result of an increase of cylinder volume during the expansion stroke, explaining the asymptotic tail observed on the rate of heat release [129], especially for the CNG85 case. It is to be noted that these tested cases have the roughly the same measured IMEP. Figure 5.4 shows that the overall retarded combustion phasing is due to a progressive increase in the ignition delay and the combustion duration – due to the lower diesel fuel mass as discussed above. It can be concluded that the effect on the overall combustion phasing is dominated by the premixed CNG/air equivalence ratio.

5.3.1.2 Natural Flame Luminosity Imaging

The focus of these NL images shown is to distinguish between and identify the lean premixed CNG combustion, indicated by the blue flame, and richer diffusion combustion indicated by the bright orange flames. The blue color of the flame is characteristic of soot-less hydrocarbon flames and is due to the excitation and ionization of radical species, such as CH, C_2 and OH, which emit

at wavelengths in the blue portion of the visual spectrum. Due to differences in phasing between the tested cases, the images are not arranged based on the same crank angle location, but rather arranged such that the stages of combustion can be clearly identified.

Figure 5.5 shows a comparison of NL images at various substitution ratios. Firstly, it is clear that the premixed, entrained CNG mixture ignites first at multiple zones near the wall and these zones propagate towards the center. Secondly, even at a relatively lower equivalence ratio of 0.57, there is some evidence of flame propagation, i.e., merging of reaction zones leading to a 'wave'-like pattern (rows 3 and 4) when using two pilot diesel injections. Previously, this was observed with high equivalence ratios (Φ>0.8) in [129] with a single diesel injection, however, it is suspected that the early pilot injection of diesel enhances overall equivalence ratio distribution in the chamber which leads to this behavior at relatively lower equivalence ratios. These results confirm the findings of Dronniu et al. [129]. The direction of propagation of these reaction zones is likely dictated by the equivalence ratio distribution. In the CNG70 cases, there is merging of the reaction zones to form a 'wave'-like flame. As the substitution is further increased to CNG85, there is a single reaction zone observed which develops into a flame front that begins near the top of the frame, then spreads out, and propagates throughout the rest of the combustion chamber. From these images, the transition from diesel spray/diffusion combustion to a mechanism with a flame front can be clearly observed. This agrees well with, and confirms Dronniu et al's [129] theory that that flame propagation could be the predominant combustion mode under this condition.

5.3.1.3 Soot Temperature and Soot Volume Fraction (KL factor)

Figure 5.6 and Figure 5.7 show soot temperature and soot volume fraction (KL factor) evolution comparing single and dual diesel injections at CNG70. From the KL factor images, it can be

observed that in the lower CNG substitution cases, soot formation occurs predominantly from the diesel jets, whereas at the higher CNG substitution rates, a significant reduction in overall soot volume fraction is observed. Figure 5.8 and Figure 5.9 show the soot temperature and KL factor information in a quantitative manner in terms of the soot temperature KL factor distributions within the combustion chamber as a function of CAD. A CNG0 (pure diesel combustion) case has also been included to compare how CNG addition affects these distributions.

From the soot temperature distributions, it can be observed that pure diesel combustion shows a substantial high temperature (T > 2200 K) distribution in the beginning of the combustion process, indicating premixed combustion. At about 20° ATDC, there is an increase in temperature (T > 1800 K), indicating the late diffusion combustion period. With the addition of a smaller amount of CNG (CNG30), it can be seen that the premixed combustion period (T > 2200 K) is greatly enhanced and the diffusion combustion period is shortened. This is due to the lean CNG/air mixture entrainment onto the diesel jets which increases the overall equivalence ratio enough to be highly combustible. As the CNG substitution is increased further, the early high-temperature zone gets reduced and relatively low-temperature diffusion combustion dominates the combustion process. At higher substitution ratios (CNG 70, CNG85), there are no high-temperature zones observed and the combustion is diffusion-dominant, predominantly showing a temperature T <2000 K.

From the KL factor distributions, it can be observed that diesel combustion shows a high soot concentration (KL > 2) throughout the combustion chamber, with a sizeable portion of KL>2.5. At CNG30, this heavy soot concentration (KL> 2.5) increases greatly. CNG50 also shows this high soot region but it is reduced relative to CNG30. With higher CNG substitution (CNG70, CNG85), the high soot concentration regions are negligible and the soot centration throughout the combustion chamber is 1.5<KL<2.5.

5.3.2 Single vs Multiple Injections

5.3.2.1 Combustion Characteristics

Table 5.5 shows the test conditions comparing single and multiple diesel injections in diesel/CNG dual-fuel combustion. For these cases, the CNG/air premixed Figure 5.10 and Figure 5.11 show the pressure and heat release rate curves, and the quantitative combustion characteristics, respectively, comparing single and dual diesel injections at CNG70. At this condition, the premixed CNG/air equivalence ratio was 0.66. With 70% CNG substitution, the injected diesel amount was 10.5 mg. Two single injection cases were tested at injection timings of 20° and 15° BTDC. Further, three dual diesel injection cases were tested, where the second injection of 7.5 mg, referred to as the main injection, was injected at 15° BTDC, and the first injection of 3 mg, referred to as the pilot injection was injected at 20°, 25° and 30° BTDC. From the figure, it can be observed that the single injection cases show characteristics of typical DDF combustion, wherein a long diffusion combustion tail is observed in the HRR curve. When a pilot injection is added, combustion shifts considerably towards being more premixed, with a higher HRR peak and a shorter combustion duration – this can be observed in Figure 5.11, where the initial combustion duration is significantly shorter for the double injection cases. With a pilot injection at 30° BTDC, the mixture appears to be over-mixed which leads to shorter premixed peak on the HRR curve, relative to the 25° pilot injection case. It should be noted that even with a pilot diesel injection, the heat release begins at the main injection timing of 15° ATDC for all the dual diesel injection cases. Therefore, the first pilot injection affects the overall equivalence ratio distribution within the combustion chamber and thus affects the rate of the initial premixed combustion period, which

consists of auto-ignition of the premixed diesel fuel as well as the entrained CNG mixture [136], as observed in the slope of the HRR curve.

5.3.2.2 Natural Flame Luminosity Imaging

This section shows NL images for the various tested cases. Figure 5.12 shows the NL images comparing the single and dual diesel injection cases. The first two columns show the combustion process of a single 10.5 mg injection at 20° BTDC and 15° BTDC case respectively. The next three columns show the double injection cases with a fixed 7.5 mg main injection at 15° BTDC and a 3 mg pilot injection at 20°, 25° and 30° BTDC respectively. Some general observations can be made from Figure 5.12. Comparing the first two columns, it can be observed that an advanced injection timing (first column) leads to a more intense premixed combustion, due to more time available for the CNG mixture to entrain the injected diesel fuel. It should also be noted that the flames do not propagate all the way to the central part of the combustion chamber, which is a potential cause of unburned hydrocarbon (methane) emissions. Columns 3, 4, and 5 show the dual diesel injection cases. The key difference observed between these images and those in the first 2 columns is the occurrence of multiple ignition zones all over the periphery of the chamber, including localized rich luminous zones within the lean premixed reaction zone. Furthermore, it can be observed that there is much better propagation of the flame towards the center of the combustion chamber as observed in rows 4 and 5 of the images. As such, a dual diesel injection could lead to enhanced ignition of the CNG mixture due to the enhanced equivalence ratio distribution in the chamber and thus enhance flame propagation towards the center and partly alleviate the unburned methane emissions issue. However, the dwell between the two injections also plays a role and from the images, it appears that a 15-degree dwell (column 5) between the

two injections leads to over-mixing and less penetration of the flame towards the center, whereas a 10-degree dwell (column 4) shows relatively favorable combustion at the center.

Towards the end of combustion, almost all the images show a rapid temperature increase in the central part of the charge, as shown by the evolution of the luminosity of bright spots in the near-nozzle region. These bright spots are due to soot incandescence from locally fuel-rich zones exiting the nozzle. These are likely due to "injector dribbling" as observed in various other optical investigations [129, 137, 138, 139].

5.3.2.3 Soot Temperature and Soot Volume Fraction (KL Factor)

Figure 5.13 and Figure 5.14 show soot temperature and soot volume fraction (KL factor) evolution comparing single and dual diesel injections at CNG70. Figure 5.15 and Figure 5.16 show the corresponding soot temperature and KL factor distributions within the combustion chamber as a function of CAD. From Figure 5.15, it can be seen that under CNG70, the flame area was dominated by temperatures below 2000 K; however, some differences were observed in the proportion of the high temperature zones. Among the single injection cases, only the retarded 15° case showed pixels exhibiting temperatures above 2200 K, whereas the 20° BTDC case did not. The addition of a second diesel injection largely did not affect the temperature distribution, however, all double injection cases showed flame regions with temperatures above 2200 K.

From Figure 5.16, it can be observed that the all cases display a KL factor primarily between 2 and 2.5. The high soot concentration are ($KL>2.5$) is only observed for the retarded single injection case and the double injection cases, although this region was relatively small for all these cases. Among the double injection cases, it can be seen that there is formation and oxidation of low soot concentration ($1.5<KL<2$) later into the combustion process and this process gets further retarded

as the pilot diesel injection is progressively advanced relative to the main injection. This late soot formation/oxidation is likely due to the late combustion period.

5.3.3 Equivalence ratio (load) comparison [CNG70]

5.3.3.1 Combustion Characteristics

In this test, the pilot diesel injection strategy was further explored using two diesel injection events at various equivalence ratios, at a CNG substitution rate of 70% to investigate penetration of the lean premixed zones towards the center of the combustion chamber. Table 5.6 shows the experimental conditions used for the equivalence ratio comparison. Based on the results from the previous section, the dwell between the two diesel injections was maintained at 10 degrees. The injection timings for the two diesel injections was constant while changing the main injection quantity with increasing load - a pilot injection of 3 mg at 20° BTDC and 3 mg, 4.5 mg, 6 mg, and 7.5 mg at 10° BTDC respectively. Figure 5.17 shows the pressure and heat release rate curves comparing various premixed CNG equivalence ratios (increasing overall equivalent load) at CNG70; Figure 5.18 shows quantitative combustion characteristics. It can be observed that combustion phasing gets progressively retarded as load and thus, CNG equivalence ratio increases, which is consistent with the literature. From the HRR curves, it can be observed that as load increases, the long tail near the end of combustion gets extended further indicating a prolonged diffusion combustion. This can be clearly seen in Figure 5.18. The first stage of combustion is the auto-ignition of a mixture of air, premixed CNG and diesel followed by mixing and ignition mechanisms between the hot burned gases and fresh unburned fuel. These combustion mechanisms tend to progress from richer to leaner regions and are slowed down as a result of an increase of cylinder volume during the expansion stroke, explaining the asymptotic tail observed on the rate

of heat release [129]. Another observation from Figure 5.18 is that the overall retarded combustion phasing is due to an increase in the ignition delay and the diffusion combustion period, whereas, the initial premixed combustion duration shows a relatively smaller change, indicating that the initial combustion duration depends more on the injection timings, and less on the premixed CNG/air equivalence ratio.

5.3.3.2 Natural Flame Luminosity Imaging

Figure 5.19 shows a comparison of NL images at various equivalence ratios (0.38, 0.47, 0.57, 0.66 – left to right) at CNG70. It can be observed that multiple ignition zones occur around the periphery of the chamber and the reaction zones propagate towards the center. This is significant because propagation of these zones towards the center had previously been observed only at higher equivalence ratios [129]. Even at lower equivalence ratios, using a dual diesel injection strategy significantly enhances flame propagation towards the center of the combustion chamber due to a more favorable equivalence ratio distribution in the chamber owing to the enhanced mixing between the CNG and the pilot-injected diesel fuel. Ignition occurs closer to the main injection timing and combustion after that is dictated by the relative equivalence ratio distribution, as discussed earlier.

At the lowest equivalence ratio of 0.38, multiple ignition zones are observed around the periphery of the chamber. Both lean premixed zones and rich luminous ignition zones are observed simultaneously but separately in different regions in the combustion chamber and premixed combustion and mixing mechanisms occur simultaneously, which was previously observed only at high equivalence ratios ($\Phi>0.8$) with a single diesel injection. The plume structure is evident on both sides of the image, but the plumes on the left are blue and those on the right are orange,

indicating that the ignition mode varies from plume to plume. Another observation is that regardless of the mode, all of the images in Figure 5.19 indicate that ignition happens in the plumes. Given that the overall premixed charge (CNG + air) is lower in this case and that there is enough time to mix, most of the CNG is entrained into the pilot diesel injection and ignites readily, and as such, there is much less CNG mixture which still needs to mix and ignite. At such a low equivalence ratio, there is no 'wave' propagation observed. Reaction zones are clearly separate and there is no merging. As equivalence ratio is increased to 0.47, lean premixed combustion is more intense but there is still no merging of reaction zones. However, with further increase of the premixed equivalence ratio to 0.57, merging of reaction zones is observed and two 'waves' propagating from the periphery to the center from opposite sides are observed (rows 3 and 4). Further increasing Φ to 0.66 leads to a quite luminous and intense premixed combustion. Localized rich zones within the lean premixed reaction zone are observed. These reaction zones subsequently merge and propagate towards the center in a continuous flame front-like manner – so it is suspected that this could be an evidence of flame propagation.

In Dronniu et al. [129], under high equivalence ratios (Φ = 0.9), it was found that the progressive displacement of the reaction zones appeared to be continuous such that combustion propagates from neighboring zones, which suggested that flame propagation could be the predominant combustion mode under this condition. Secondly, based on [140], it is possible to obtain a measurement of laminar flame speed when equivalence ratio exceeds the threshold of 0.6. As such, it is possible that the images shown in Figure 5.19 show evidence of flame propagation. Therefore, using a pilot injection strategy with two diesel injection events, flame propagation could be observed at relatively lower equivalence ratios (~0.6) and propagation of these merged reaction

zones towards the center could be improved and unburned methane emissions could potentially be reduced at low loads.

5.3.3.3 Soot Temperature and Soot Volume Fraction (KL factor)

Figure 5.20 and Figure 5.21 show soot temperature and soot volume fraction (KL factor) evolution comparing various loads (premixed CNG/air Φ) at CNG70. Figure 5.22 and Figure 5.23 show the corresponding soot temperature KL factor distributions within the combustion chamber as a function of CAD. From the temperature distribution, it can be observed that when the premixed CNG/air equivalence ratio is lean (0.38), the combustion duration is quite short, and there are no high temperature zones observed beyond 20° ATDC, indicating that the CNG/air mixture is too lean to combust. As the CNG/air equivalence ratio is increased beyond 0.4, a more prolonged combustion duration, with high temperature zones (T > 2000 K) are observed. The proportion of zones with T > 2200 K also increases progressively as the CNG/air equivalence ratio is increased. From the KL distributions, it is observed that the KL factor predominantly lies between 2 and 2.5. As the CNG/air equivalence ratio increases, the proportion of high soot concentration zones (KL > 2.5) is increased. The rise of soot concentration (1.5<KL<2) indicating the late combustion period also increases with CNG/air equivalence ratio and gets progressively more pronounced, indicating the slow combustion of the entrained CNG/air mixture.

5.3.4 Equivalence ratio (load) comparison [CNG50, CNG30]

5.3.4.1 Combustion Characteristics

In this test, the pilot diesel injection strategy was further explored using two diesel injection events at lower substitution ratios of 50% and 30% and lower equivalence ratios to investigate the

combustion characteristics. Table 5.7 and Table 5.8 show the experimental conditions used for the equivalence ratio comparison at 50% and 30% substitution ratios, respectively. The dwell between the two diesel injections was maintained at 10 degrees. The injection timings for the two diesel injections was constant while changing the main injection quantity with increasing load. Figure 5.24 and Figure 5.31 show the pressure and heat release rate curves comparing various premixed CNG equivalence ratios (increasing overall equivalent load) at CNG50 and CNG30, respectively. Figure 5.25 and Figure 5.32 show quantitative combustion characteristics - ignition delay, initial combustion, and main combustion duration in terms of crank angle degrees at CNG50 and CNG30, respectively.

At these lower substitution ratios, the changes observed as load is increased are less severe, relative to those observed for the CNG70 case earlier. However, combustion phasing gets slightly retarded as load (and thus, Φ) is increased. Based on Figure 5.25 and Figure 5.32, the increasing diesel injection amount in the main injection does not affect the ignition delay or the initial combustion duration, but increases the main combustion duration – which is characteristic of conventional diesel combustion using two injections [117]. Among these results, the premixed CNG/air Φ ranges from 0.16 (CNG30, lowest load) to 0.4 (CNG50, highest load). The lower flammability limit of natural gas/air is ~0.55; however, this could be extended to ~0.45 with techniques like hydrogen addition, increasing ignition energy etc. [141]. Therefore, it is likely that at such low equivalence ratios, the CNG/air mixture is barely combustible and this would result in high UHC emissions consisting of methane. This is further supported by the lower values of measured IMEP for the CNG50 and CNG30 cases, relative to the CNG70 case.

5.3.4.2 Natural Flame Luminosity Imaging

Figure 5.26 and Figure 5.33 show a comparison of NL images at various equivalence ratios at CNG50 and CNG30, respectively. Minor differences are observed among the various cases shown. The blue flame previously observed under CNG70 is not observed in these images and there is no evidence of any 'wave'-like flame behavior characteristic of diesel/CNG dual-fuel combustion. In fact, from Figure 5.33, typical diesel combustion characteristics, such as spray/diffusion combustion can be observed. The luminosity is considerably higher for these cases, relative to the CNG70 cases. It is to be noted that CNG70, CNG50, and CNG30 were tested at the same loads – the global equivalence ratio is constant across these cases (see Table 5.6, Table 5.7 and Table 5.8). It is therefore concluded that the parameter primarily affecting the combustion mode/mechanism is the premixed CNG/air equivalence ratio.

5.3.4.3 Soot Temperature and Soot Volume Fraction (KL factor)

Figure 5.27 and Figure 5.28 show soot temperature and soot volume fraction (KL factor) evolution comparing various loads (premixed CNG/air Φ) at CNG50, and those under CNG30 care shown in Figure 5.34 and Figure 5.35. Figure 5.29 and Figure 5.30 show the corresponding soot temperature KL factor distributions within the combustion chamber as a function of CAD under CNG50, and those for CNG30 are shown in Figure 5.36 and Figure 5.37.

For these lower CNG substitution ratios, the distributions vary quite similarly. From the temperature distribution, a clear growth of the high-temperature zones ($T > 2200$ K) near the beginning of combustion indicating premixed combustion is observed with increasing CNG/air equivalence ratio. These high-temperature zones are observed to extend all the way up to the end of the combustion process. From the KL factor distribution, it is observed that the KL factor

predominantly shows values above 2.5 (high soot concentration). Another important observation is that the shape of the soot formation/oxidation profile in the late combustion period is similar for all the cases under a given CNG substitution ratio. Therefore, it is likely that under these low substitution ratios, the late combustion is only due to diesel combustion and increasing the CNG/air equivalence ratio does not affect this, and the effect of the CNG is primarily to increase the high-temperature premixed combustion.

5.3.5 Injection Strategy Comparisons – Main Timing Sweep

5.3.5.1 Combustion Characteristics

In this test, the pilot diesel injection strategy using two diesel injection events was tested at CNG70, varying the main injection timing while maintaining the pilot injection timing at 5° BTDC. Table 5.9 shows the experimental conditions used for this comparison. The injection quantities for the two diesel injections were constant. Figure 5.38 and Figure 5.39 show the pressure and HRR curves and quantitative combustion characteristics under the different substitution ratios, respectively.

It can be observed that as the main injection timing is retarded, the ignition delay gets extended. For the main timing of 15° BTDC, it appears that the relatively smaller dwell of 5° between the injections merges the injection events together, leading to a more drawn out diffusion combustion process. With a dwell of 10°, the injection events are sufficiently separated and the equivalence ratio distribution is more uniform. Further retarding the main injection timing to 5° BTDC, the relatively higher pressure and temperature in the chamber cause faster ignition of the diesel jets, however insufficient time for the CNG mixture to get entrained, combined with the retarded phasing leads to a long diffusion combustion tail on the HRR curve, as observed previously. The

asymptotic tail observed on the rate of heat release can be explained by the increase of cylinder volume during the expansion stroke.

5.3.5.2 Natural Flame Luminosity Imaging

Figure 5.40 shows a comparison of NL images at various main injection timings. From the images, it can be observed that a main injection timing of 10° BTDC, with a 10° dwell provides the most uniform equivalence ratio distribution among these tested cases, as evidenced by the presence of a relatively uniform distribution of reaction zones all over the combustion chamber. Both the earlier and later main injections cause an uneven equivalence ratio distribution, with the reaction zones not uniformly distributed. In the former case, this is likely due to merging of the injection events, whereas in the latter case, this is due to the shorter ignition delay combined with the retarded phasing. This argument is supported by the fact that the highest measured IMEP value is obtained for the 10° BTDC main injection timing. Therefore, the main injection timing must be sufficiently separated from the pilot injection timing such that there is enough time for the diesel jets to be entrained by the CNG/air mixture and sufficiently advanced such that the increasing cylinder volume in the expansion stroke does not slow down the combustion process.

5.3.5.3 Soot Temperature and Soot Volume Fraction (KL factor)

Figure 5.41 and Figure 5.42 show soot temperature and soot volume fraction (KL factor) evolution comparing various main injection timings at CNG70. Figure 5.43 and Figure 5.44 show the corresponding soot temperature and KL factor distributions within the combustion chamber as a function of CAD.

From the soot temperature distributions, it can be observed that retarding the main injection timing considerably increases the high-temperature zone (T>2000 K) which extends throughout the combustion process, likely due to the longer mixing time for the CNG/air mixture and the pilot-injected diesel fuel due to the increased dwell period between injections.

Likewise, the KL factor distributions show that retarding the main injection timing increases the high soot concentration zone (KL > 2.5), which is not observed in the advanced timing cases. This retarded timing also displays a relatively sharp late combustion period, relative to the other cases, where it is more gradual.

5.3.6 Injection Strategy Comparisons – Pilot Timing Sweep

5.3.6.1 Combustion Characteristics

In this test, the pilot diesel injection strategy using two diesel injection events was tested at CNG70, varying the pilot injection timing while maintaining the main injection timing at 10° BTDC. Table 5.10 shows the experimental conditions used for this comparison. The injection quantities for the two diesel injections were constant. Figure 5.45 and Figure 5.46 show the pressure and HRR curves and quantitative combustion characteristics under the different substitution ratios, respectively.

It is observed that variation in the pilot timing leads to a non-uniform trend in that, the 10° dwell case shows the shortest ignition delay and the most advanced combustion phasing, followed by the 15° dwell, and finally the 5° dwell displays the largest ignition delay. The relatively retarded phasing of the early pilot timing of 25° BTDC might be due to the longer dwell, which may cause over-mixing, and thus when the main injection event occurs additional time is required to achieve flammability limits, relative to the 10° dwell case. For the 5° dwell case, it is likely that the

injection events merged leading to a long ignition delay and retarded combustion phasing which leads to slow diffusion combustion reaching well into the expansion stroke.

5.3.6.2 Natural Flame Luminosity Imaging

Figure 5.47 shows a comparison of NL images at various pilot injection timings. From the images, it can be observed that as the pilot injection timing is retarded (and the dwell shortened), the penetration of the reaction zones towards the center of the combustion chamber gets reduced. The overall luminosity of the 5° dwell case with the retarded pilot injection timing is the highest among these cases. Comparing the other two cases tested, the 20° BTDC pilot causes the most uniform distribution of luminosity throughout the combustion chamber. Meanwhile, the 25° BTDC pilot causes an overall lower luminosity with better penetration towards the center, however, a region of the combustion chamber exhibits a bright orange reaction zone, which likely points to over-mixing, leading to accumulation of the pilot-injected diesel fuel at a certain position in the combustion chamber possibly due to the air motion inside the cylinder. The measured IMEP values vary as follows in terms of the pilot injection timing: 20° BTDC>25° BTDC>15° BTDC, suggesting that there exists an ideal timing that provides the highest IMEP.

5.3.6.3 Soot Temperature and Soot Volume Fraction (KL factor)

Figure 5.48 and Figure 5.49 show soot temperature and soot volume fraction (KL factor) evolution comparing various pilot injection timings at CNG70. Figure 5.50 and Figure 5.51 show the corresponding soot temperature and KL factor distributions within the combustion chamber as a function of CAD.

There are no major difference in the actual temperature distributions among the various pilot injection timings; however, as mentioned earlier, a retarded pilot injection timing increases the overall combustion duration. The KL factor distributions show that the increased combustion duration is likely due to the prolonged late diffusion combustion duration, which gets progressively sharper/shorter as the pilot injection timing is advanced.

5.3.7 Injection Strategy Comparisons – Pilot/Main Split Sweep

5.3.7.1 Combustion Characteristics

In this test, the pilot diesel injection strategy using two diesel injection events was tested at CNG70, varying the pilot/main mass split. Table 5.11 shows the experimental conditions used for this comparison. The dwell between the two diesel injections was maintained at 10 degrees. The injection timings for the two diesel injections was constant while changing the pilot/main injection quantities as follows: 3 mg/7.5 mg, 4mg/6.5 mg, 5 mg/5.5 mg. Figure 5.52 and Figure 5.53 show the pressure and HRR curves and quantitative combustion characteristics under the different substitution ratios, respectively.

The figures show that as the ratio of the pilot injection mass to the total injection mass is increased, the ignition delay is shortened and the combustion phasing gets advanced, owing to a reduced initial combustion duration as well as a reduced main combustion duration. This is likely due to the enhanced equivalence ratio distribution in the combustion chamber, which leads to an increase in the burning velocity leading to faster combustion. In other words, having a relatively larger pilot injection mass leads to an optimum usage of the dwell period between injections to create a uniform fuel distribution that leads to favorable conditions as the main injection event occurs.

5.3.7.2 Natural Flame Luminosity Imaging

Figure 5.54 shows a comparison of NL images at various pilot/main mass splits. The images show that as the ratio of the pilot injection mass to the total injection mass is increased, the reaction zones get progressively uniform (and lower) in terms of luminosity, and the penetration towards the center is improved. As the pilot mass is increased, the equivalence ratio distribution is improved, and a relatively higher distribution of ignition spots (diesel) is present before the main injection event which causes ignition.

5.3.7.3 Soot Temperature and Soot Volume Fraction (KL factor)

Figure 5.55 and Figure 5.56 show soot temperature and soot volume fraction (KL factor) evolution comparing various pilot injection timings at CNG70. Figure 5.57 and Figure 5.58 show the corresponding soot temperature and KL factor distributions within the combustion chamber as a function of CAD. There are no major differences observed between temperature and KL factor distributions due to variations in the pilot/main injection split. However, the 1800 K <T< 2000 K zone near the beginning of combustion gets more pronounced with increased pilot injection mass, which is due to more time available for the pilot-injected mass to mix and reach combustible limits as the main injection event occurs.

It can be concluded that based on the various injection strategies tested, the main injection timing has the major impact on soot temperature and KL factor distributions.

5.4 Conclusions

In this study, diesel dual-fuel combustion was investigated in an optically accessible single-cylinder light duty diesel engine using a Phantom v7.3 color camera, in order to obtain high-speed

combustion images, as well as soot temperature and soot volume fraction (KL factor) information using the two-color method. Pressure and HRR curves were also obtained simultaneously to study the combustion characteristics. Various CNG substitution ratios, loads and diesel injection strategies were investigated. The following observations were made from the study:

- From the NL images, it was observed that the premixed, entrained CNG mixture ignites first at multiple zones near the wall and these zones propagate towards the center. From the CNG substitution (premixed CNG/air Φ), the transition from diesel spray/diffusion combustion to a mechanism with a flame front was clearly observed. At Φ~0.38 and 0.47, no merging of reaction zones and wave-like flame propagation was observed. However, with increasing Φ~0.6, reaction zones were observed to merge and evidence of flame propagation was observed (previously only observed at Φ~0.9), wherein two waves approached each other from opposite sides. It is suspected that the early pilot injection of diesel enhances overall equivalence ratio distribution in the chamber which leads to this behavior at relatively lower equivalence ratios. At CNG85, a single reaction zone was observed which developed into a flame front that began near the top of the frame and then spread out and propagated throughout the rest of the combustion chamber.
- From the images obtained using the 2-color method, it was found that the addition of a smaller amount of CNG (CNG30), enhanced the premixed combustion period (T > 2200 K) and the diffusion combustion period is shortened. As the CNG substitution is increased further, the early high-temperature zone gets reduced and relatively low-temperature diffusion combustion dominates the combustion process. At higher substitution ratios (CNG 70, CNG85), there are no high-temperature zones observed and the combustion is diffusion-dominant, predominantly showing a temperature T <2000 K, and the high soot

concentration regions are negligible; the soot centration throughout the combustion chamber is 1.5<KL<2.5.

- It was found that using two diesel injections could enhance propagation of reaction zones towards the center, even at low equivalence ratios (Φ~0.4-0.6) and could thus, partly alleviate the unburned methane emissions issue at low loads. Compared to a single main diesel injection, when a pilot injection is added, combustion shifts considerably towards being more premixed, with a higher HRR peak and a shorter combustion duration. The first pilot injection affects the overall equivalence ratio distribution within the combustion chamber and thus enhances the rate of the initial premixed combustion period, which consists of auto-ignition of the premixed diesel fuel as well as the entrained CNG mixture. Compared to single diesel injection, more ignition zones all over the periphery of the chamber, including localized rich luminous zones within the lean premixed reaction zone were observed.
- Based on tests using different diesel injection strategies, it was observed that the main injection timing must be sufficiently separated from the pilot injection timing such that there is enough time for the diesel jets to be entrained by the CNG/air mixture and sufficiently advanced such that the increasing cylinder volume in the expansion stroke does not slow down the combustion process. Based on the soot temperature and KL factor results, it was found that the main injection timing had the most pronounced impact on the combustion phasing and the soot temperature and KL factor distributions, while minor changes were observed with pilot injection timing variations and pilot/main injection mass variations.

In summary, this study shows through combustion visualization that multiple diesel injections could enhance overall fuel conversion in diesel dual-fuel combustion by enhancing the overall equivalence ratio distribution and thus the propagation of the reaction zones from the walls towards the center. This study also showed soot temperature and volume fraction results for the first time for CNG/diesel dual-fuel combustion.

Table 5.1 Engine Specifications

Engine Type	Single-cylinder, 4-stroke, Naturally aspirated
Displacement	0.664 L
Bore x Stroke	92 x 94 mm
Connecting Rod Length	160 mm
Geometric Compression Ratio	17:1
Number of valves	4 (2 intake, 2 exhaust)
Injection System	Bosch common rail, P_{max} = 1600 bar

Table 5.2 NL Imaging System

Camera	Phantom v7.3 CMOS Color
Lens	60mm-f/2.8 Micro-Nikkor
Aperture	f/16
Exposure time	98 μs
Frame Rate	10000 fps
Resolution	512x512
Image Enhancement	MATLAB

Table 5.3 Fuel Properties

Parameter	Diesel	CNG (Methane)
Density @ 20 C (kg/m3)	839.3	0.66
Viscosity @ 20 C (mm2/s)	4.367	0.011
Cetane Number	52.6	-
Lower Heating Value (MJ/kg)	44	50

Table 5.4 Test Conditions – CNG% (Φ) Sweep

Engine Speed (rpm)	1200	1200	1200	1200
Injection Pressure (bar)	1000	1000	1000	1000
Equivalent Diesel Load (mg)	30	30	30	30
Measured IMEP (bar)	3.7	4	4	4
CNG Substitution (%)	30	50	70	85
Diesel Injection 1 (Pilot) Timing (°BTDC)	20	20	20	20
Diesel Injection 1 (Pilot) Mass (mg)	3	3	3	3
Diesel Injection 2 (Main) Timing (°BTDC)	10	10	10	10
Diesel Injection 2 (Main) Mass (mg)	18	12	6	3
CNG Flow Rate (L/min)	7.2	12	16.8	23.25
CNG/air Premixed Φ	0.245	0.4	0.57	0.79
Global Φ (calculated [130])	0.79	0.8	0.8	0.94

Table 5.5 Test Conditions – Single vs Multiple Injection

Engine Speed (rpm)	1200	1200	1200	1200	1200
Injection Pressure (bar)	1000	1000	1000	1000	1000
Equivalent Diesel Load (mg)	35	35	35	35	35
Measured IMEP (bar)	4.6	4.7	4.7	5	4.6
CNG Substitution (%)	70	70	70	70	70
Diesel Injection 1 (Pilot) Timing (°BTDC)	-	-	20	25	30
Diesel Injection 1 (Pilot) Mass (mg)	-	-	3	3	3
Diesel Injection 2 (Main) Timing (°BTDC)	20	15	15	15	15
Diesel Injection 2 (Main) Mass (mg)	10.5	10.5	7.5	7.5	7.5
CNG Flow Rate (L/min)	19.6	19.6	19.6	19.6	19.6
CNG/air Premixed Φ	0.66	0.66	0.66	0.66	0.66
Global Φ (calculated [130])	0.94	0.94	0.94	0.94	0.94

Table 5.6 Test Conditions – CNG70 Φ (load) Sweep

Engine Speed (rpm)	1200	1200	1200	1200
Injection Pressure (bar)	1000	1000	1000	1000
Equivalent Diesel Load (mg)	20	25	30	35
Measured IMEP (bar)	2.8	3.2	4	5
CNG Substitution (%)	70	70	70	70
Diesel Injection 1 (Pilot) Timing (°BTDC)	20	20	20	20
Diesel Injection 1 (Pilot) Mass (mg)	3	3	3	3
Diesel Injection 2 (Main) Timing (°BTDC)	10	10	10	10
Diesel Injection 2 (Main) Mass (mg)	3	4.5	6	7.5
CNG Flow Rate (L/min)	11.2	14	16.8	19.6
CNG/air Premixed Φ	0.38	0.47	0.57	0.66
Global Φ (calculated [130])	0.53	0.67	0.8	0.94

Table 5.7 Test Conditions – CNG50 Φ (load) Sweep

Engine Speed (rpm)	1200	1200	1200
Injection Pressure (bar)	1000	1000	1000
Equivalent Diesel Load (mg)	20	25	30
Measured IMEP (bar)	2.2	2.9	4
CNG Substitution (%)	50	50	50
Diesel Injection 1 (Pilot) Timing (°BTDC)	20	20	20
Diesel Injection 1 (Pilot) Mass (mg)	3	3	3
Diesel Injection 2 (Main) Timing (°BTDC)	10	10	10
Diesel Injection 2 (Main) Mass (mg)	7	9.5	12
CNG Flow Rate (L/min)	8	10	12
CNG/air Premixed Φ	0.27	0.34	0.4
Global Φ (calculated [130])	0.53	0.67	0.8

Table 5.8 Test Conditions – CNG30 Φ (load) Sweep

Engine Speed (rpm)	1200	1200	1200
Injection Pressure (bar)	1000	1000	1000
Equivalent Diesel Load (mg)	20	25	30
Measured IMEP (bar)	2.4	2.5	3.6
CNG Substitution (%)	30	30	30
Diesel Injection 1 (Pilot) Timing (°BTDC)	20	20	20
Diesel Injection 1 (Pilot) Mass (mg)	3	3	3
Diesel Injection 2 (Main) Timing (°BTDC)	10	10	10
Diesel Injection 2 (Main) Mass (mg)	11	14.5	18
CNG Flow Rate (L/min)	4.8	6	7.2
CNG/air Premixed Φ	0.16	0.2	0.245
Global Φ (calculated [130])	0.53	0.66	0.79

Table 5.9 Test Conditions – CNG70 Main Timing Sweep

Engine Speed (rpm)	1200	1200	1200
Injection Pressure (bar)	1000	1000	1000
Equivalent Diesel Load (mg)	35	35	35
Measured IMEP (bar)	4.5	5	4.7
CNG Substitution (%)	70	70	70
Diesel Injection 1 (Pilot) Timing (°BTDC)	20	20	20
Diesel Injection 1 (Pilot) Mass (mg)	3	3	3
Diesel Injection 2 (Main) Timing (°BTDC)	15	10	5
Diesel Injection 2 (Main) Mass (mg)	7.5	7.5	7.5
CNG Flow Rate (L/min)	19.6	19.6	19.6
CNG/air Premixed Φ	0.66	0.66	0.66
Global Φ (calculated [130])	0.94	0.94	0.94

Table 5.10 Test Conditions – Pilot Timing Sweep

Engine Speed (rpm)	1200	1200	1200
Injection Pressure (bar)	1000	1000	1000
Equivalent Diesel Load (mg)	35	35	35
Measured IMEP (bar)	5.1	5	4.6
CNG Substitution (%)	70	70	70
Diesel Injection 1 (Pilot) Timing (°BTDC)	25	20	15
Diesel Injection 1 (Pilot) Mass (mg)	3	3	3
Diesel Injection 2 (Main) Timing (°BTDC)	10	10	10
Diesel Injection 2 (Main) Mass (mg)	7.5	7.5	7.5
CNG Flow Rate (L/min)	19.6	19.6	19.6
CNG/air Premixed Φ	0.66	0.66	0.66
Global Φ (calculated [130])	0.94	0.94	0.94

Table 5.11 Test Conditions – Pilot/Main Split Sweep

Engine Speed (rpm)	1200	1200	1200
Injection Pressure (bar)	1000	1000	1000
Equivalent Diesel Load (mg)	35	35	35
Measured IMEP (bar)	5	4.9	4.7
CNG Substitution (%)	70	70	70
Diesel Injection 1 (Pilot) Timing (°BTDC)	20	20	20
Diesel Injection 1 (Pilot) Mass (mg)	3	4	5
Diesel Injection 2 (Main) Timing (°BTDC)	15	10	5
Diesel Injection 2 (Main) Mass (mg)	7.5	6.5	5.5
CNG Flow Rate (L/min)	19.6	19.6	19.6
CNG/air Premixed Φ	0.66	0.66	0.66
Global Φ (calculated [130])	0.94	0.94	0.94

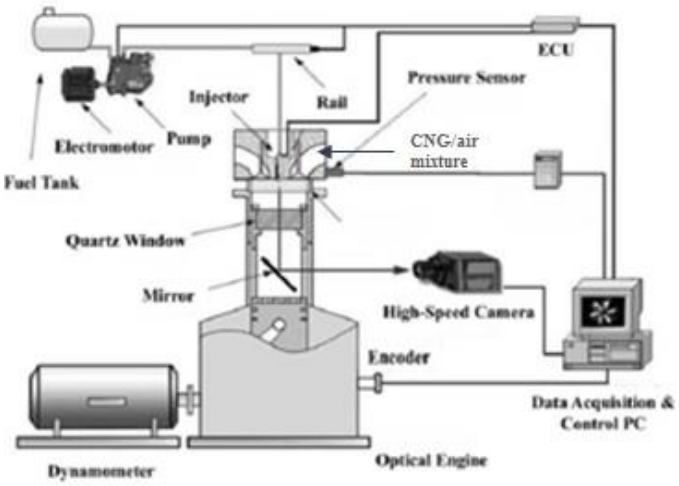

Figure 5.1 Schematic of the optical engine setup

(a)

(b)

Figure 5.2 (a) Original image, (b) Enhanced image

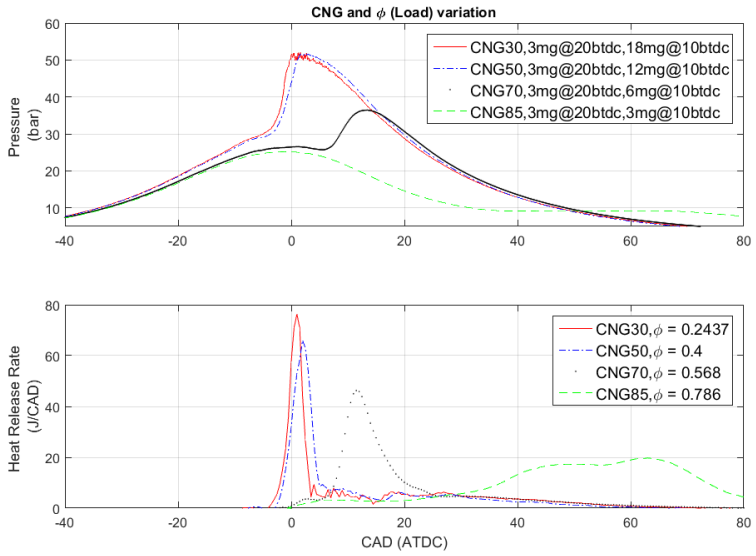

Figure 5.3 Pressure and HRR curves comparing various substitution ratios

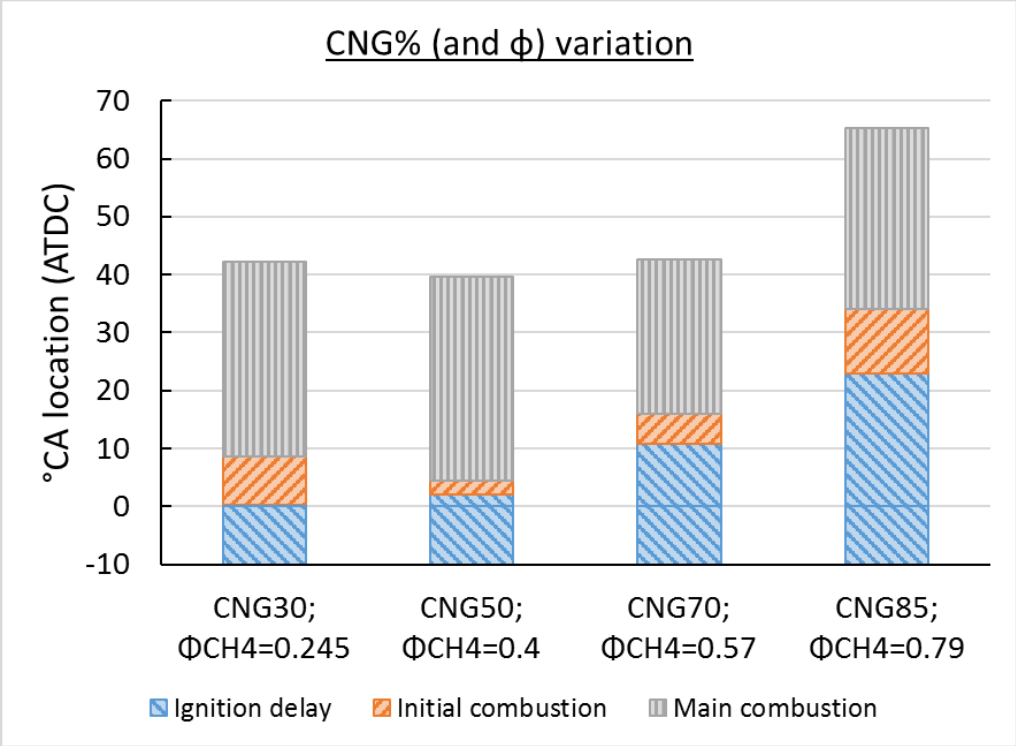

Figure 5.4 Combustion characteristics at various substitution ratios

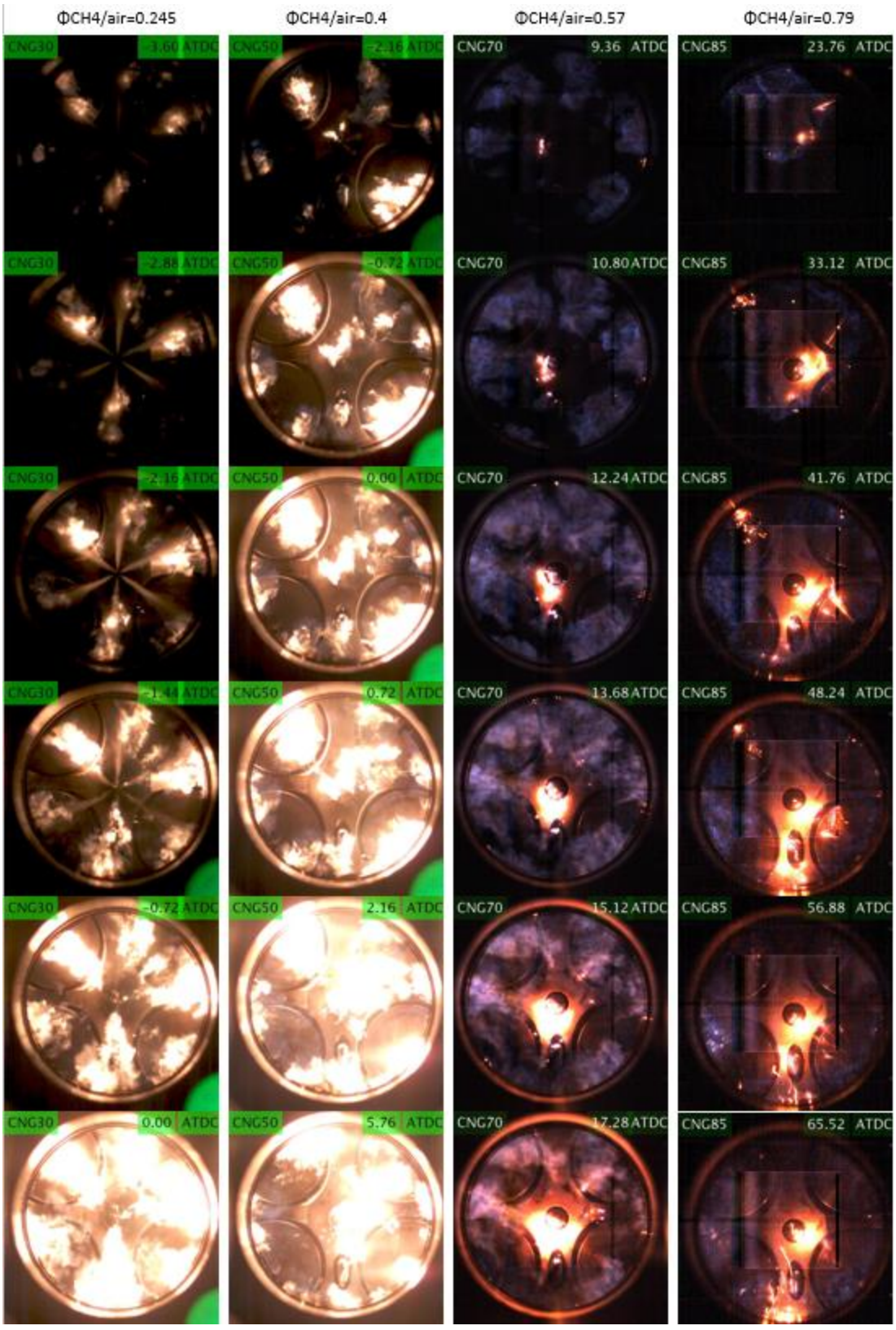

Figure 5.5 NL images comparing various substitution ratios

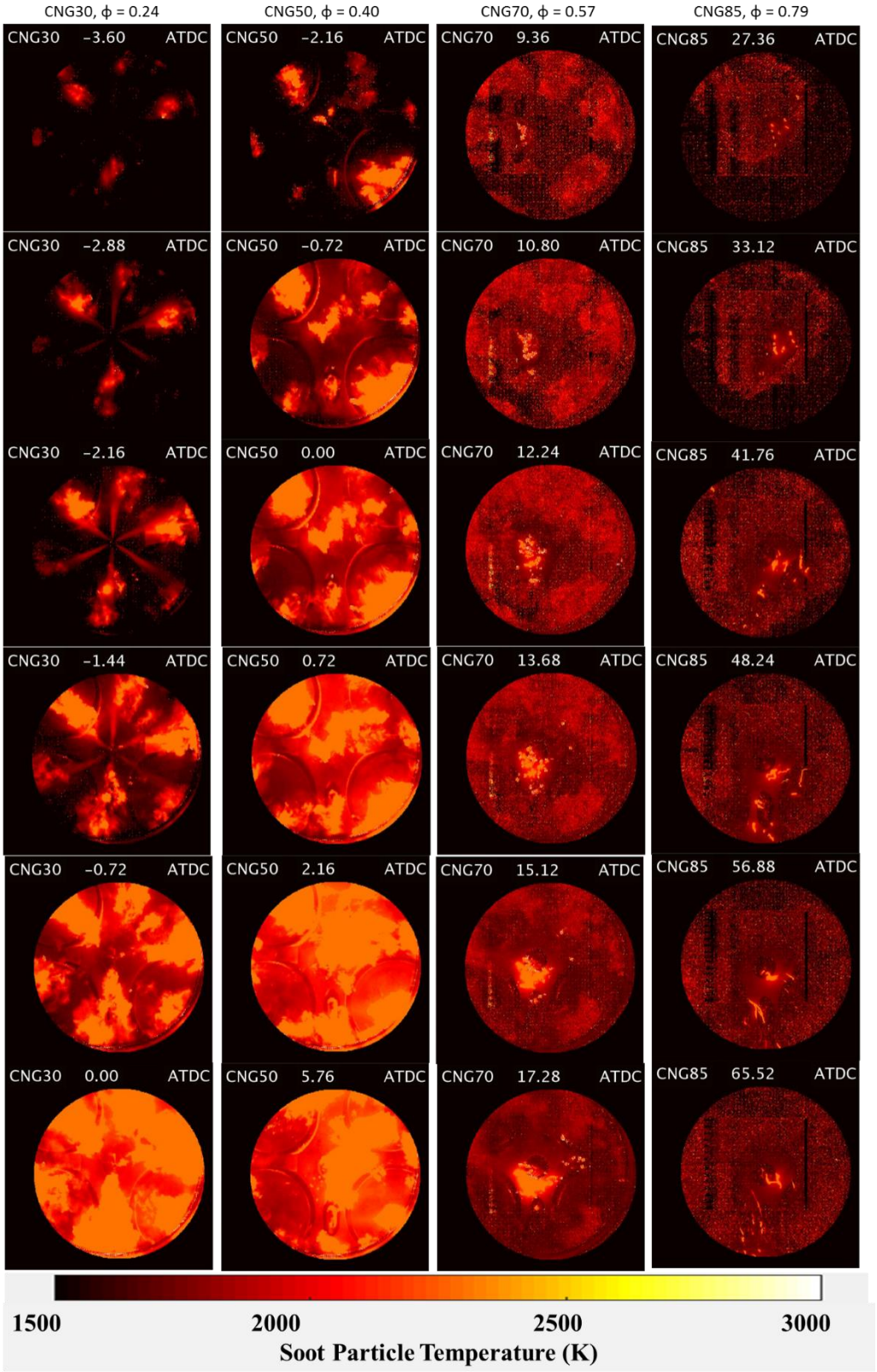

Figure 5.6 Soot temperature images comparing various substitution ratios

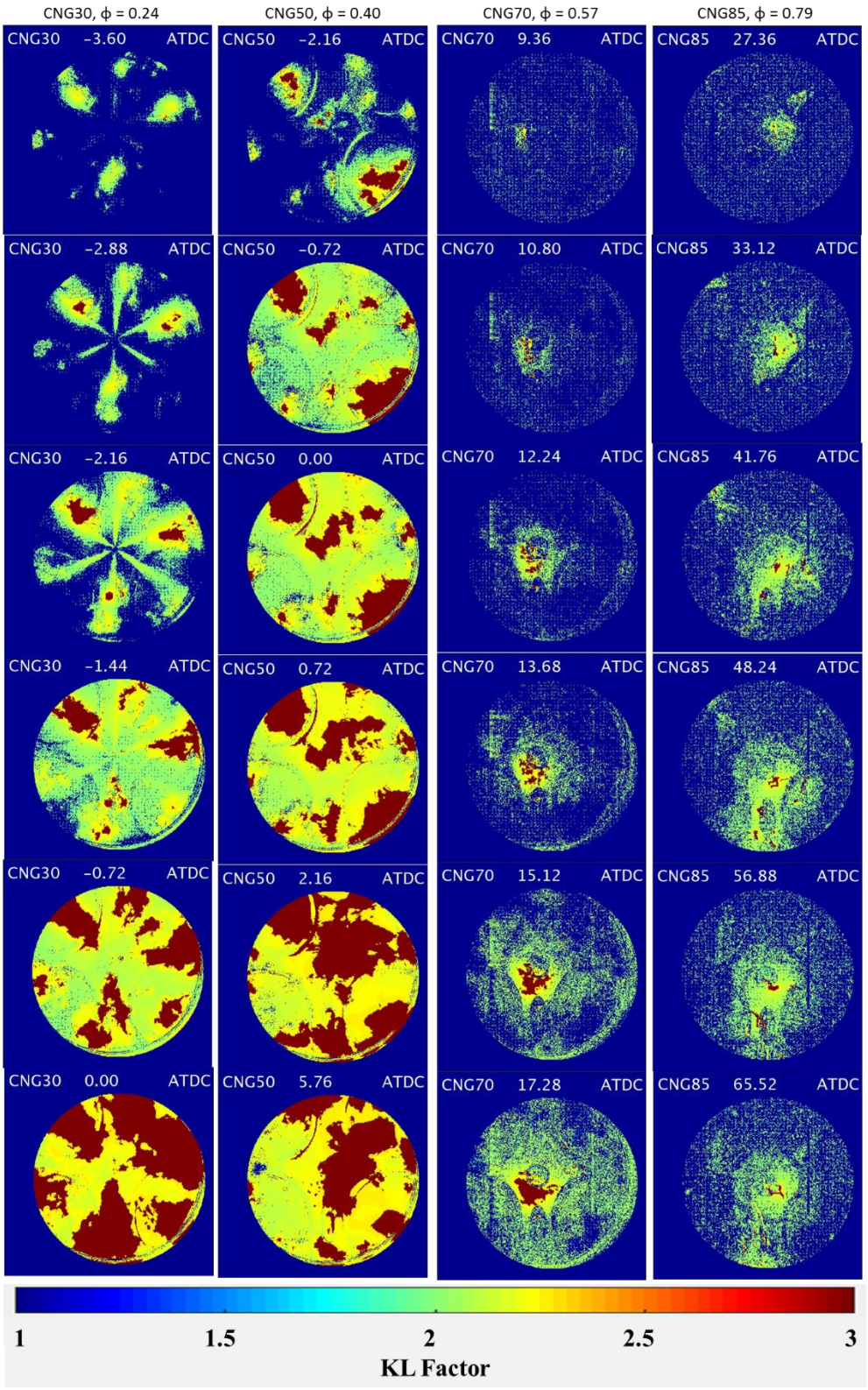

Figure 5.7 KL factor images comparing various substitution ratios

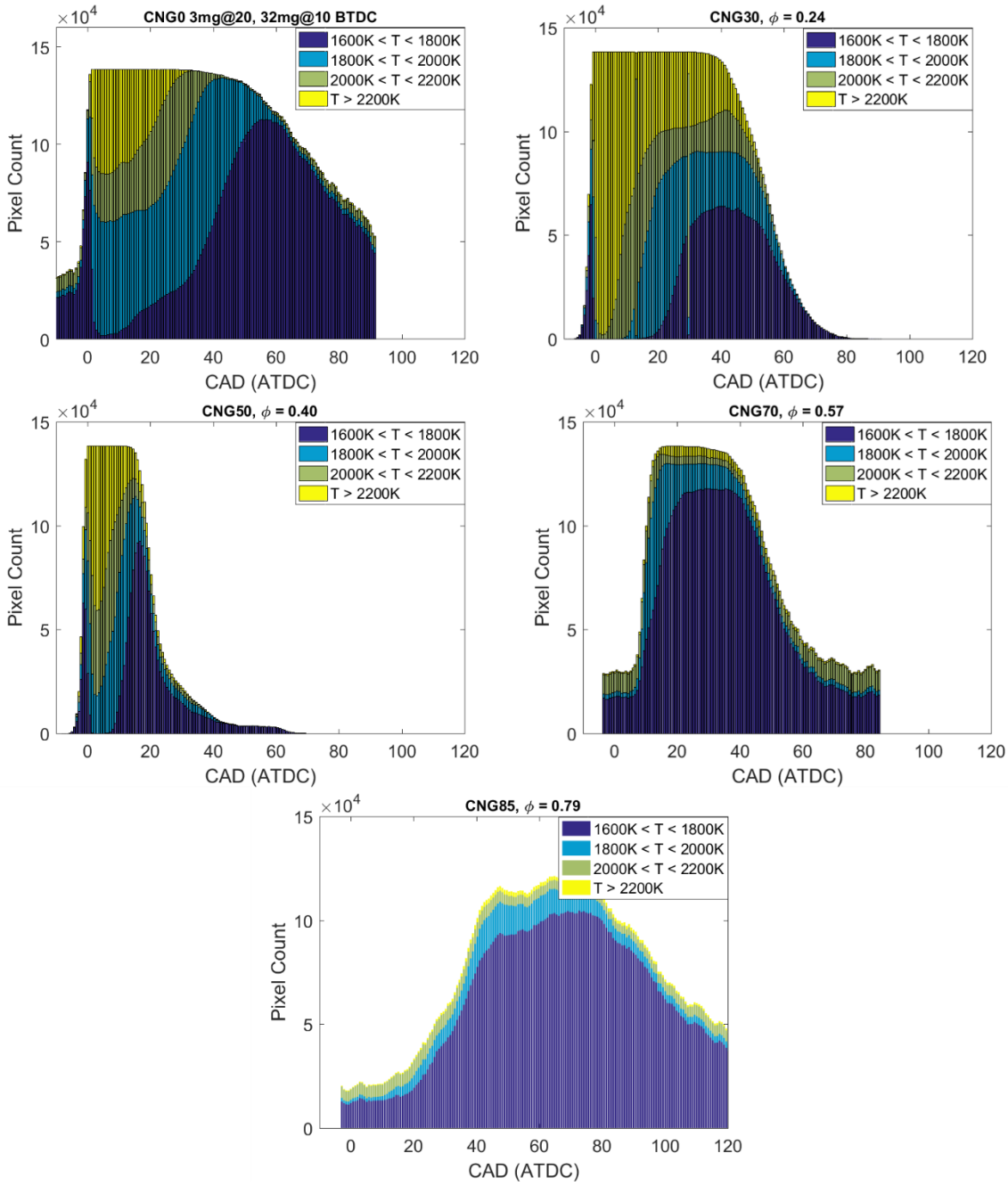

Figure 5.8 Soot temperature distributions comparing various substitution ratios (including CNG0)

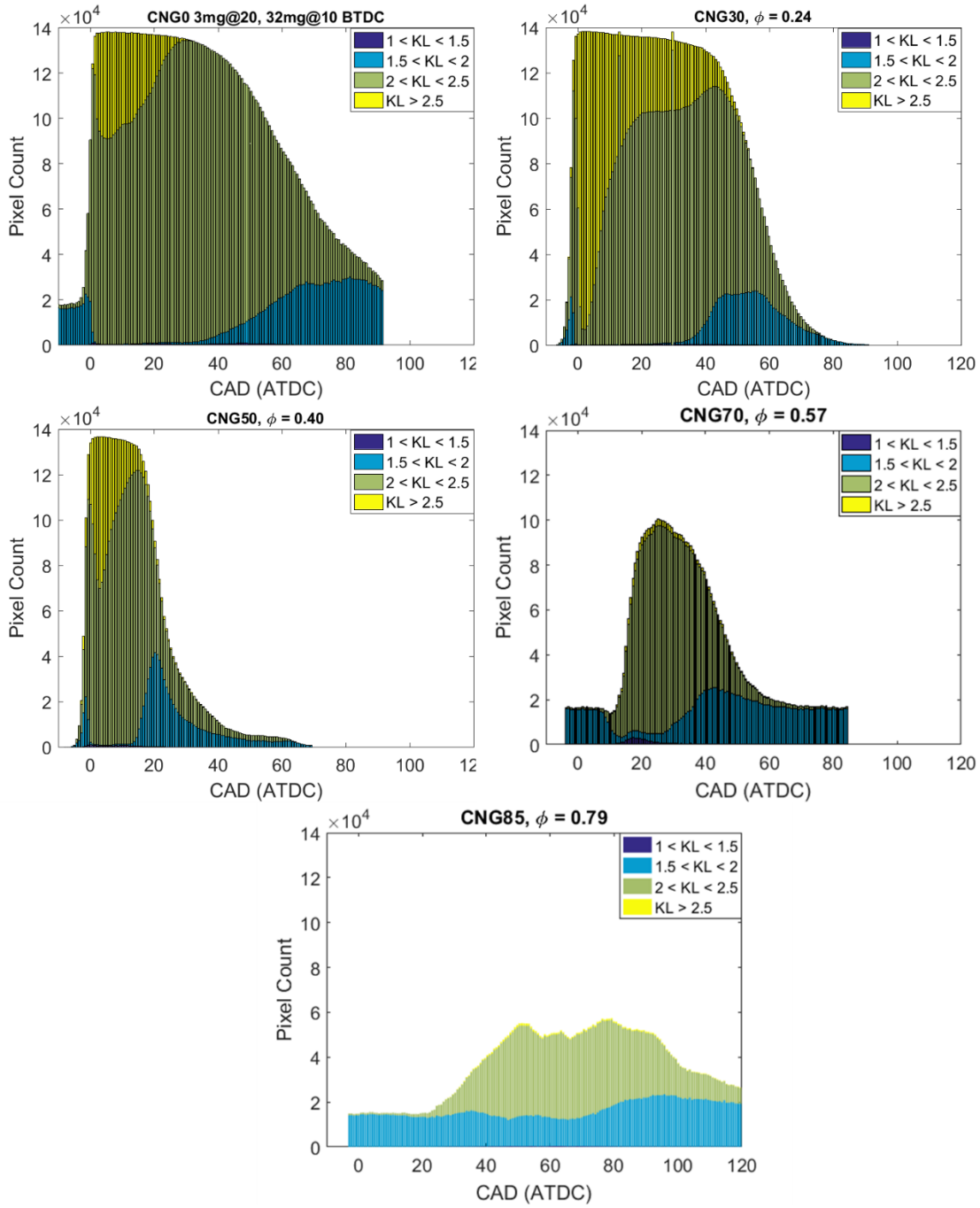

Figure 5.9 KL factor distributions comparing various substitution ratios (including CNG0)

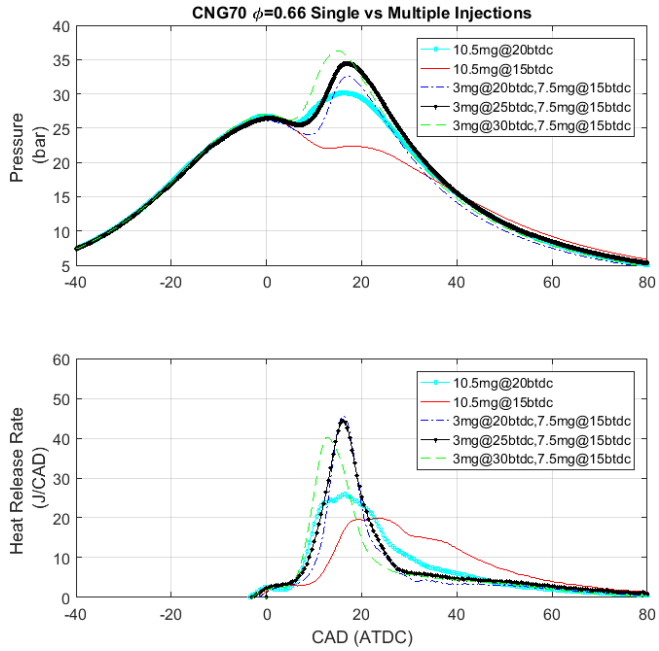

Figure 5.10 Pressure and HRR curves comparing single and multiple diesel injections (CNG70, Φ = 0.66)

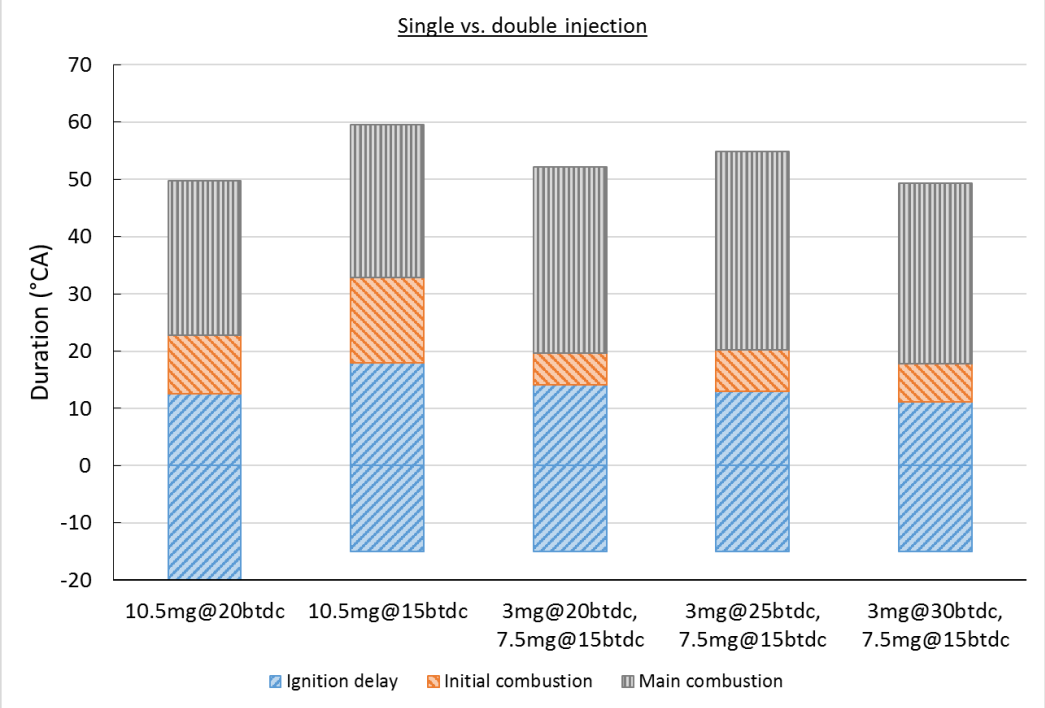

Figure 5.11 Combustion characteristics comparing single and multiple diesel injections

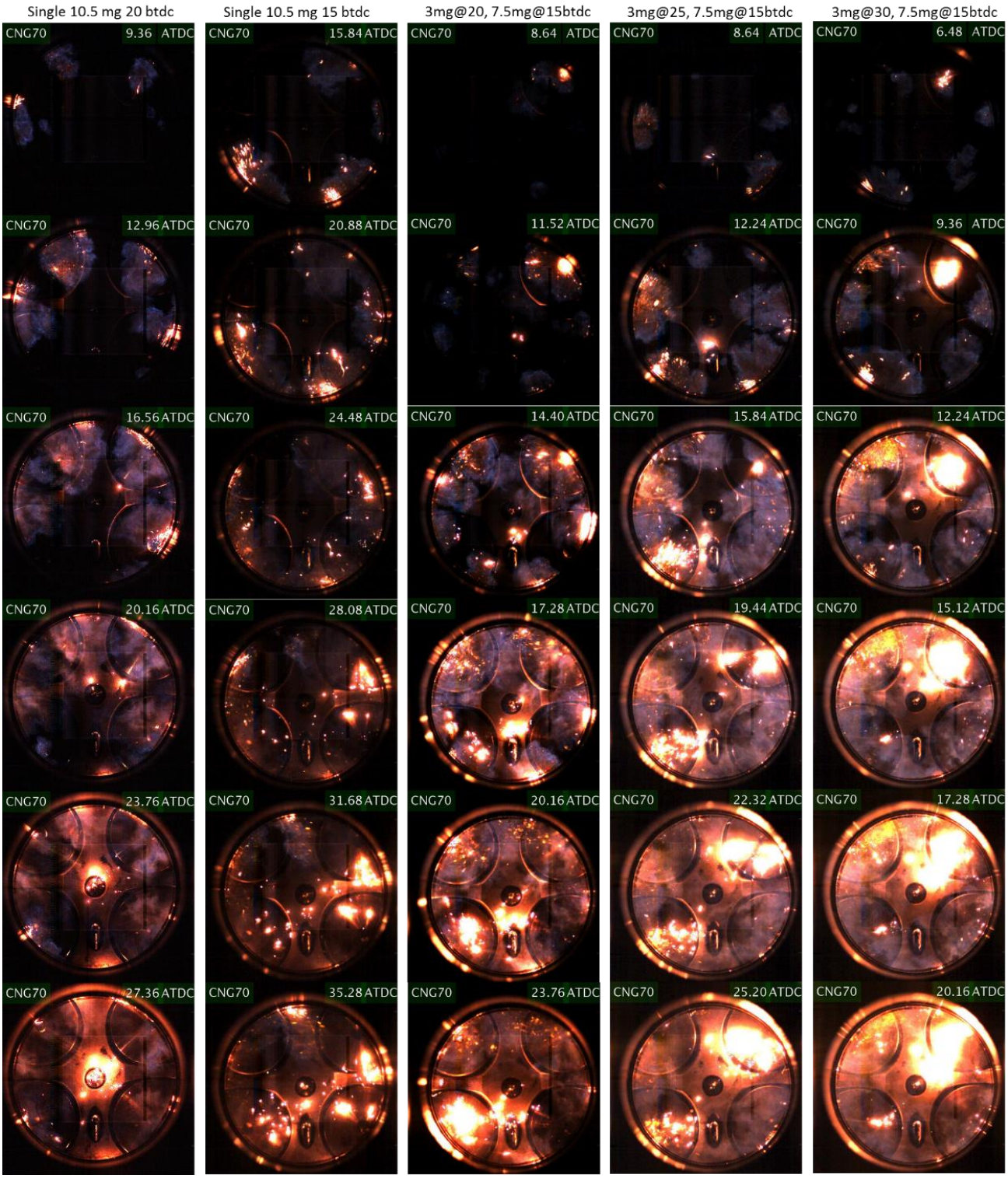

Figure 5.12 NL images comparing single and dual diesel injections (CNG70, Premixed CNG/air phi = 0.66)

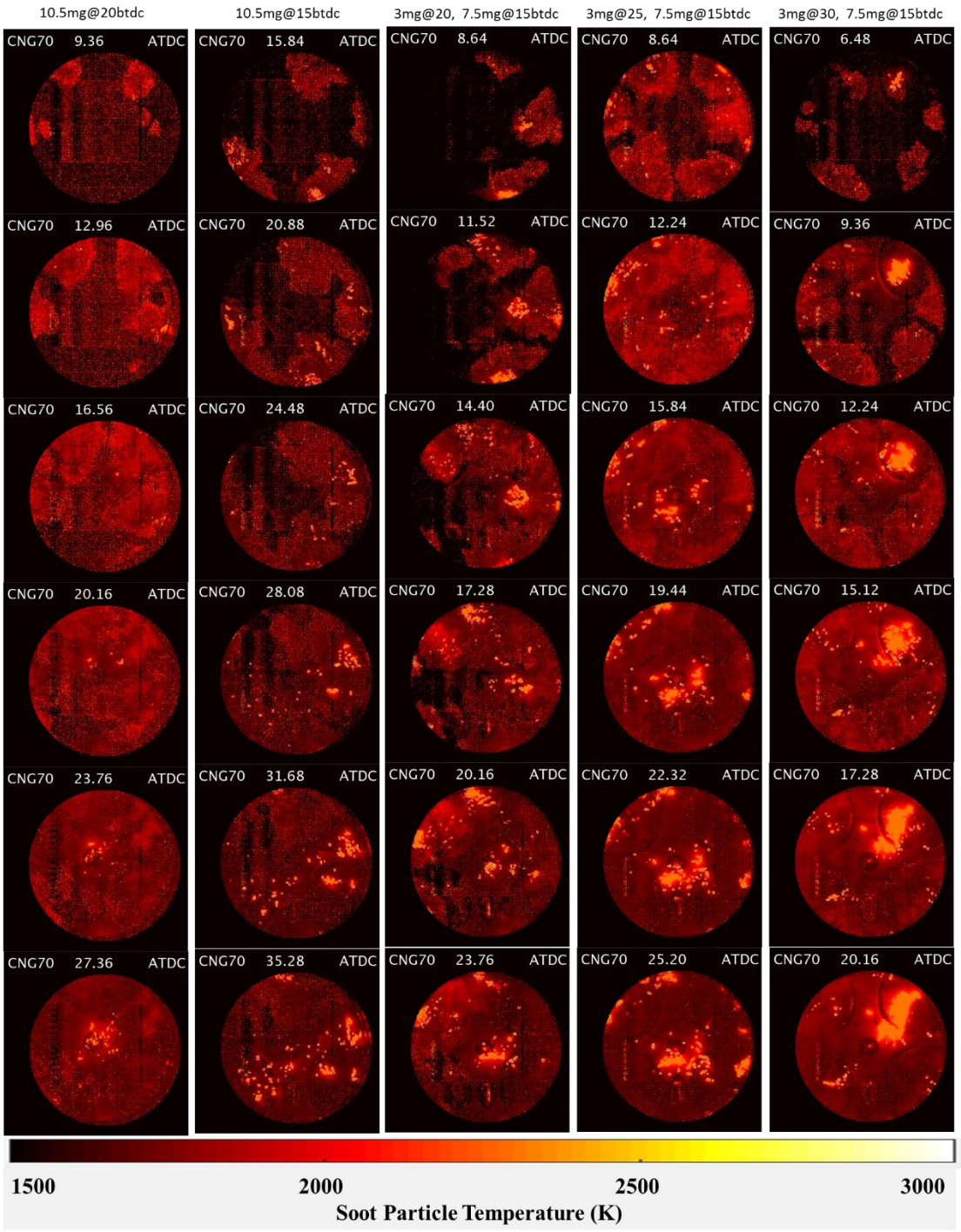

Figure 5.13 Soot temperature images comparing single and dual diesel injections (CNG70, Premixed CNG/air phi = 0.66)

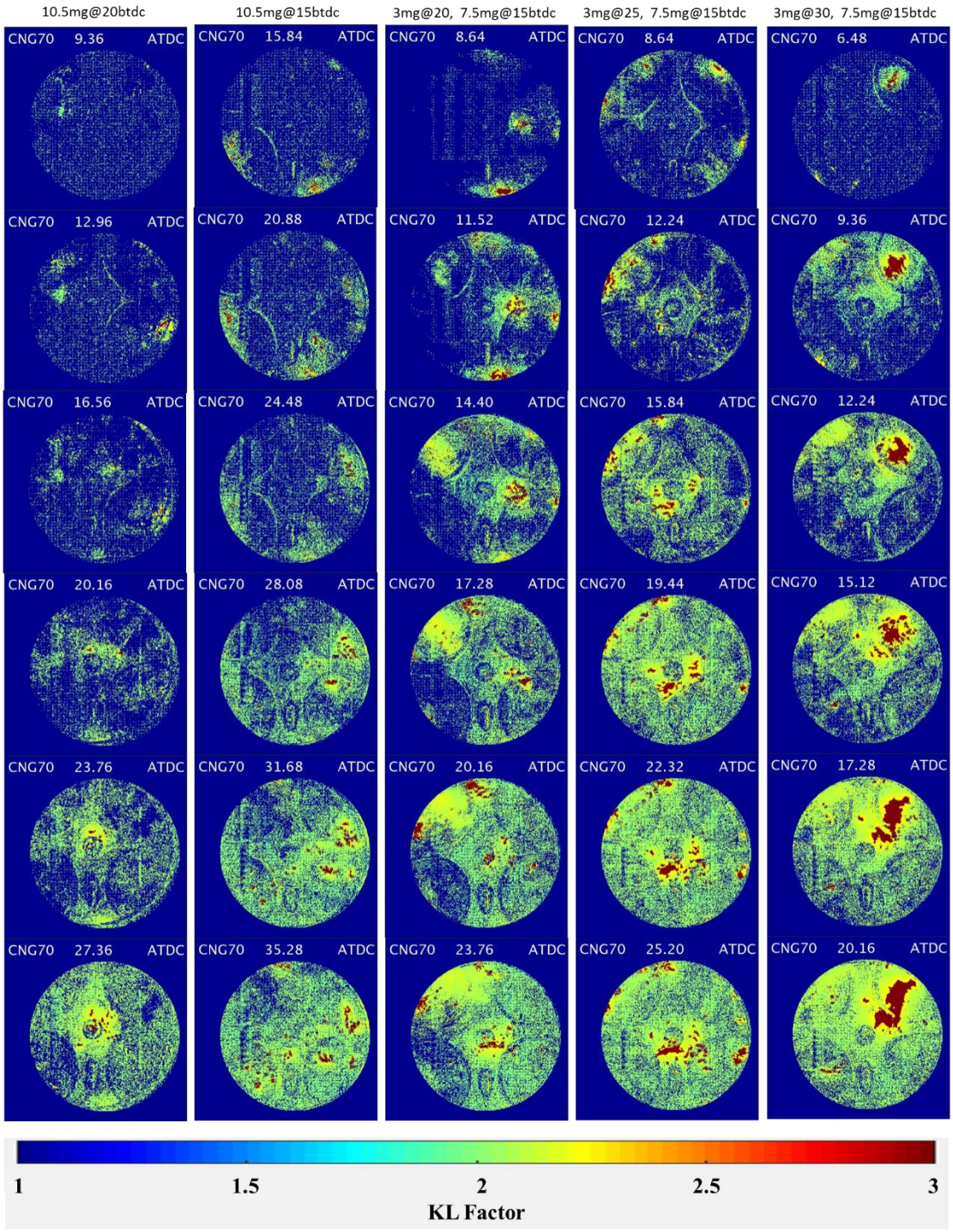

Figure 5.14 KL factor images comparing single and dual diesel injections (CNG70, Premixed CNG/air phi = 0.66)

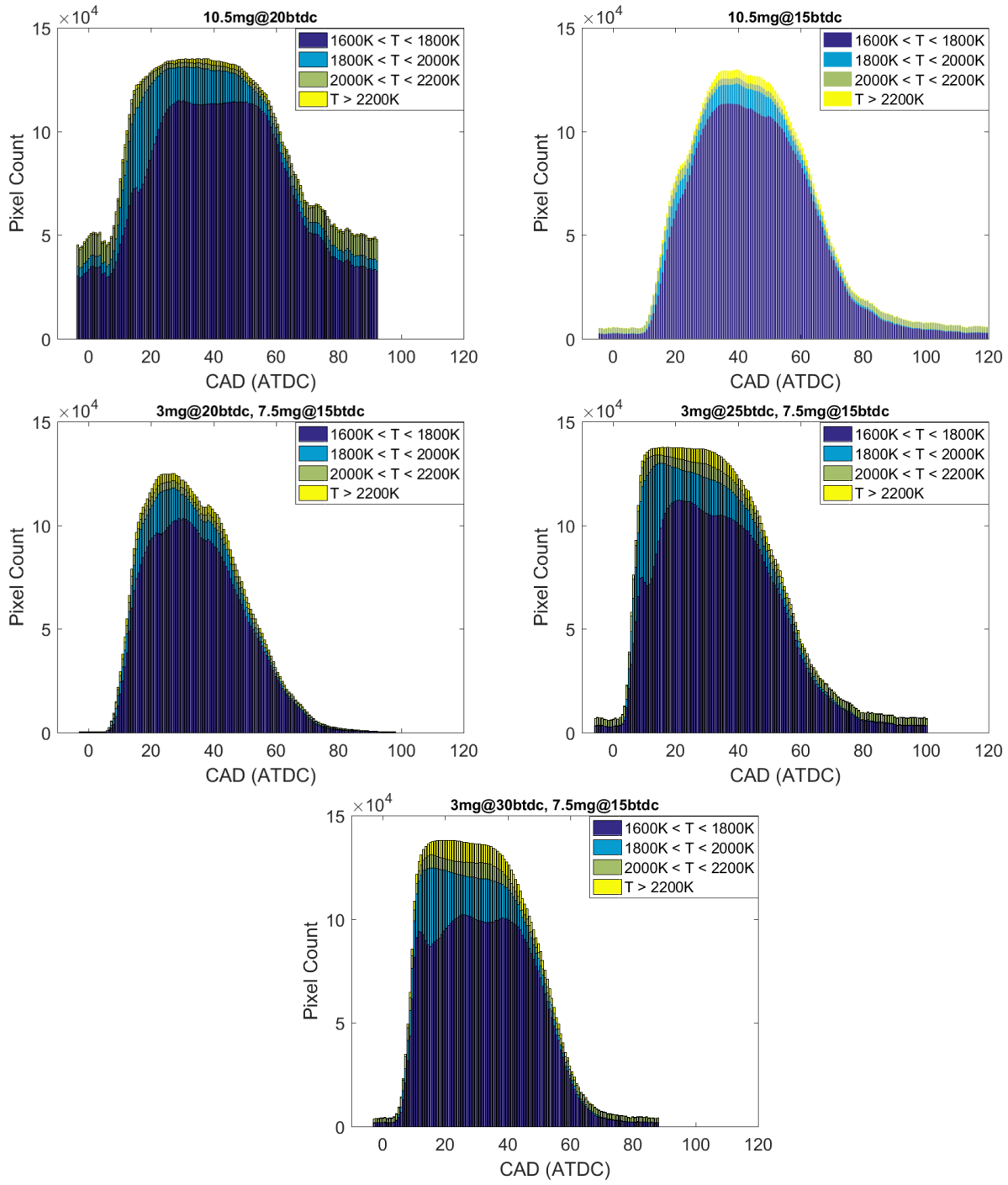

Figure 5.15 Soot temperature distributions comparing single and dual diesel injections (CNG70, Premixed CNG/air phi = 0.66)

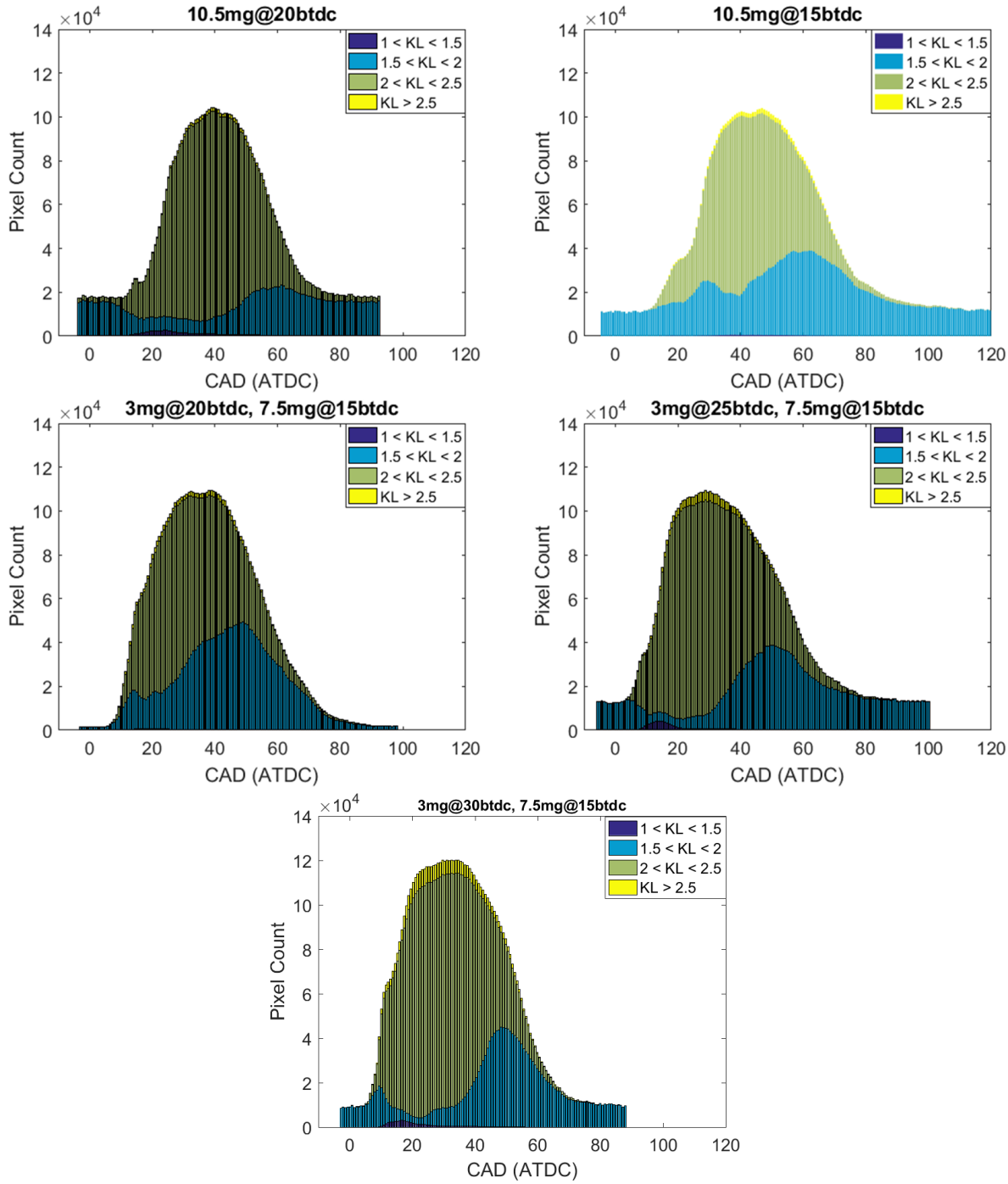

Figure 5.16 KL factor distributions comparing single and dual diesel injections (CNG70, Premixed CNG/air phi = 0.66)

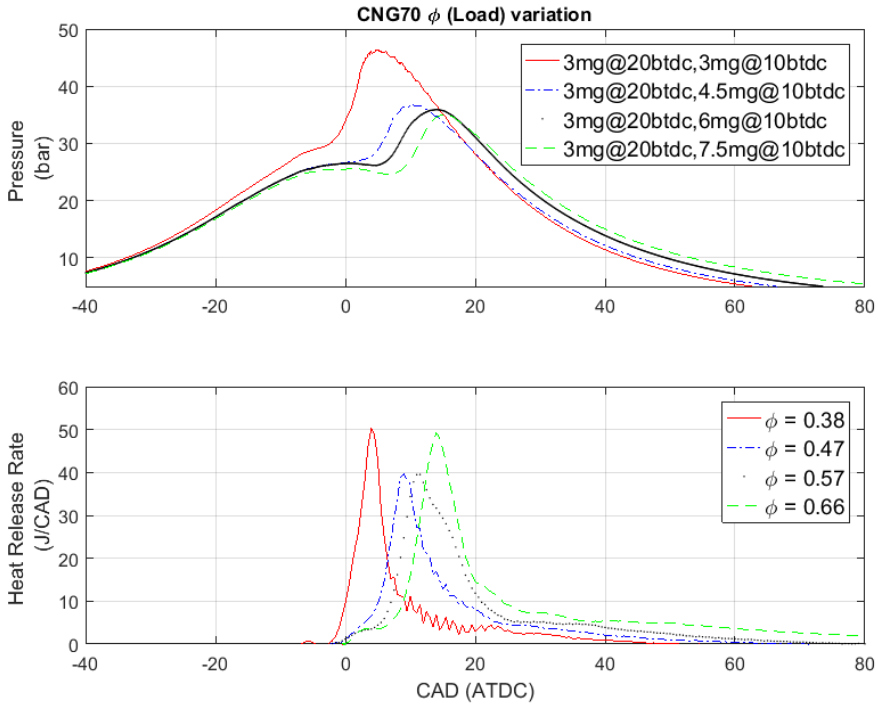

Figure 5.17 Pressure and HRR curves comparing various premixed equivalence ratios (loads) (CNG70)

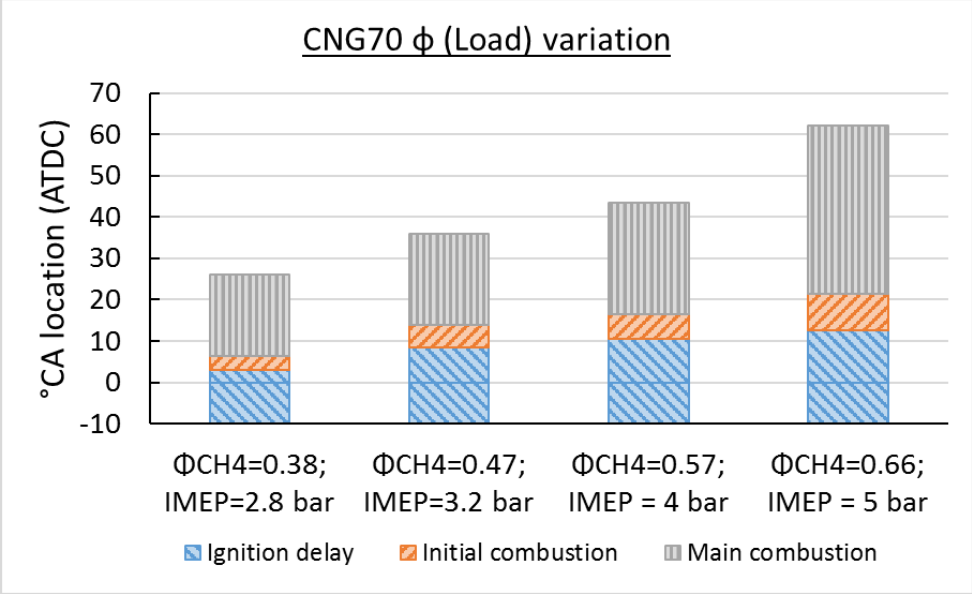

Figure 5.18 Combustion characteristics - various premixed equivalence ratios (loads) (CNG70)

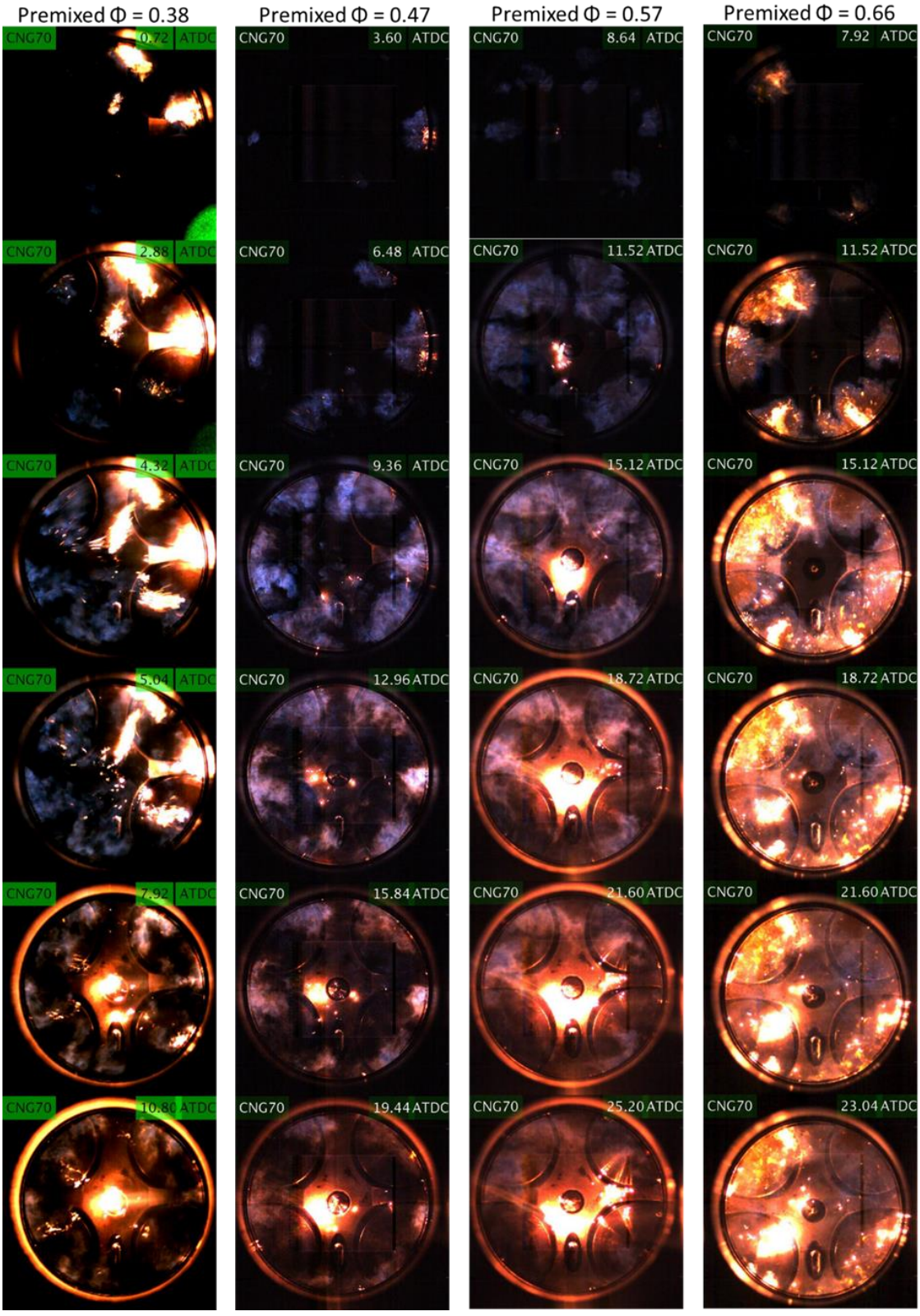

Figure 5.19 NL images comparing various loads at CNG70

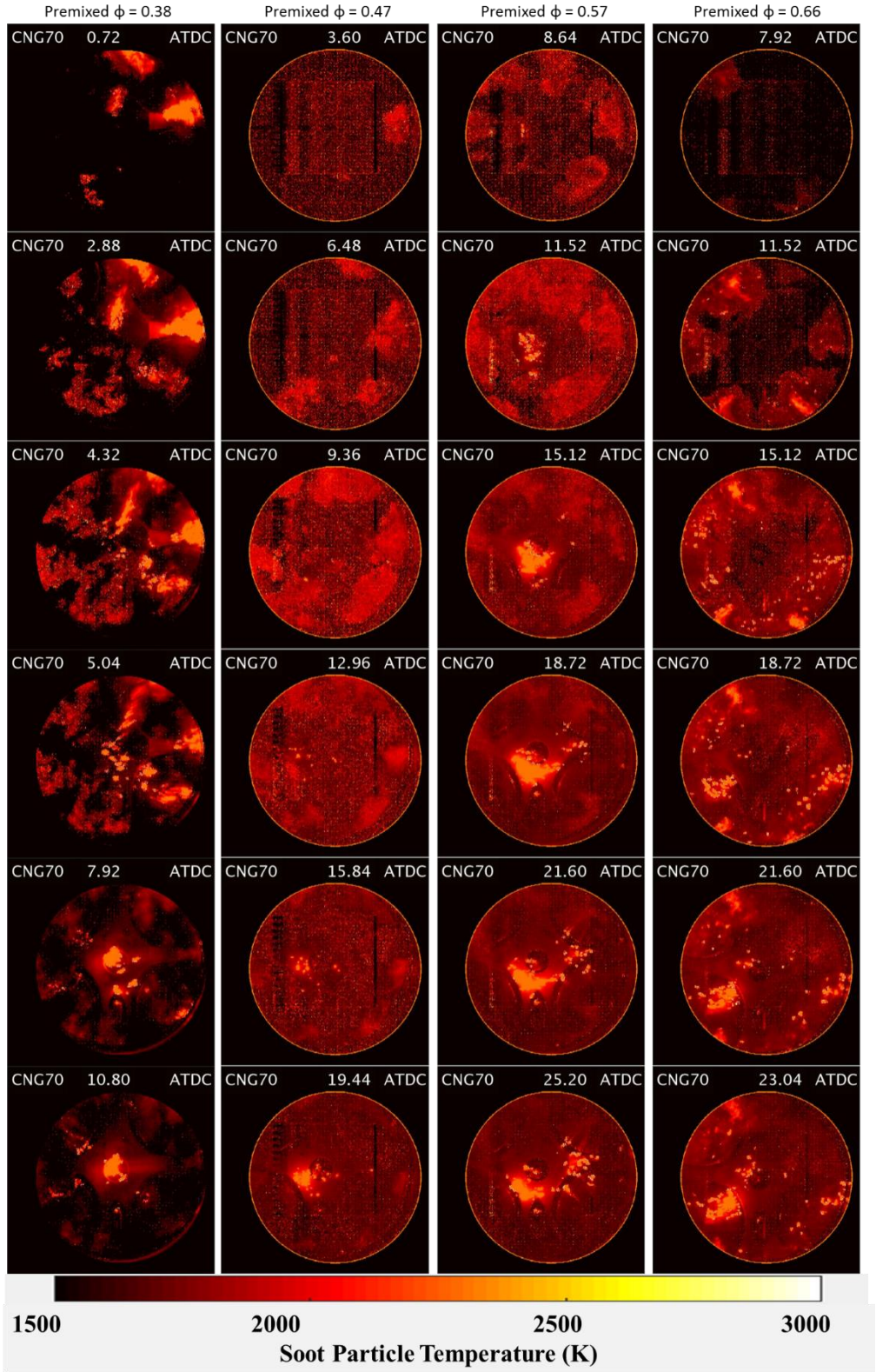

Figure 5.20 Soot temperature images comparing various loads at CNG70

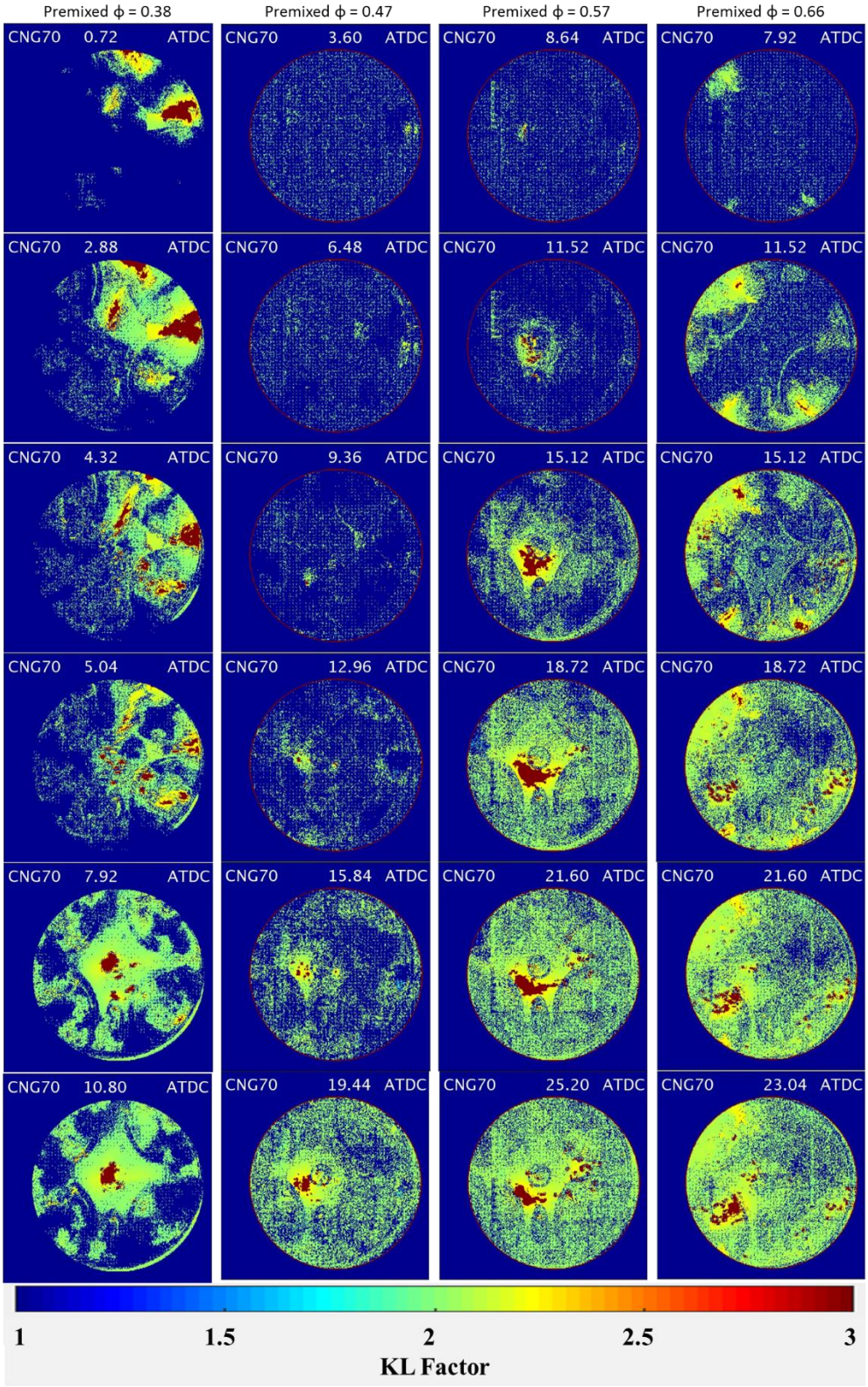

Figure 5.21 KL factor images comparing various loads at CNG70

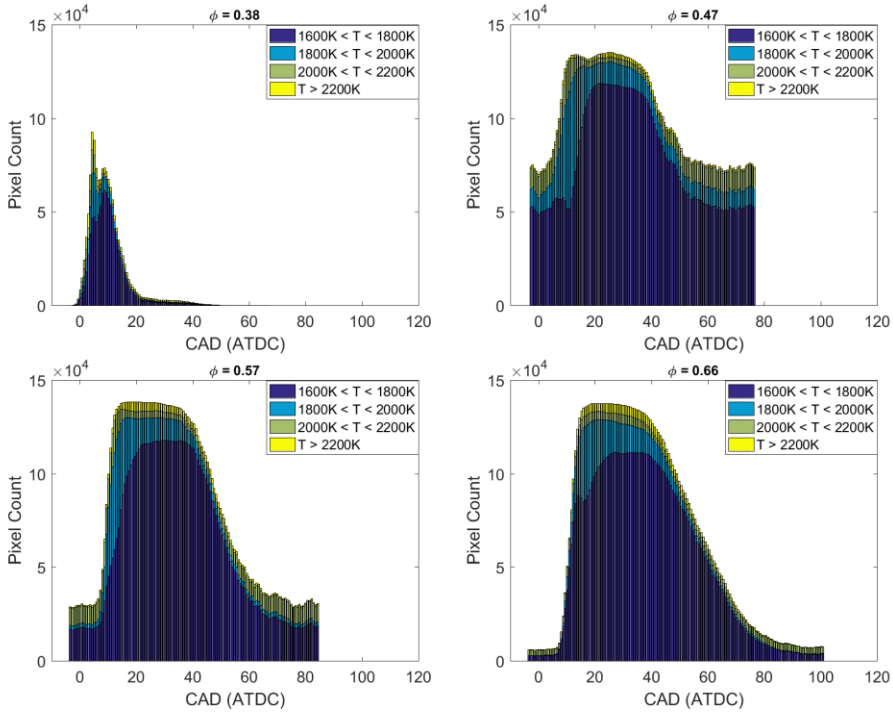

Figure 5.22 Soot temperature distributions comparing various loads at CNG70

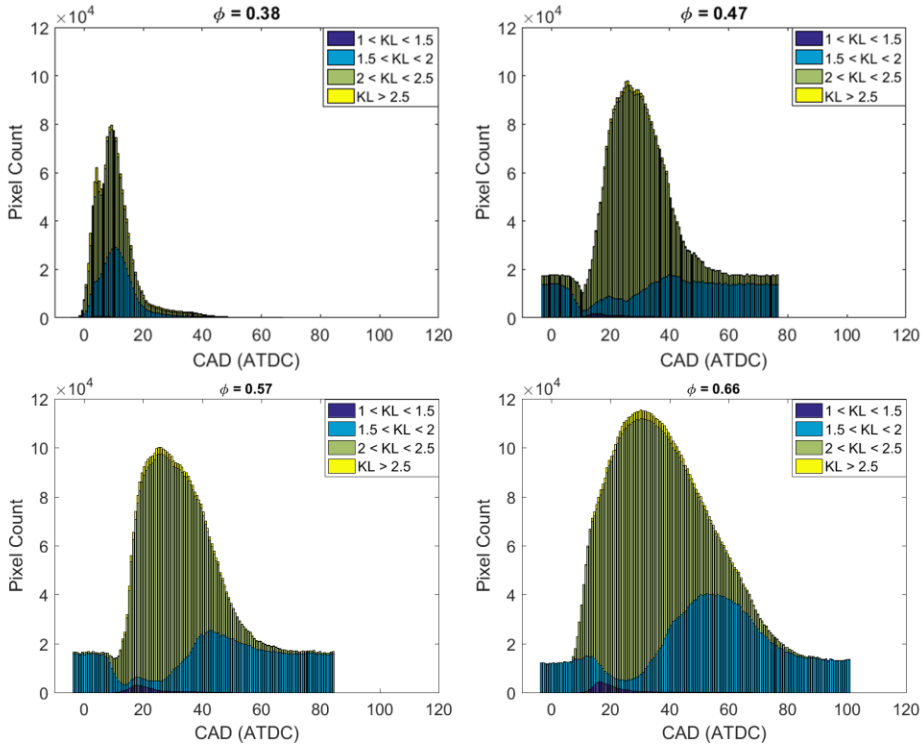

Figure 5.23 KL factor distributions comparing various loads at CNG70

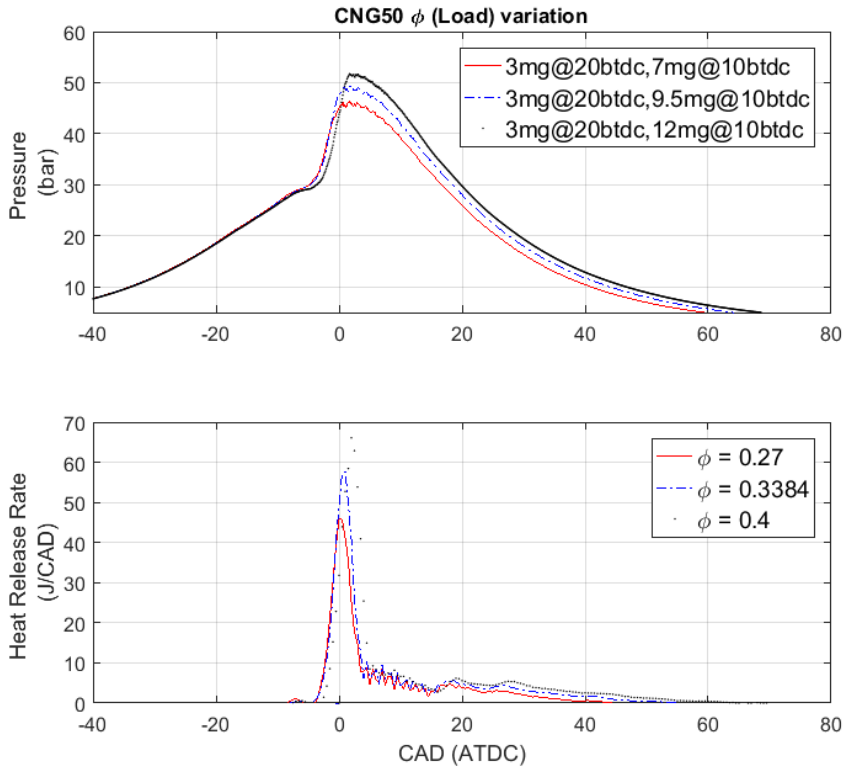

Figure 5.24 Pressure and HRR curves comparing various premixed equivalence ratios (loads) (CNG50)

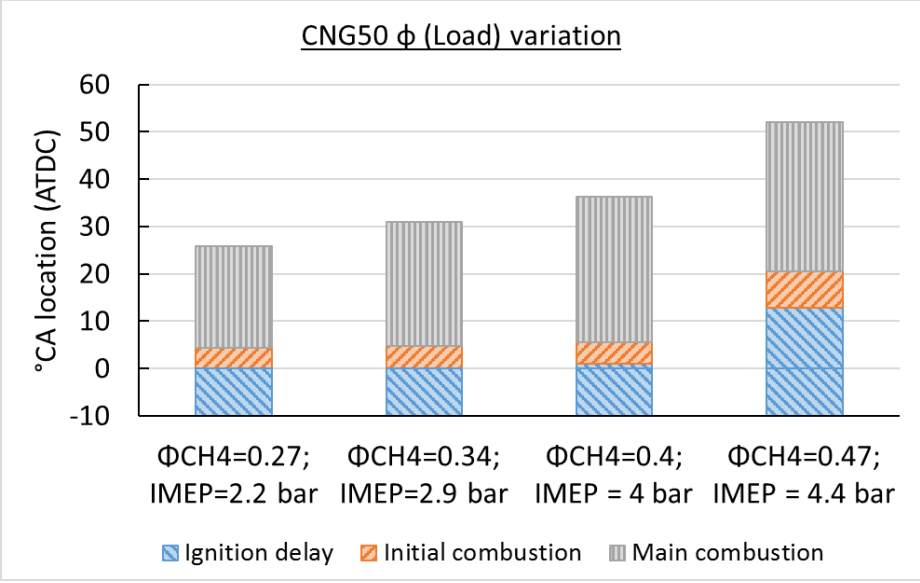

Figure 5.25 Combustion characteristics various premixed equivalence ratios (loads) (CNG50)

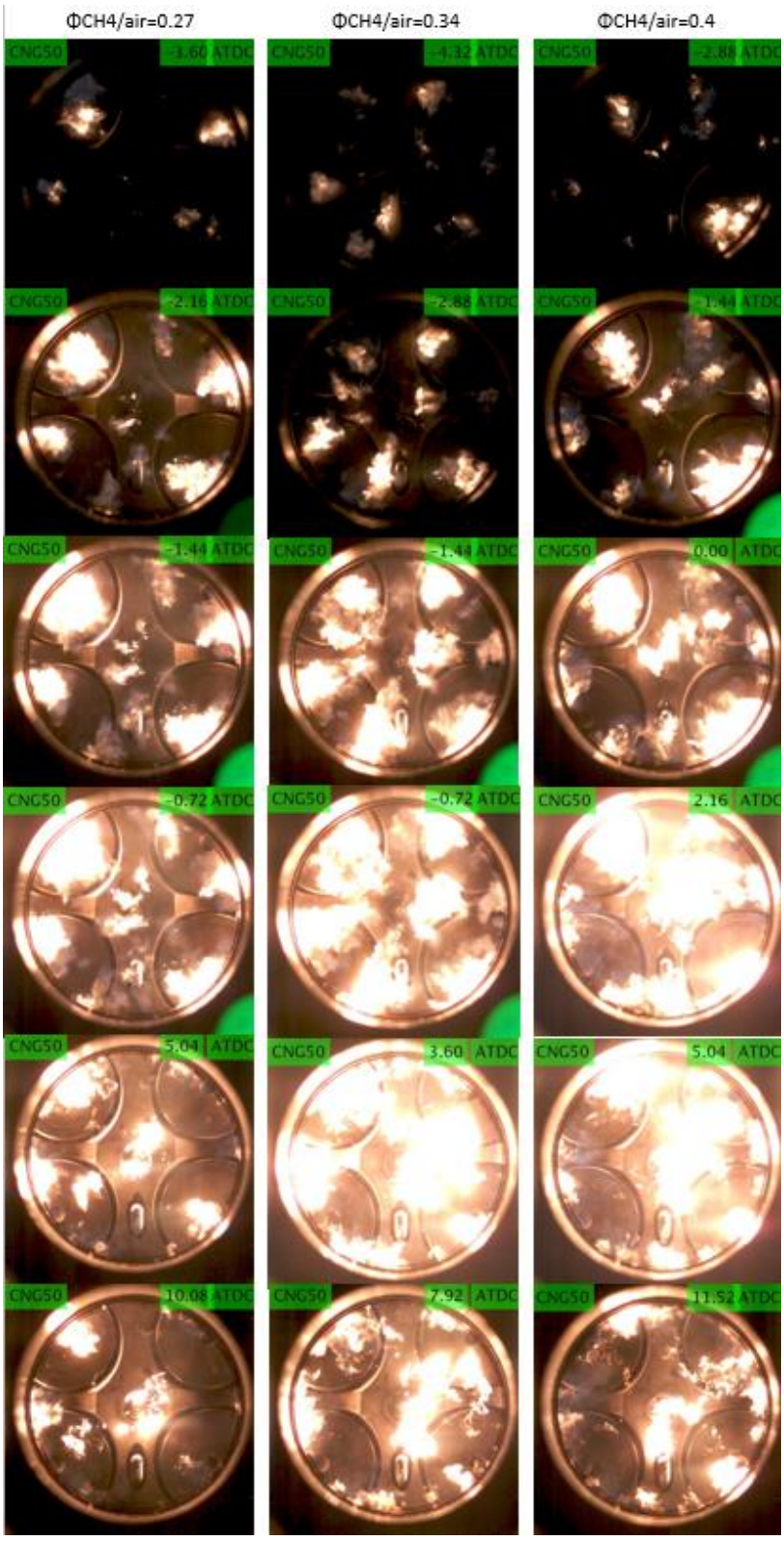

Figure 5.26 NL images comparing various loads at CNG50

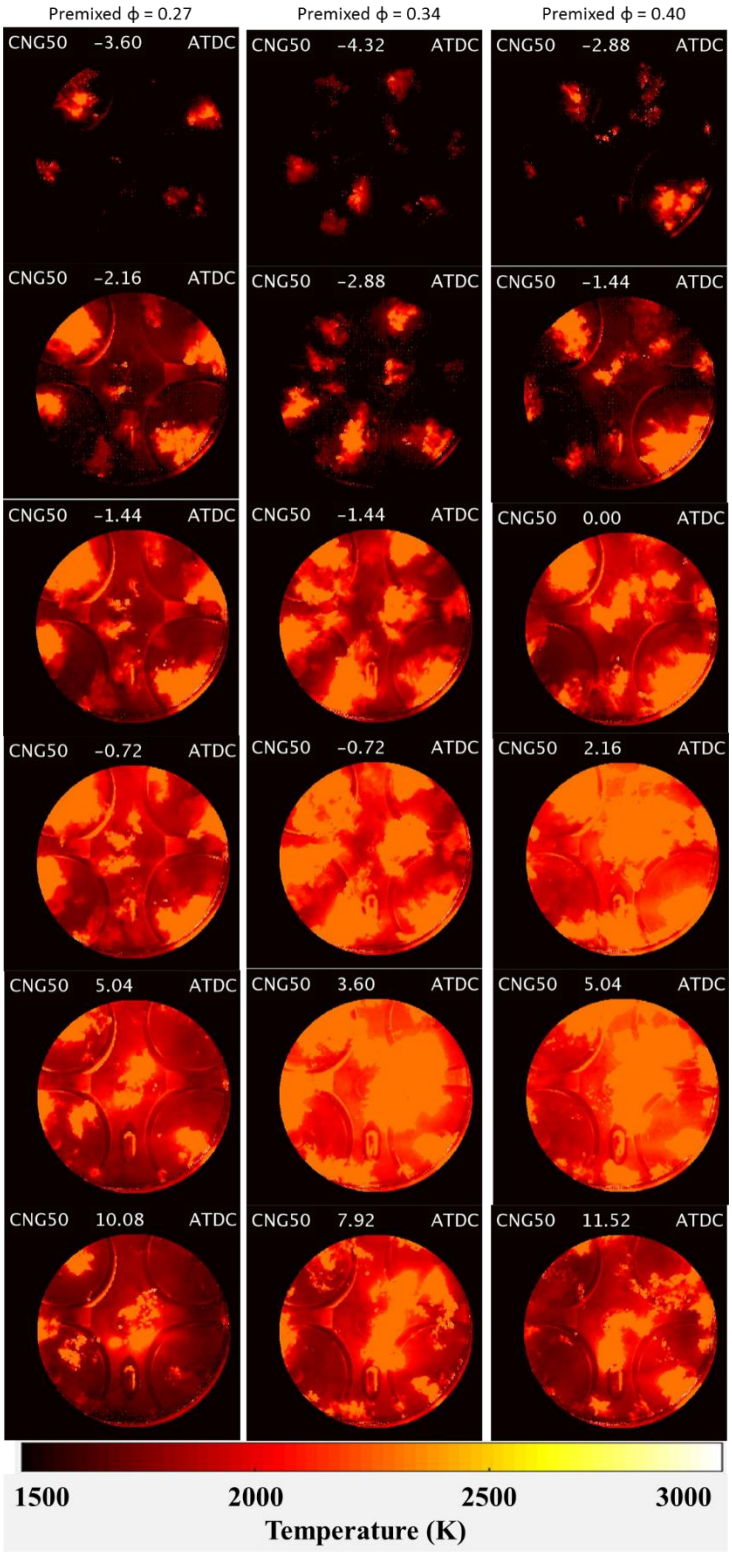

Figure 5.27 Soot temperature images comparing various loads at CNG50

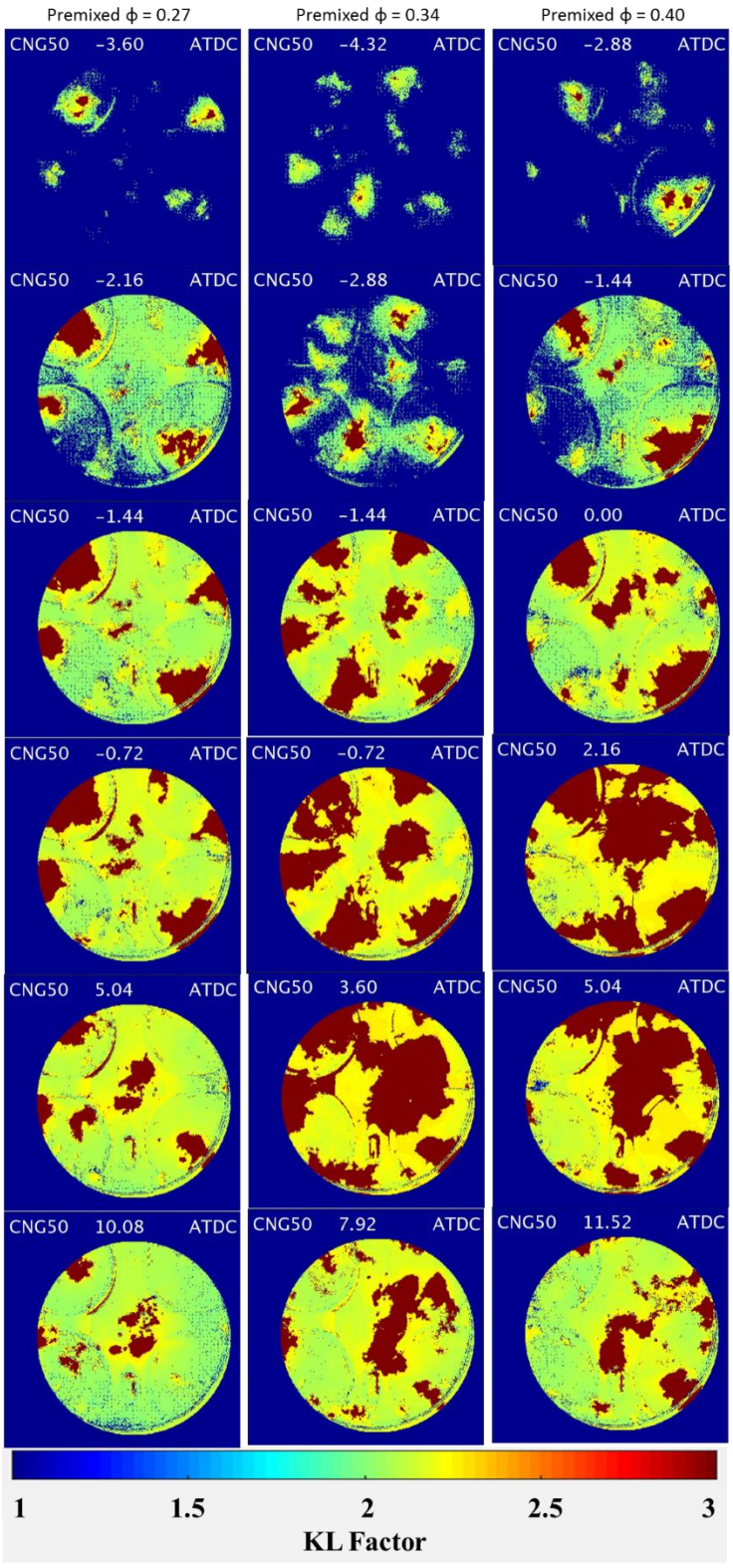

Figure 5.28 KL factor images comparing various loads at CNG50

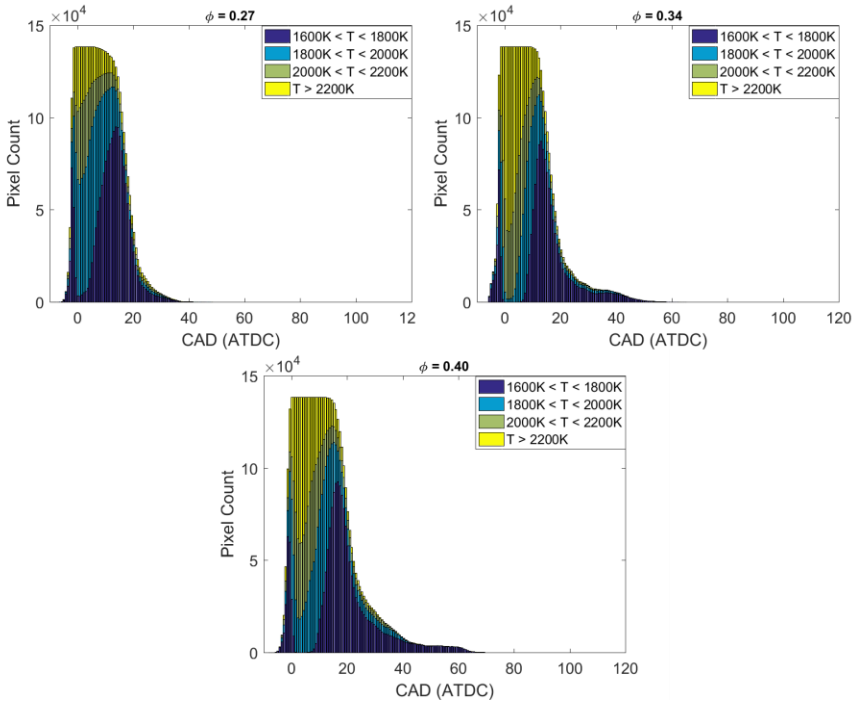

Figure 5.29 Soot temperature distributions comparing various loads at CNG50

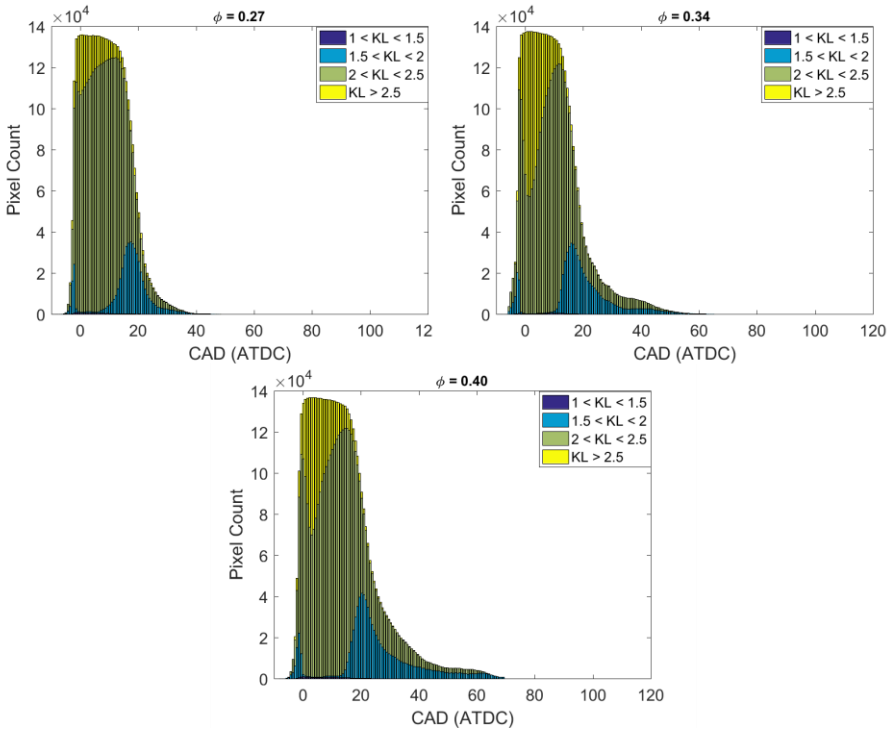

Figure 5.30 KL factor distributions comparing various loads at CNG50

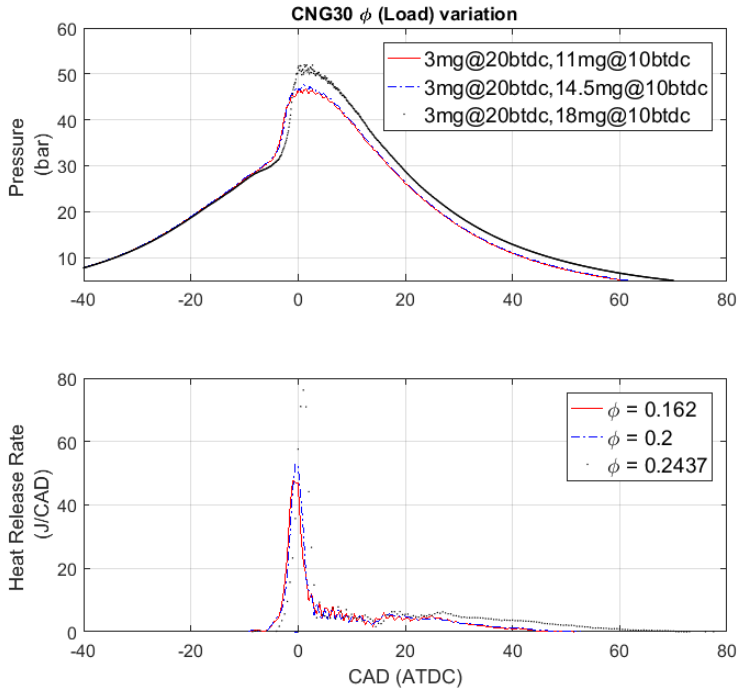

Figure 5.31 Pressure and HRR curves comparing various premixed equivalence ratios (loads) (CNG30)

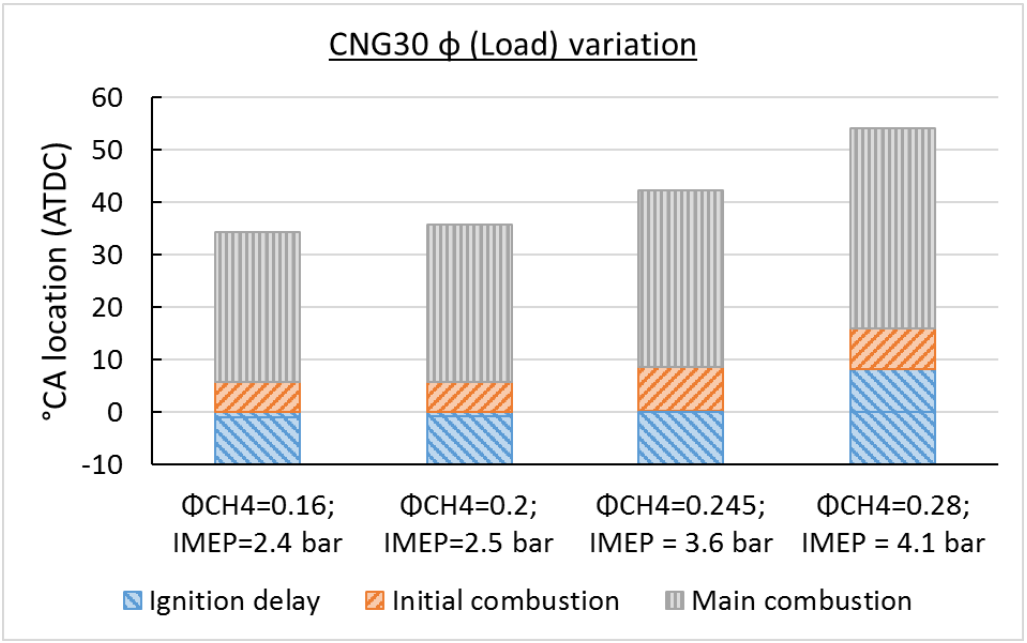

Figure 5.32 Combustion characteristics various premixed equivalence ratios (loads) (CNG30)

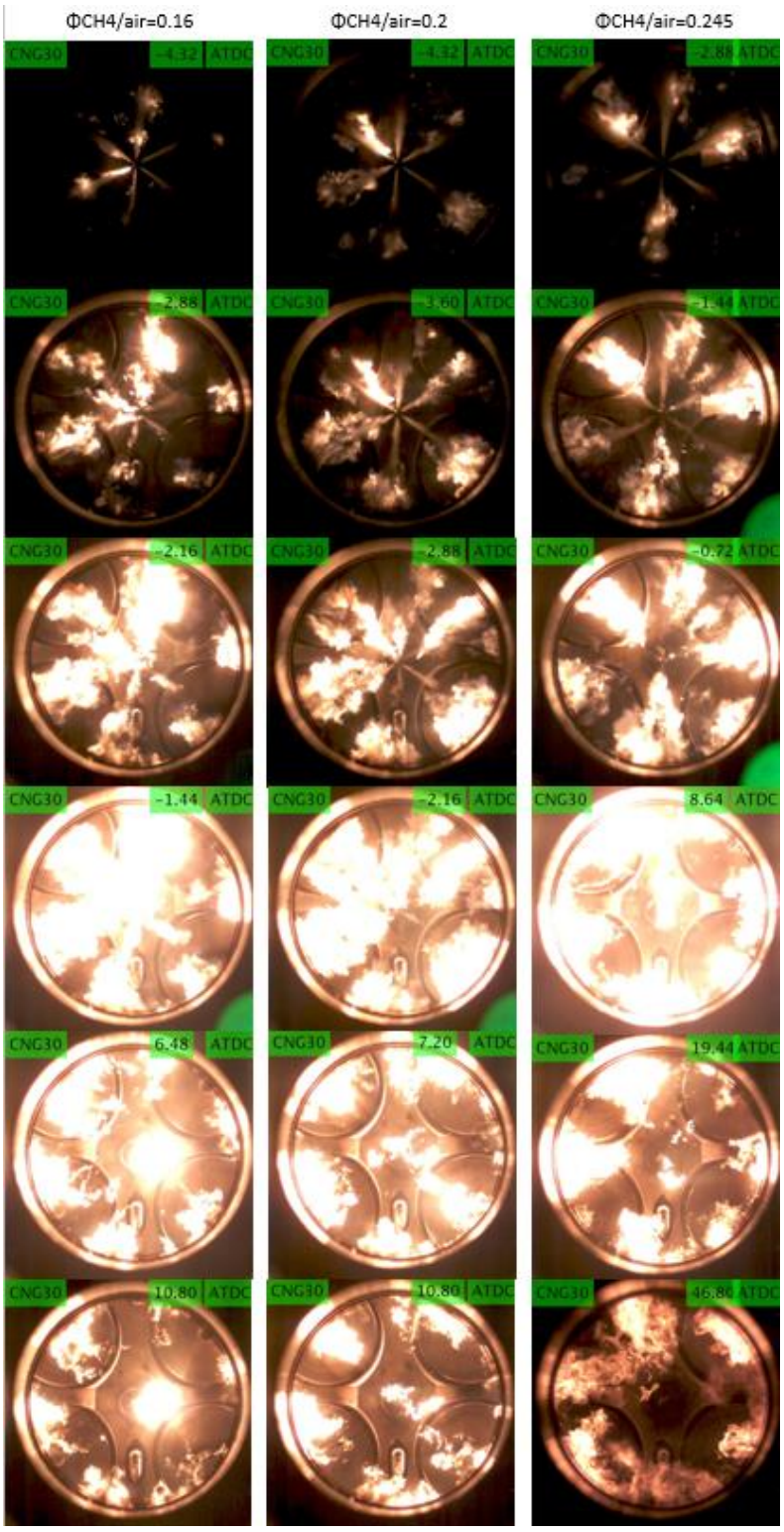

Figure 5.33 NL images comparing various loads at CNG30

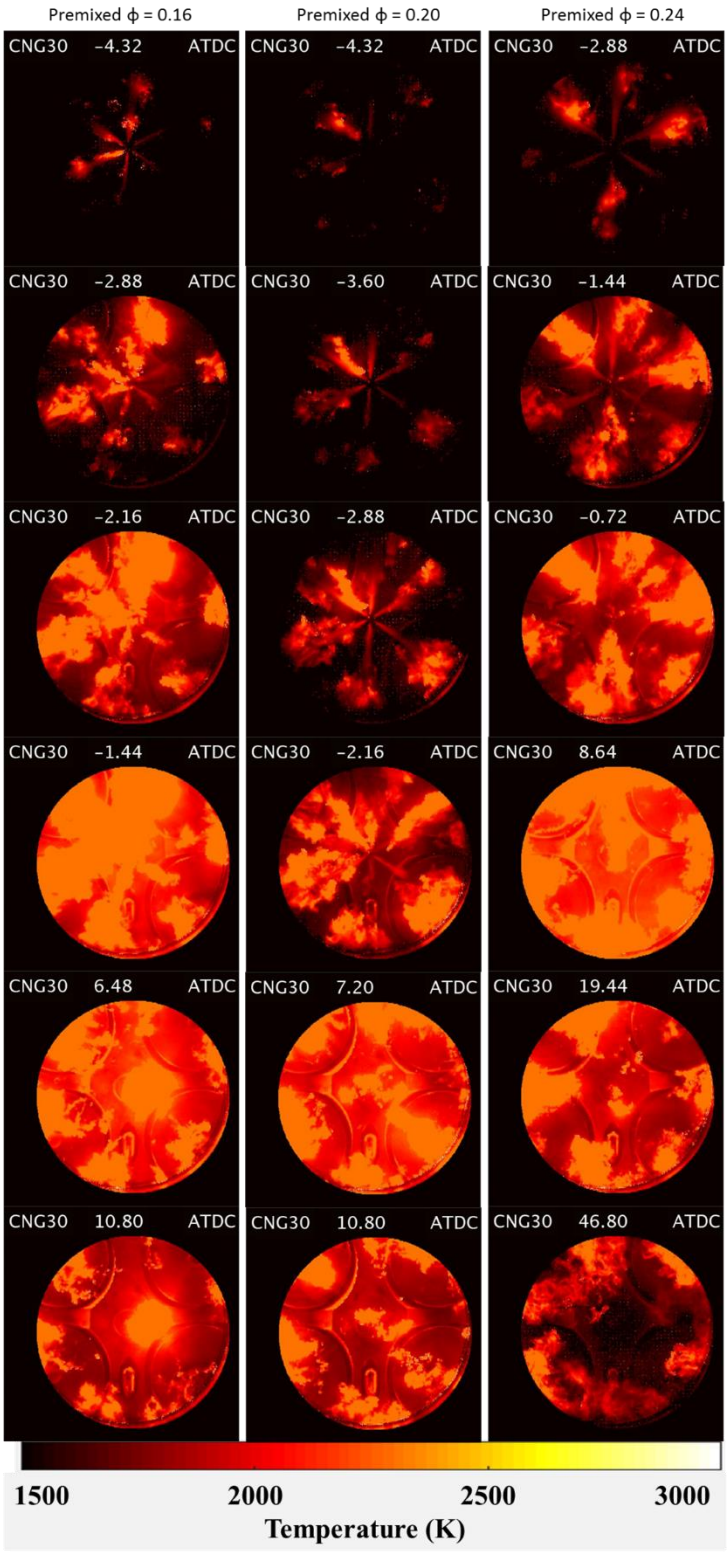

Figure 5.34 Soot temperature comparing various loads at CNG30

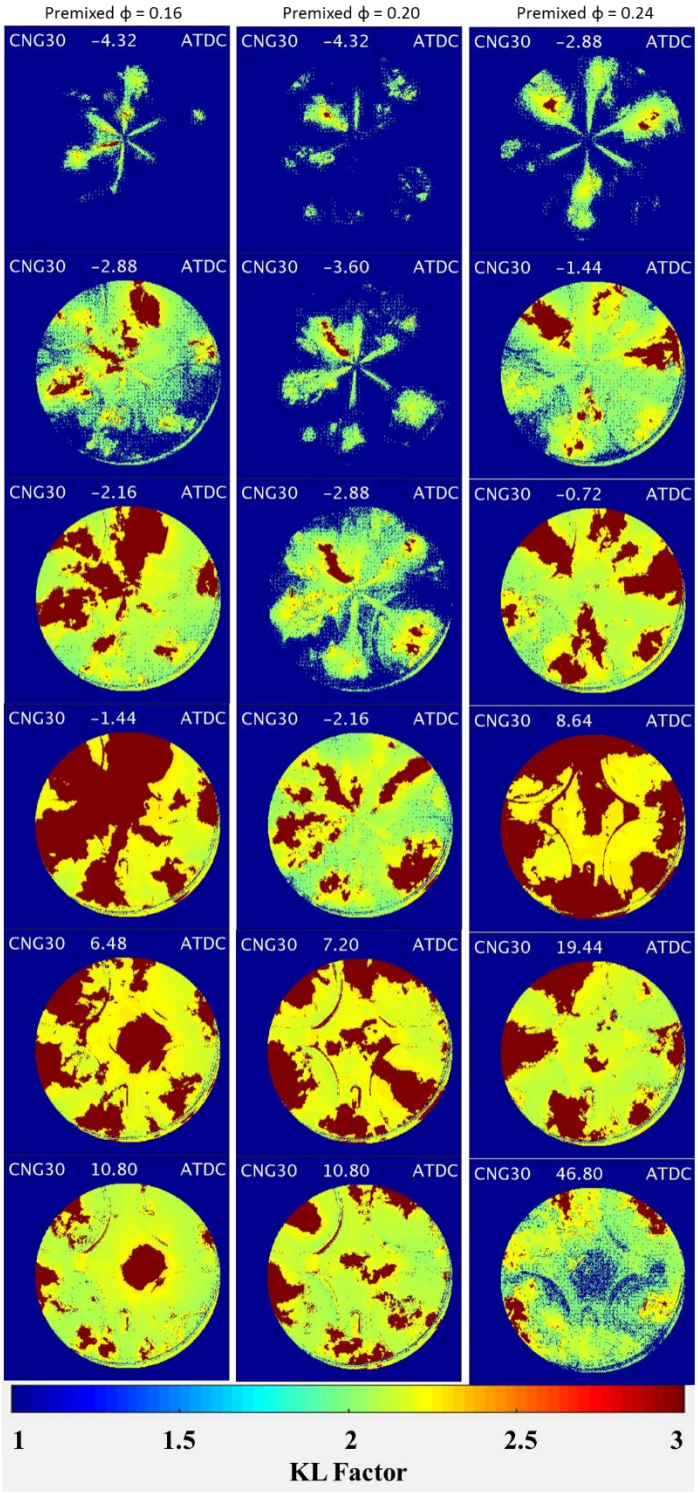

Figure 5.35 KL factor images comparing various loads at CNG30

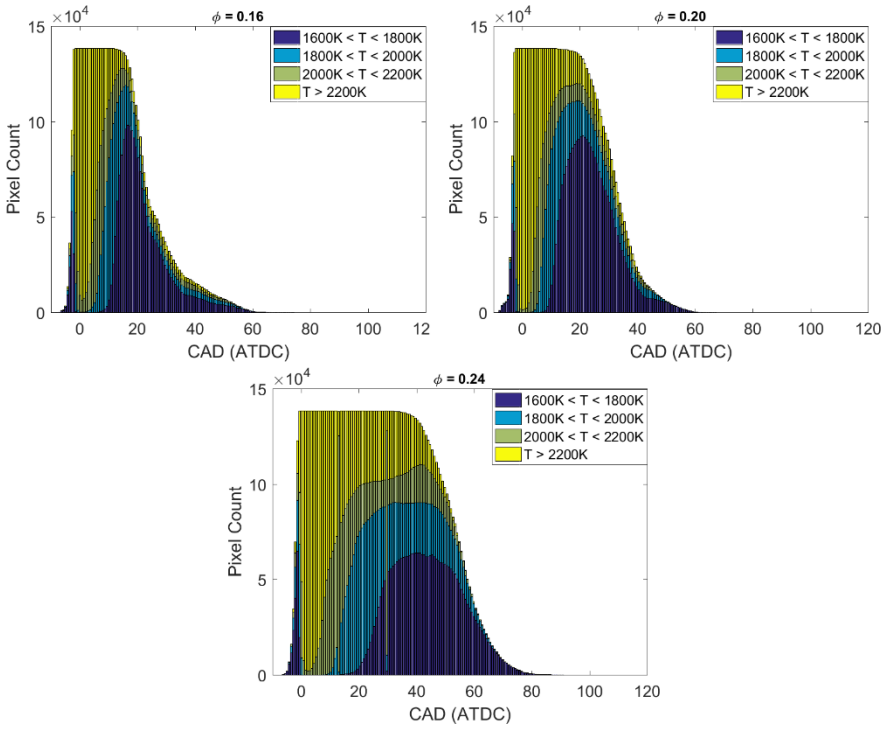

Figure 5.36 Soot temperature distributions comparing various loads at CNG30

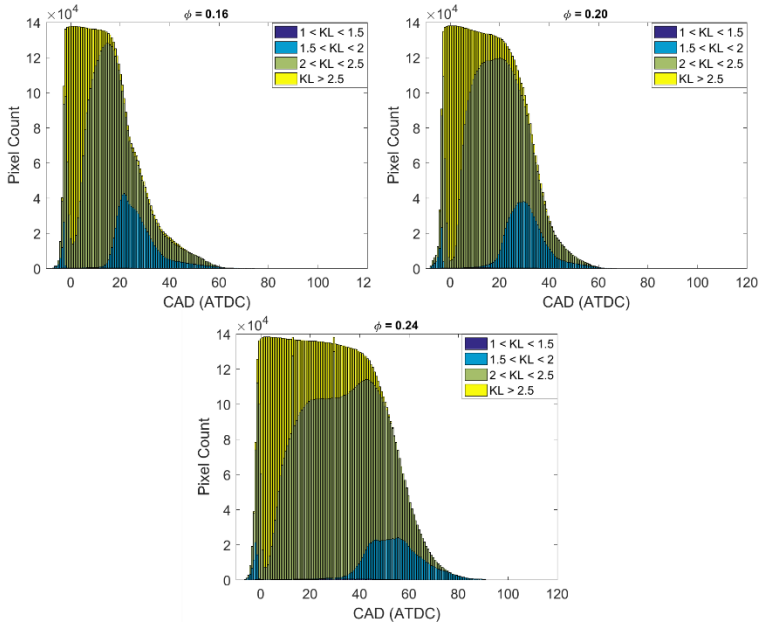

Figure 5.37 KL factor distributions comparing various loads at CNG30

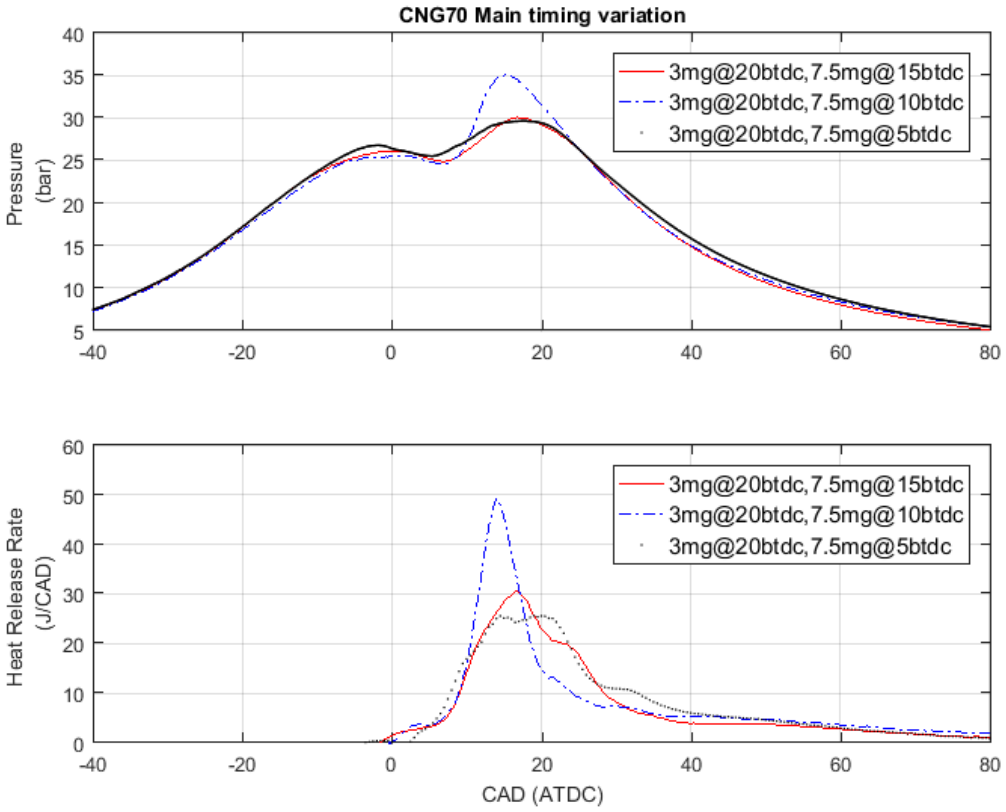

Figure 5.38 Pressure and HRR curves – Main Timing Sweep

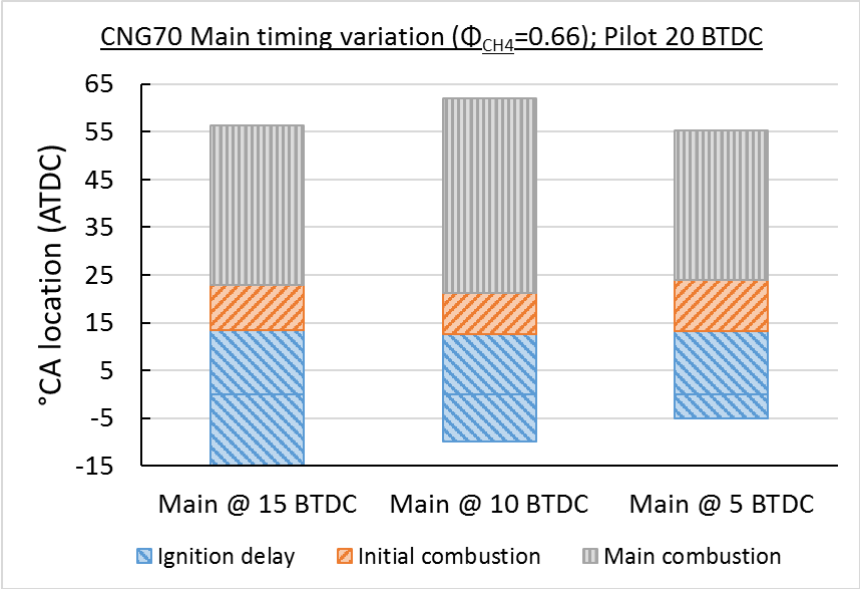

Figure 5.39 Combustion characteristics – Main Timing Sweep

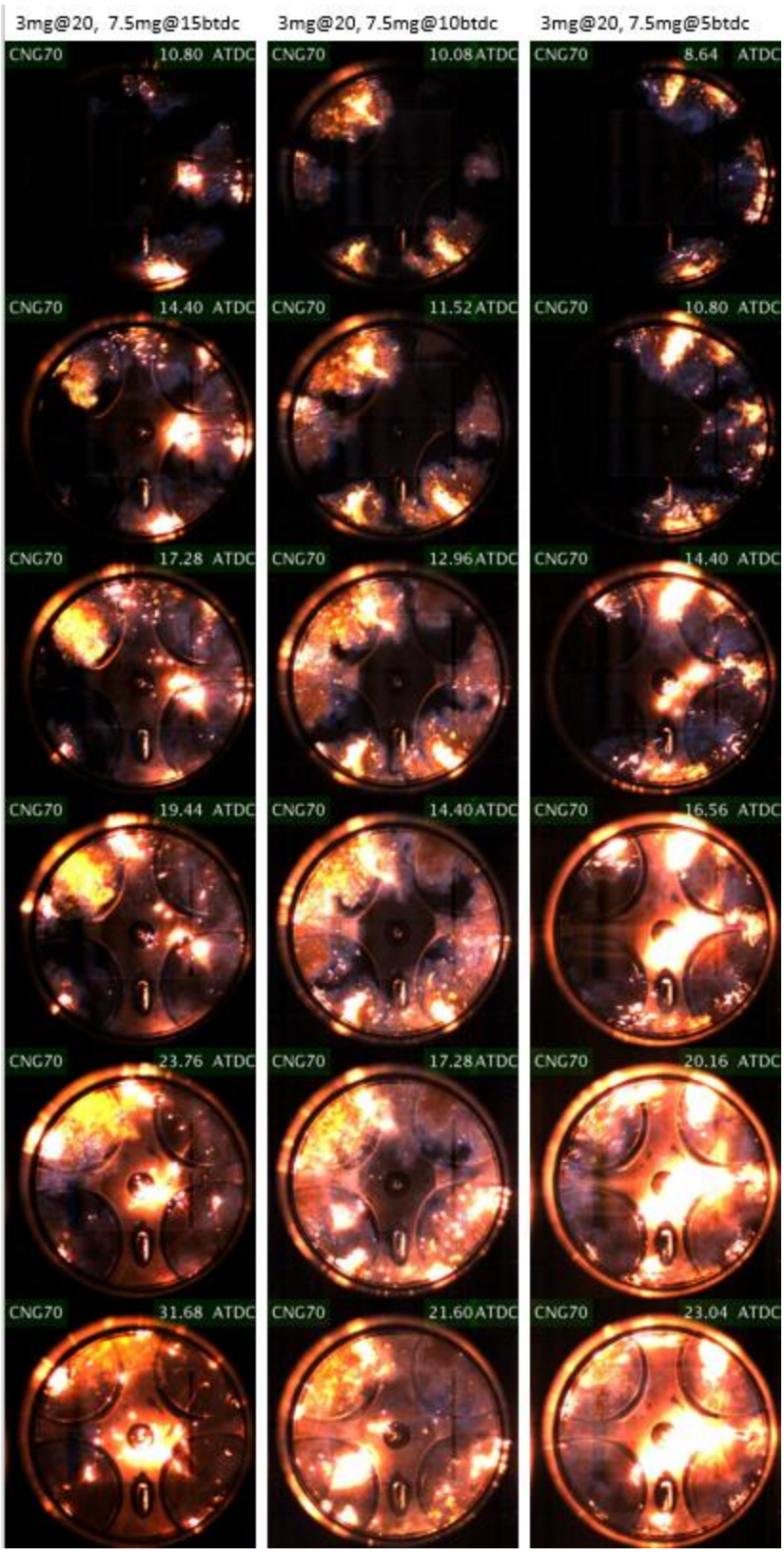

Figure 5.40 NL images – Main Timing Sweep

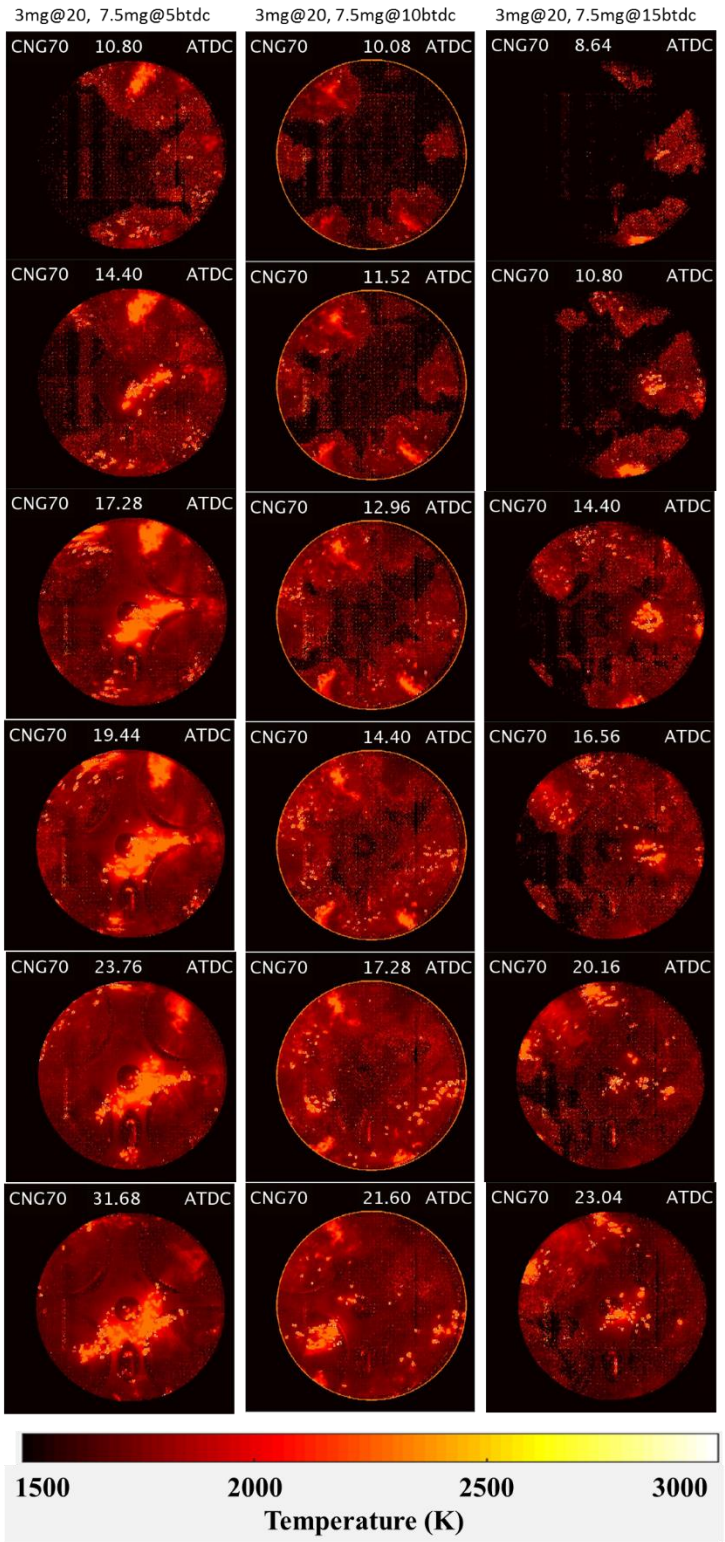

Figure 5.41 Soot temperature images - Main Timing Sweep

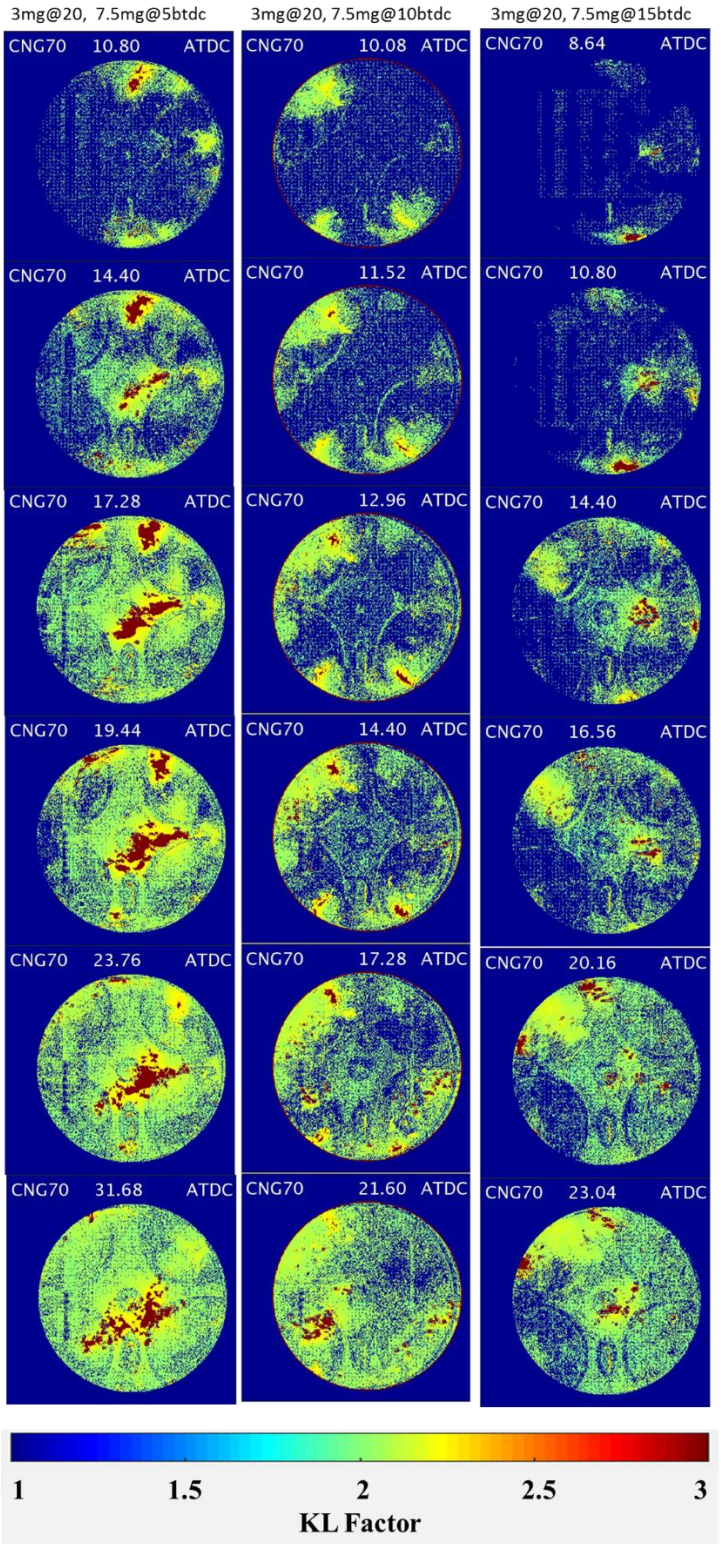

Figure 5.42 KL factor images - Main Timing Sweep

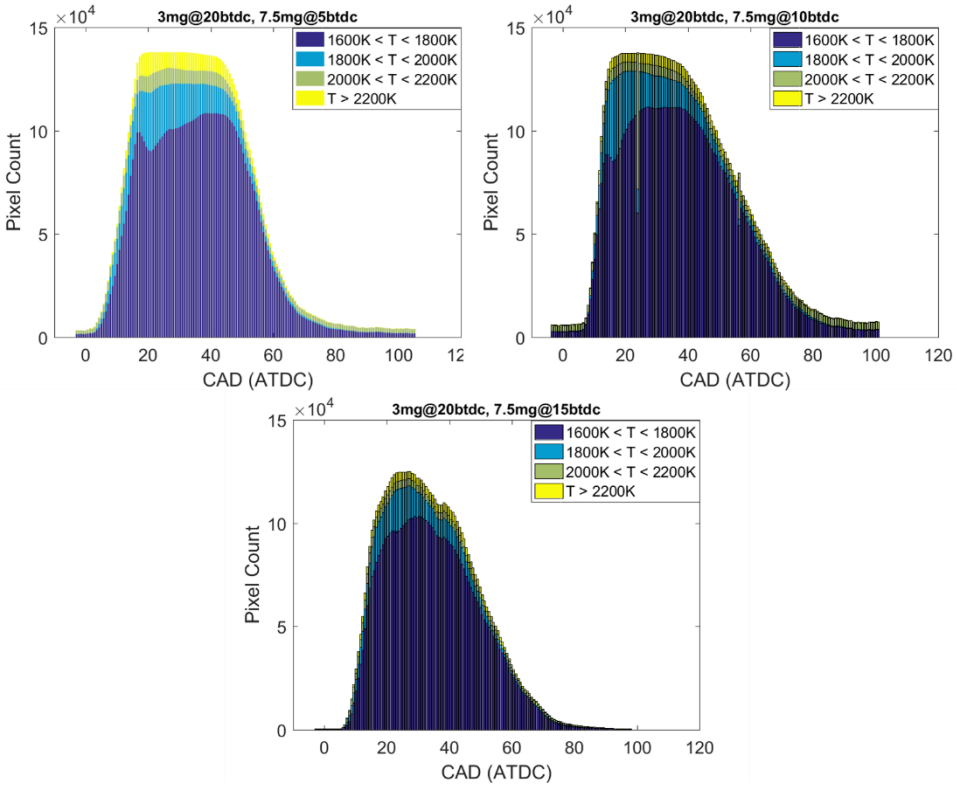

Figure 5.43 Soot temperature distributions - Main Timing Sweep

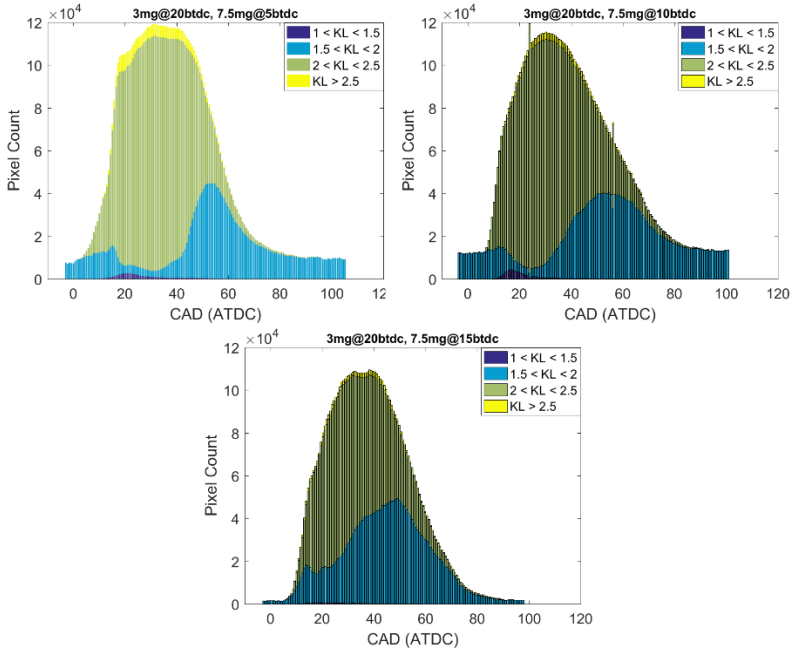

Figure 5.44 KL factor distributions - Main Timing Sweep

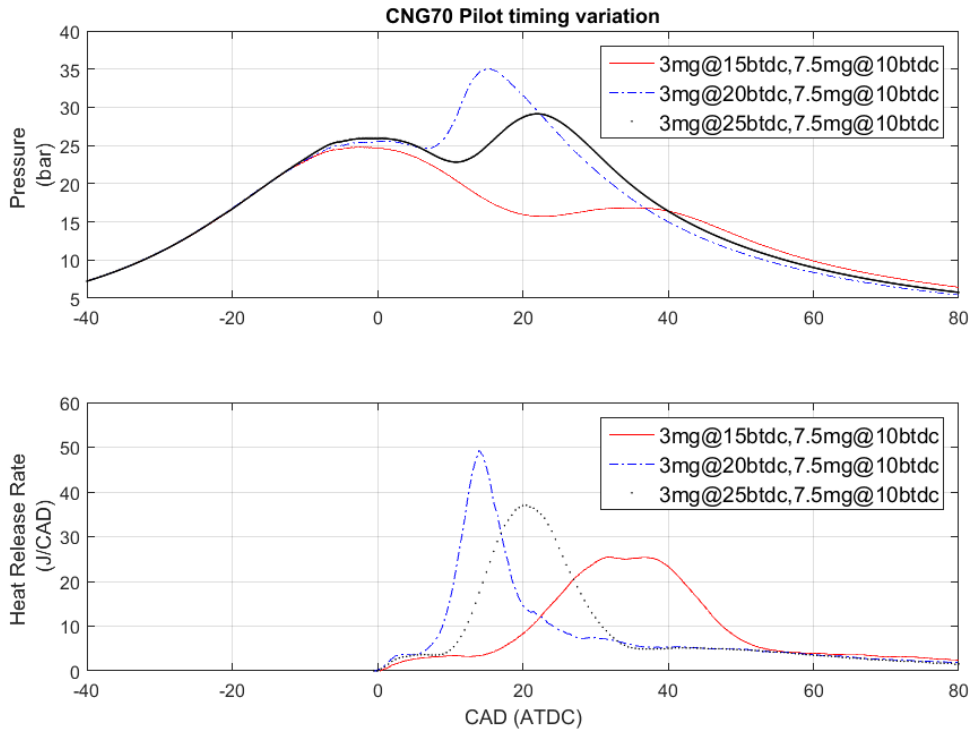

Figure 5.45 Pressure and HRR curves – Pilot Timing Sweep

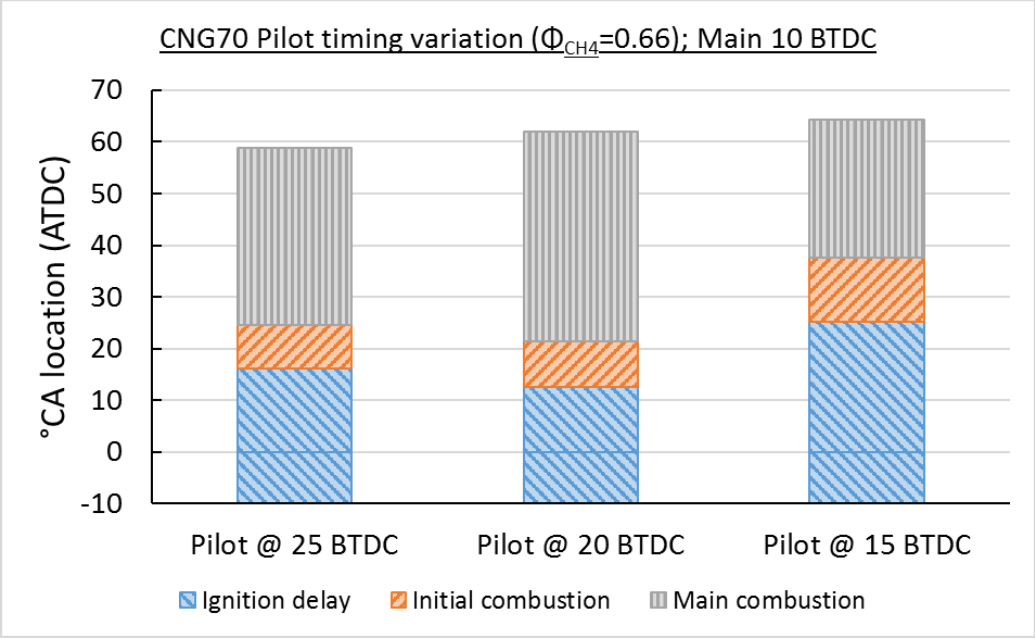

Figure 5.46 Combustion characteristics – Pilot Timing Sweep

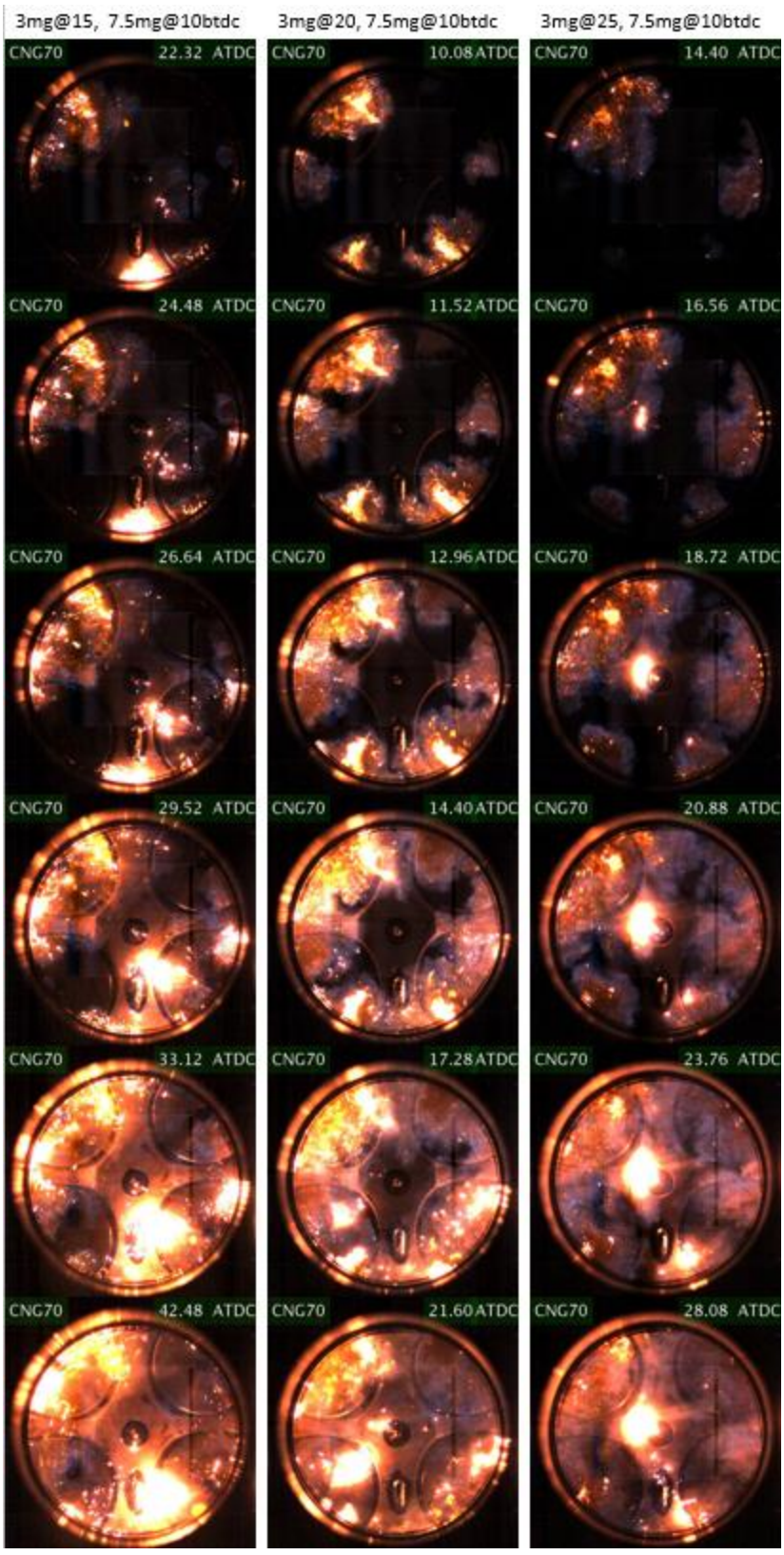

Figure 5.47 NL images – Pilot Timing Sweep

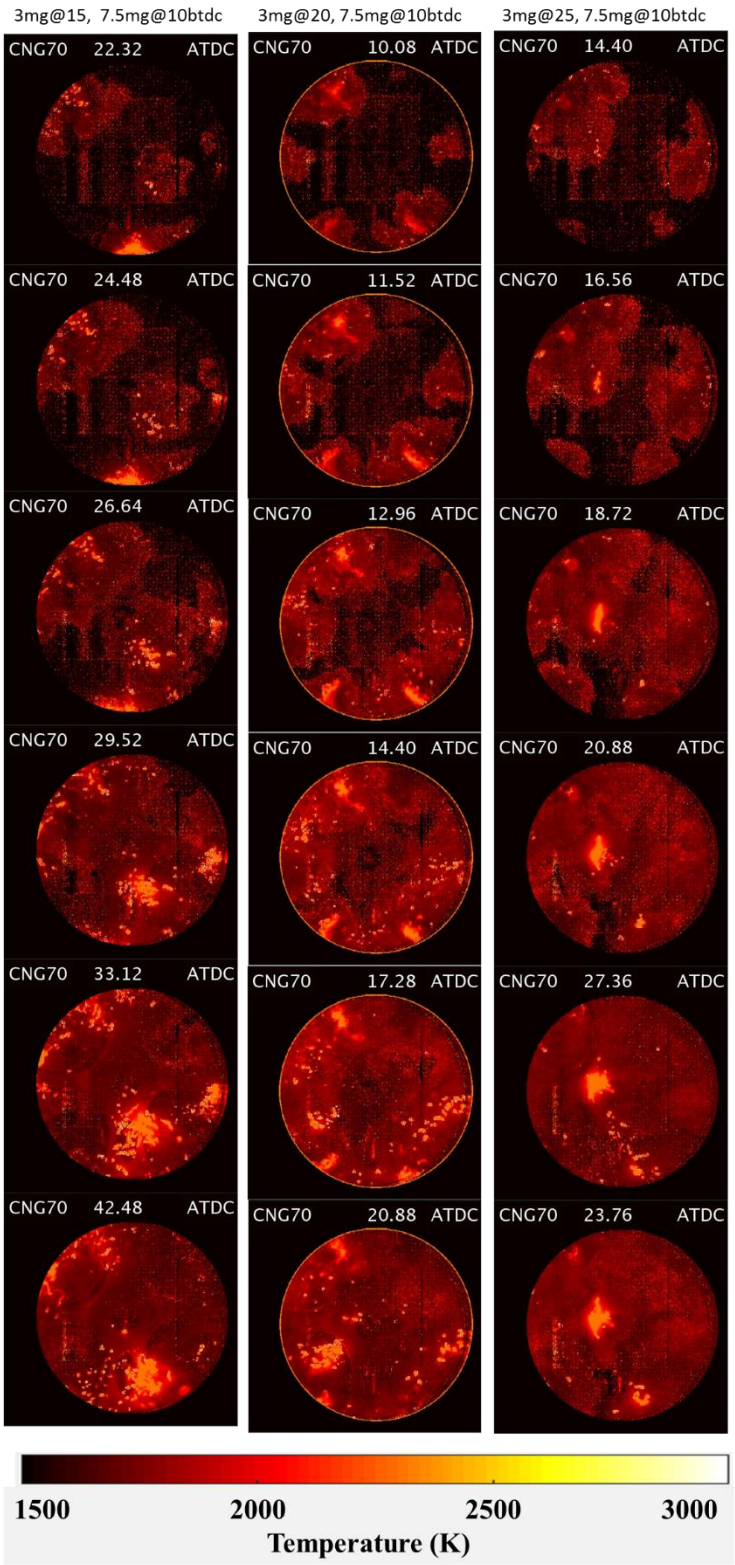

Figure 5.48 Soot temperature images – Pilot Timing Sweep

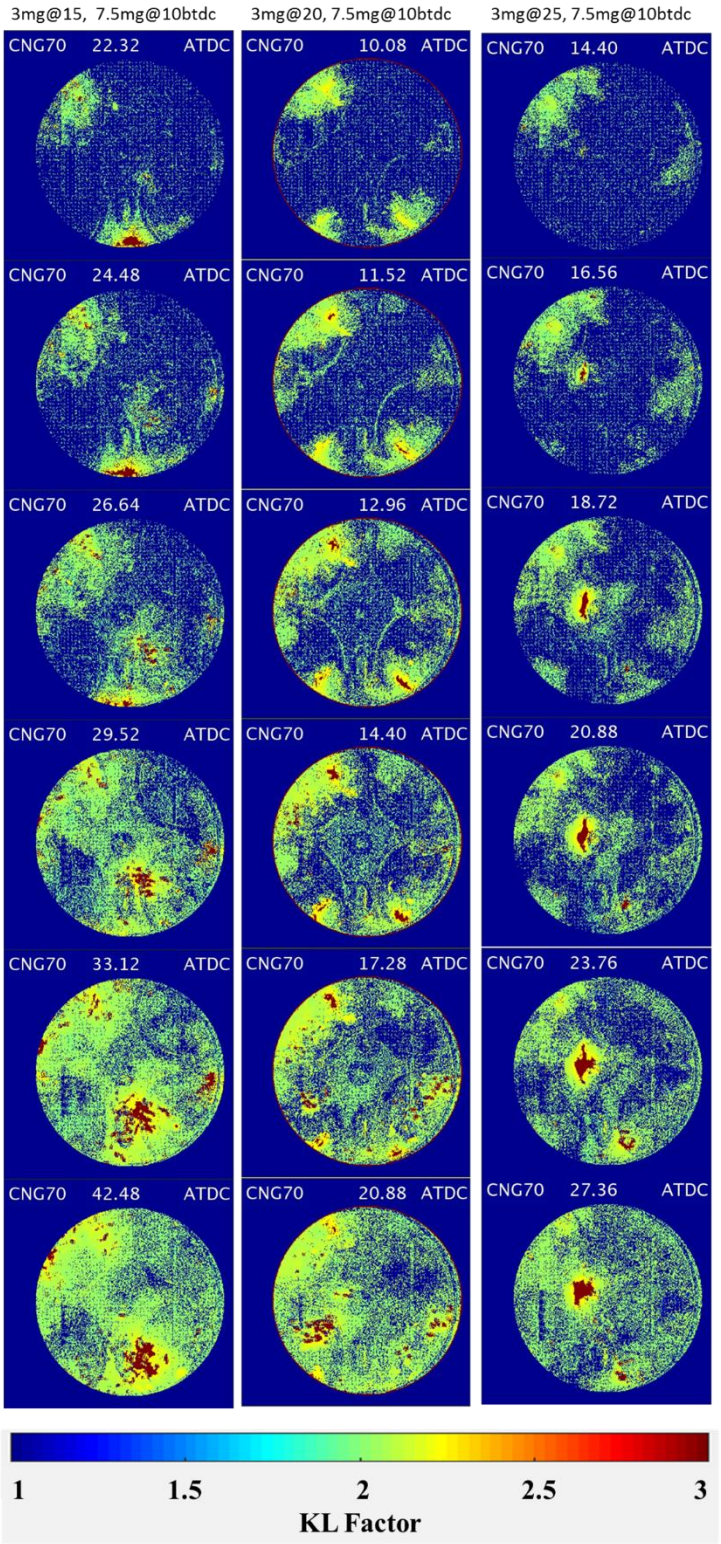

Figure 5.49 KL factor images – Pilot Timing Sweep

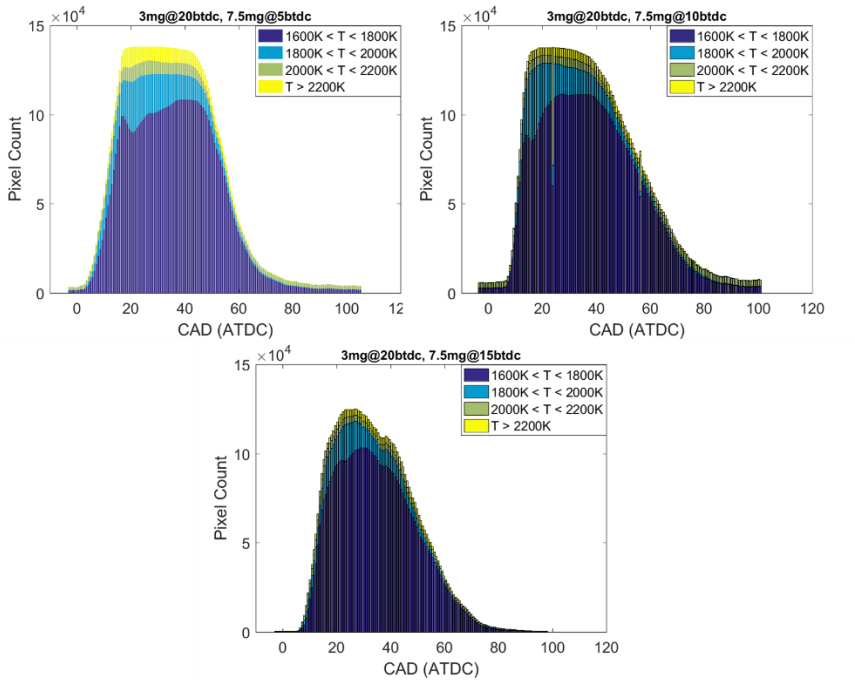

Figure 5.50 Soot temperature distributions – Pilot Timing Sweep

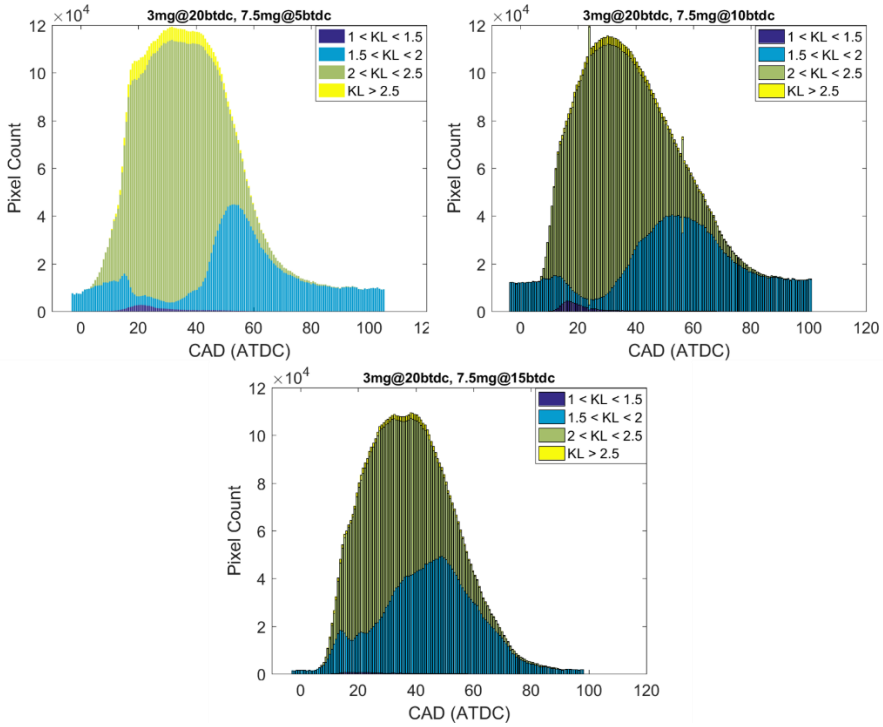

Figure 5.51 KL factor distributions – Pilot Timing Sweep

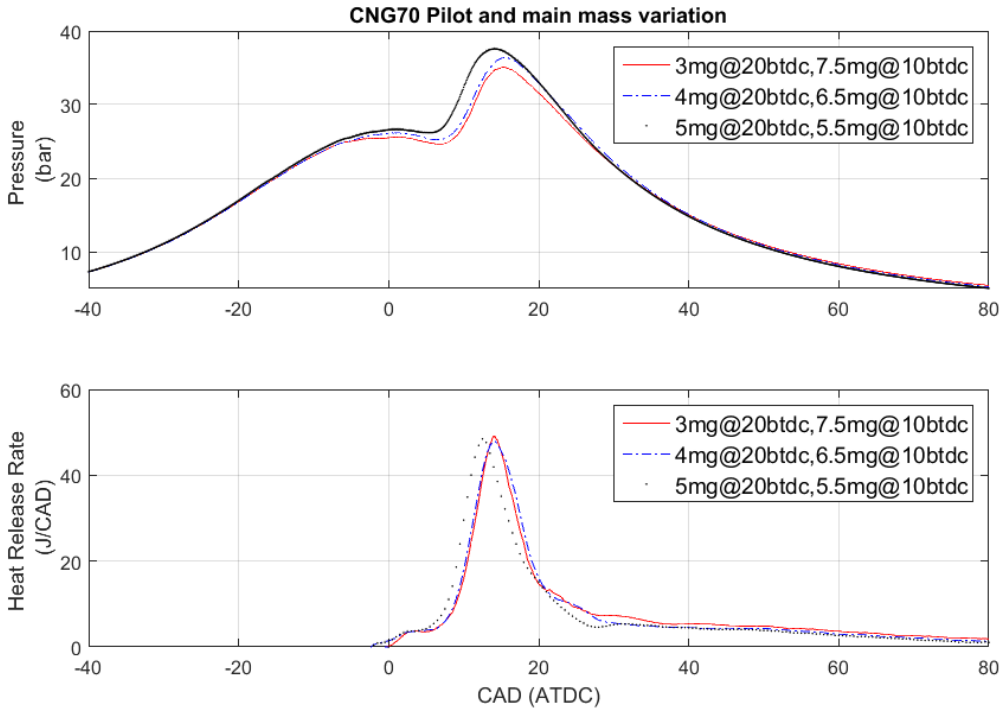

Figure 5.52 Pressure and HRR curves – Pilot/Main Split Sweep

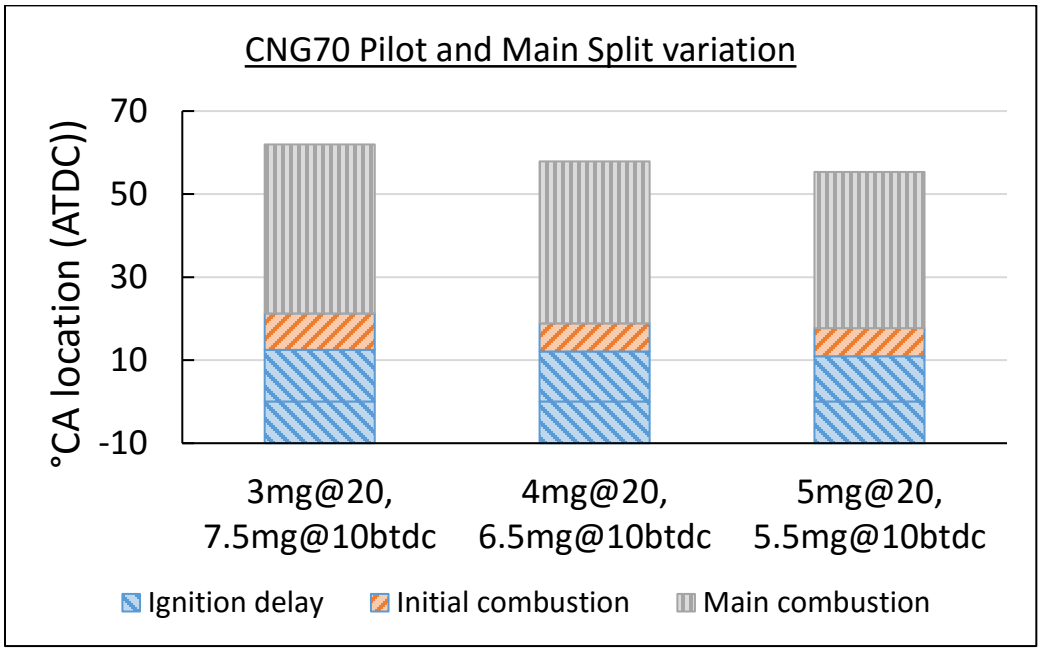

Figure 5.53 Combustion characteristics – Pilot/Main Split Sweep

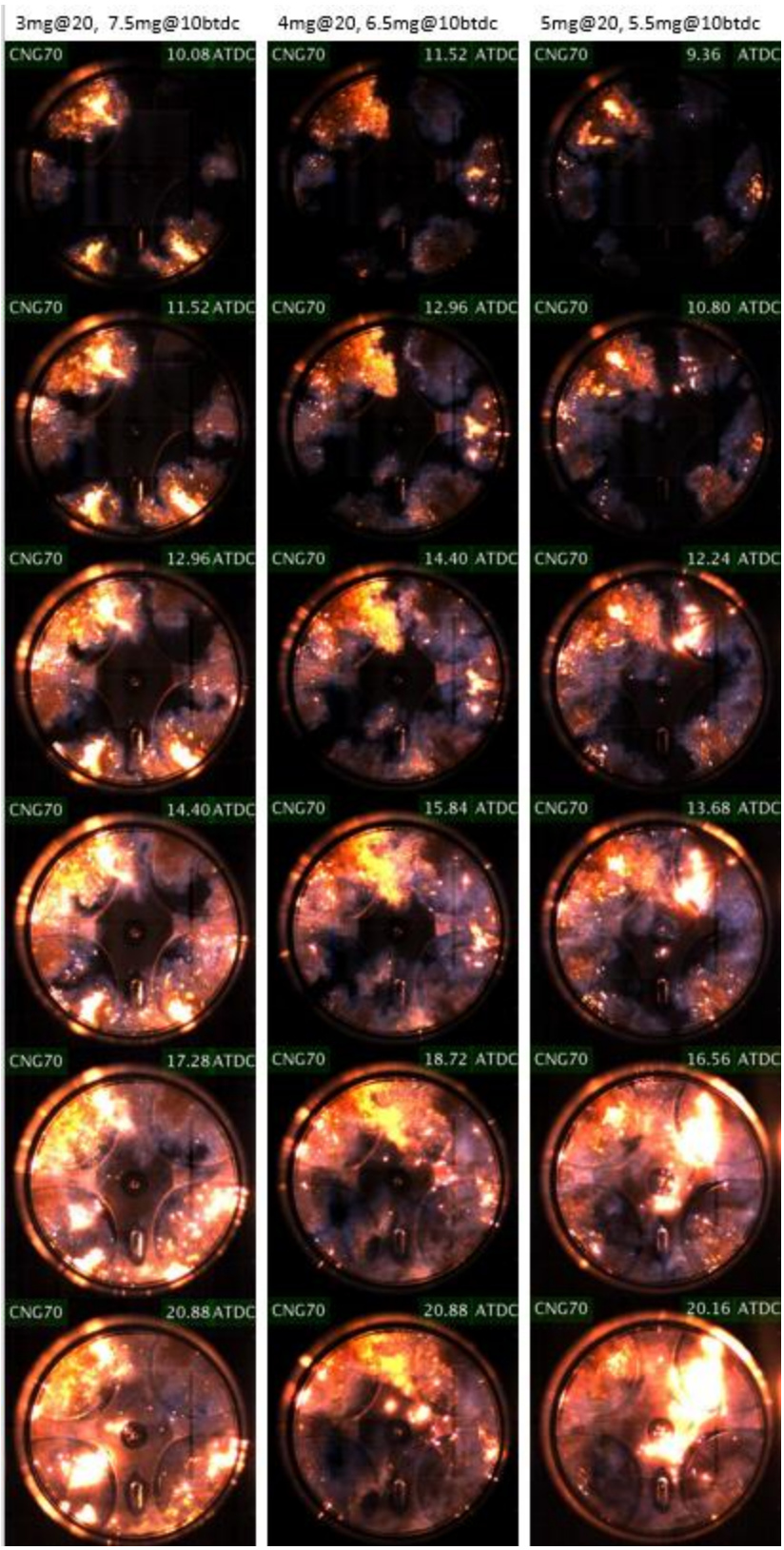

Figure 5.54 NL images – Pilot/Main Split Sweep

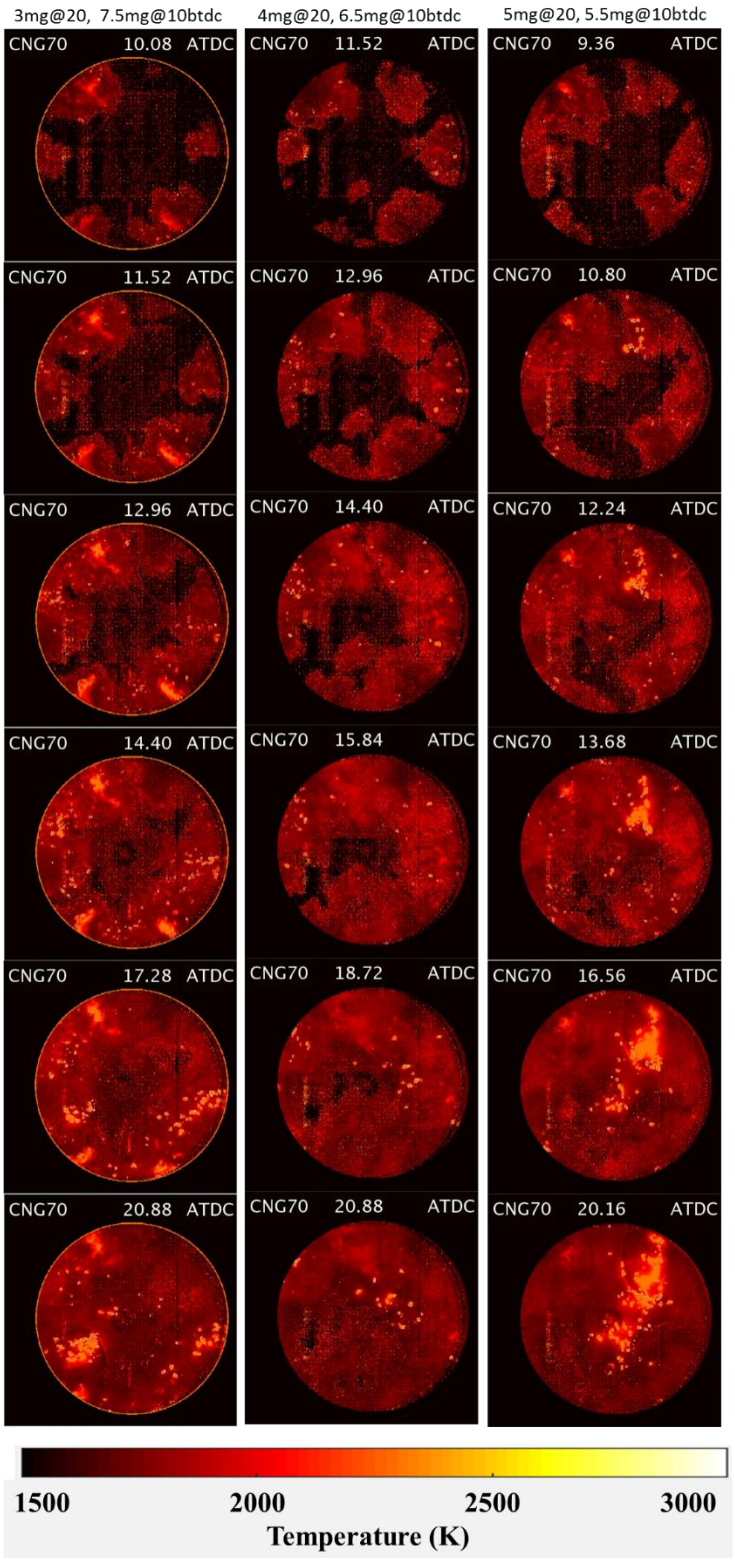

Figure 5.55 Soot temperature images – Pilot/Main Split Sweep

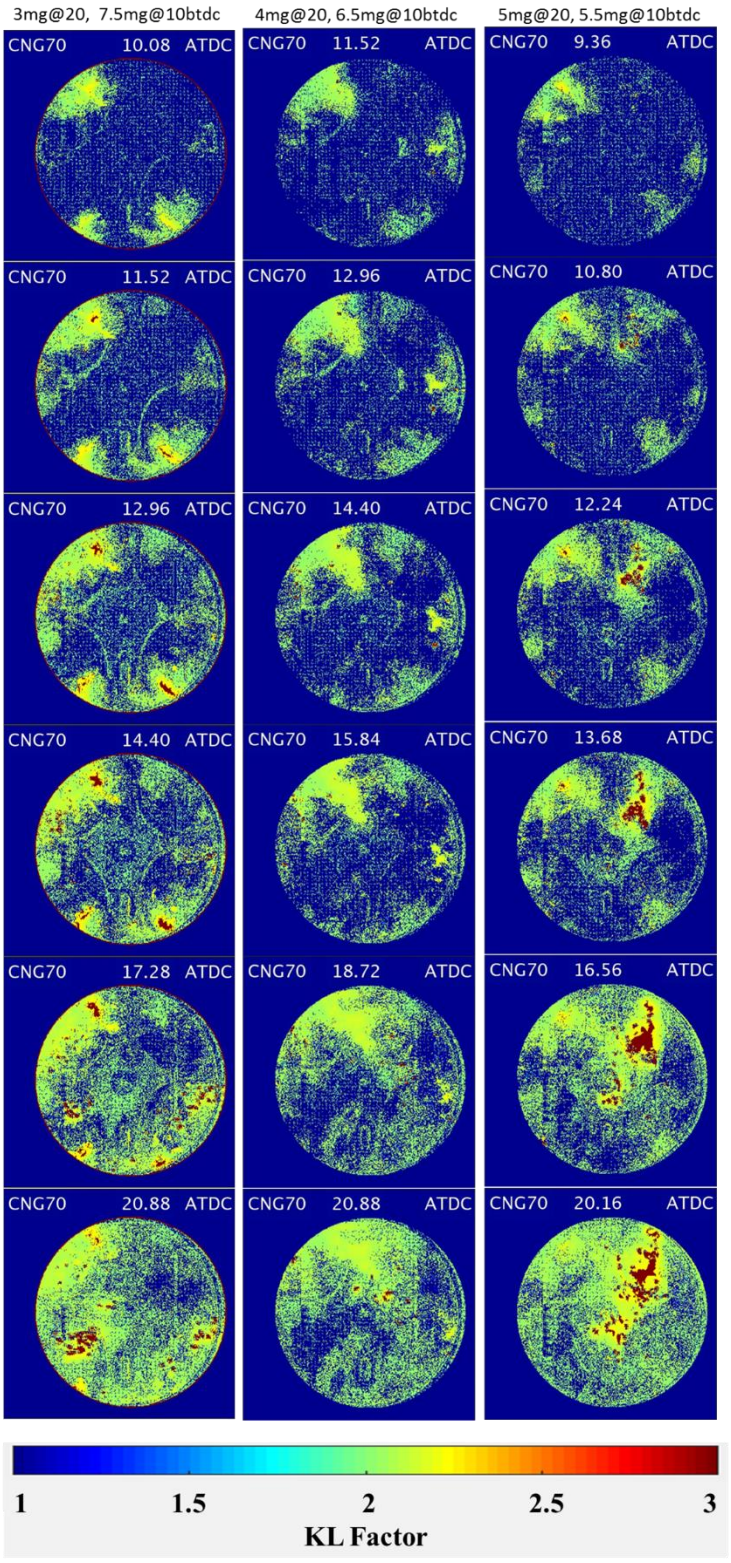

Figure 5.56 Kl factor images – Pilot/Main Split Sweep

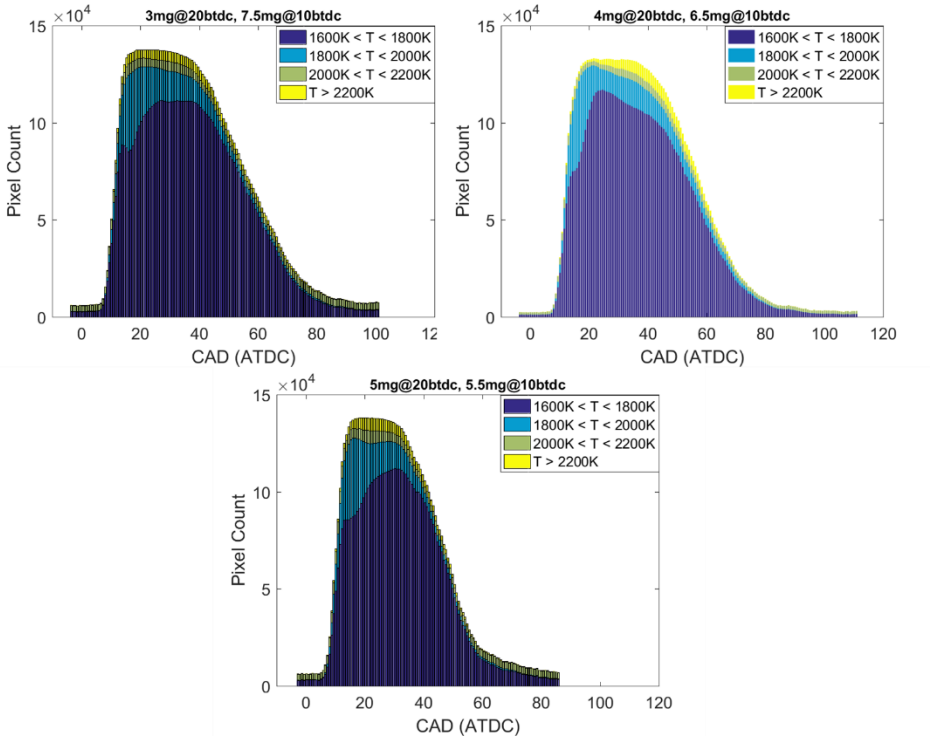

Figure 5.57 Soot temperature distributions – Pilot/Main Split Sweep

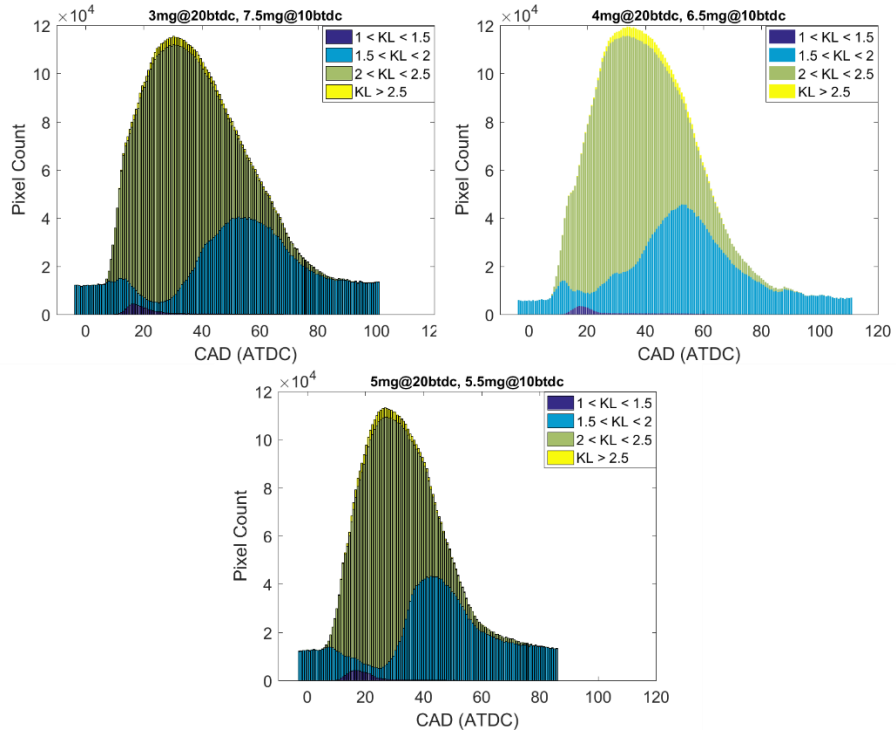

Figure 5.58 KL factor distributions – Pilot/Main Split Sweep

Chapter 6 Optical Investigation of Stratified GDI Combustion

Vehicles powered by GDI engines improve engine efficiency and reduce fuel consumption compared to that of PFI engines. However, in recent years, particulate emissions from GDI engines, especially the emission of ultrafine particulates, have become a subject of concern. Stratified charge lean-burn GDI combustion is a promising combustion regime that can alleviate PM emissions. Meanwhile, blending ethanol with gasoline has shown to provide benefits in terms of efficiency, stability, and emissions. In this study, a Micro-Jet Enhanced Ignition (MJEI) – Embedded Micro-chamber (EMC) concept with a variable orifice fuel injector for high efficiency lean-burn combustion is investigated to address the efficiency and sooting concerns of lean-burn GDI combustion. This approach combines the use of an optimized fuel injector spray, combined with an optimized two-zone piston-bowl shape, which incorporates a micro-chamber. In this study, a single-cylinder GDI SI engine has been used to test combustion using the MJEI-EMC concept using both a metal piston, while measuring in-cylinder pressure and exhaust emissions such as UHC, CO, NO_x, soot, and using an optical piston, to perform high-speed imaging and obtain Mie-scattering spray, as well as natural flame luminosity information. The following topics will be addressed in this chapter:

- Combustion performance and emissions measurements along with optical investigation of the spray and combustion process of various ethanol-gasoline blends.
- Spray visualization and characterization of a commercial injector and a prototype injector
- Combustion performance and emissions measurements along with optical investigation of the spray and combustion process comparing the commercial and prototype injectors.

6.1 Literature Review

6.1.1 Introduction

Vehicles powered by GDI engines aiming to improve engine efficiency and reduce fuel consumption have entered the car market since the late 1990s. In addition, the global volume of GDI engines is expected to overtake that of PFI engines by 2020. There are two main variants of Direct Injection Spark Ignition (DISI) technology currently of interest – the ‘‘homogeneous’’ DISI operated with stoichiometric mixtures, and the mixed mode DISI, where the mixture is stratified with an overall lean equivalence ratio composition during low load and speed operation, while at higher load and speed, the engine is operated in the ‘‘homogeneous’’ mode [142]. In homogeneous-charge DISI engines, a side-mounted or centrally located high-pressure fuel injector sprays fuel directly into the combustion chamber early enough in the cycle to promote homogeneous fuel–air mixing [143]. The mixed mode DISI engine runs with a stratified charge and with lean mixtures during low load/speed operation, and runs with a ‘‘homogeneous’’ charge at higher load/speed points.

Historically, particulate emissions have been related to diesel engines. However, in recent years, particulate emissions from GDI engines, especially the emission of ultrafine particulates, have become a subject of concern [12]. There is a great deal of interest in lean burn technology, which is an option for reducing engine-out particle emissions while simultaneously increasing fuel efficiency. Lean burn occurs when the air to fuel ratio (AFR) is greater than stoichiometric or $\lambda > 1$, where λ is equal to the actual AFR divided by the stoichiometric AFR (or the reciprocal of the equivalence ratio Φ). One advantage of running an engine lean occurs as the introduction of

additional air increases the specific heat ratio (γ) which leads to an increase in thermal efficiency as can be seen in Equation 6.1, which is for the ideal Otto cycle.

$$\eta_{th} = 1 - \frac{1}{CR^{\gamma-1}} \ldots (6.1)$$

where CR is the compression ratio (maximum cylinder volume / clearance volume) and γ is the specific heat ratio equal to C_p/C_v.

Lean engine operation has the potential to increase efficiency by affecting γ as well as reduce pumping losses by tending towards throttle-less operation, which can further improve fuel economy for the same road load. Lean burn technology has not been extensively implemented for several reasons including compromised combustion stability and three-way catalyst incompatibility. The narrow flammability limits of most fuels make it difficult to run lean while maintaining adequate combustion stability with low misfire rates. Poor combustion stability leads to low power output, and increased HC emissions due to misfire and partial burning cycles.

In this regard, fuel stratification is one of the most promising ways of enhancing combustion of overall lean mixtures and stratified charge lean-burn GDI combustion is a promising combustion regime that can alleviate PM emissions while maintaining combustion stability and efficiency [142 - 145]. During stratified combustion, the fuel is injected shortly before the ignition, so that the small amount of air-fuel mixture is optimally placed near the spark plug. This technique enables the usage of ultra-lean mixtures with very high air-fuel ratio, impossible with traditional carburetors or even PFI [144]. At high load and high speed, fuel is injected early during the intake stroke (allowing nearly complete fuel–air mixing), and the engine operates as a stoichiometric homogeneous-charge DI engine, with all of the associated power and emissions benefits. At lower loads and speeds, the air flow remains unthrottled to minimize pumping losses, yielding substantially higher part-load fuel economy compared to a throttled PFI engine. However, as the

amount of fuel is reduced for lighter loads the average equivalence ratio becomes too lean to burn and the required stratified fuel–air mixtures are obtained by injecting fuel just before ignition [143].

Apart from fuel/charge stratification, there have been a number of technologies designed to gain the advantages of lean burn while circumventing the disadvantages, such ignition enhancement, which facilitates lean burn by raising the ignition energy and/or intensifying turbulence, which increases flame speed. Another method to control combustion of lean burn mixtures is with jet ignition, which utilizes a pre-chamber combustion initiation system. The jet ignition concept involves the use of a chemically active, turbulent jet to initiate combustion in lean fuel mixtures. With jet ignition, the combustion of the main charge is reliable over a much broader range of air-fuel ratios since the jet acts as a distributed ignition source. The large number of distributed ignition sites ensures that the flame travel distances are relatively small enabling short combustion durations even in traditionally slow burning lean mixtures [146].

6.1.2 Previous Work

6.1.2.1 Stratified Charge Combustion

Although GDI has been studied since the 1930s, much work has been done on stratified GDI combustion since the 1990s owing to the development of fully electronic fuel injection systems [147]. Serras-Pereira et al. [148, 149] investigated the extent to which stratified GDI combustion is affected by in-cylinder flow affects spray formation and wall impingement using different fuel types and injection strategies in an optical engine using gasoline and iso-octane. A sweep of different locations around the cylinder bore revealed the locations of highest fuel impingement levels, which did not correspond directly to the nominal spray plume trajectories as a result of

spray-flow interactions. They found that a multiple injection strategy was better than single injections based on reduced heat loss and reduced emissions; however, the variability in peak pressure was higher than that for single injection. Flame growth was very different to that with single injection, being more 'spherical' and 'centralized' at the spark plug. They concluded that injection strategy and type of fuel play an important role in the mixture preparation process, even for homogeneous early direct injection, and that different types of multiple-injection strategies alone have the potential to modify significantly in-cylinder phenomena, affect combustion and potentially exhaust emissions. Aleiferis [150] studied flame variability in an optical, stratified-charge, SI engine close to the lean limit of stable operation (A/F = 22). The images showed that the flame always preserved its shape while growing in size, even when it had been initiated with a highly convoluted shape. Image processing showed that the flame-growth speed decreased from spark-induced high values to laminar burning speed values at 10°–15° CA after ignition timing and then increased to values, at most, 10 times higher than this when the flame had reached the piston crown on the tumble plane of view or the cylinder walls on the swirl plane of view. Drake et al. [151] studied stratified combustion in an experimental SG-SIDI engine using detailed computational fluid dynamics (CFD) modeling, high-speed spectrally resolved combustion luminosity imaging, and cylinder pressure analysis. It was found that optimum phasing occurs for somewhat rich equivalence ratios (0.9–1.6) and relatively low flow velocities (<15 m/s) at the spark location. Li et al. [152] studied the effects of split injection with various dwells and mass ratios on the spray and mixture characteristics in a DISI engine. It was found that using split injection prevented liquid phase fuel from piling up at the leading edge of the spray and the subsequent spray penetration length for both liquid and vapor phases was reduced. In addition, the width of the combustible mixture region was extended. Finally, the quantity of 'over lean' (Φ<0.7)

mixture in the spray was significantly reduced. It was concluded that split injection could enhance stratified lean operation and reduce smoke and UHC emissions of DISI engines. Costa et al. [153] also found through numerical simulations that split injections could be used to improve the quality of the charge stratification under lean operation; while a positive effect was observed on HC emissions, the formation of NO suffered due to the enhancement of the combustion efficiency, and hence the increase of the local temperature. Hemdal et al. [154] studied the combustion in a spark-ignited spray-guided gasoline direct-injection engine operating in a stratified mode by in-cylinder imaging of the fuel, OH*, and soot distributions. They observed that conditions were less favorable for efficient soot oxidation in the later part of the combustion for retarded injections. Retarding the injection timing resulted in higher levels of engine-out soot but lower NO_x and HC emissions. Dividing the injection into a double pulse had no obvious effect on the soot and OH luminescence, but the engine-out soot emissions indicated lower values. The NO_x emissions were unaffected by changing the injection strategy, whereas the HC emissions decreased. Park et al. [155] analyzed the effects of a spray-guided direct injection (SG-DI) combustion system on stratified lean combustion in a single-cylinder engine with a piezo-injector. It was found that the injection and ignition times were closely related and sensitive to the combustion efficiency since retarded or advanced ignition resulted in the formation of an inadequate mixture near the spark plug. At an injection pressure of 20 MPa, they demonstrated a sufficiently rich mixture for ignition near the spark plug even at ultra-lean mixture conditions (Φ~0.5). Finally, EGR with optimized ignition timing reduced harmful NO_x and THC emissions more effectively than retarded ignition timing. Oh et al. [156] investigated the effects of injection timing on spray and combustion characteristics in a spray-guided direct injection spark ignition (SG-DISI) engine under lean stratified operation. For the early injection timing, non-luminous flame and low combustion efficiency were observed

due to the over-mixed mixture formation. On the contrary, luminous sooting flame was shown at the late injection timing because of under-mixed mixture formation. In addition, smoke emission and incomplete combustion products were increased at the late injection timing due to increased locally rich area of the mixture. On the other hand, NO_x emissions were decreased while IMEP was increased as the injection timing was retarded. The retarded combustion phasing was verified as the reason in this observation.

6.1.2.2 Ethanol in DISI engines

Ethanol has also been studied as an alternative fuel for SI combustion due to its due to its better anti-knock characteristics, allowing the use of higher compress ion ratios and higher thermal efficiencies, and also as a means of potentially reducing PM emissions due to the fuel-borne oxygen content. However, few studies have been conducted in DISI engines. Wallner et al. [44, 45] studied the combustion performance of 10% ethanol and 10%butanol addition to gasoline in a 4-cylinder DISI engine. Data were taken at engine speeds in the range 1000–4000
RPM. Relatively minor differences were found between all three fuels in terms of HRR, 50% MFB location, and coefficient of variation (COV) IMEP at low and medium engine loads.
Smith and Sick [157] studied iso-octane, ethanol and iso-butanol mixing and combustion with late injection strategy for stratified operation in an optical DISI engine and found that ethanol tended to ignite faster but otherwise burned similarly to the other fuels. Combustion phasing with iso-butanol was very similar to that of iso-octane, despite a longer ignition delay. Stable operation with the latter fuels was possible over a window of spark timing from 5° to 8° CA after the end of injection, whilst ethanol required an even narrower window of 5–7° CA. Aleiferis et al. [58] performed an optical study of combustion in a direct-injection spark-ignition research engine with

gasoline, iso-octane, ethanol and butanol fuels injected from a centrally located multi-hole injector. They found that flame growth for Φ = 1was fastest for ethanol, followed by butanol, gasoline and iso-octane, and in addition, the flames of alcohols showed noticeable differences in visual contrast or 'texture', and their average luminosities were lower than those of iso-octane and gasoline. Fatouraie et al. [158] used a single cylinder DISI engine with optical access to investigate the effects of ethanol/gasoline blends on in-cylinder formation of PM and fuel spray characteristics. Significant reduction in in-cylinder soot formation was observed with the higher ethanol content in the fuel, regardless of fuel injection timing. Maricq et al. [159] identified ethanol blends <20 vol. % to be of small benefit for particulate number emission reduction. A significant decrease in PM exhaust emission was measured for higher ethanol contents (>30 vol. %). Karavalkis et al. [160] and Lee et al. [161] obtained similar results for fuels with low ethanol content. However, there are also studies reporting increasing particulate concentration for gasoline engine fuels with higher ethanol content [162, 163].

In this study, an MJEI-EMC concept as a means to achieve high efficiency lean-burn combustion is investigated to address the efficiency and sooting concerns of lean-burn GDI combustion. First various ethanol blends were tested using a commercially available injector. Next, a prototype injector was tested and compared with the commercial injector to assess the two-zone piston-bowl shape.

6.2 Experimental Setup

Ford Motor Company supplied the engine that was modified for optical access. The geometry of the engine was based on the 1.2-liter, 4-cylinder Ford DIATA (Direct-Injection Aluminum Through-bolt Assembly) engine. Features of this engine include an all-aluminum structure, a small

displacement (300 cc) per cylinder, a four-valve combustion system, and a high-pressure common-rail injection system. A single-cylinder equivalent of this engine is used. The engine has a flat-roof combustion chamber design, with two intake and exhaust valves per cylinder. Dual-overhead cams with hydraulic lifters are employed to operate the valve train. Two independent runners supply the intake charge, while the exhaust is discharged through a single runner. Optical access to the combustion chamber is attained from the side through a window just below the head, or from below through the fused silica piston top, which is attached to a Bowditch-type piston through a piston extension. The optical engine design maintains the geometry of the ports and combustion chamber of the original engine. A schematic of the optical engine is illustrated in Figure 6.1. A photograph of the optical engine is shown in Figure 6.2. Typical engine specifications are listed in Table 6.1. Detailed information about this engine can be found in [164, 165]. For completeness, some general features of the optical engine are discussed below. To convert the optical engine to run on gasoline, the cylinder head was modified and a spark plug (NGK ER9EH) was installed. A detailed discussion of the modifications made to convert the original CI DIATA engine into a GDI SI engine, as well as details on sub-systems and operating procedures can be found in [166].

6.2.1 General Optical Engine Setup

The optical engine design maintains the geometry of the ports and combustion chamber of the original engine. The key piece in attaining optical access to the combustion chamber is the fused silica piston top. This design retains all the features of the stock piston, including bowl geometry and valve cutouts. With this design, a laser beam can pass unobtrusively through the piston into the combustion chamber. Access for imaging of the combustion chamber is obtained through the bottom of the piston. The design of the lower half of the piston top allows it to be locked into a

sleeve, which in turn is attached to the piston extension on the engine. The piston top is machined from Corning 7980 fused silica, which has high transmissivity far into ultraviolet wavelengths. In addition, it has elevated tensile and compressive strengths in comparison with other types of fused silica.

Fused silica windows are incorporated into the engine design to allow for laser access into the combustion chamber. In order to accomplish this, a window spacer is placed just below the existing head. The spacer is machined from 304 stainless steel. Each of the four pockets can house either a window machined from Corning 7980 fused silica, or a blank that is machined from the same material as the window spacer. These pockets afford the necessary restraint for securing the windows in the spacer at in-cylinder pressures above atmospheric pressure. In order to keep the windows from being pulled into the cylinder under the slight vacuum during the intake stroke, the windows were set into the pockets using RTV60, a silicone rubber compound. In addition, this compound helped to eliminate leakage around the windows during the compression stroke. With the windows in place, the dimension of the inner wall matches the bore of the research engine, and simply replaces a portion of the cylinder liner.

An extended cylinder liner mates with the bottom of this window spacer. For proper alignment between these two parts, the design incorporates an angled surface on the bottom half of the spacer. The piston sleeve that matches the contour on the lower half of the piston top is machined from a nickel alloy, Invar, chosen for the similarity in coefficient of expansion with the fused silica. The piston top could possibly crack from an induced stress concentration if the two materials were to expand at different rates. The sleeve is designed with three keyways through which the lobes of the locking ring epoxied onto the piston top can pass. A high-temperature epoxy is applied to the piston top and sleeve for sealing purposes as well as to add rigidity to the assembly. In addition to

housing the piston top, the piston sleeve also includes the necessary grooves for the piston rings. Special oil-less rings are used in order to avoid fouling of the optical components. Two compression rings and a single rider ring, which serves to locate the piston within the cylinder, are used in the optical design. All three rings are machined out of Vespel. The Bowditch piston extension attaches to the original piston in the engine block and accounts for the distance that the head is displaced in order to obtain optical access. The piston sleeve bolts onto the other end of the extension. The piston extension is machined from an aluminum alloy, 2024-T4. In order to view the combustion chamber through the piston top from below, the piston extension is hollow to allow for an optical path. In addition, slots are machined to allow for a 45-degree mirror and supports to be placed inside the piston extension during engine operation. This mirror redirects the diagnostic signal from the combustion chamber to the cameras as depicted in Figure 6.5.

In addition to providing optical access, the design of the optical engine incorporates a means to clean the side windows and piston top without having to disassemble the engine, which saves a great amount of time. The creation of soot during the GDI combustion process requires frequent cleaning of the optical surfaces. Therefore, the design includes the ability for the drop liner assembly to be lowered while the piston is at bottom dead center, providing access to the piston top and side windows. The extended cylinder liner provides the required distance in order to maintain the full stroke of the engine and allows for the heating of the piston to working temperatures prior to operation. The top portion of the cylinder liner incorporates the angled surface with which proper location with the window spacer is ensured. The angled surface on the liner includes a land for the inclusion of an O-ring, which provides the seal between the two pieces during operation. As with the window spacer, the inner dimension of the extended cylinder liner matches the bore of the research engine. The liner is machined from 304 stainless steel, and is

assembled from two separate parts. The inner portion of the liner incorporates passages through which coolant is circulated, while the outer portion serves as a shell.

The liner is raised and lowered using the drop liner support. When the drop liner is raised, the mount rests upon the drop liner support posts, which bring the angled surface of the drop liner to within a few millimeters of the bottom of the window spacer. In order to operate the engine, the drop liner assembly must be raised an additional few millimeters in order to seal the cylinder liner with the window spacer. The hydraulic assembly provides the necessary translation and sealing force. Nitrogen is used to pressurize an external reservoir of hydraulic fluid that feeds up through the base of the hydraulic assembly and drives the hydraulic piston, which in turn drives the drop liner assembly attached to the top of the hydraulic piston. The hydraulic retainer is used to ensure that the hydraulic piston does not travel beyond its design limit if the hydraulic piston is pressurized when the drop liner is lowered. When cleaning of the optical components is necessary, the hydraulic pressure is relieved and the drop liner mount is turned ninety degrees, subsequently fitting between the supports and lowering the liner.

All the parts of the hydraulic assembly were machined from 304 stainless steel. The final component for the optical design is the block adapter. This piece is designed to fit onto the existing engine block and provide the bolting patterns that are used to assemble the optical design. The block adapter is also machined from 304 stainless steel.

6.2.2 Engine Sub-systems

6.2.2.1 Air Supply System

Air was supplied to the engine through a VALTEK controller. Using a LabVIEW code containing a PID loop, intake air pressure and temperature can be set to desired values. A full DIATA prototype has the capability of electronically deactivating one of the intake ports to achieve higher swirl within the combustion chamber. This is simulated on the research engine through the insertion of a ball valve prior to one of the intake ports. To maintain symmetry in the intake system, a similar valve is placed in the same position on the other intake port, but remains unused. To reduce the effects of pressure waves on the intake flow, a damping chamber is located as close to the engine as possible. This chamber has a volume of 26.5 liters, which is 88.3 times the volume of the engine. The intake mass flow rate was measured through a calibrated orifice plate flow meter.

6.2.2.2 Cooling/Lubrication Systems

External cooling and oiling pumps were installed to provide coolant and lubrication oil. External reservoirs with immersion heaters were used on both the cooling and oiling systems in order to pre-heat the engine to its operating temperature without actually running the engine. The oil and coolant temperatures were regulated by two external tube-in-shell heat exchangers with Johnson Controls T-8000 controllers.

6.2.2.3 Fuel System

The fuel injection system is shown schematically in Figure 6.8. For the gasoline fuel circuit, the fuel was supplied by a non-return loop comprised of a fuel canister pressurized with nitrogen gas.

The can was made from 1 1/2” schedule 120 stainless steel pipe and capped on both ends with pipe fittings. The nitrogen inlet was on the top and the fuel outlet was on the bottom. The fuel pressure was set with a Tescom high-pressure regulator connected to the can with a braided stainless steel hose. A check valve prevented any liquid fuel from entering the nitrogen supply line. Stainless steel 1/4” tubing was used for the fuel line and compression fittings were used to assemble the system. A bleed valve at the top of the fueling system was used to expel vapor from the system. After the bleed valve, another braided stainless steel hose supplied fuel to the injector.

The injection system is controlled by a locally-made injector driver, which provides the required current to lift the needle inside the injector at a given timing. The injection duration and frequency of injections are controlled using a Digital Pulse Generator, in conjunction with the LabVIEW interface.

6.2.2.4 Ignition System

To convert the optical engine to run on gasoline, the cylinder head was modified and a spark plug (NGK ER9EH) was installed. In addition to adding a spark plug, a system to fire the plug and properly time it with the crankshaft was necessary to convert the engine from diesel to GDI. A spark circuit was designed using a VB921ZVFI ignition coil driver. This chip is a monolithic integrated circuit that combines vertical current flow power with a coil current limiting circuit and a collector voltage clamping. It is specifically designed for high performance electronic vehicle ignition systems. It is essentially an electronic method of emulating a points system. A Dynatek DBR-1 ignition booster box was also added to the circuit to sufficiently boost spark energy – this booster was specifically designed for an engine with one ignition coil such as the DIATA. This allowed the engine to fire properly, and did not cause interference with the data acquisition. A

schematic of the ignition system is shown in Figure 6.9. An image of the spark plug installed in the cylinder head is shown in Figure 6.10. The position of the spark plug relative to the fuel injector can also be observed in this image.

6.2.2.5 Starting/Motoring System:

An air-cooled General Electric DC dynamometer (10 hp delivering, 15 hp absorbing) was used to motor the optical engine. Both the engine and the dynamometer were mounted on a steel bedplate and are coupled with a shaft manufactured by Spicer Corporation. This shaft was designed for the connection of engines to dynamometers and has a universal joint at each connection location. The dynamometer controller was manufactured by DyneSystems Co. (model DYN-LOC-IV), and is capable of both speed and torque control.

6.2.2.6 Data Acquisition and Control System:

The engine was instrumented with a number of sensors to monitor its operation. An optical shaft encoder with quarter crank angle resolution was used to provide the time basis on which all data acquisition timing systems are operated. Temperatures were recorded using thermocouples in various key locations (e.g., intake, fuel supply, coolant, oil, etc.). Strain gauge-type pressure transducers were used to measure pressures that were relatively steady (e.g., intake, oil, fuel supply, fuel rail). The in-cylinder pressure was measured by a Kistler 606IB piezoelectric pressure transducer in conjunction with a Kistler model 504E charge amplifier. National Instruments LabVIEW was used as the control and data acquisition software for the engine. Monitoring of engine temperatures and pressures was done by a multifunction data acquisition board (PCIe-6341)

using an external signal conditioning unit. The timing control involved in running the engine, laser, and cameras was all implemented through two 16 up/down 32-bit counter/timers PCI-6602 boards.

6.2.2.7 Imaging System:

Two imaging techniques were used in this study – Mie scattering for liquid spray imaging, and imaging of natural flame luminosity. Liquid fuel distribution visualization in engine cylinders using Mie scattering provides useful information on the evolution of fuel spray penetration, spray-wall interaction, and fuel droplet dispersion. A Copper Vapor laser from Oxford Lasers was used as the light source. The scattered light from liquid droplets was imaged by a high-speed video camera (Phantom V7.0 from Vision Research Inc.) synchronized with the laser. The images gave qualitative information about the transient liquid phase distributions showing the extent of the liquid fuel penetration and the extent of liquid fuel impingement on the bowl surface. For combustion visualization, the same setup was used; however, no laser illumination was used. Again, the Phantom v7.0 high-speed digital video camera was used to capture the natural flame emission for the whole cycle, through the 45-degree mirror placed inside the piston extension during engine operation. This mirror redirects the diagnostic signal from the combustion chamber to the camera. The response spectrum covers the range from 400 nm to 1000 nm. The non-linearity of the camera response to incident light is below 3%, which makes it suitable for direct comparison of light intensity.

6.2.2.8 Exhaust Gas Analysis

The same emission analysis equipment used in Chapters 2 and 3 was used to obtain emission information when operating the engine with the metal piston.

6.2.3 Laser Diagnostics – Spray Visualization and Injector Characterization

For injector characterization, back light illumination was used for capturing the time resolved injection event. A phantom V7 high speed camera was used at a speed of 16000 fps, corresponding to a time resolution of 62.5 μs. An Oxford copper vapor laser (Model: LS20-50), synchronized with the camera, was used as the backlight source. The high-speed camera and copper vapor laser were synchronized up to 15K fps to get time-resolved measurement. The copper vapor laser has stable output with fluctuation less than 2%. Each laser pulse lasts 25 to 30 ns, and is ideal for freezing the transient movement. The copper vapor laser has two-color output at 511 nm and 578 nm with a power ratio of 2:1. The injector was positioned such that the spray was parallel to the light source/camera to obtain the images. The laser light was delivered through a fiber and projected onto a black surface to form a homogeneous background. The camera was triggered by the injection signal and the exposure time was set to 6 μs. For each case, a minimum of five injections were conducted for any quantitative analysis.

A 2D Dantec PDA system with a BSA P60 processor coupled with a 58N70 detector unit was used for the measurement of the droplet velocities and diameters. The transmitting and receiving optics were installed on a three-dimensional traverse so that the measuring position can be precisely controlled. An argon-ion laser with a maximum power of 8.5 W was used and the output was aligned with the fiber optic unit. This unit was responsible for splitting the laser beam into two pairs of different wavelengths; each pair delivering two beams with equal intensity after proper alignment with the manipulators. The first pair consisted of green beams with a wavelength of 514.5 nm, responsible for the axial velocity component, while the second pair consisted of blue beams with a wavelength of 488 nm, responsible for the radial velocity component. A Bragg cell

unit is positioned inside this fiber optical unit to provide a 40 MHz frequency shift between two the beams within each pair. Light scattered by the droplets was collected by a 310 mm focal length lens positioned at 30 degrees to the plane of the two incident green beams to ensure that refraction dominated the scattered light. The signal from the photomultipliers was transmitted to the processor unit where all the data processing was carried out. The processor was connected to a desktop computer via an Ethernet adapter where all the acquired data was saved for further analysis. The measurements, similar to the high speed images, were synchronized with the injection signal, and a time window of 20 ms after SOI was used as the limit for each injection event.

A proper configuration of parameters such as signal to noise ratio (SNR), signal gain, record length, applied photomultiplier voltage was chosen according to different testing cases to ensure a reasonably good data rate (above 500 samples/second) and validation rate (above 80%).

The entire fuel injection and laser diagnostic setup (High-speed imaging as well as the PDA) is shown in Figure 6.11.

There are several validation criteria for PDA. First, there is the burst detector, which is triggered by a signal that exceeds a certain threshold. Then a check is performed to see that the frequency of the signal found via FFT is at least 4X higher than the next highest peak in the spectrum. If not, the signal is rejected. Another rejection criteria is based on bandwidth - i.e. if the particle velocity is 10 m/s but the range is limited to a lower value (say 8 m/s) so the resulting histogram is cut off, the higher speed particles will of course not be validated. There are additional validations such as the so-called spherical validation, which requires consistent spherical droplets.

6.2.4 Engine Operation

6.2.4.1 General Engine Operation

The engine was first operated using a metal piston to assess performance, stability and emissions behavior at various operating conditions. Then the optical piston was installed to obtain spray and combustion images. All tests within the optical engine were performed under conditions typical of an operating metal engine. The conditions that remain constant for the operation of the optical engine are shown in Table 6.2. For the optical engine, external heaters were used to obtain similar oil and coolant temperatures to the metal engines without engine operation.

The engine was operated in a “skip fire” mode to reduce the thermal load on the optical parts. By doing this, the engine was fired for 3 cycles, with 10 non-firing flushing cycles in between each burst. Pressure data and combustion images were taken during the third firing cycle. When using the metal piston, the pressure trace was obtained by averaging the third firing trace over 250 skip-fired cycles. When using the optical piston, the pressure traces corresponding to the cycles imaged were obtained. Emissions data was also acquired when using the metal piston. In the figures, error bars represent the variability in the data in terms of standard deviation between runs. To account for the skip-fired operation of the engine, the reported emission results have been multiplied by a factor of 13/3 to approximate what they would be in a continuously-fired, single-cylinder engine [171]. More details can be found in [166].

6.2.4.2 Fuel Quantity Calibration

In this study, the engine speed was maintained constant at 1200 RPM. The engine load was varied by adjusting the intake air pressure. In order to estimate the equivalence ratio at various operating

conditions, the intake mass air flow rate was measured at various intake pressures ranging from 8 to 14.5 psi. Next, in order to inject precise amounts of fuel, calibration of the injector was necessary. The right injection pulse width should be found by a series of calibration of fuel quantities. Due to the unavailability of single-injection fuel quantity measurement equipment, the fuel was injected over a certain number of injections and collected. Fuel was injected into a closed chamber. Then the fuel mass for several injections was weighed and averaged to get the fuel quantity for one injection cycle. It was found that it was important to use the same injection sequence as running the engine in skip-fire mode at the same speed, because the injection frequency and rail pressure fluctuations affected the fuel quantity. During the fuel calibration, a series of 5 runs with 200-500 injections (depending on duration) for each run was performed for each calibration point. The averaged fuel quantity based on the 5 runs was used and the standard deviation was calculated based on the 5 runs. Combining the air flow rate measurements with the fuel injector calibration, the equivalence ratio was accurately estimated for different intake pressures (loads).

6.2.4.3 Optical Distortion Estimation

In order to estimate the distortion due to the side window and the optical piston, imaging was performed using a grid sheet with grid size 5x5 mm. This is shown in Figure 6.3. From the bottom view images, it was found that the ‘bowl’ region of the piston remains relatively undistorted (negatively distorted by 0.1 mm). However, moving away from TDC leads to distortion in the ‘donut’ region of the piston. It was found from the bulk of the luminous images from the combustion process extend from -20° BTDC to about 20° ATDC. Based on this, combustion imaging results shown are limited to +/- 20° BTDC, where optical distortion is minor. From the

side view image, it can be observed that the grid size is negatively distorted to 3.2x4.5 mm due to the concavity of the side window, which enables viewing of the entire bore of the combustion chamber. It should also be noted that the various optical surfaces in the engine are a significant source of glare, and these glare patterns vary quite a bit with the crank angle location. The varying glare patterns combined with the optical distortion inhibits quantitative measurements.

6.2.4.4 Combustion Visualization

Due to the extensive optical access provided by the optical DIATA engine, 3-D like (simultaneous bottom view and side view) combustion imaging is feasible by adding two mirrors beside the optical engine. The schematic is shown in Figure 6.4. The emitted light from the flame coming out of the side window is directed by two 45° mirrors to the camera. In order to obtain the combustion images from the side and bottom windows at the same time, one high-speed video camera was used by setting the resolution at 288x560 to capture both images. For all of the high-speed combustion images taken in the current study, the operating frame rate was 12000 frames per second, which was corresponding to 0.75 CAD intervals between two consecutive images. Because the optical path for the side window image and the bottom-view image is the same from the injector tip to the camera imager, the focus of the camera was adjusted according to the bottom-view image with a clear picture of the injector tip. The luminosity obtained through the camera was a line-of-sight integrated signal from the flame radiation. For all of the cases, the exposure time was about 10 μs (aperture: f/4.5), being slightly adjusted for different operating conditions, but it was kept constant for direct comparison within a certain group of tests.

The digital images of combustion flames obtained using the high-speed video camera were processed in MATLAB using the same color map (MATLAB's 'hot' color map) for a certain

group of test and scales to compare the influences from different operation and control parameters. For each case, five combustion movies were obtained and a typical whole cycle movie was selected for analysis and presentation. Once the luminosity images were acquired, integrating the pixel value over an image provided the value of spatially integrated natural luminosity (SINL). SINL varying with crank angles was obtained for the all of the cases by summing up the pixel values of the bottom-view combustion images. To better quantify the natural luminosity characteristics of the entire combustion duration, time integrated natural luminosity (TINL) is calculated by further integrating the SINL with time. TINL is an indication of the soot temperature and concentration over the entire combustion cycle [51]. Because of the setup limitation, the side window flame images were not complete due to the blockage from the side of the window spacer. Generally speaking, flame luminosity mainly depends on soot concentration and flame temperature. Lower flame luminosity indicates low soot concentration or low flame temperature, which inhibits NO formation. Qualitatively speaking, for the burning of a certain fuel mass, the more the heat released and the lower the flame luminosity are, the better the efficiency and emissions are [165].

6.2.4.5 Spray Imaging

Two kinds of Mie-scattering techniques were used in the current study. The first one was a volume-illuminated Mie-scattering technique to visualize the liquid spray from both the bottom of the piston and the side window to study the spray penetration, dispersion and spray-wall interactions. For this technique, the setup was similar to the combustion imaging setup. The setup schematic is shown in Figure 6.5. The only difference is the illumination light from the copper vapor laser using an optic fiber. To obtain good quality images of both views, the direction of the incident laser light was quite critical. By adjusting the laser light incident direction, the light intensity of bottom view

image should be strong enough to identify the spray and the side window image should not be too strong to saturate the camera imager. The incident light angle was along the axis of the spray with an angle of 15 degrees to avoid the reflected light from the side-window flat surface going to the camera [165]. The camera synchronized with the laser was operated at 12000 fps with resolution of 288x560 pixels. The exposure time was 2 μs (aperture: f/11). The image was processed by improving the brightness or the contrast to get a better view of the transient spray in the engine cylinder.

The second Mie-scattering technique is the background corrected Mie scattering technique. In this technique, the Mie-scattering image was taken through the side window. The setup schematic is shown in Figure 6.6. The laser light was introduced from the bottom of the piston to rpvoide volume illumination. Scattered light from the spray was collected from the side window. Because the piston was moving, the background image and the Mie-scattering image must be taken at the same timing relative to the TDC pulse. The camera was synchronized with the copper vapor laser and operated at 12000 fps with a resolution of 464x336 pixels using an exposure time of 2 μs (aperture: f/8). Due to sources of reflection from the optical engine such as the liner and the piston surface, it is quite challenging to obtain a clean image. Image processing was necessary, especially for the second injection which scatters very little light due to the short injection duration and small amount of fuel injected. The image processing procedure of the background corrected Mie-scattering technique is as follows – first, the background image (without spray) was subtracted from the original Mie-scattering image at the same timing. Secondly, the brightness and contrast of the background corrected Mie-scattering images were improved. Figure 6.7 shows a comparison between the raw image and the processed image.

6.3 Results and Discussion

6.3.1 Ethanol-Gasoline Blends

A commercially available Delphi GDI injector was used for this study. The mass flow rate of the injector was calibrated for different injection pressures as well as various injection durations. High-speed imaging was also performed to assess the spray pattern of the injector, shown in Figure 6.13. The Delphi injector has six uniform jets, with a wide cone angle, that would favor targeting the outer 'donut' profile of the piston for early injections and the central bowl region with late injections. In this section, results from the combustion of ethanol-gasoline blends are discussed. Laboratory grade ethanol was splash blended with ethanol-free 90 AKI pump gasoline to create blends containing 20% by vol., 40% vol., 60% vol. and 85% vol. ethanol, referred to as E20, E40, E60 and E85, respectively. The properties of ethanol and gasoline have been listed in Table 6.3.

6.3.1.1 Metal piston tests

The blends were first tested using the metal piston to obtain combustion pressure, stability information in terms of the CoV-IMEP, and various tailpipe emission measurements consisting of UHC, CO, NO_x and soot (FSN). For each fuel, an equivalence ratio sweep was performed at an intake pressure of 11 psi, and a load sweep was performed by varying the intake pressure from 10 – 12 psi under stoichiometric conditions. These intake pressures were selected because they correspond to a nominal IMEP in the 3-5 bar range, which is suitable for testing using the optical piston. Based on prior testing [166], it was found that optimum engine performance is obtained with two injections. The first injection was at 180° BTDC. Earlier injection timings caused impingement on the valves and led to over-mixing which leaned out the mixture. Later injection

timings provided insufficient mixing time. 90% of the total fuel mass was injected in the first injection. For the second injection, a timing of 40° BTDC was used. The spark timing was fixed at 30° BTDC. The reason for using two injections is summarized in Figure 6.12, which compares various engine output parameters normalized by the values obtained for the single injection case. It can be observed that splitting the fuel injection into two events provides advantages in NO_x, CO, soot (FSN), and most importantly, stability as shown by the COV-IMEP, which is 4% for the double injection case and 8% for the single injection case. In stratified conditions, the flame front spreads faster than the homogeneous case in the first phase of combustion due to the higher Φ in the piston bowl region; this could reduce the probability for the flame front to be influenced by in-cylinder motion. It must be noted that since the stoichiometric air/fuel ratio for each blend was different, injection duration increased with increasing ethanol content to maintain the same equivalence ratio. A summary of the test conditions are shown in Table 6.4.

Figure 6.14 shows the cylinder pressure and heat release rate curves for the various ethanol-gasoline blends tested, at an intake pressure of 11 psi and stoichiometric conditions. It can be observed that addition of ethanol advances combustion phasing, due to ethanol's higher flame speed. As a result, the peak combustion pressure is also higher. E60 shows the most advanced combustion phasing. However, with further increase in ethanol content, E85 shows relatively retarded combustion phasing, likely due to a decrease in laminar flame speed due to the decrease in temperature at the spark timing due to E85's high latent heat of evaporation, which causes a significant charge-cooling effect. In general, these trends agree well with those found by [58, 167].

Figure 6.15 shows the cylinder pressure and heat release rate curves for E20, at an intake pressure of 11 psi under different equivalence ratios. It can be observed that combustion phasing gets progressively retarded with decreasing equivalence ratio. The peak cylinder pressure also

decreases. This is due to a combination of lower flame speed and the slower flame-kernel growth development at leaner conditions [58].

Figure 6.16 shows the IMEP and indicated efficiency for the equivalence ratio and intake pressure sweeps for the various fuels. From the equivalence ratio sweeps, it can be observed that the peak IMEP of 3.5 bar occurs at stoichiometric conditions and steadily drops with decreasing equivalence ratio. On the other hand, the indicated efficiency steadily rises with decreasing equivalence ratio due to an increase in the ratio of specific heats of the air/fuel mixture, which decreases compression work. Comparing the fuels, it can be observed that E60 shows the highest IMEP under stoichiometric conditions. The indicated efficiency was also highest for E60 across the equivalence ratio range tested. Net indicated efficiency benefits from faster flame speed and then the lower combustion duration [175]. This is probably due to E60 showing a relatively better balance between increase in laminar flame speed due to ethanol addition and the reduction in flame speed due to a decrease in temperature due to charge-cooling. Secondly, it is likely that heat transfer losses are lower due to lower burned gas temperatures, which is a consequence of two charge cooling due to ethanol's high HoV which results in lower charge temperature at the start of combustion [176]. From the load sweep tests, it was found that the indicated efficiency was generally higher at higher loads, due to a higher pressure and temperature at the spark timing and the increased charge motion, which could potentially increase the turbulent flame speed and reduce the combustion duration. Figure 6.17 shows the COV-IMEP for the equivalence ratio and intake pressure sweeps for the various fuels. Generally, the COV-IMEP for these tests was found to be between 5-9%. Overall, stability was negatively affected with higher substitutions of ethanol, i.e., with E60 and E85 showing COV values higher than 6%. Similar results were obtained in [177], where it was found that the increased injection duration for ethanol-gasoline blends would likely

increase the inhomogeneity of the mixture, causing a reduction in combustion stability. At leaner conditions, however, the higher ethanol-containing blends show similar or slightly lower COV values than that of E20. This can be correlated to in-cylinder flow and piston movement. At these leaner conditions, the injection duration is shorter; however the ethanol blends show faster combustion due to the increase in laminar flame speed. The faster the combustion is, the less time there is for the flame front to be influenced by in-cylinder motion and gas expansion, and hence resulting in greater stability [178]. Figure 6.18 shows the UHC and CO emissions for the equivalence ratio and intake pressure sweeps for the various fuels. The UHC emissions generally decrease with increasing ethanol content – under stoichiometric conditions, E20 shows UHC emissions of about 3000 ppm and this progressively decreases to about 1950 ppm with E85. As far as the CO emissions are concerned, they increase with ethanol content, under stoichiometric conditions. This is likely due to the shorter combustion durations and relatively reduced temperature in the expansion stroke, which leads to less CO oxidation. At leaner equivalence ratios, the CO emissions are generally similar for all the fuels. UHC and CO emissions both decrease with increasing load due to enhanced charge motion and mixing at higher intake pressures, and higher temperatures, which enhance CO oxidation. Figure 6.19 shows the NO_x and soot emissions for the equivalence ratio and intake pressure sweeps for the various fuels. NO_x emissions decrease initially with E40 but increase with increasing ethanol content, with E60 and E85 showing values greater than both E20 and E40. Generally, NO_x trends agree with the peak pressure trends observed in Figure 6.14. The rapid rise in pressure and advanced combustion phasing of E60 leads to it having higher NO_x emissions. NO_x emissions decreasing equivalence ratios due to more oxygen availability to form NO_x. NO_x emissions increase with load due to higher pressure and temperatures. Soot emissions decrease steadily with decreasing equivalence ratio and

with increasing ethanol content. The higher fuel-borne oxygen content significantly enhances soot oxidation and reduces tailpipe soot emissions.

6.3.1.2 Spray Imaging

In this section, Mie scattering spray imaging was performed for the various ethanol-gasoline blends. The images shown here correspond to the combustion images shown in the next section taken at 11 psi intake pressure and stoichiometric conditions. The first injection was at 180° BTDC and the second injection was at 40° BTDC. Although the mass split between the two injections was 90/10 for combustion testing (both metal and optical piston testing), this was changed to 70/30 during 3-D-like spray imaging as the 2nd injection containing 10% of total fuel mass was quite small and could not be clearly observed. Table 6.5 shows the testing conditions for the spray imaging. To facilitate viewing and interpretation of the various spray images provided, Figure 6.20 shows a comparison between the spray images obtained at ambient conditions during injector characterization and those obtained in-cylinder. The injector orientation and the visualization of jets is shown in the image. Figure 6.21 shows an example background-corrected image of the spray from the Delphi injector using E20. The injector is centered at the top; the borders of the side window are also shown. The spray jets, indicated by the white area in the images, start from the center and move outward laterally towards the cylinder walls. The spray appears as a cloud due to overlap between multiple fuel jets in the viewing plane. Figure 6.22 shows the evolution of the spray of the first injection for various fuels. At this injection timing, the bottom view through the piston is blocked by the piston extension; however, the side view images show differences between fuels. The images are arranged such that the sprays of the different fuels could be compared at the same crank angle location. Each row displays the spray of a fuel blend. From the figure, it can be

observed that the spray collapse is more pronounced as ethanol content increases. The spray mist is finer and more widely distributed as ethanol content is increased. Given that the injector (tip) temperature was 80° C, and that the boiling point decreases with ethanol increase, it makes sense that the blends containing higher ethanol content evaporate at a faster rate near the tip of the injector. Similar results were observed in [168, 169]. Figure 6.23 shows the background-corrected spray images for the same conditions, except that the mass split between the two injections was changed to 90/10, to be representative of the combusting cases. This imaging setup allowed the small second injection to be visualized. It can be observed that the spray impinges on the walls for all fuels. The lateral penetration (towards the wall) increases with increasing ethanol content, likely due to ethanol's higher viscosity and surface tension. In the first row of images (-175.98 CA ATDC), a fine cloud of fuel can be observed below the spray, which is probably the lighter components in the fuels detaching from the spray and vaporizing. In the next few rows of images, it can be seen that this cloud is progressively less observable with increasing ethanol content, which is due to better evaporation characteristics (low boiling point) of ethanol. Figure 6.24 shows the evolution of the spray of the second injection for various fuels. At this injection timing, both views are available for imaging. From the side view, a general observation can be made that the fuel jet impinges on the piston surface, at the edge of the central bowl on the piston. However, as mentioned above, the jet becomes finer as ethanol content increases. This fuel impingement could potentially have a negative impact on soot emissions. From the bottom view, it can be observed that with increasing ethanol content, the spray jets show a clearer, more defined spray boundary. This is likely related to the higher viscosity and surface tension of ethanol, which both resist 'break-up'. Figure 6.26 shows the background-corrected spray images for the same conditions, except that the mass split between the two injections was changed to 90/10, to be representative of

the combusting cases. Due to the short duration and the small amount of fuel injected, it is relatively hard to obtain a clear spray image for this condition, even after processing the raw image. Figure 6.25 shows an example image of a background-corrected Mie-scattering image of a 2nd injection at 40° BTDC. The spray jets, piston surface and the optical window edges have been marked on this image. From Figure 6.26, it can be observed that the spray impinges on the piston surface for all fuels. The differences in vaporization between fuels are most visible in the 3rd and 4th rows (-36.92 CA ATDC and -35.72 CA ATDC, respectively). It can be seen how a higher ethanol content improves vaporization and dispersion of the fuel spray.

6.3.1.3 Combustion Imaging

In this section, combustion luminosity imaging was performed for the various ethanol-gasoline blends. The test conditions for combustion imaging are shown in Table 6.6. First, combustion imaging was performed using a single injection at 180° BTDC, and a spark timing of 30° BTDC. The intake pressure was 11 psi. Figure 6.27 shows the pressure and HRR curves for the single injection fuel blend sweep. E60 shows the most advanced combustion phasing, followed by E40, E20 and E85. The combustion phasing of E85 was retarded likely due to its higher charge-cooling effect. Figure 6.28 and Figure 6.29 show the evolution of the combustion process for the various fuels, using a camera exposure of 30 µs and 10 µs, respectively. Figure 6.30 and Figure 6.31 show the SINL and TINL for the corresponding exposure times for this test. For the sake of this discussion, the 30 µs images are used. The 10 µs images were acquired in order to have a uniform comparison between single and double injection strategies. The flame front begins near the spark and then rapidly grows outward burning through the relatively premixed air/fuel mixture. The overall flame luminosity decreases with increasing ethanol content. From the SINL data, it can be

observed that peak luminosity (soot formation) decreases with increasing ethanol content; and from the TINL data, it can be concluded that with ethanol content of 40% vol. or higher, significant reduction of soot can be achieved, with the TINL of E40, E60 and E85 being roughly half of that of E20.

Next, the fuel blends were tested using two injections. The results shown here correspond to the spray images shown in the previous section and the metal piston data shown earlier. These combustion images were taken at 11 psi intake pressure and stoichiometric conditions. The first injection was at 180° BTDC and the second injection was at 40° BTDC, with the spark timing being held at 30° BTDC. The mass split between the two injections was 90/10. Figure 6.32 shows the pressure and HRR curves for the double injection fuel blend sweep. Firstly, comparing single injection to double injection, it can be observed that the peak pressure is lower, and combustion phasing is retarded for all fuels. Similar to the corresponding metal piston tests, E60 shows the most advanced combustion phasing, followed by E85, E40 and E20. For the double injection case, a long diffusion-like combustion tail can be observed - the mixing and ignition mechanisms between the hot burned gases and fresh unburned fuel tend to progress from richer to leaner regions and are slowed down as a result of an increase of cylinder volume during the expansion stroke, explaining the asymptotic tail observed. Figure 6.33 shows the evolution of the combustion process for the various fuels with two injections. It can be observed that the combustion process is quite different from that observed for a single injection. Luminous zones exhibiting diffusion-like combustion can be observed along the spray jet axes. This is due to the relatively short gap between the second injection and the spark. However, these luminous spots display a progressively reduced brightness with increasing ethanol content. It should be noted that with increasing ethanol content, the mass of fuel in the second injection increases. In spite of the higher injected mass, mixing is

improved and soot luminosity is reduced. This is due to improved vaporization and mixing due to ethanol's lower boiling point and higher diffusivity [171]; the fuel-borne oxygen in ethanol is also a major reason for this reduced soot. In [174], it was found that at an engine speed of 1000 rpm and stratified condition, the fuel takes about 8 ms, from injection to spark, to evaporate and mix with the air. This time is not enough for the evaporation of the heavy hydrocarbons component of gasoline. For this reason, at the spark time, the combustion chamber is divided in two different zones. One located between the spark plug and the injector which is characterized by a globally rich mixture. In particular the bowl is covered by a liquid film of heavy hydrocarbons fraction. The remaining region of the combustion chamber is affected by a globally lean mixture made off the lighter hydrocarbons fraction. With regard to ethanol, the time between injection and spark is sufficient for the evaporation of a large part of fuel. This leads to a lower gradient of the local AFR with respect to distance to the spark plug due to a lower amount of liquid droplets of fuel, which ultimately reduces soot emissions. The combustion of the relatively premixed charge can also be seen as a uniform glow behind the bright spots, which also is more pronounced with increasing ethanol content, likely due to ethanol's higher diffusivity as mentioned above. Figure 6.34 show the SINL and TINL for this test. From the SINL data, it can be observed that peak luminosity (soot formation) decreases drastically with increasing ethanol content; secondly, the slope of the SINL curves is quite different for the fuels. As ethanol content increases, the soot formation and oxidation rates are found to both decrease. From the TINL data, it can be concluded that the overall soot emissions are reduced when using two injections. This effect is especially pronounced for E60 and E85.

It is important to note that a high degree of swirl was used in this engine. As such, the longer first injection would cause the fuel to be near the periphery of the piston causing the mixture to lean

out in/near the central bowl. It is likely that the second injection helps to enrich the fuel/air mixture and thereby promoting more complete combustion in the overly-lean area very close to the injector tip [171]. From metal engine tests, it was found that the engine-out soot emissions (FSN) was either the same or slightly lower when using two injections, compared to that using a single injection. As far as the soot reduction due to two injections, it can be observed from the SINL curves that the combustion duration is extended due to the slower combustion rate of the diffusion-like combustion of the second injection as well as the combustion rate being slowed down by expansion cooling in the early power stroke. This extended combustion duration provides more time for high-temperature soot oxidation as seen by the slow rate of soot oxidation in the SINL curves, and the relatively extended HRR curves for the double injection case seen in Figure 6.32. It is assumed that the fuel rich cloud still contains incompletely evaporated fuel droplets at later points in time. For the blends tested, these droplets may suffer from poor evaporation at late points in time during injection because of reduced ambient temperature. This is due to high enthalpy of evaporation for ethanol and also heat losses by the cylinder wall [173]. This may be the reason for higher probability of droplet combustion as indicated by the bright spots.

Figure 6.35 shows the evolution of the combustion process for E20 at various equivalence ratios with two injections. Figure 6.36 show the SINL and TINL for this test. Figure 6.37, Figure 6.39 and Figure 6.41 show the evolution of the combustion process for various blends at $\Phi = 0.9$, $\Phi = 0.8$ and $\Phi = 0.7$, respectively. Figure 6.38, Figure 6.40 and Figure 6.42 show the corresponding SINL and TINL curves. Similar to the previous double injection images, it can observed that the second injection combusts with a high luminance, and the combustion of the relatively premixed charge can also be seen as a uniform glow behind the bright spots. However, since the quantity of fuel injected reduces with decreasing equivalence ratio, the duration of the bright luminance is

progressively reduced. Also, as the injection duration is shortened for the second injection (decreasing Φ), the bright spots are limited to the central bowl region. This is likely due to the leaner cases having slightly more time for mixing since the gap between the second injection and spark remains the same for these cases. As observed previously, with increasing ethanol content, soot luminosity decreases progressively. Overall, no major changes in the combustion mechanism are observed as the equivalence ratio is varied. From the SINL curve, it is clear that the rate of soot formation, peak luminance, and soot oxidation rate all become lower with decreasing equivalence ratio. As expected, the TINL is progressively reduced as equivalence ratio is decreased.

These tests demonstrate that using ethanol-gasoline blends in the two-zone piston has the potential to enable low-sooting, stable, and efficient combustion at equivalence ratios up to 0.6.

6.3.2 Injector Comparison – Delphi vs Prototype

6.3.2.1 Spray Visualization and Characterization of injectors

In an attempt to further take advantage of the unique piston profile, a prototype injector was developed by Quantlogic Corporation. The prototype injector features two sets of orifices that are activated based on the injection duration signal. The spray images for the Prototype injector are shown in Figure 6.43 (duration sweep) and Figure 6.44 (injection pressure sweep). The Prototype injector has two sets of holes, one set with six jets spaced 60° apart radially, and a second set spaced 120° apart. It can be seen from the images that the penetration for the set of three jets is longer, and the three jets have a wider cone angle than the six jets. Liquid penetration clearly increases with increasing injection pressure. However, with changing injection duration, the penetration does not change. For comparison with the commercial Delphi injector, Figure 6.45 shows PDA results for the two injectors. Based on the SMD shown, it can be observed that the

Delphi injector shows superior atomization. To further investigate this, the orifice sizes of the two injectors were measured using a digital video micrometer. The Prototype has a total of 9 orifices with an average orifice diameter of 375 µm, and the Delphi has 6 orifices with an average orifice diameter of 175 µm – therefore, the orifice cross sectional area of the Delphi injector is nearly 5 times smaller than that of the Prototype. Based on flow rate calibrations for the injector, it was found that the Prototype has about twice the mass flow rate than that of the Delphi. From Table 6.8, it can be observed that the Prototype has a much shorter injector duration for the same fuel mass injected. Based on the flow rate and the cross sectional area of the orifices, it can be estimated that the Delphi injector would have a velocity twice than that of the Prototype. This increased velocity significantly increases the shear between the liquid spray jets and the quiescent atmosphere, which enhances atomization in the case of the Delphi injector. Comparing Figure 6.13 and Figure 6.43, it can be observed that the Delphi spray shows a relatively larger rate of penetration increase at the same injection pressure and duration. As shown in the following sections, the improved atomization of the Delphi injector significantly enhances combustion overall, and especially at leaner equivalence ratios.

6.3.2.2 Metal piston tests

The injectors were first tested using the metal piston to obtain combustion pressure, stability information in terms of the CoV-IMEP, and various tailpipe emission measurements consisting of UHC, CO, NO_x and soot (FSN). E20 was used as the fuel. For each injector, an equivalence ratio sweep was performed at an intake pressure of 11 psi, and a load sweep was performed by varying the intake pressure from 10 – 12 psi under stoichiometric conditions. For tests with the metal piston, a double injection strategy was used. The first injection was at 180° BTDC. In these test,

90% of the total fuel mass was injected in the first injection. For the second injection, a timing of 40° BTDC was used. The spark timing was fixed at 30° BTDC. It must be noted that since the flow rate for each injector was different, injection duration changed for each injector to maintain the same injected fuel mass. A summary of the test conditions are shown in Table 6.7.

Figure 6.46 shows the cylinder pressure and heat release rate curves comparing the two injectors, at an intake pressure of 11 psi and stoichiometric conditions. It can be observed that the overall shape of the pressure and HRR curves are similar, however, combustion is slightly advanced using the prototype injector. Figure 6.47 shows the cylinder pressure and heat release rate curves for E20, at an intake pressure of 11 psi under different equivalence ratios. It can be observed that peak pressure reduces drastically as equivalence ratio decreases. The $\Phi = 0.8$ case shows deteriorated combustion. It must be noted that when Φ was further decreased to 0.7, the engine misfired. Compared to the pressure traces obtained for the Delphi injector (Figure 6.15), the pressure and rate of combustion are found to be much lower. One factor affecting this is the relatively poor atomization provided by the prototype injector. The spray pattern/impingement also significantly affects the combustion, and this will be discussed later in the spray imaging section.

Figure 6.48 shows the IMEP and indicated efficiency for the equivalence ratio and intake pressure sweeps for the two injectors. The results show that for the same intake pressure and injected fuel mass, the prototype injector shows a lower IMEP and thus, a lower indicated efficiency, with the efficiency being lower by almost 2 percentage points, across the load and equivalence ratio range tested.

Figure 6.49 shows the COV-IMEP for the equivalence ratio and intake pressure sweeps for the two injectors. Based on these results, it can be concluded that the prototype injector displays

similar or slightly better stability relative to the Delphi injector at stoichiometric conditions, however, at leaner conditions ($\Phi = 0.8$), the stability is drastically reduced to unacceptable levels. Figure 6.50 shows the UHC and CO emissions for the equivalence ratio and intake pressure sweeps for the two injectors. It can be observed that the UHC emissions are much higher for the prototype injector and this effect is pronounced at leaner conditions. At an intake pressure of 11 psi and $\Phi = 1$, the prototype injector displays an increase of 500 ppm in UHC emissions relative to the Delphi. However, CO emissions are significantly reduced. Due to a large amount of fuel being impinged on the piston surface and cylinder wall, the UHC emissions are very high for the prototype. This will be discussed in the spray imaging section later. It is likely that this reduces the overall equivalence ratio of the vaporized and mixed combustible mixture which reduces CO emissions. Figure 6.51 shows the NO_x and soot emissions for the equivalence ratio and intake pressure sweeps for the two injectors. In general, NO_x emissions are higher for the prototype injector. The low NO_x value at $\Phi = 0.8$ is due to deteriorated combustion. Soot emissions, on the other hand, are relatively lower for the prototype injector, likely due to the available combustible mixture being lean, as mentioned above.

6.3.2.3 Spray Imaging

In this section, Mie scattering spray imaging was performed for the different injectors. The images shown here correspond to the combustion images shown in the next section taken at 10, 11, and 12 psi intake pressures and stoichiometric conditions. The first injection was at 180° BTDC and the second injection was at 40° BTDC. Although the mass split between the two injections was 90/10 for combustion testing (both metal and optical piston testing), this was changed to 70/30 during spray imaging as the 2nd injection containing 10% of total fuel mass was quite small and

could not be clearly observed. Table 6.8 shows the testing conditions for the spray imaging. Figure 6.52 shows a comparison of background-corrected Mie-scattering images for the two injectors. In these images, the injector is at the center of the top edge. The spray jets move outward on either side towards the side walls. One of the intake valves can also be seen on the top right corner of the image. Figure 6.53 shows the evolution of the spray of the first injection for the Delphi injector and Figure 6.55 shows the same for the Prototype injector. At this injection timing, the bottom view through the piston is blocked by the piston extension, however, the side view images show differences between injectors. The images are arranged such that the sprays of the different injectors could be compared at the same crank angle location. From the side view of the Prototype injector, sprays from both sets of orifices can be observed. The narrow-angle group shows a conical spray structure targeting the center of the piston bowl. The wide-angle group shows impingement on the side window and significant wall wetting. This forms a rather thick fuel film on the combustion chamber walls, which explains the large amount of UHC emissions observed earlier. Figure 6.54 and Figure 6.56 show the corresponding background-corrected spray images for the same conditions, except that the mass split between the two injections was changed to 90/10, to be representative of the combusting cases. It can be observed that the impingement becomes clearer from these images. Specifically, the surface area of impingement on the walls is relatively larger for the Prototype injector.

Figure 6.57 shows the evolution of the spray of the second injection for the Delphi injector and Figure 6.59 shows the same for the Prototype injector. Since the flow rate of the prototype injector is larger, the required duration for the second injection is quite low and can be seen clearly only for 2-3 frames. Figure 6.58 and Figure 6.60 show the corresponding background-corrected spray images for the same conditions, except that the mass split between the two injections was changed

to 90/10, to be representative of the combusting cases. From the side view, it can be observed that the narrow-angle group targets the central bowl region very well. In spite of the short duration, however, the narrow-angle spray causes significant impingement and wall wetting on the piston surface, which as shown in the combustion images next, is detrimental to the low-soot combustion at leaner equivalence ratios.

6.3.2.4 Combustion Imaging

In this section, combustion luminosity imaging was performed for comparing the two injectors. The test conditions for combustion imaging are shown in Table 6.9. First, combustion imaging was performed using a single injection at 180° BTDC, and a spark timing of 30° BTDC. The intake pressure was varied from 10-12 psi. Figure 6.61 and Figure 6.62 show the pressure and HRR curves for the Delphi and Prototype injectors, respectively. Overall, using a single injection, no major differences are observed based on the pressure traces, however, the prototype injector showed slightly advanced combustion phasing. Figure 6.63 and Figure 6.65 show the evolution of the combustion process using a camera exposure time of 30 μs at various intake pressures (Φ =1) for the Delphi and Prototype injectors, respectively. Figure 6.64 and Figure 6.66 show the corresponding SINL and TINL curves. For comparison with the double injection cases shown later, Figure 6.68 and Figure 6.70 show the evolution of the combustion process using a camera exposure time of 10 μs at various intake pressures (Φ =1) for the Delphi and Prototype injectors, respectively; Figure 6.69 and Figure 6.71 show the corresponding SINL and TINL curves. From Figure 6.63, it can be observed that for the Delphi cases, soot formation and oxidation rates increase with increasing load, likely due to the increasing amount of fuel injected with higher load and the increased charge motion at higher intake pressures. The peak luminance also decreases

with decreasing load. From Figure 6.65, it can be observed that there is a remarkable difference between the combustion images and the corresponding SINL, TINL curves of the Delphi and Prototype cases. In the prototype cases, after an initial combustion period observed as a uniform distribution of luminance throughout the combustion chamber, a bright luminous zone is observed in the central bowl which extends from about -2° CAD ATDC to about 50° CAD ATDC (see Figure 6.67). As the piston moves further downwards in the expansion stroke, this luminous zone continues to be observed anchored to the piston surface. This is, in fact, the combustion of the film formed in the bowl region due to wetting from the narrow-angle group of orifices. This is reflected by the second stage of soot formation and oxidation reflected in the SINL curves. As a result, the TINL values for the prototype cases are significantly higher (more than twice) than those observed for the corresponding Delphi cases. Also observed from Figure 6.65, in the -1.23° frame of the 11 psi case, is blow-by of the combusting mixture. This is likely partly due to the significant wall wetting of this region due to the wide-angle group of orifices.

Next, the injectors were tested using two injections. The results shown here correspond to the spray images shown in the previous section and the metal piston data shown earlier. These combustion images were taken at different intake pressure and stoichiometric conditions. The first injection was at 180° BTDC and the second injection was at 40° BTDC, with the spark timing being held at 30° BTDC. The mass split between the two injections was 90/10. Figure 6.72 and Figure 6.73 show the pressure and HRR curves for the Delphi and Prototype injectors, respectively. Overall, using two injections, no major differences are observed based on the pressure traces, however, the prototype injector again showed slightly advanced combustion phasing. Figure 6.74 and Figure 6.76 show the evolution of the combustion process at various intake pressures (Φ =1) for the Delphi and Prototype injectors, respectively. Figure 6.75 and Figure 6.77 show the corresponding SINL

and TINL curves. From Figure 6.74, it can be observed that for the Delphi cases, the peak luminance decreases with decreasing load. The TINL increases steadily with load. As far as the Prototype injector is concerned, at all intake pressures, two SINL peaks can be observed from the curves, one corresponding to the relatively premixed combustion due to the first injection and the second due to the combustion of the film formed in the bowl region due to wetting. Compared to the single injection case, this second peak is much more pronounced for the double injection case due to the second injection, which further exacerbates the wetting issue. The overall combustion duration is extended due to the slower combustion rate of the diffusion-like combustion of the second injection as well as the combustion rate being slowed down by expansion cooling in the early power stroke. This extended combustion duration provides more time for soot oxidation as seen by the slow rate of soot oxidation in the SINL curves. Similar to the Delphi, TINL values increase with load, however, the values are lower than those observed for the Delphi cases. From these tests, it can be concluded that although the Prototype injector has a spray pattern that is suitable for the two-zone piston design, poor atomization and high penetration combine to severely deteriorate lean combustion and soot emissions.

6.4 Conclusions

In this study, a single-cylinder research optical diesel engine was modified into a spark ignition engine in order to investigate the Micro-Jet Enhanced Ignition (MJEI) – Embedded Micro-chamber (EMC) concept for high efficiency lean-burn combustion to address the efficiency and sooting concerns of lean-burn GDI combustion.

Combustion performance and emissions measurements along with optical investigation of the spray and combustion processes of various ethanol-gasoline blends (E20, E40, E60, E85) were performed. The observations can be summarized as follows:

- Addition of ethanol advances combustion phasing due to ethanol's higher flame speed. As a result, the peak combustion pressure is also higher. E60 shows the most advanced combustion phasing.
- E60 shows the highest IMEP under stoichiometric conditions. The indicated efficiency was also highest for E60 across the equivalence ratio range tested.
- The UHC emissions generally decrease with increasing ethanol content – under stoichiometric conditions As far as the CO emissions are concerned, they increase with ethanol content, under stoichiometric conditions. This is likely due to the higher fuel-borne oxygen content as ethanol content is increased.
- NO_x emissions decrease initially with E40 but increase with increasing ethanol content, with E60 and E85 showing values greater than both E20 and E40. Generally, NO_x trends agree with the peak pressure trends. Soot emissions decrease steadily with decreasing equivalence ratio and with increasing ethanol content. The higher fuel-borne oxygen content significantly enhances soot oxidation and reduces tailpipe soot emissions.
- From the spray imaging, it was found that the spray jets become finer as ethanol content increases. The spray jets show a clearer, more defined spray boundary. This is likely related to the higher viscosity and surface tension of ethanol, which both resist 'break-up'.
- The overall flame luminosity decreases with increasing ethanol content. From the SINL data, it can be observed that peak luminosity (soot formation) decreases with increasing

ethanol content; and from the TINL data, it can be concluded that with ethanol content of 40% vol. or higher, significant reduction of soot can be achieved.

- When a double injection strategy is used, the combustion duration is extended due to the slower combustion rate of the diffusion-like combustion of the second injection as well as the combustion rate being slowed down by expansion cooling in the early power stroke. This extended combustion duration provides more time for soot oxidation as seen by the slow rate of soot oxidation in the SINL curves.
- These tests demonstrate that using ethanol-gasoline blends with the two-zone piston has the potential to enable low-sooting, stable, and efficient combustion at equivalence ratios up to 0.6.

Combustion performance and emissions measurements along with optical investigation of the spray and combustion process comparing the commercial and prototype injectors were also performed. The following observations were made:

- The Prototype injector has two sets of holes, one set with six jets spaced 60° apart radially (narrow-angle group), and a second set spaced 120° apart (wide-angle group). Based on the SMD data obtained from PDA experiments, it can be observed that the Delphi injector shows superior atomization.
- For the same intake pressure and injected fuel mass, the prototype injector shows a lower IMEP and thus, a lower indicated efficiency, with the efficiency being lower by almost 2 percentage points, across the load and equivalence ratio range tested.
- Similar or slightly better stability relative to the Delphi injector at stoichiometric conditions, however, at leaner conditions ($\Phi = 0.8$), the stability is drastically reduced to unacceptable levels.

- The wide-angle group shows impingement on the side window and significant wall-wetting. This forms a rather thick fuel film on the combustion chamber walls; the narrow-angle spray causes significant impingement and wall wetting on the piston surface, which causes a large amount of UHC emissions. Due to a large portion of the fuel being lost as UHC emissions, the available combustible mixture is leaned out, causing low CO, high NO_x and low soot emissions, relative to the Delphi injector.
- It was found that there is a remarkable difference between the combustion processes using the two injectors. In the prototype cases, after an initial combustion period observed as a uniform distribution of luminance throughout the combustion chamber, combustion of the film formed in the bowl region due to wetting from the narrow-angle group of orifices is observed. This is reflected by the second stage of soot formation and oxidation reflected in the SINL curves. As a result, the TINL values for the prototype cases (single injection) are significantly higher (more than twice) than those observed for the corresponding Delphi cases.
- Compared to the single injection case, the second peak on the SINL curve is much more pronounced for the double injection case due to the second injection, which further exacerbates the wetting issue.
- In the future, it is expected that combustion performance and emissions characteristics could be significantly improved by tuning the prototype injector to have better atomization and shorter jet penetration.

Table 6.1 Ford DIATA Research Engine Specifications

Number of Valves per Cylinder	4
Original Compression Ratio	19.5:1
Modified Compression Ratio	16:1
Bore	70 mm
Stroke	78 mm
Displacement Volume	0.3 L
Swirl Ratio	2.5 (low); 4.0 (high)
Intake Valve Diameter	24 mm
Exhaust Valve Diameter	21 mm
Maximum Valve Lift	7.30/7.67 mm (Intake/Exhaust)
Valve Timings : IVO	13 CAD ATDC (at 1 mm valve lift)
IVC	20 CAD ABDC (at 1 mm valve lift)
EVO	33 CAD BBDC (at 1 mm valve lift)
EVC	18 CAD BTDC (at 1 mm valve lift)

Table 6.2 Ford DIATA Operating Conditions

Engine speed	1200 rpm
Inlet air temperature	25 °C
Exhaust gas pressure	1.5 bar
Oil temperature	70 °C
Coolant temperature	80 °C
Fuel injection pressure	200 bar

Table 6.3 Properties of ethanol and gasoline

Parameter	Gasoline	Ethanol
Chemical Formula	C_4-C_{12}	C_2H_5OH
Composition (C,H,O) (Mass %)	86, 14, 0	52, 13, 35
Lower Heating Value (MJ/kg)	43.4	26.8
Density (kg/m^3)	715-765	790
Energy Density (MJ/l)	32.20	21.17
Octane Number ((R+M)/2)	90	100
Boiling Temperature (°C)	25-215	78
Latent Heat of Vaporization (25°C) (kJ/kg)	380-500	904
Self-Ignition Temperature (°C)	~300	420
Stoichiometric Air/Fuel Ratio (by weight)	14.7	9.0
Laminar Flame Speed (LFS) (cm/s)	~33[a]	~39[a]
Mixture Calorific Value (MJ/m^3)	3.72	3.85
Ignition Limits in Air (vol. %) [Lower-Upper]	0.6 - 8	3.5 - 15
Solubility in Water at 20°C (ml/100 ml H_2O)	<0.1	Fully Miscible
Kinematic viscosity (mm^2 /s @ 20° C)[b]	0.84	1.57
Surface tension (N/m @ 20° C) [b]	0.024	0.027
[a] p = 1 atm, T = 325 K [44]; [b] [170]		

Table 6.4 Ethanol-Gasoline Blends Metal Piston Operating Conditions

Inj.1 @ 180° BTDC (90%), Inj. 2 @ 40° BTDC (10%), Spark@ 30° BTDC							
Fuel	Intake Pressure (psi)	Φ	Total Injection Mass (mg)	Injection Mass 1 (mg)	Injection Mass 2 (mg)	Injection Duration 1 (ms)	Injection Duration 2 (ms)
E20	12	1	15.449	13.904	1.545	1.548	0.479
E20	10	1	12.016	10.814	1.202	1.390	0.405
E20	11	1	14.590	13.131	1.459	1.507	0.461
E20	11	0.9	13.131	11.818	1.313	1.440	0.430
E20	11	0.8	11.672	10.505	1.167	1.374	0.398
E20	11	0.7	10.213	9.192	1.021	1.306	0.365
E20	11	0.6	8.754	7.879	0.875	1.230	0.331
E40	12	1	16.932	15.239	1.693	1.624	0.509
E40	10	1	14.580	13.122	1.458	1.506	0.461
E40	11	1	15.992	14.393	1.599	1.575	0.490
E40	11	0.9	14.392	12.953	1.439	1.497	0.457
E40	11	0.8	12.793	11.514	1.279	1.425	0.422
E40	11	0.7	11.194	10.075	1.119	1.353	0.387
E40	11	0.6	9.595	8.636	0.960	1.275	0.351
E60	12	1	18.660	16.794	1.866	1.719	0.544
E60	10	1	16.060	14.454	1.606	1.579	0.492
E60	11	1	17.6226	15.860	1.762	1.661	0.523
E60	11	0.9	15.8603	14.274	1.586	1.568	0.487
E60	11	0.8	14.0981	12.688	1.410	1.484	0.451
E60	11	0.7	12.3358	11.102	1.234	1.404	0.412
E60	11	0.6	10.5735	9.516	1.057	1.324	0.373
E85	12	1	21.260	19.134	2.126	1.874	0.593
E85	10	1	18.300	16.470	1.830	1.699	0.536
E85	11	1	20.0798	18.072	2.008	1.803	0.571
E85	11	0.9	18.0719	16.265	1.807	1.686	0.532
E85	11	0.8	16.0639	14.457	1.606	1.579	0.492
E85	11	0.7	14.0559	12.650	1.406	1.482	0.450
E85	11	0.6	12.0479	10.843	1.205	1.391	0.406

Table 6.5 Ethanol-Gasoline Blends Spray Imaging Test Conditions

Inj.1 @ 180° BTDC, Inj. 2 @ 40° BTDC, Intake pr. = 11 psi, Φ = 1						
Fuel	First Injection Ratio	Total Injection Mass (mg)	Injection Mass 1 (mg)	Injection Mass 2 (mg)	Injection Duration 1 (ms)	Injection Duration 2 (ms)
E20	70%	14.590	10.213	4.377	1.360	0.929
E40	70%	15.992	11.194	4.798	1.409	0.976
E60	70%	17.623	12.336	5.287	1.466	1.027
E85	70%	20.080	14.056	6.024	1.556	1.095

Table 6.6 Ethanol-Gasoline Blends Combustion Imaging Test Conditions

Inj.1 @ 180° BTDC, Inj. 2 @ 40° BTDC, Intake pr. = 11 psi, Spark @ 30° BTDC							
Fuel	Φ	First Injection Ratio	Total Injection Mass (mg)	Injection Mass 1 (mg)	Injection Mass 2 (mg)	Injection Duration 1 (ms)	Injection Duration 2 (ms)
Ethanol Sweep (Single Injection)							
E20	1	100%	14.590	14.590	N/A	1.586	0.000
E40	1	100%	15.992	15.992	N/A	1.669	0.000
E60	1	100%	17.623	17.623	N/A	1.773	0.000
E85	1	100%	20.080	20.080	N/A	1.936	0.000
Ethanol Sweep (Double Injection)							
E20	1	90%	14.590	13.131	1.459	1.507	0.461
E40	1	90%	15.992	14.393	1.599	1.575	0.490
E60	1	90%	17.623	15.860	1.762	1.661	0.523
E85	1	90%	20.080	18.072	2.008	1.803	0.571
Equivalence Ratio Sweep							
E20	1	90%	14.590	13.131	1.459	1.507	0.461
E20	0.9	90%	13.131	11.818	1.313	1.440	0.430
E20	0.8	90%	11.672	10.505	1.167	1.374	0.398
E20	0.7	90%	10.213	9.192	1.021	1.306	0.365

Table 6.7 Injector Comparison Metal Piston Operating Conditions

Inj.1 @ 180° BTDC (90%), Inj. 2 @ 40° BTDC (10%), Fuel: E20, Spark @ 30° BTDC							
Injector	Intake Pressure (psi)	Φ	Total Injection Mass (mg)	Injection Mass 1 (mg)	Injection Mass 2 (mg)	Injection Duration 1 (ms)	Injection Duration 2 (ms)
Delphi	12	1	15.449	13.904	1.545	1.548	0.479
Delphi	10	1	12.016	10.814	1.202	1.390	0.405
Delphi	11	1	14.590	13.131	1.459	1.507	0.461
Delphi	11	0.9	13.131	11.818	1.313	1.440	0.430
Delphi	11	0.8	11.672	10.505	1.167	1.374	0.398
Prototype	12	1	15.449	13.904	1.545	1.102	0.154
Prototype	10	1	12.016	10.814	1.202	0.865	0.128
Prototype	11	1	14.590	13.131	1.459	1.043	0.148
Prototype	11	0.9	13.131	11.818	1.313	0.942	0.137
Prototype	11	0.8	11.672	10.505	1.167	0.841	0.125

Table 6.8 Injector Comparison Spray Imaging Test Conditions

Inj.1 @ 180° BTDC, Inj. 2 @ 40° BTDC, Fuel: E20, Φ = 1							
Injector	Intake pressure (psi)	First Injection Ratio	Total Injection Mass (mg)	Injection Mass 1 (mg)	Injection Mass 2 (mg)	Injection Duration 1 (ms)	Injection Duration 2 (ms)
Delphi	12	70%	15.449	10.814	4.635	1.390	0.958
Delphi	11	70%	14.590	10.213	4.377	1.360	0.929
Delphi	10	70%	12.016	8.411	3.605	1.262	0.830
Prototype	12	70%	15.449	10.814	4.635	0.865	0.391
Prototype	11	70%	14.590	10.213	4.377	0.819	0.372
Prototype	10	70%	12.016	8.411	3.605	0.681	0.312

Table 6.9 Injector Comparison Combustion Imaging Test Conditions

Inj.1 @ 180° BTDC, Inj. 2 @ 40° BTDC, Fuel: E20, Φ = 1, Spark @ 30° BTDC							
Injector	Intake Pressure (psi)	First Injection Ratio	Total Injection Mass (mg)	Injection Mass 1 (mg)	Injection Mass 2 (mg)	Injection Duration 1 (ms)	Injection Duration 2 (ms)
Delphi Load Sweep (Single Injection)							
Delphi	10	100%	12.016	12.016	N/A	1.450	0.000
Delphi	11	100%	14.590	14.590	N/A	1.586	0.000
Delphi	12	100%	15.449	15.449	N/A	1.636	0.000
Delphi Load Sweep (Double Injection)							
Delphi	10	90%	12.016	10.814	1.202	1.390	0.405
Delphi	11	90%	14.590	13.131	1.459	1.507	0.461
Delphi	12	90%	15.449	13.904	1.545	1.548	0.479
Prototype Load Sweep (Single Injection)							
Prototype	10	100%	12.016	12.016	N/A	0.957	0.000
Prototype	11	100%	14.590	14.590	N/A	1.155	0.000
Prototype	12	100%	15.449	15.449	N/A	1.220	0.000
Prototype Load Sweep (Double Injection)							
Prototype	10	90%	12.016	10.814	1.202	0.865	0.128
Prototype	11	90%	14.590	13.131	1.459	1.043	0.148
Prototype	12	90%	15.449	13.904	1.545	1.102	0.154

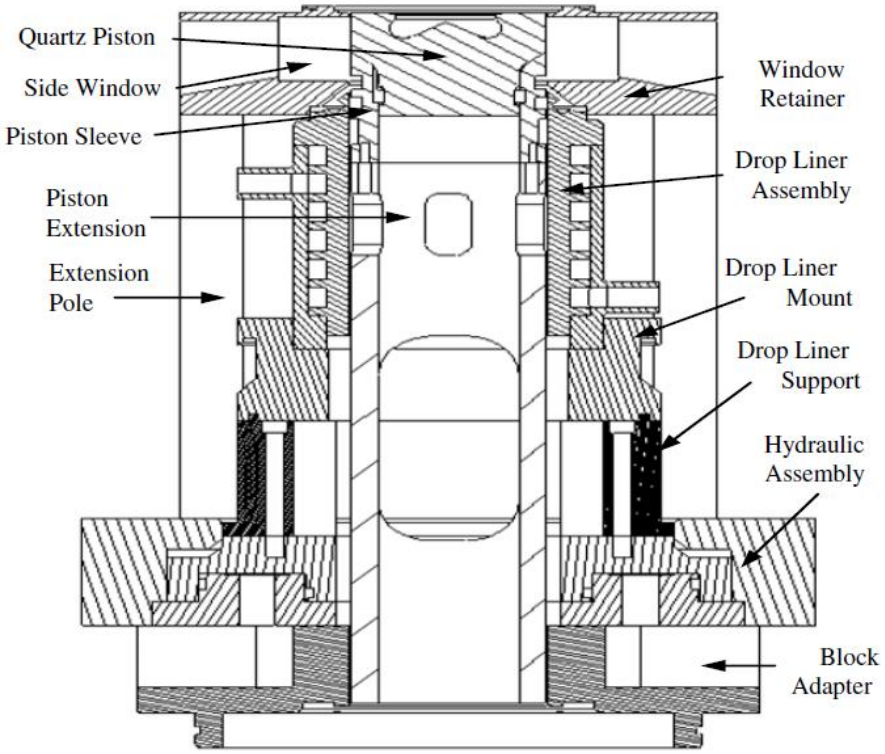

Figure 6.1 Engine Assembly Cross-section of the DIATA optical engine [164]

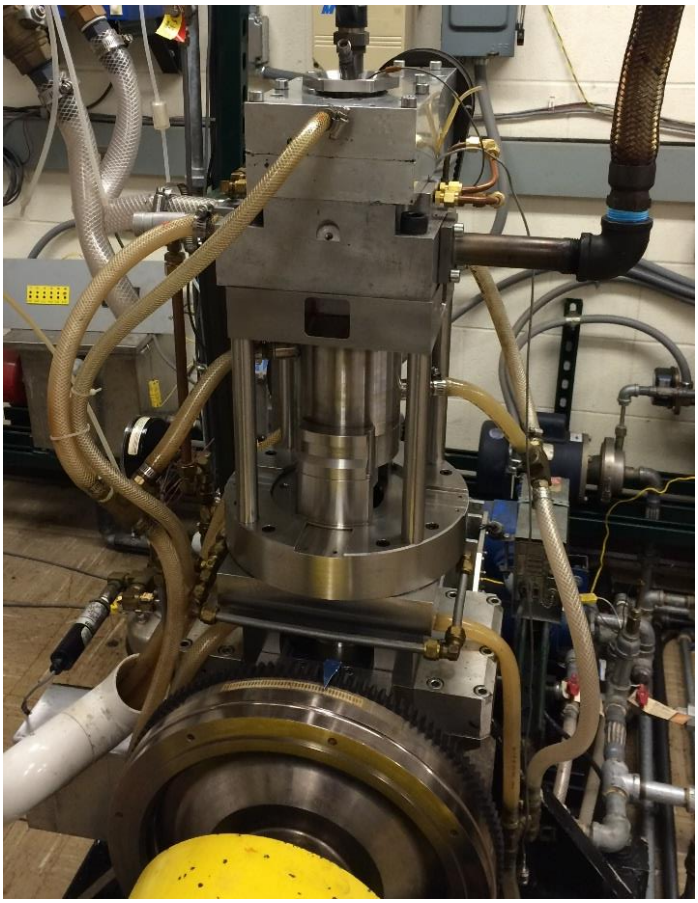

Figure 6.2 Optical engine

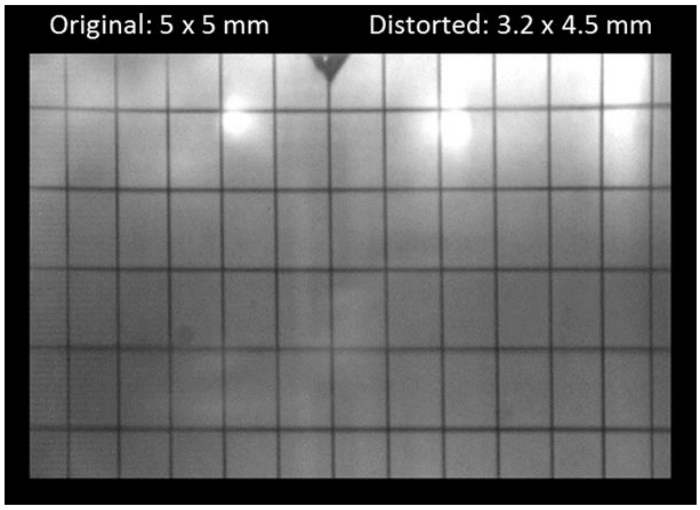

Figure 6.3 Optical distortion estimation - side view

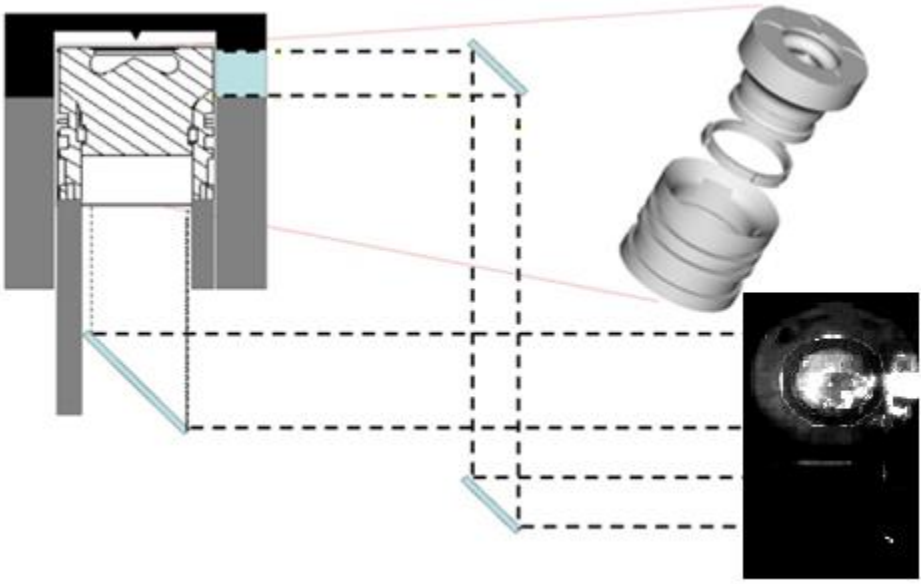

Figure 6.4 Setup of laser/camera/mirrors for combustion imaging

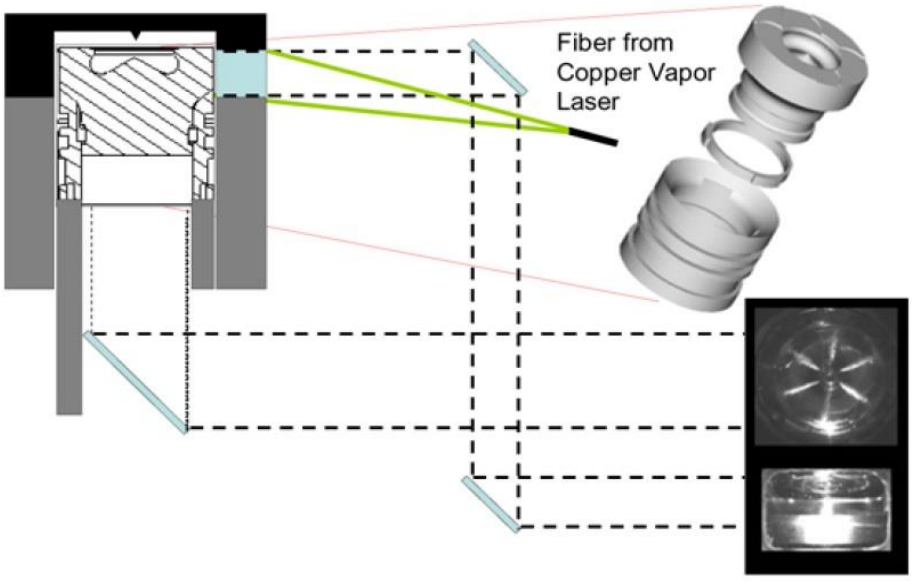

Figure 6.5 Setup of laser/camera/mirrors for 3D-like spray imaging

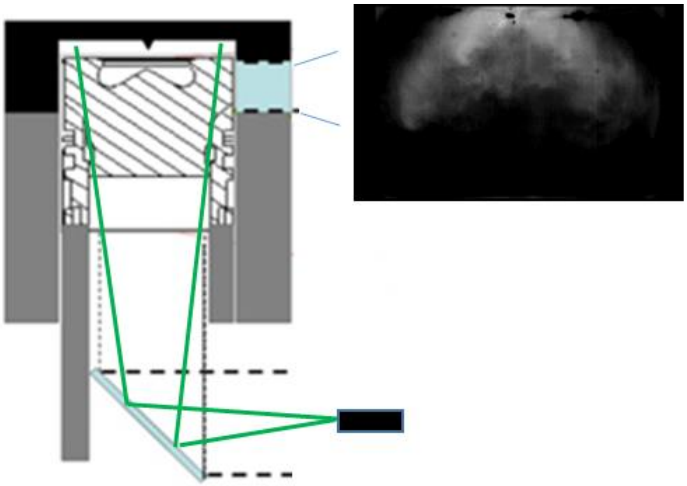

Figure 6.6 Setup of laser/camera/mirrors for background-corrected spray imaging

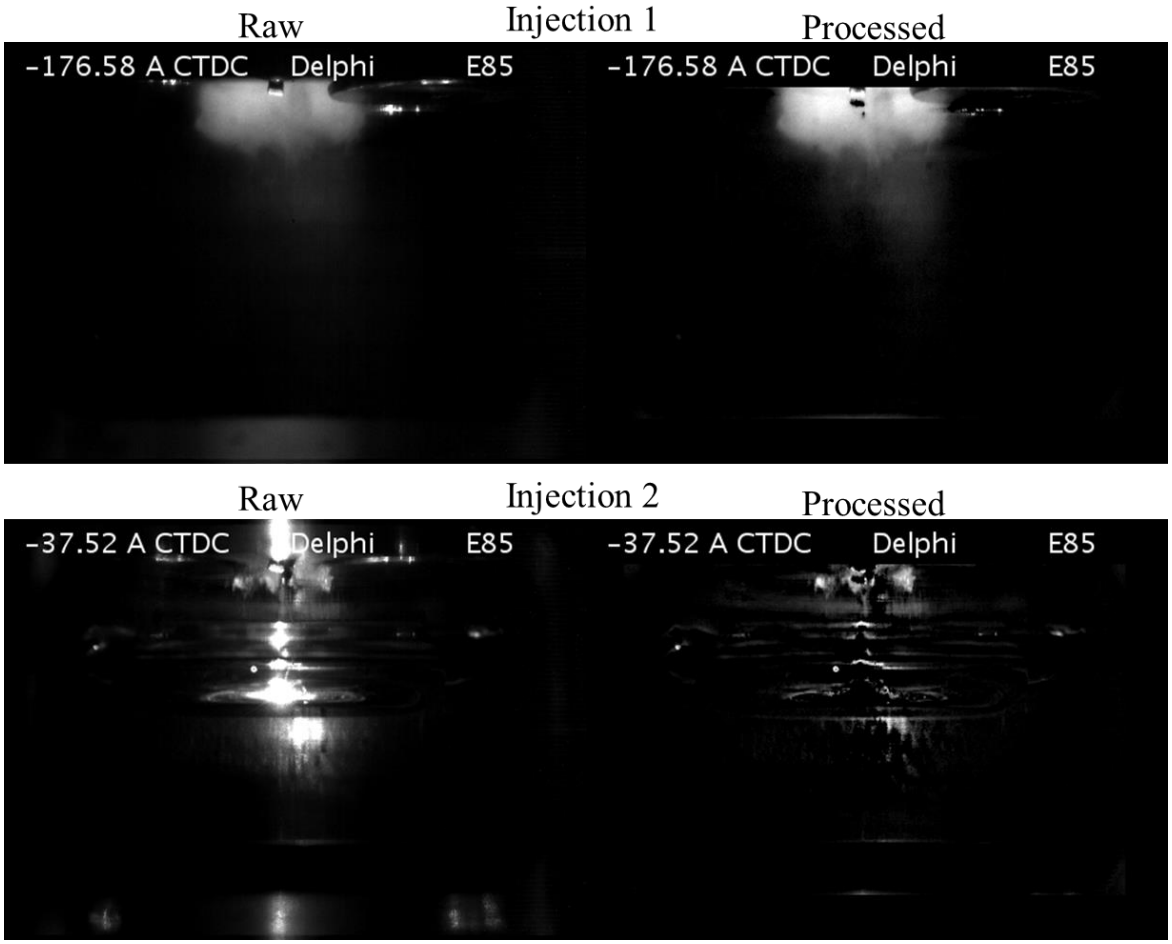

Figure 6.7 Comparison of raw and processed images

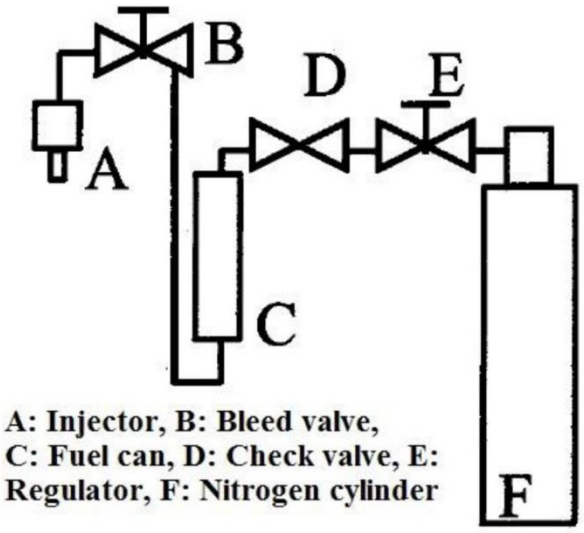

Figure 6.8 Schematic of Fuel Delivery System

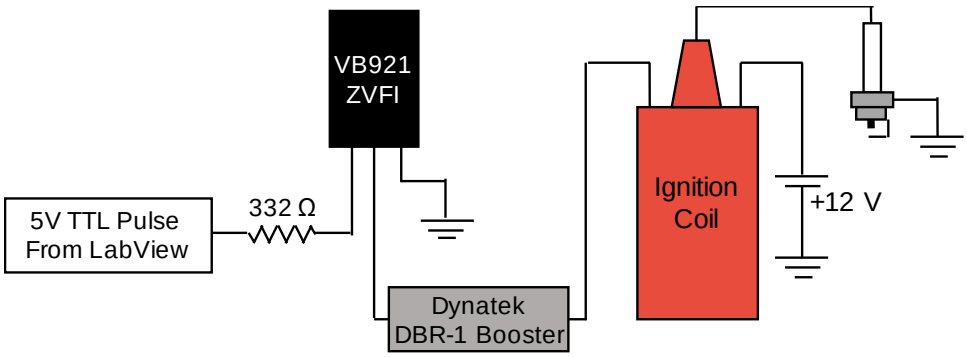

Figure 6.9 Ignition circuit, using Dynatek DBR-1 spark booster

Figure 6.10 Spark plug installed in cylinder head

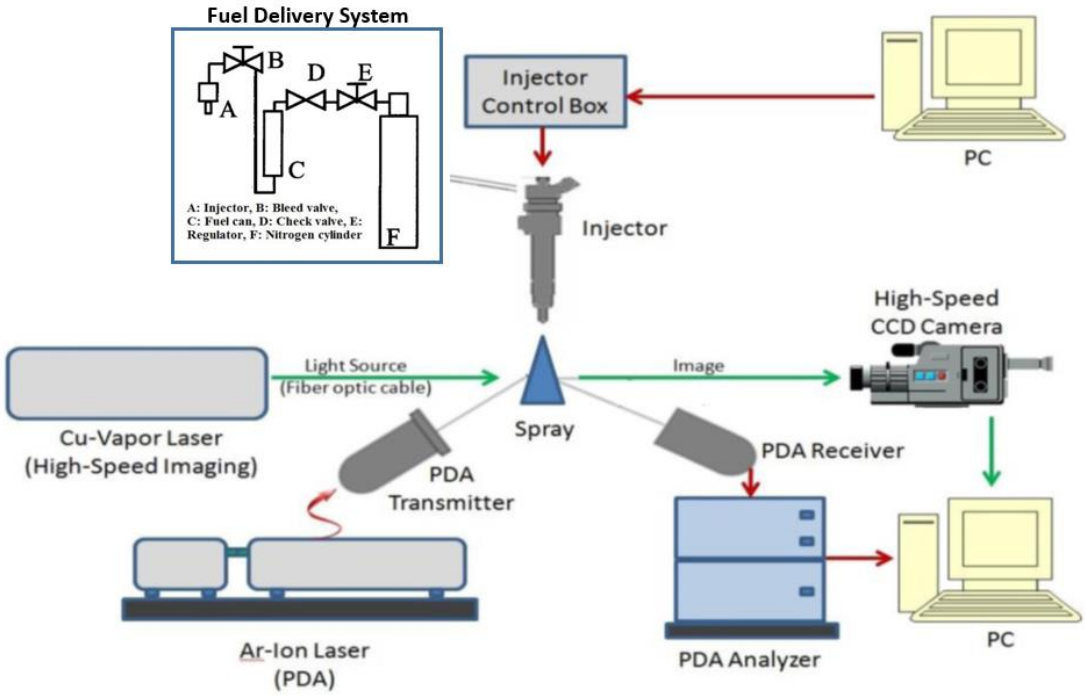

Figure 6.11 Schematic of the Imaging and PDA Setup for Spray Characterization

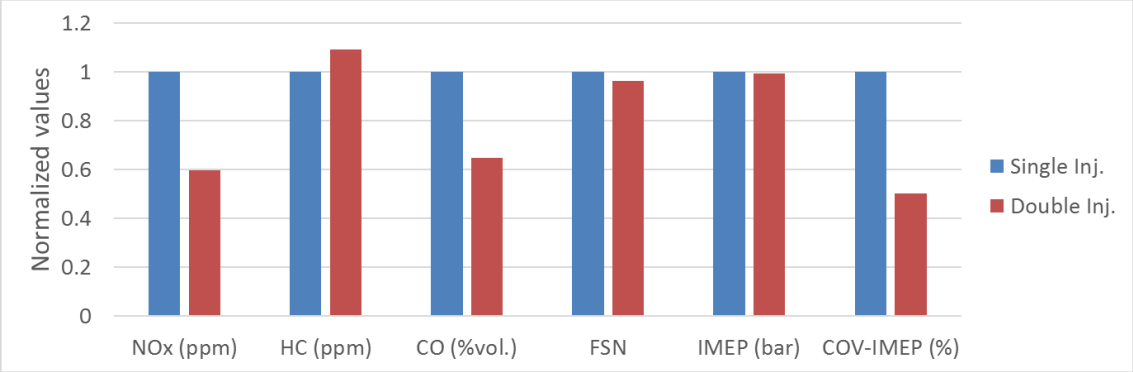

Figure 6.12 Single vs Double Inj. comparison

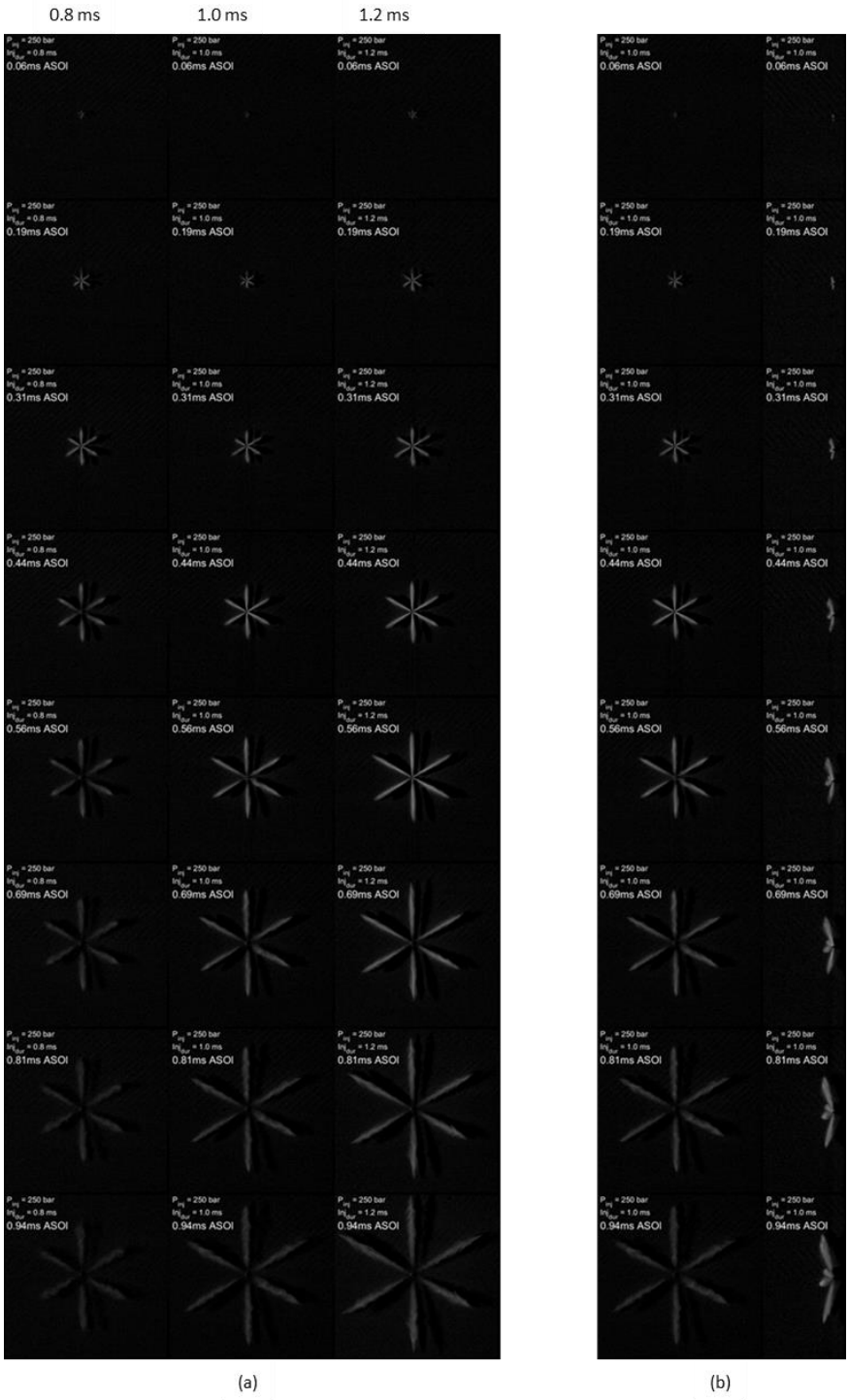

Figure 6.13 Delphi injector spray evolution for (a) 0.8, 1.0, and 1.2 ms injection duration and (b) front and side view for 1.0 ms duration at 250 bar

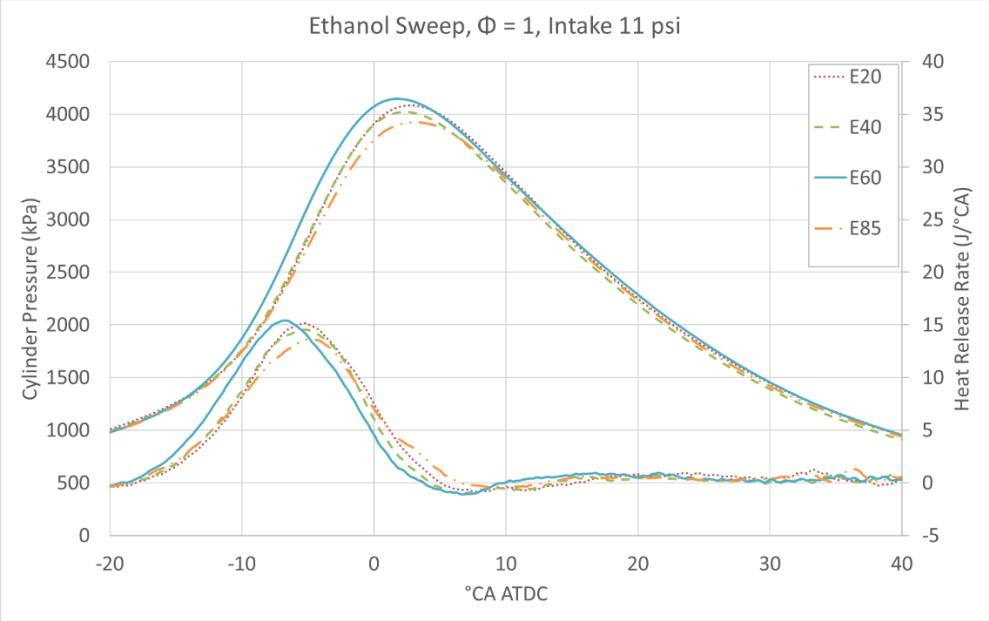

Figure 6.14 Pressure and HRR curves for various fuels at Φ=1

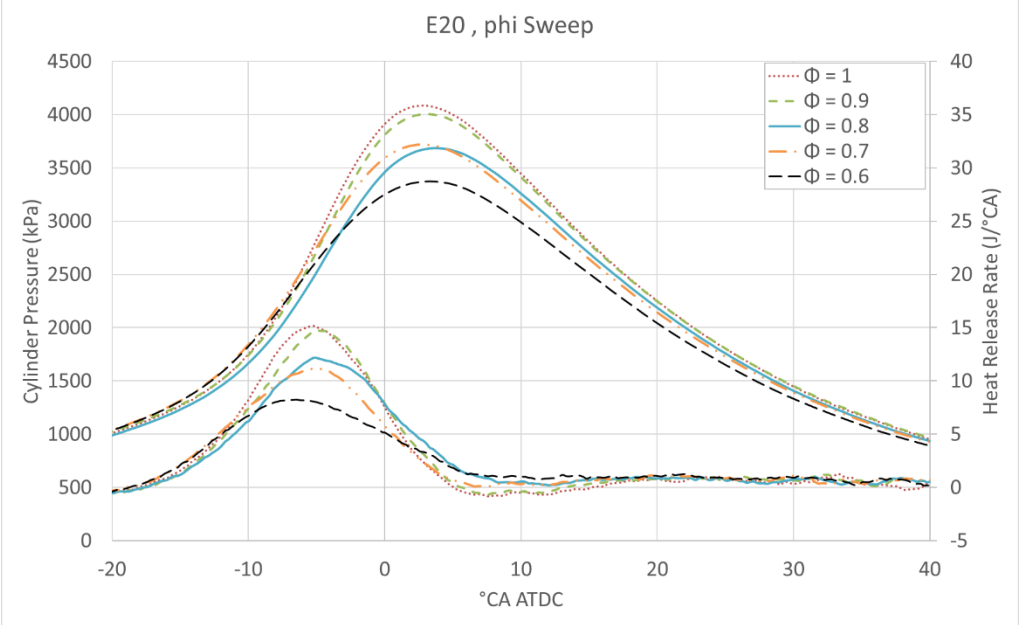

Figure 6.15 Pressure and HRR curves for E20 at various equivalence ratios

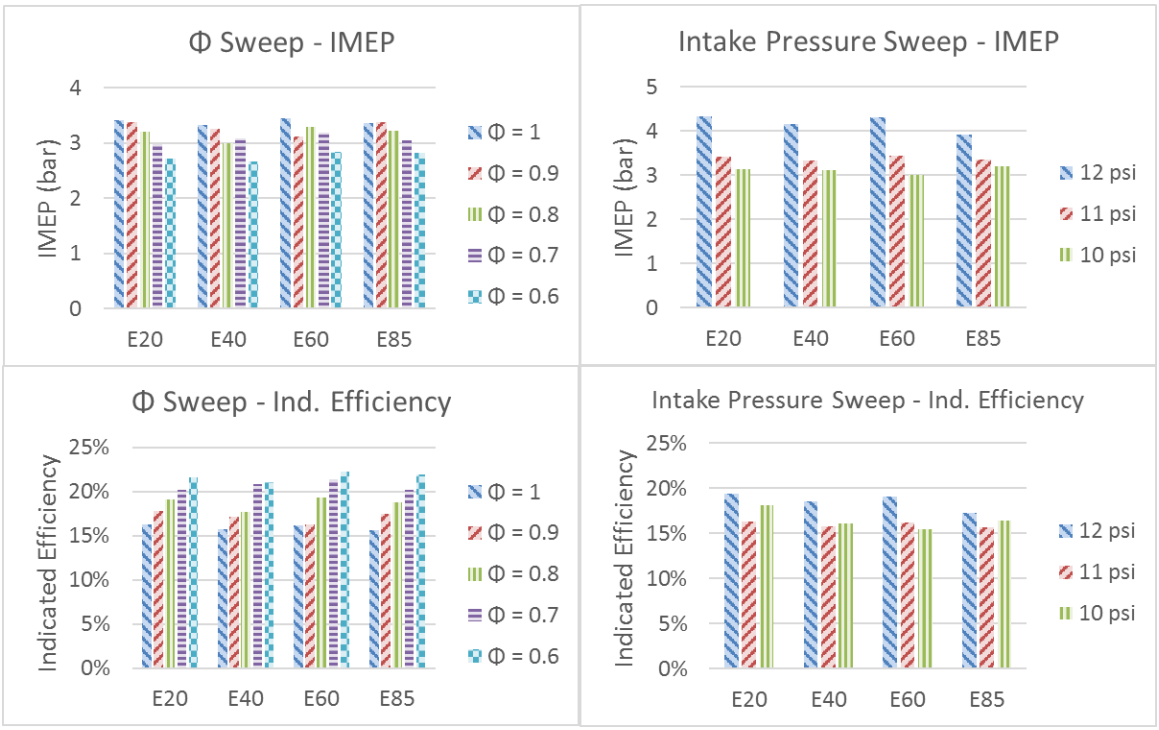

Figure 6.16 IMEP and Indicated efficiency of fuel blends

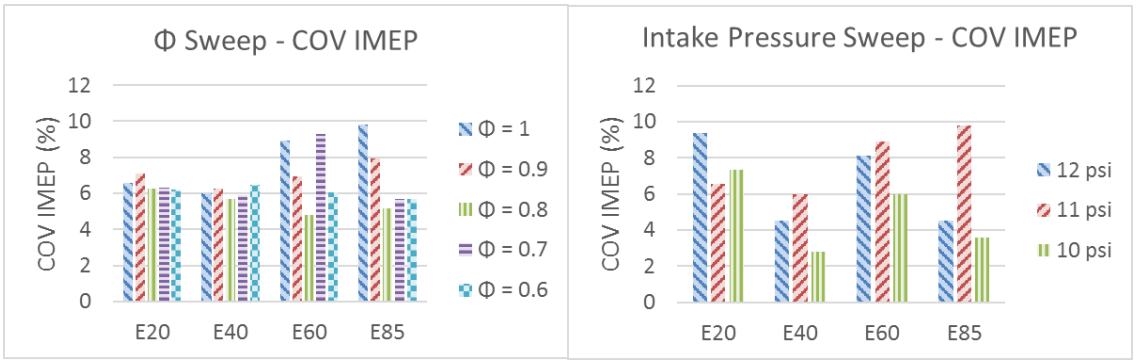

Figure 6.17 COV-IMEP of fuel blends

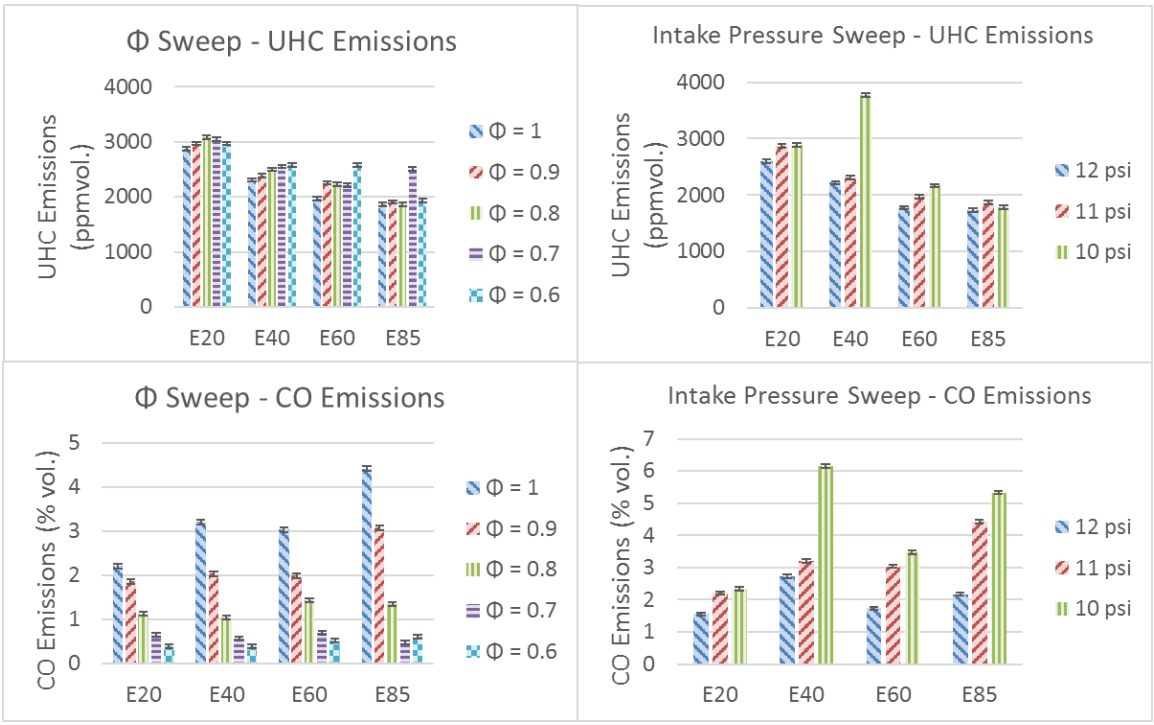

Figure 6.18 UHC, CO emissions of fuel blends

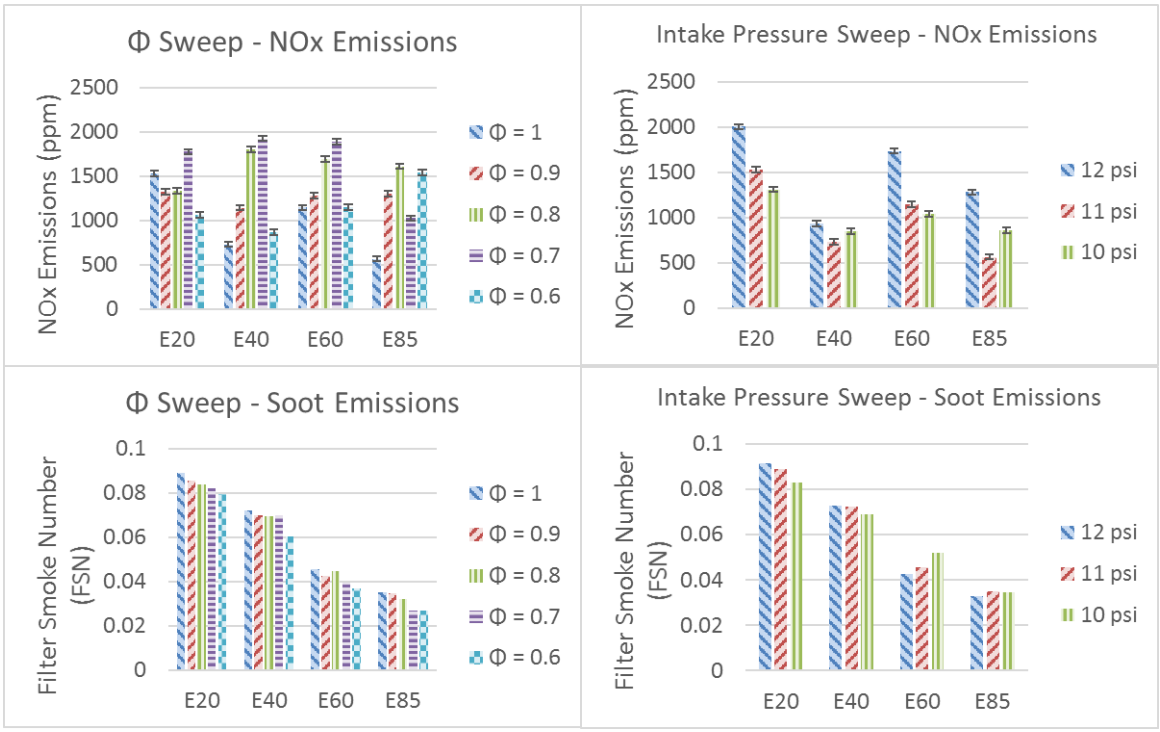

Figure 6.19 NO_x, Soot emissions of fuel blends

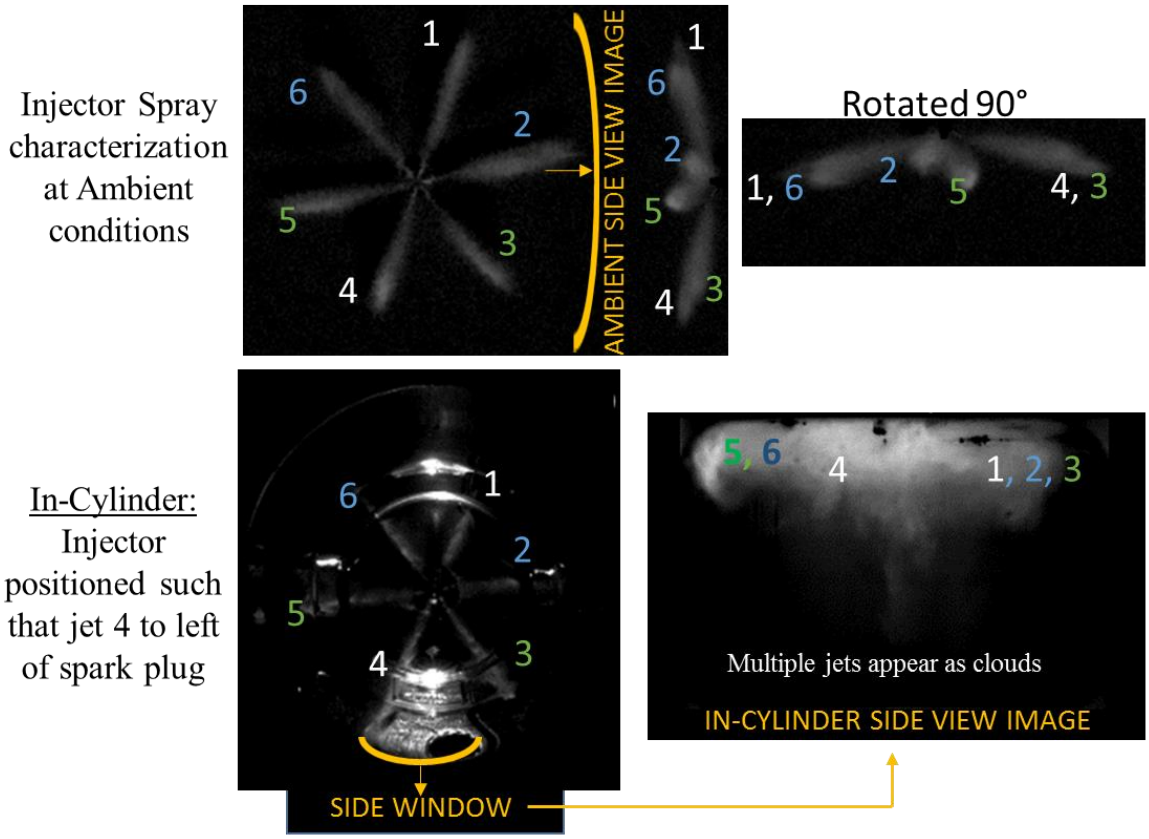

Figure 6.20 Injector orientation and spray visualization

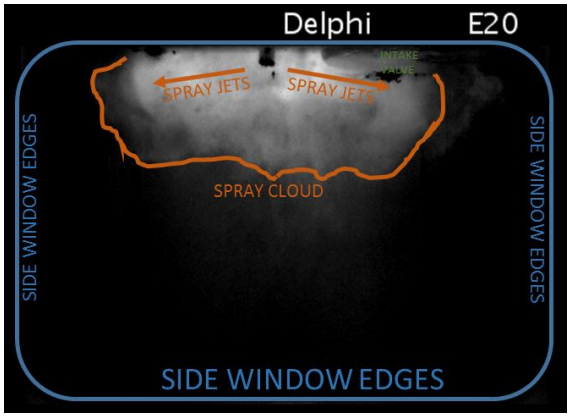

Figure 6.21 Background-corrected Mie-scattering image example of 1st injection at 180° BTDC

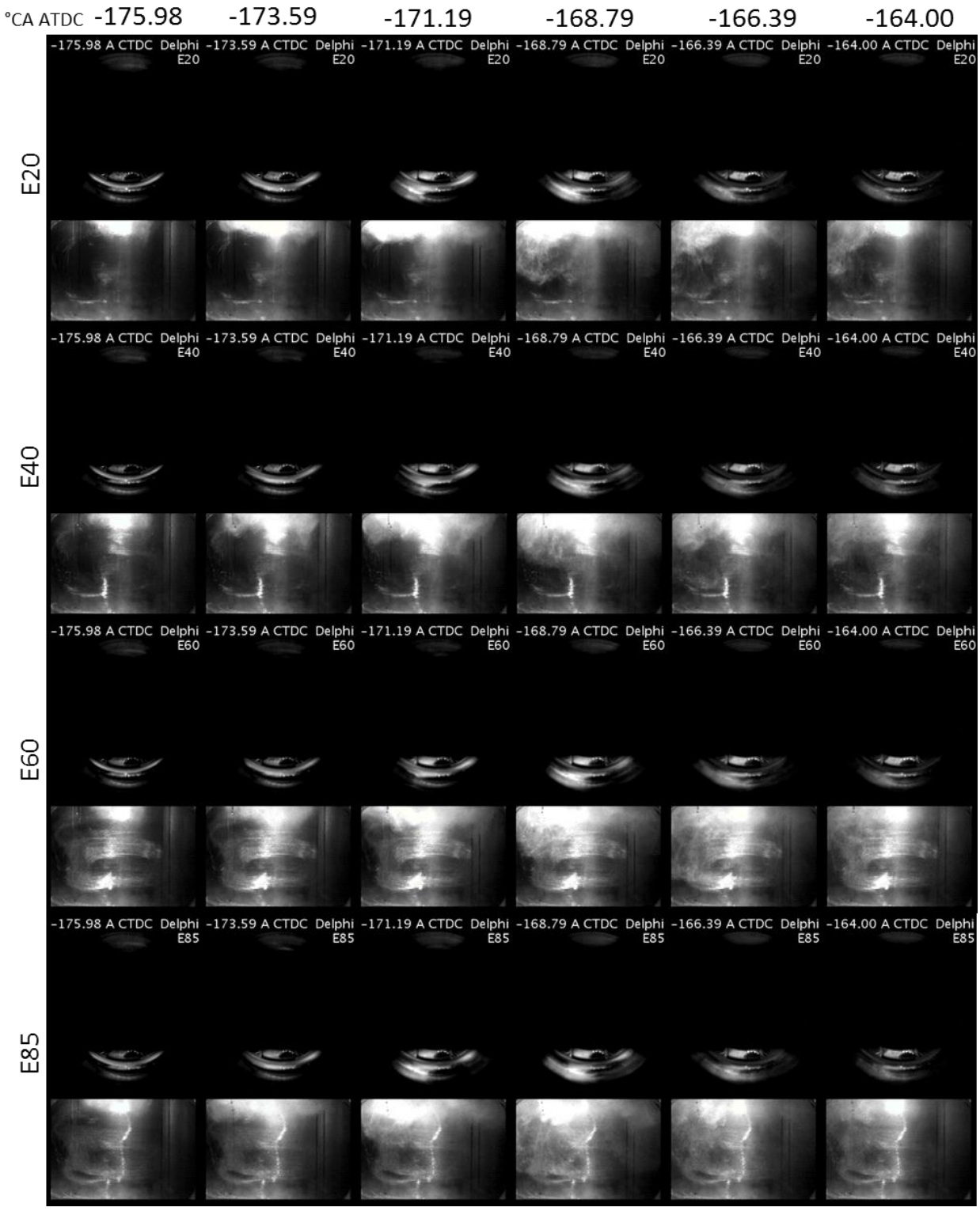

Figure 6.22 Mie-scattering spray images of fuel blends – Injection 1 at 180° BTDC

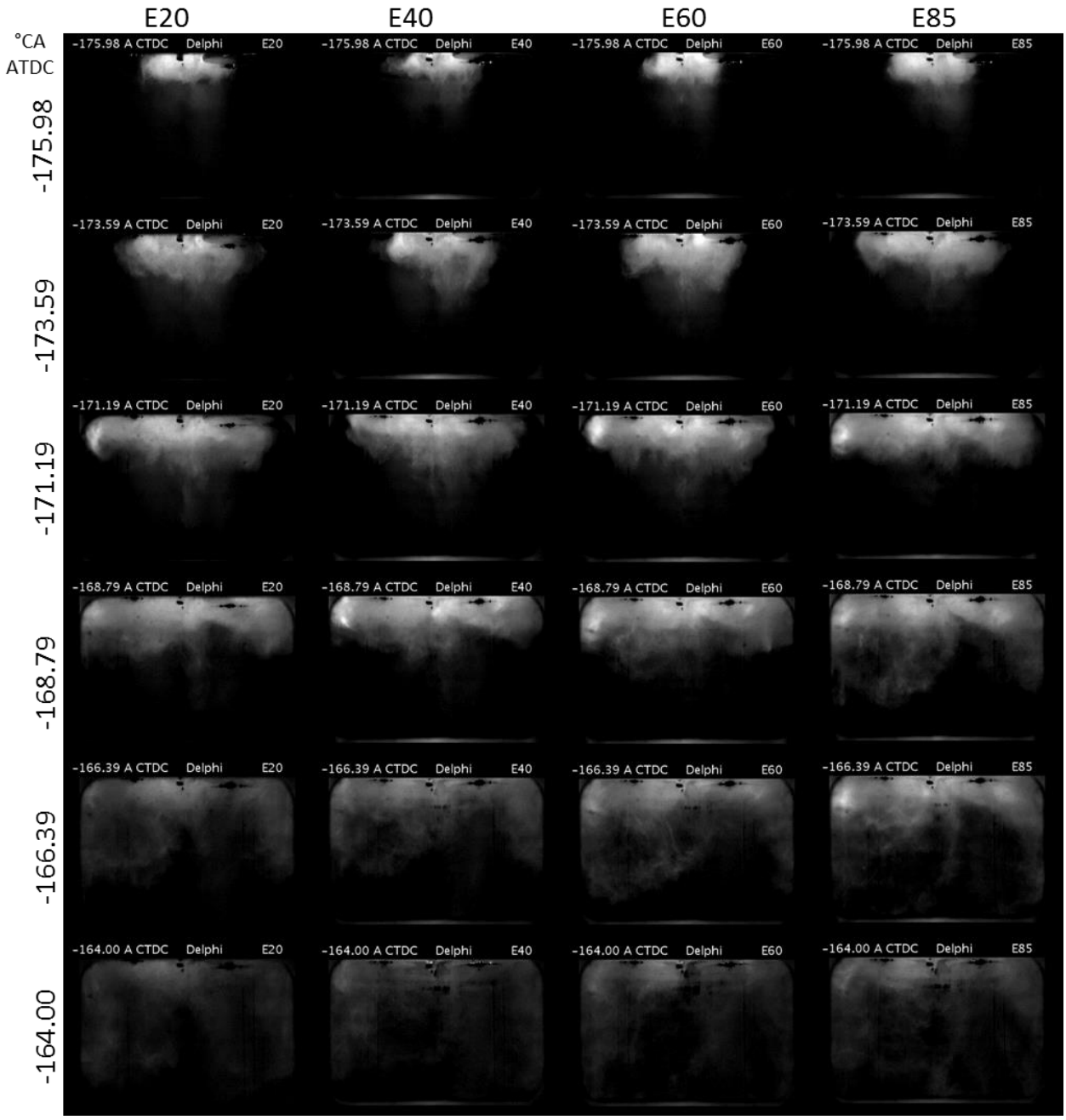

Figure 6.23 Background-corrected Mie-scattering spray images of fuel blends – Injection 1 at 180° BTDC

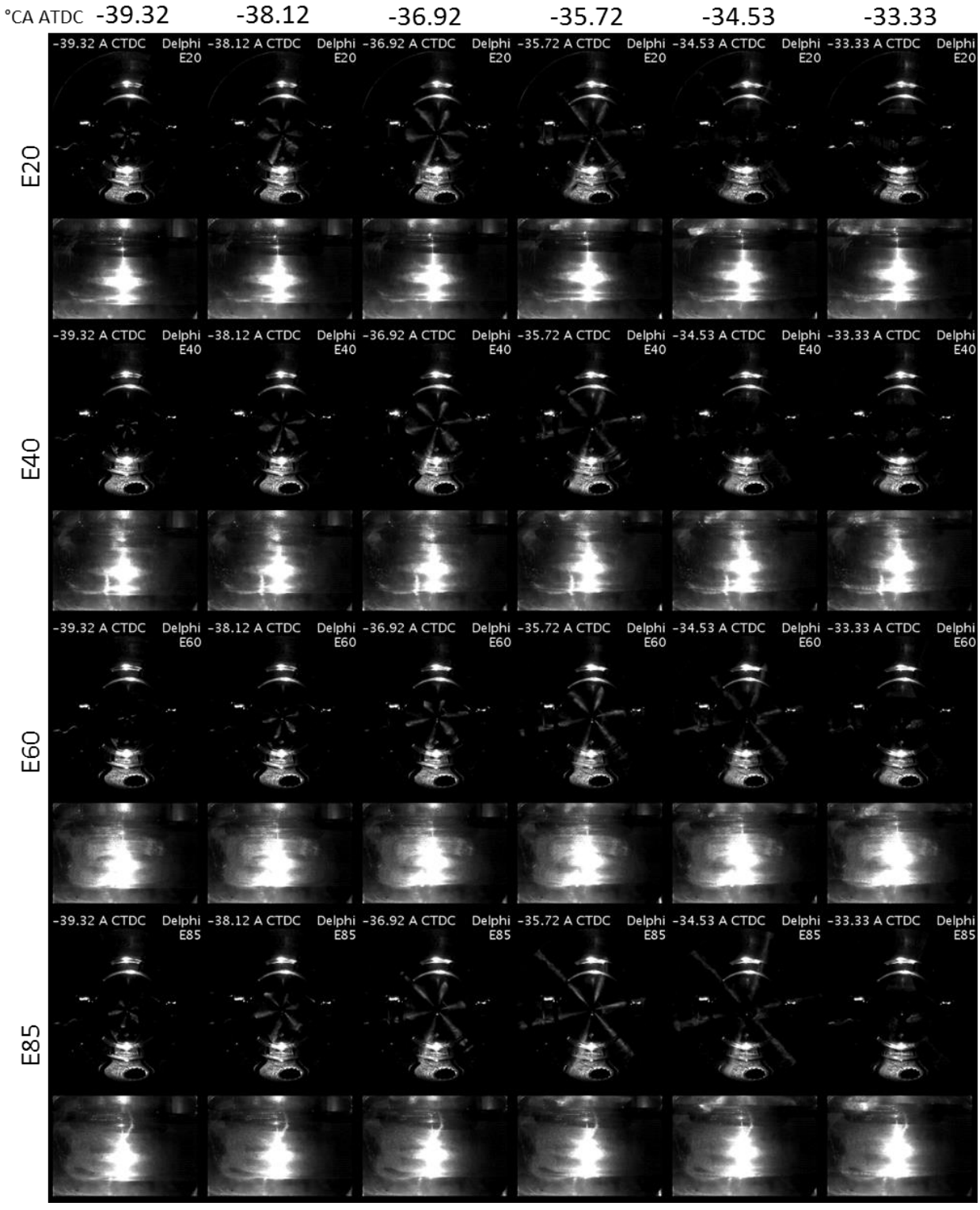

Figure 6.24 Mie-scattering spray images of fuel blends – Injection 2 at 40° BTDC

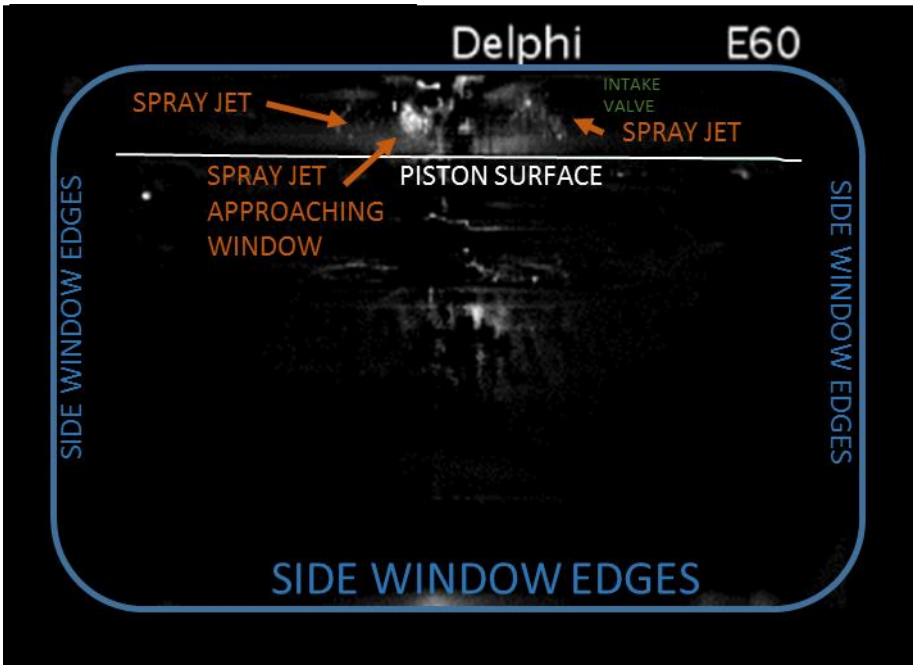

Figure 6.25 Background-corrected Mie-scattering spray image example of 2nd injection at 40° BTDC

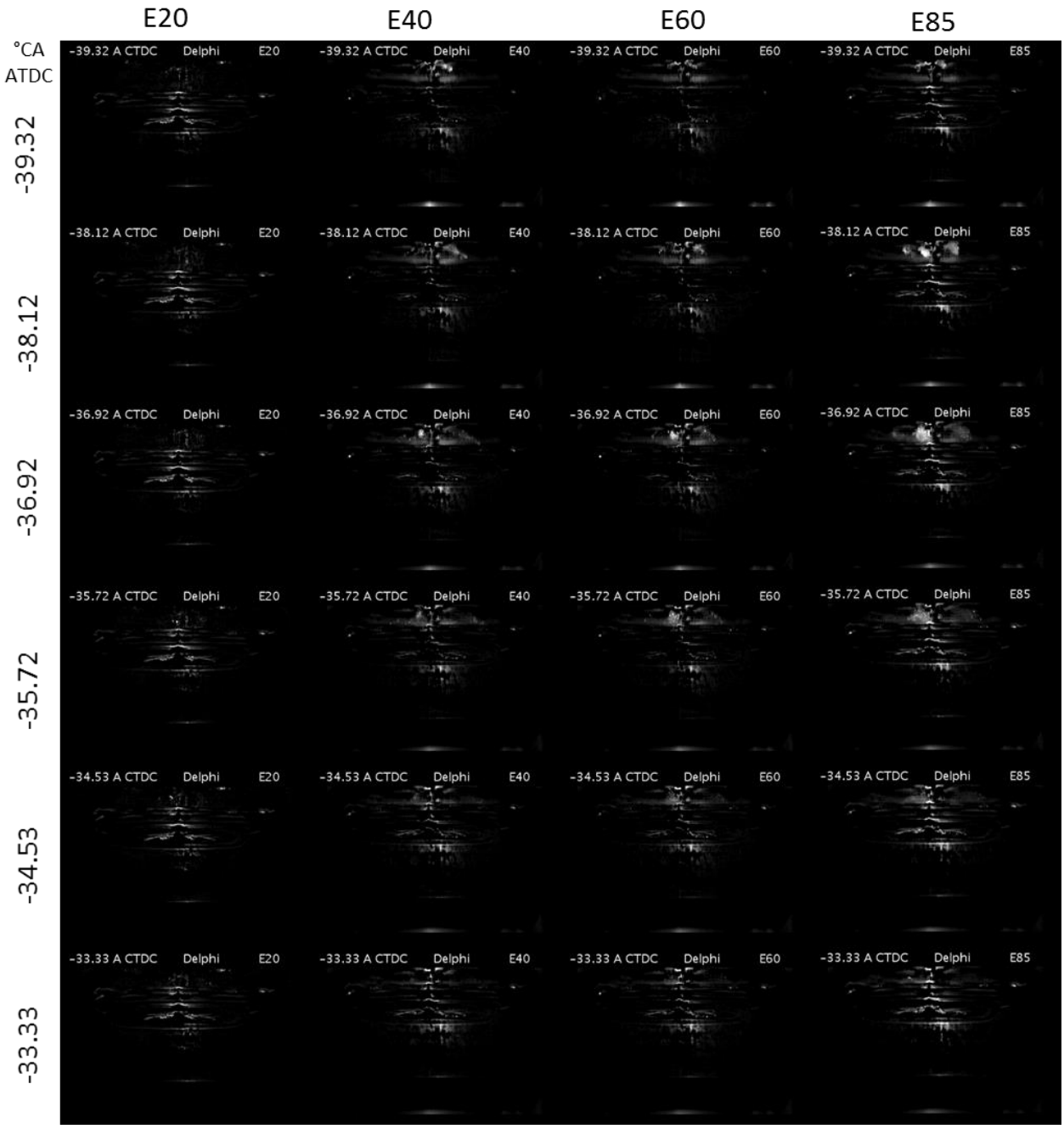

Figure 6.26 Background-corrected Mie-scattering spray images of fuel blends – Injection 2 at 40° BTDC

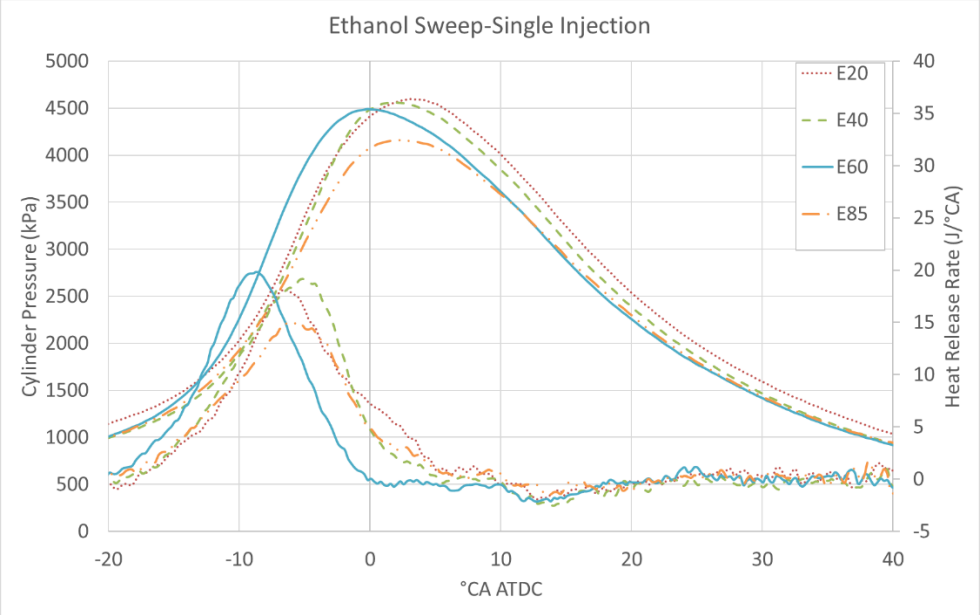

Figure 6.27 Pressure and HRR curves for various fuel blends (single injection)

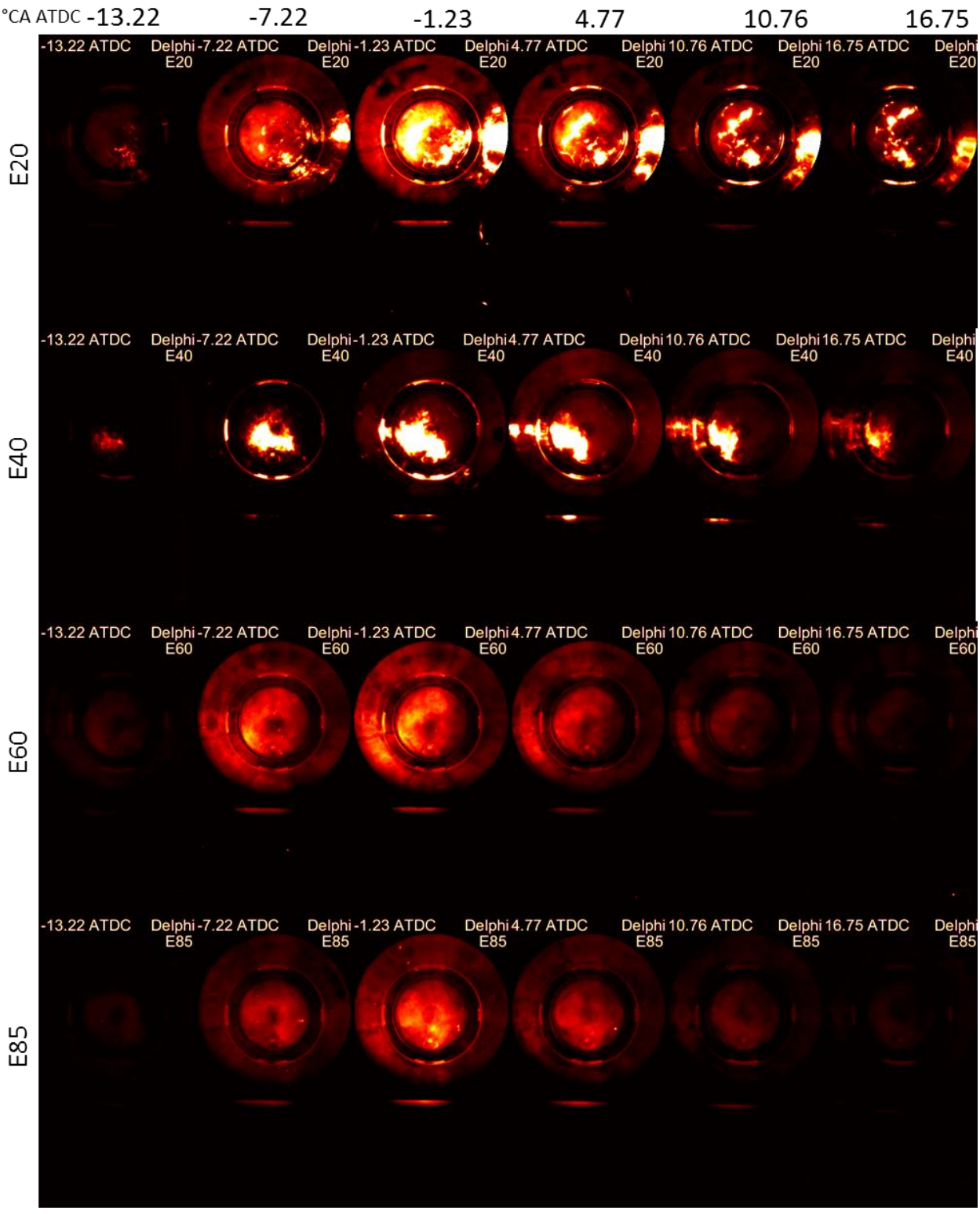

Figure 6.28 Combustion images for various fuel blends (single injection) – 30 µs exposure

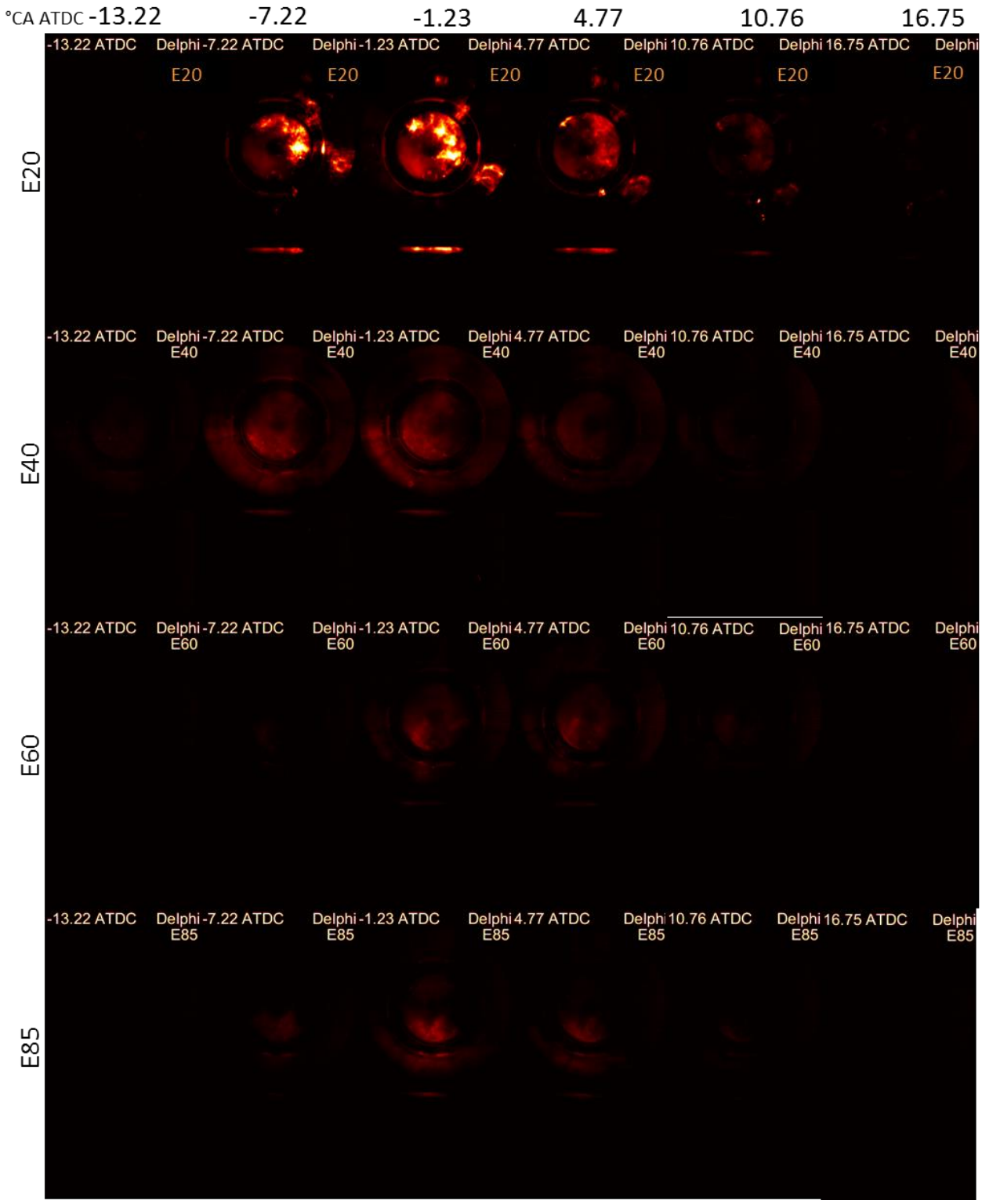

Figure 6.29 Combustion images for various fuel blends (single injection) – 10 µs exposure

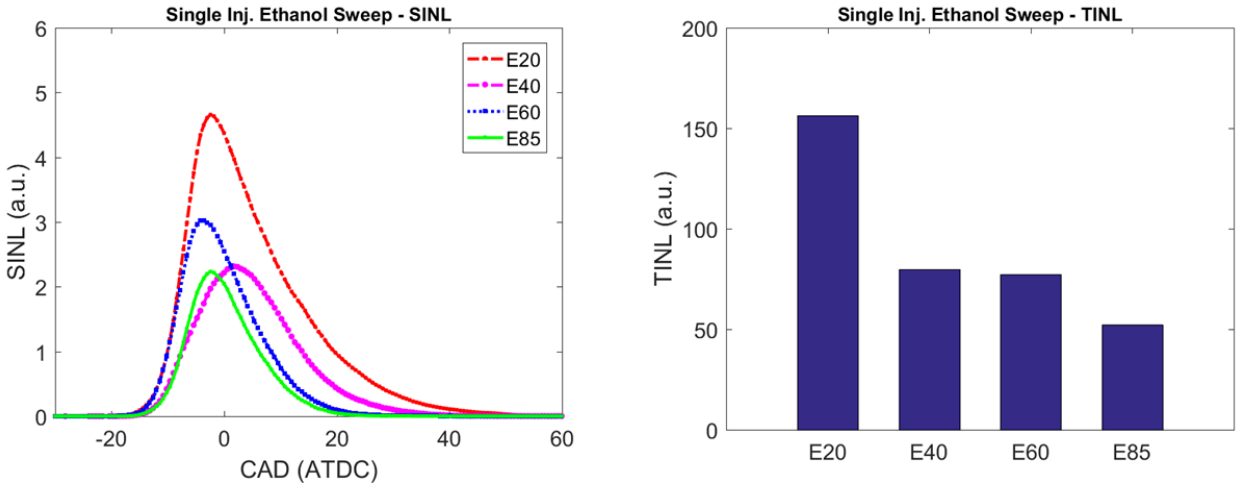

Figure 6.30 SINL and TINL for various fuel blends (single injection) – 30 µs exposure

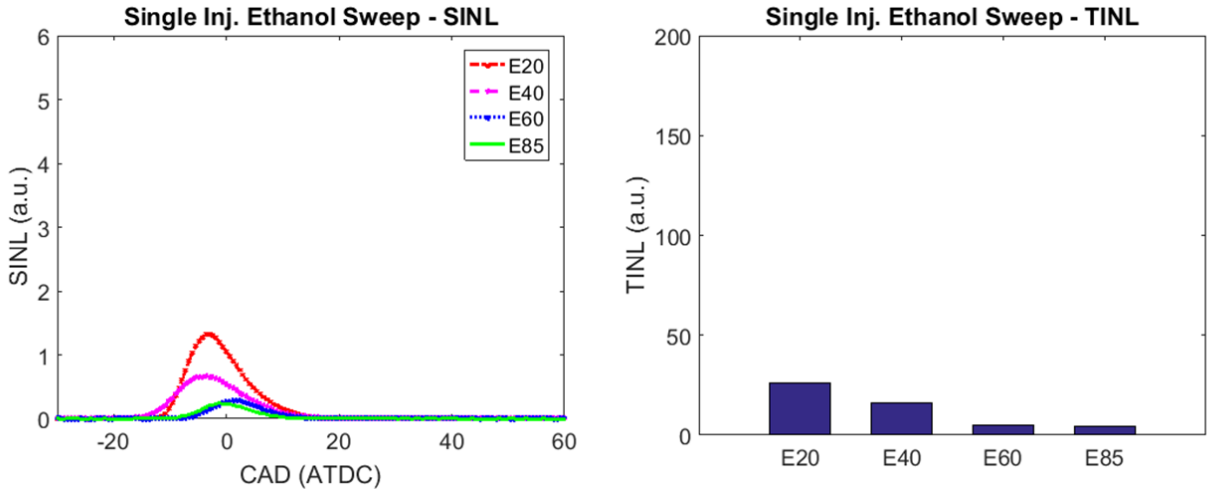

Figure 6.31 SINL and TINL for various fuel blends (single injection) – 10 µs exposure

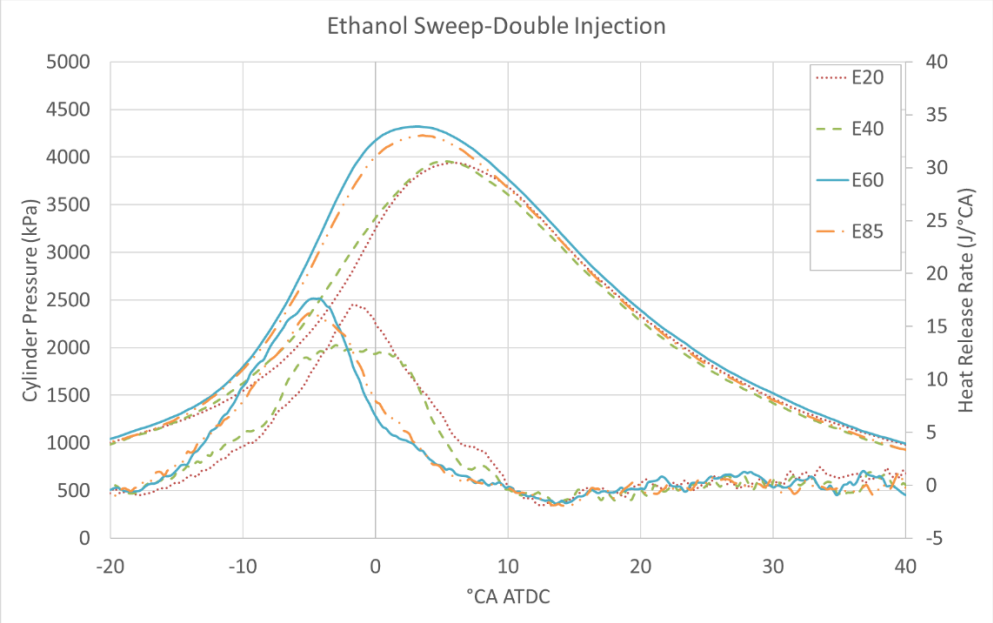

Figure 6.32 Pressure and HRR curves for various fuel blends (double injection)

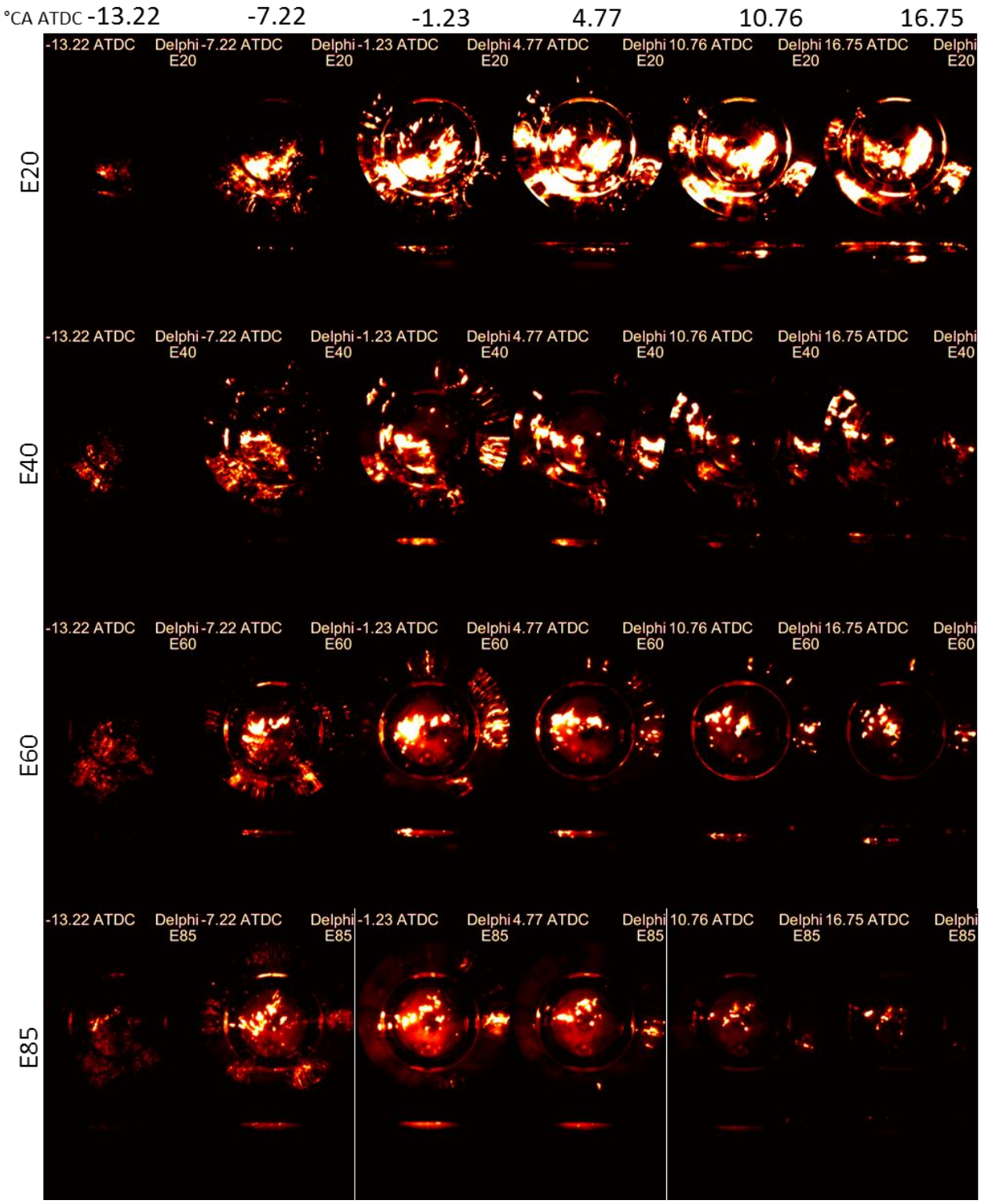

Figure 6.33 Combustion images for various fuel blends, Φ = 1 (double injection)

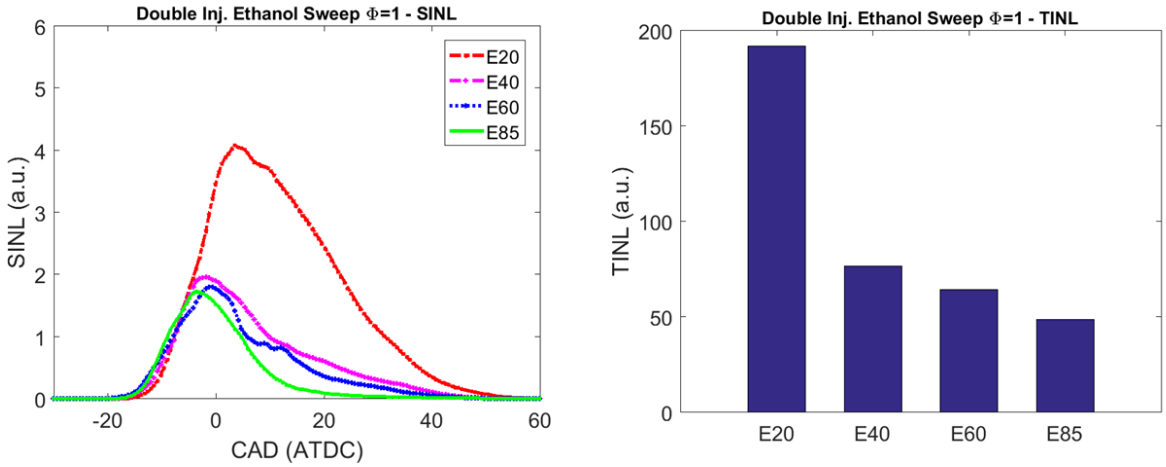

Figure 6.34 SINL and TINL for various fuel blends, Φ =1 (double injection)

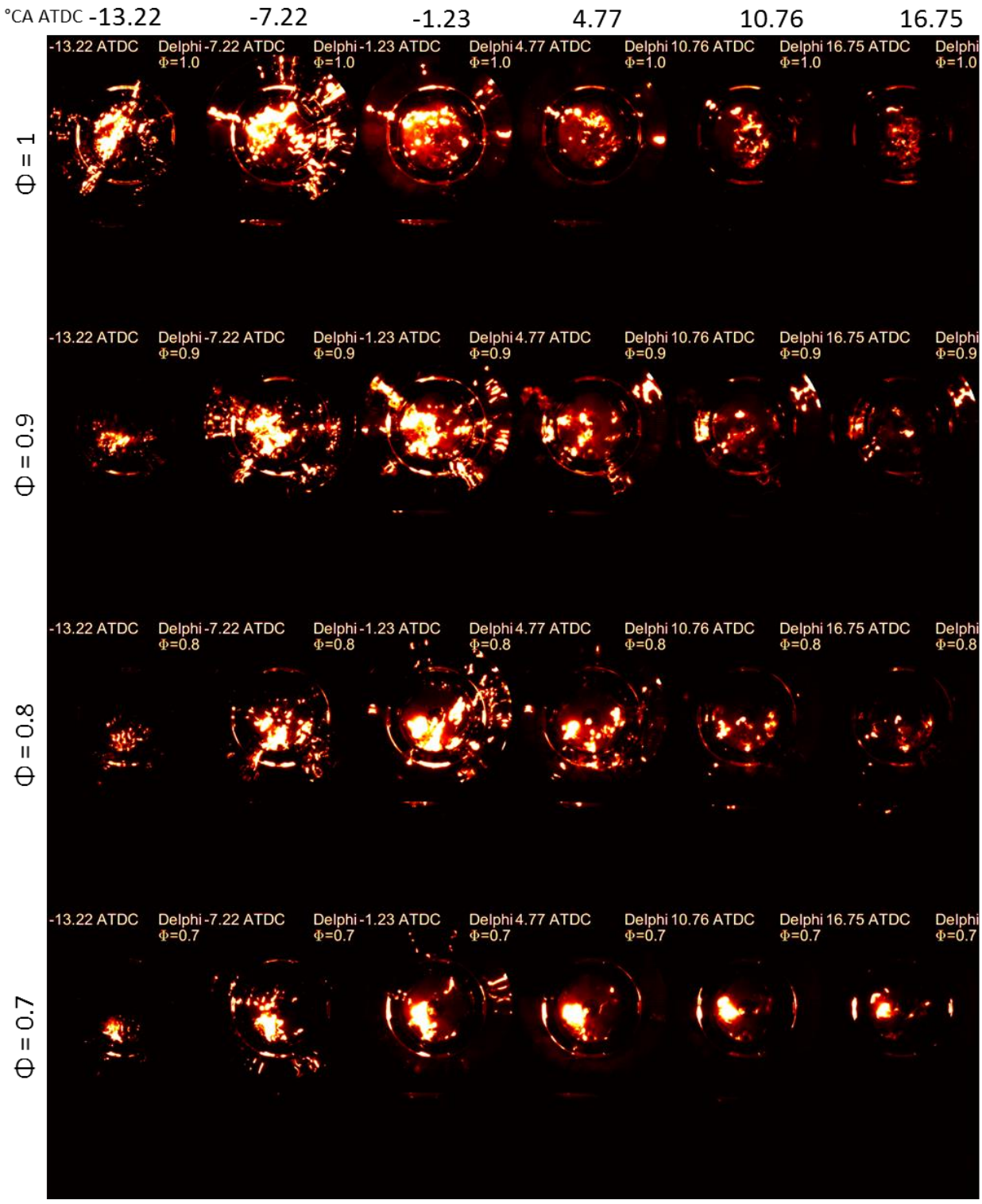

Figure 6.35 Combustion images for various Φ (E20 - double injection)

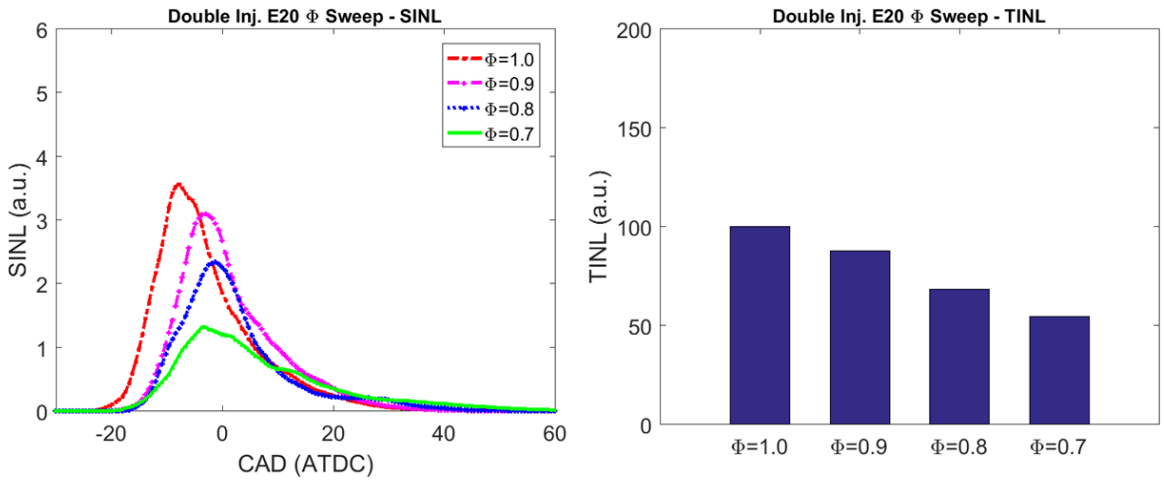

Figure 6.36 SINL and TINL for various Φ (E20 - double injection)

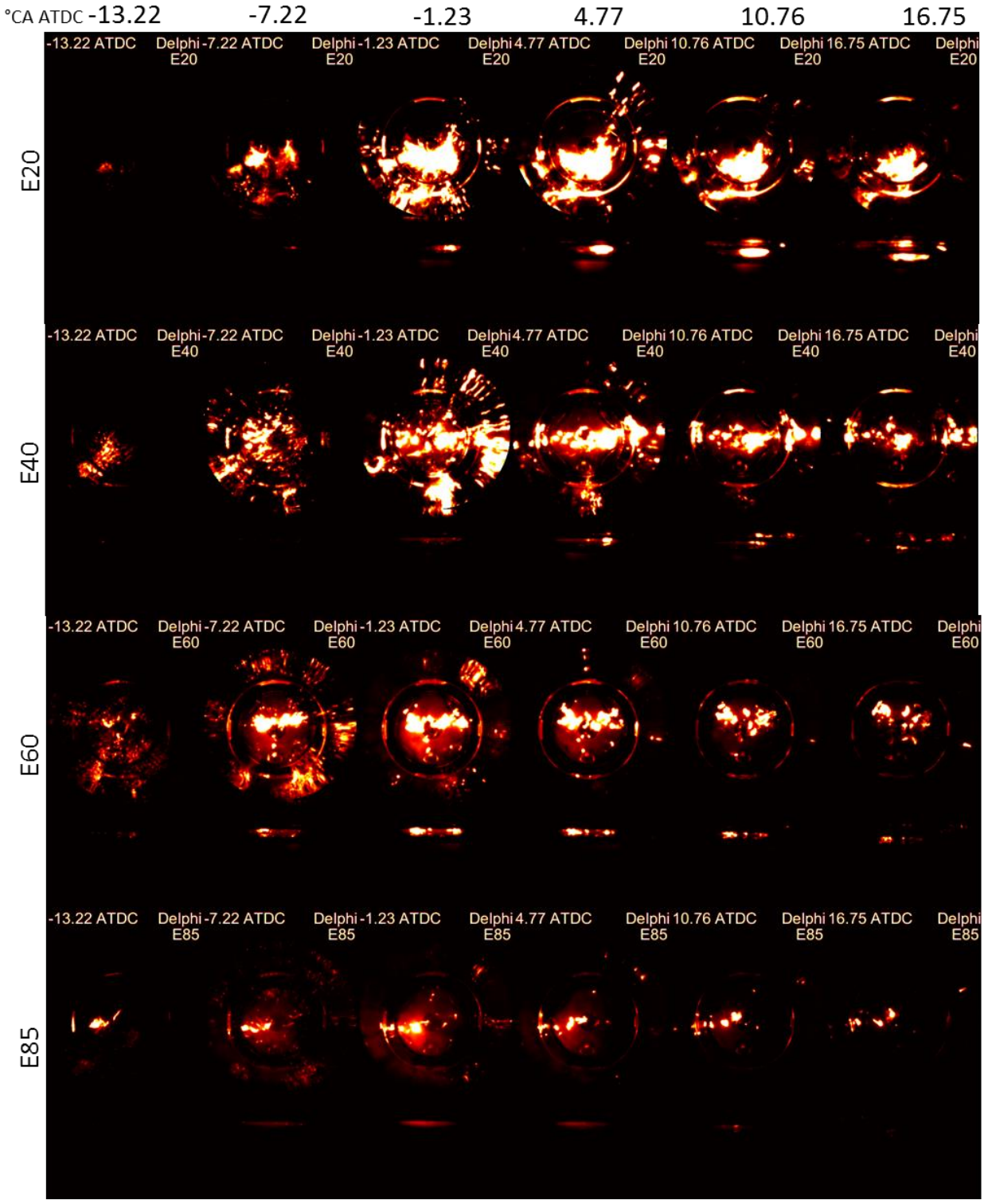

Figure 6.37 Combustion images for various fuel blends, Φ = 0.9 (double injection)

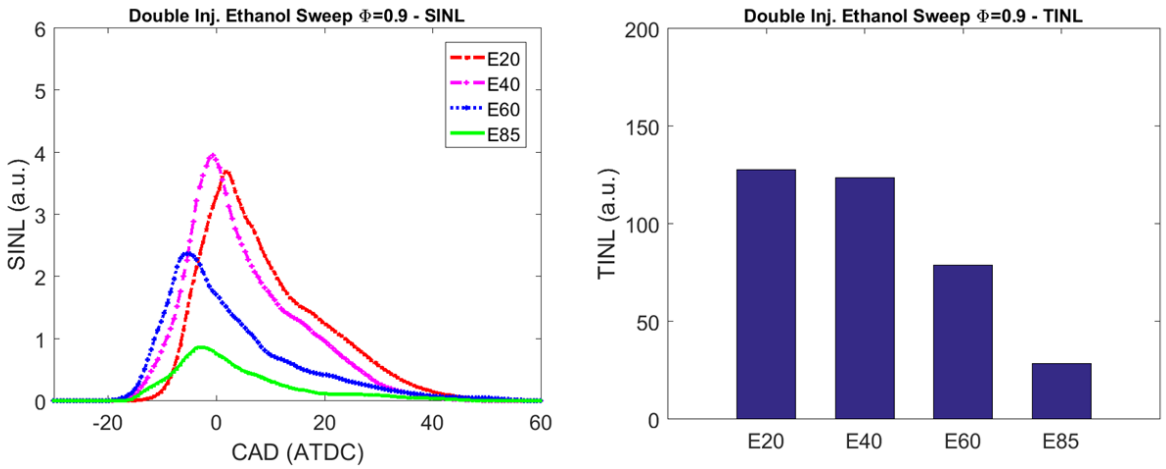

Figure 6.38 SINL and TINL for various fuel blends, Φ = 0.9 (double injection)

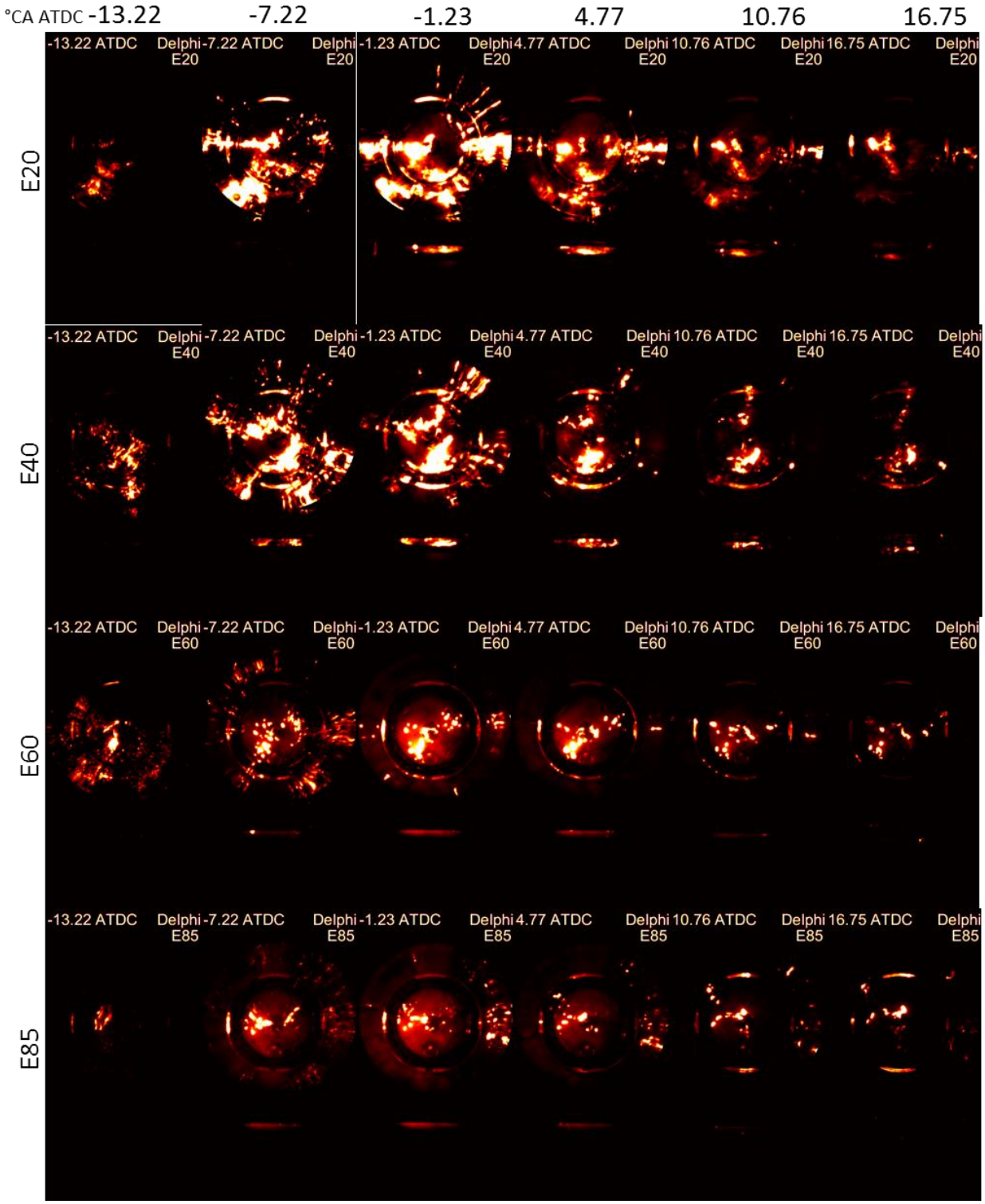

Figure 6.39 Combustion images for various fuel blends, Φ = 0.8 (double injection)

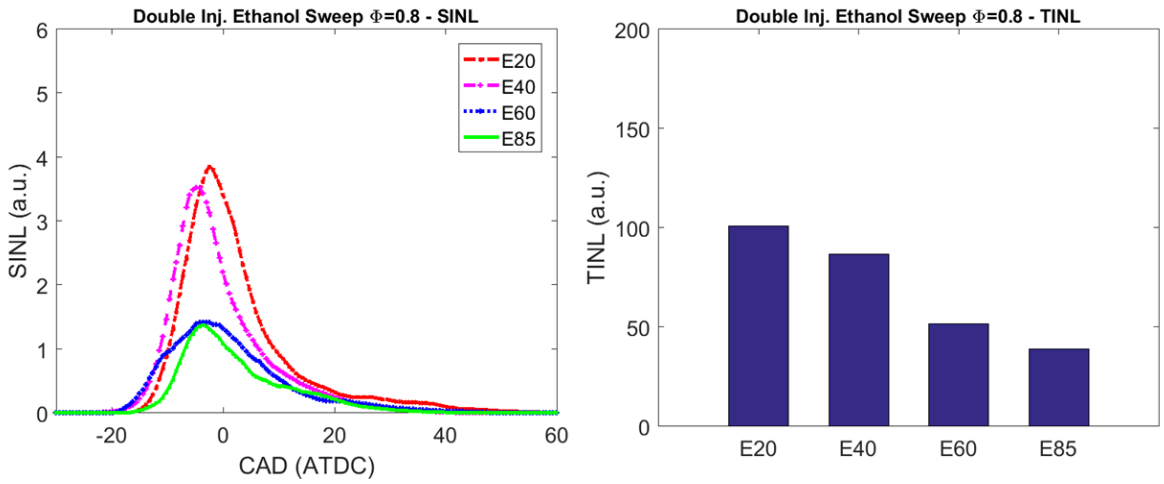

Figure 6.40 SINL and TINL for various fuel blends, Φ = 0.8 (double injection)

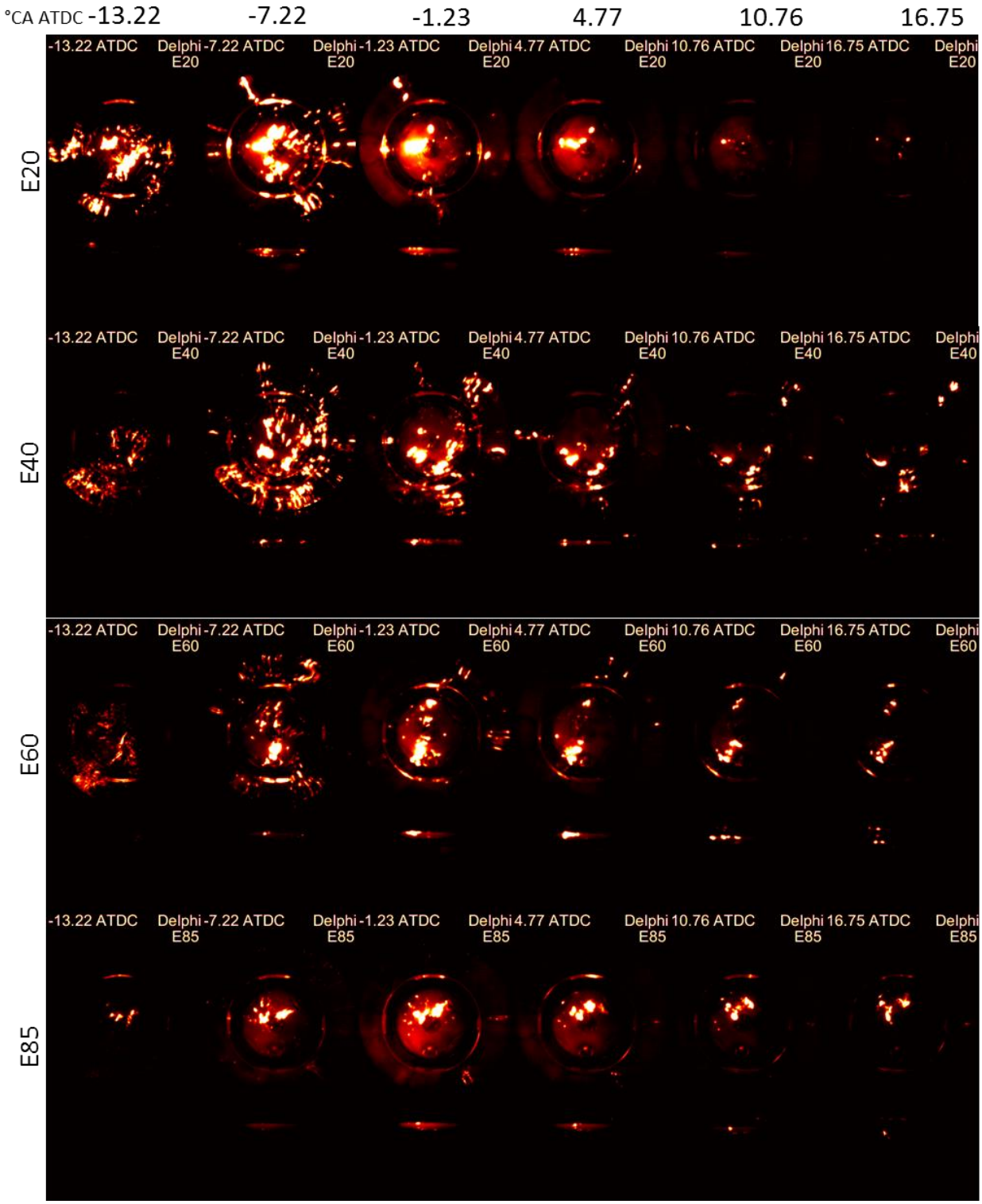

Figure 6.41 Combustion images for various fuel blends, Φ = 0.7 (double injection)

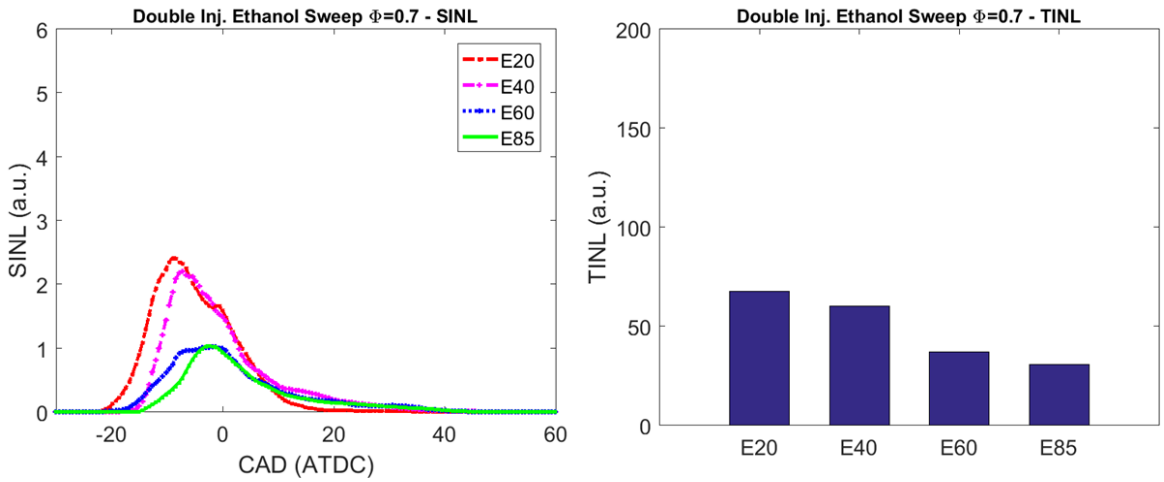

Figure 6.42 SINL and TINL for various fuel blends, Φ = 0.7 (double injection)

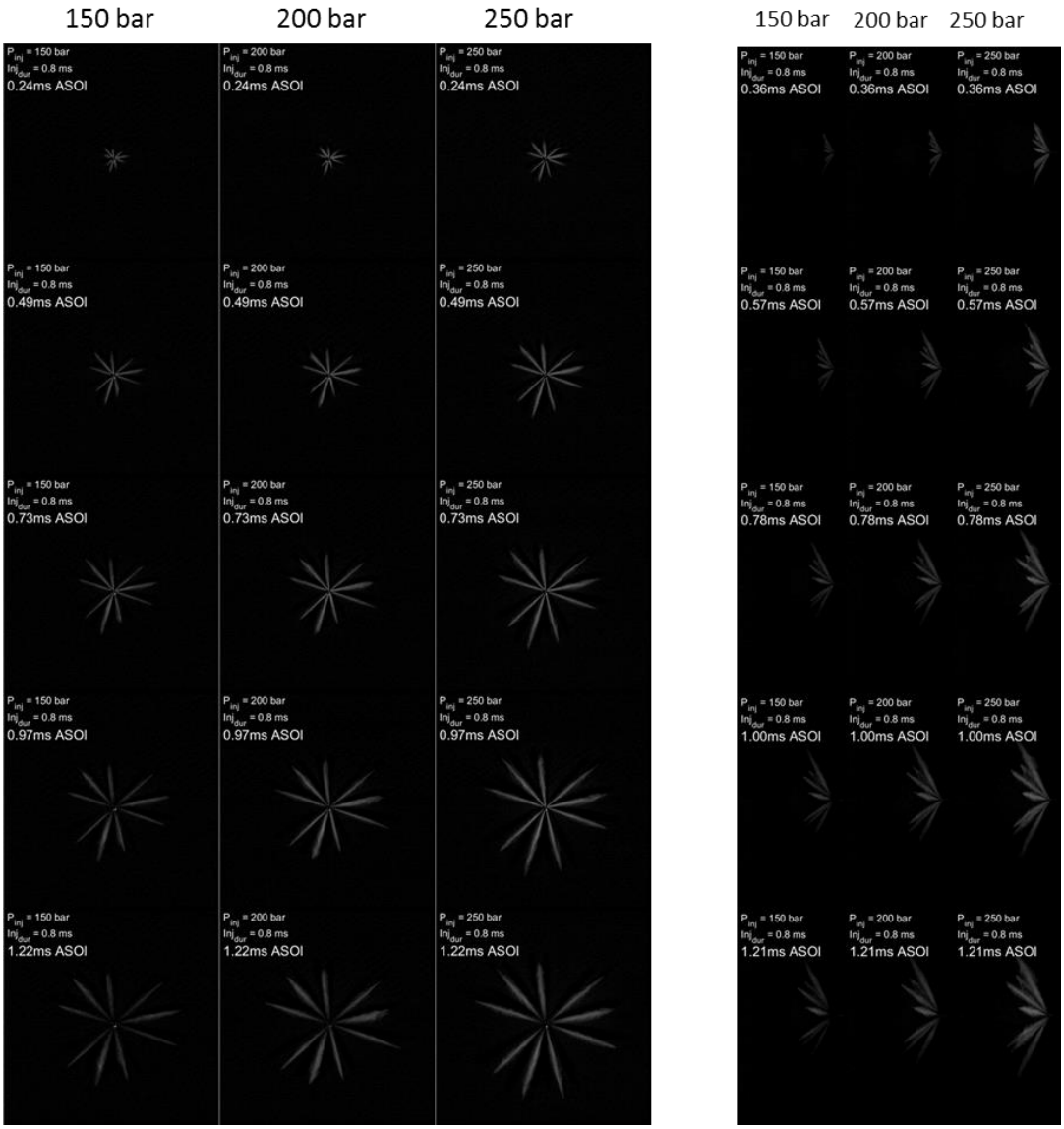

Figure 6.43 Prototype injector spray front and side view at 150, 200, and 250 bar

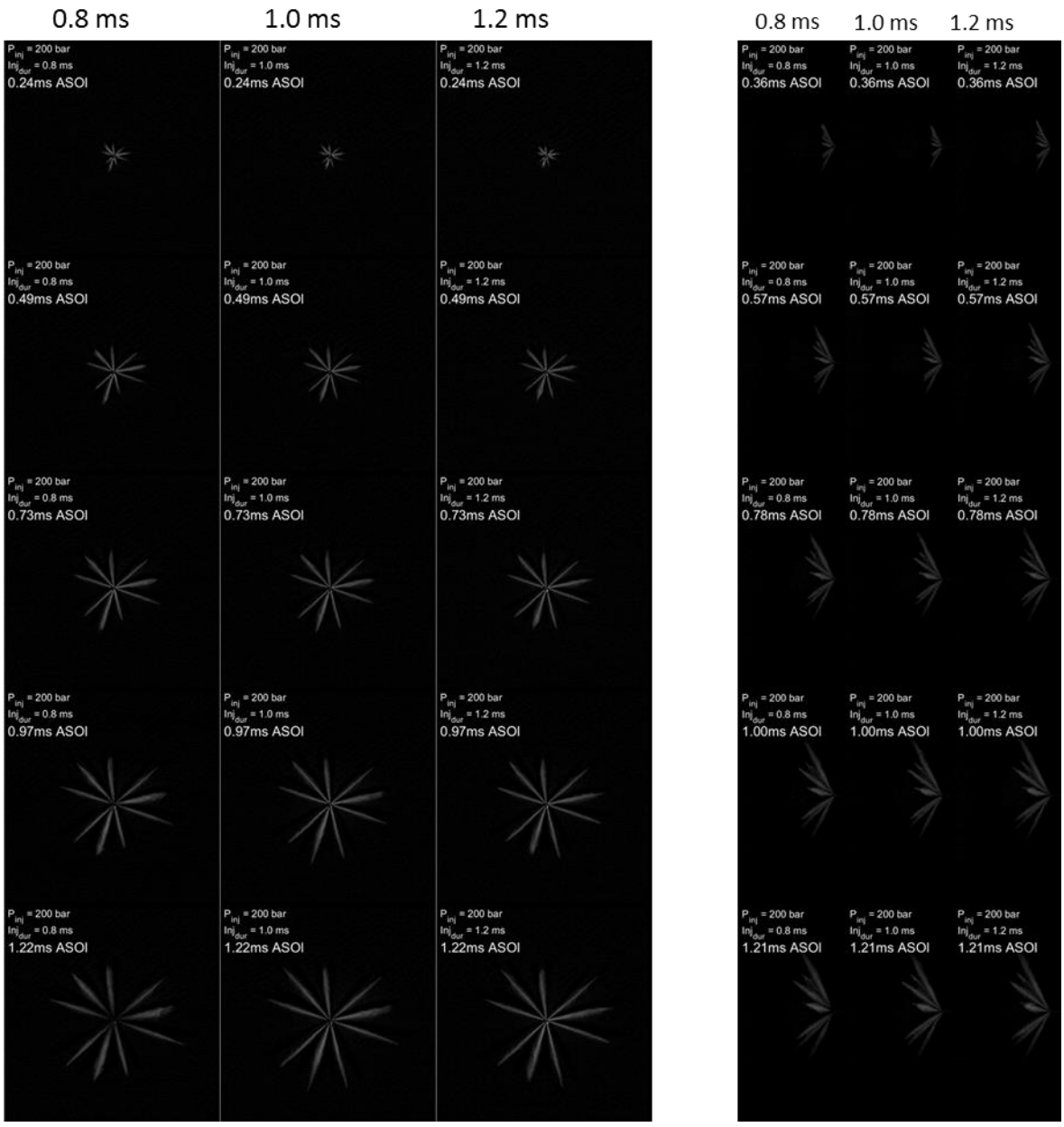

Figure 6.44 Prototype injector spray front and side view at different injection durations

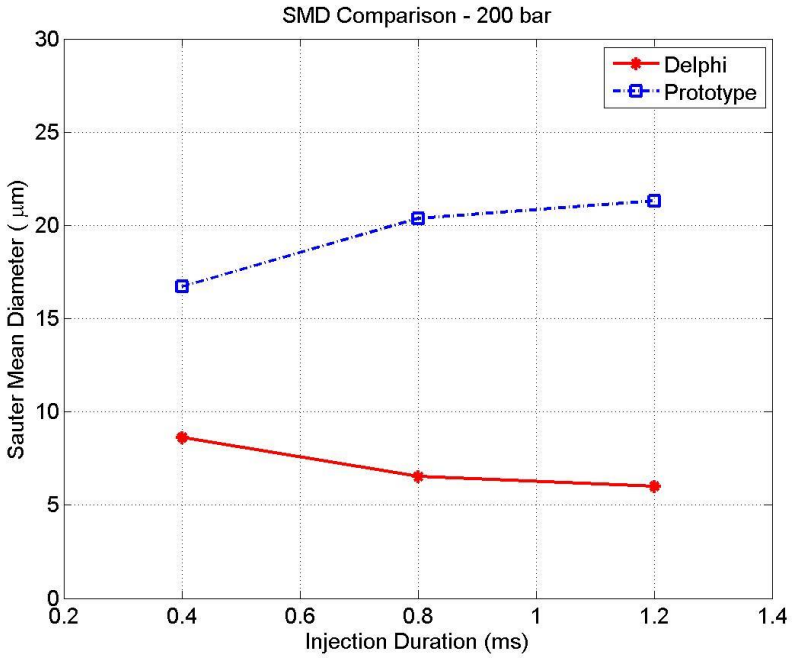

Figure 6.45 SMD – Injector Comparison

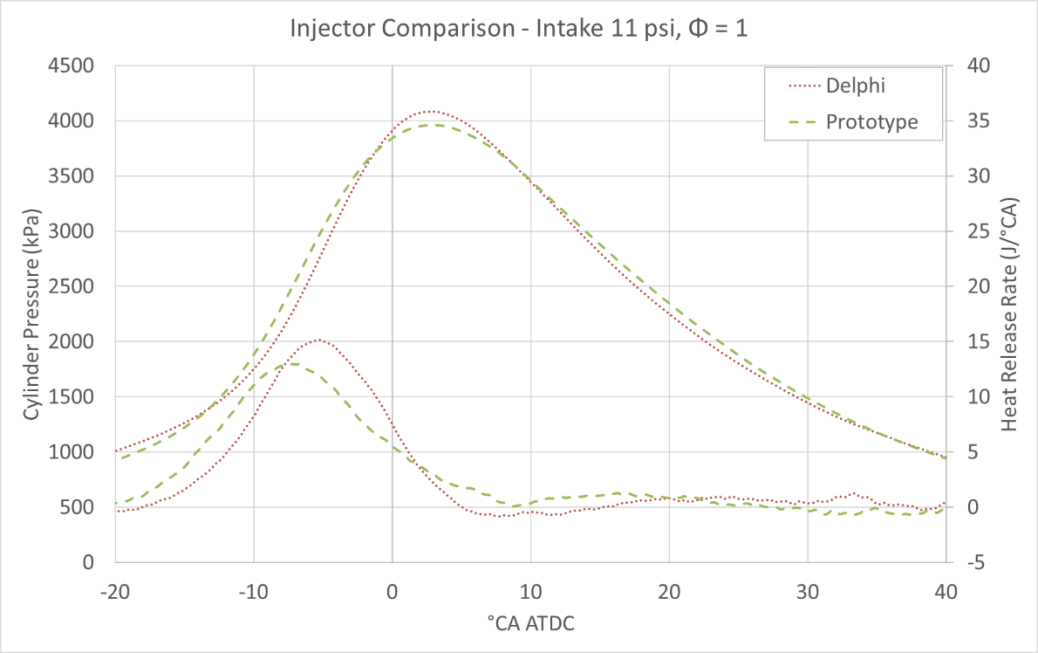

Figure 6.46 Pressure and HRR curves comparing two injectors

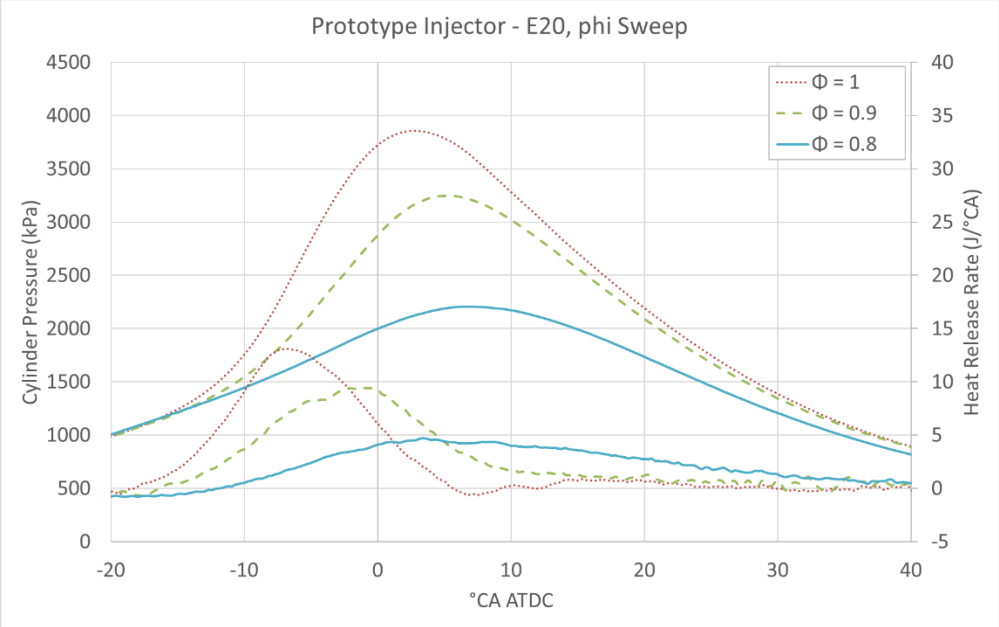

Figure 6.47 Pressure and HRR curves comparing Φ for prototype injector

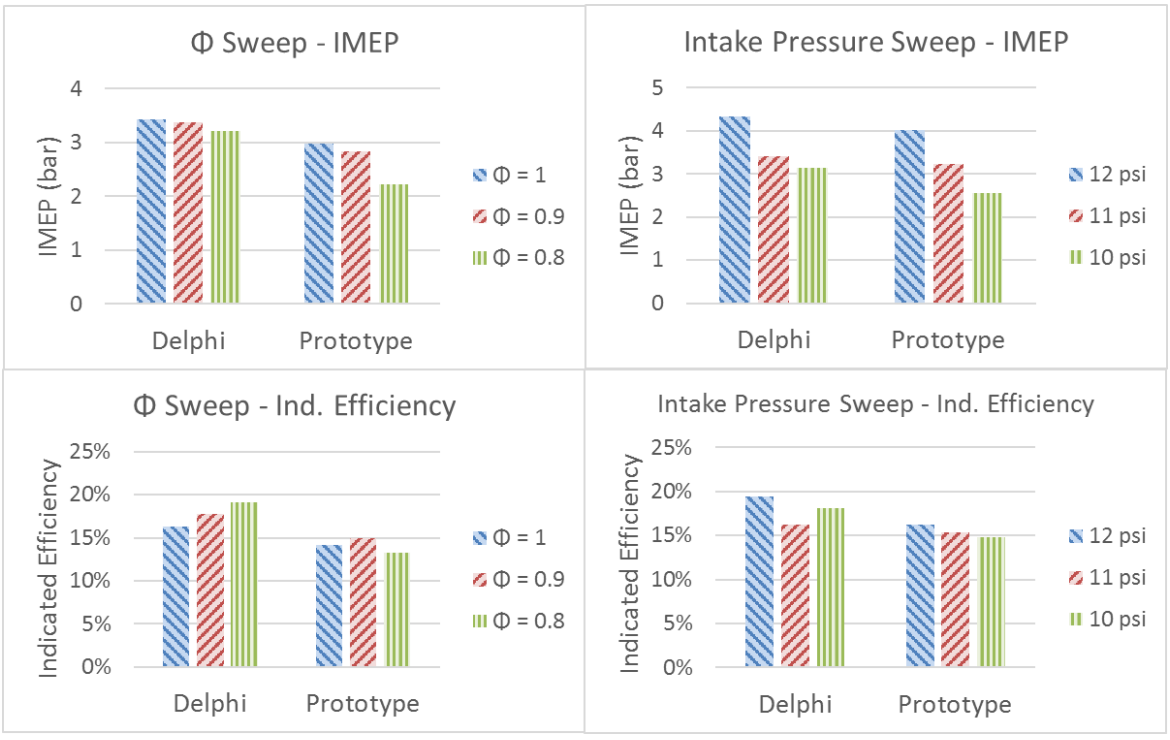

Figure 6.48 Injector comparison - IMEP and Indicated efficiency

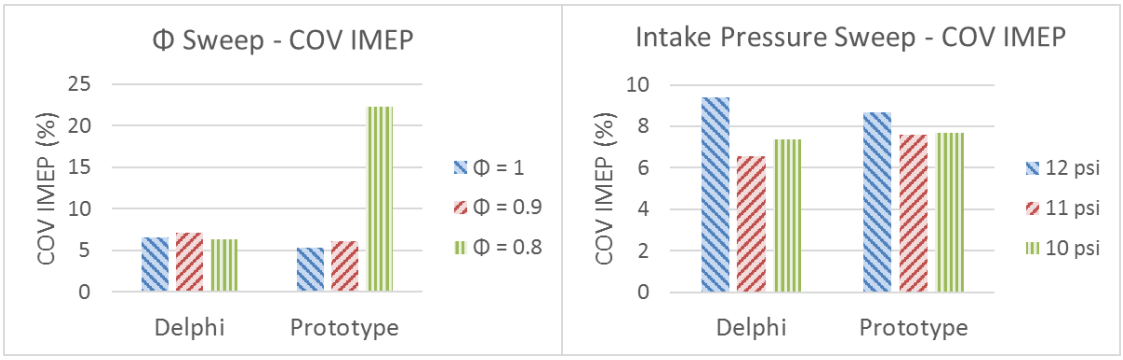

Figure 6.49 Injector comparison - COV-IMEP

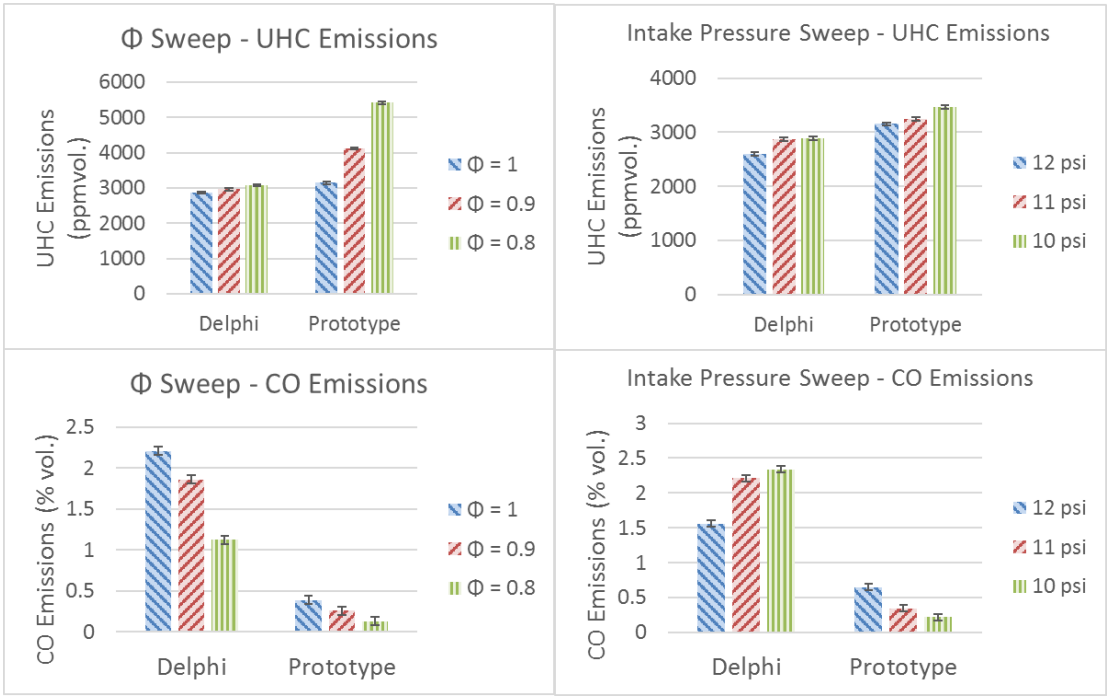

Figure 6.50 Injector comparison - UHC, CO emissions

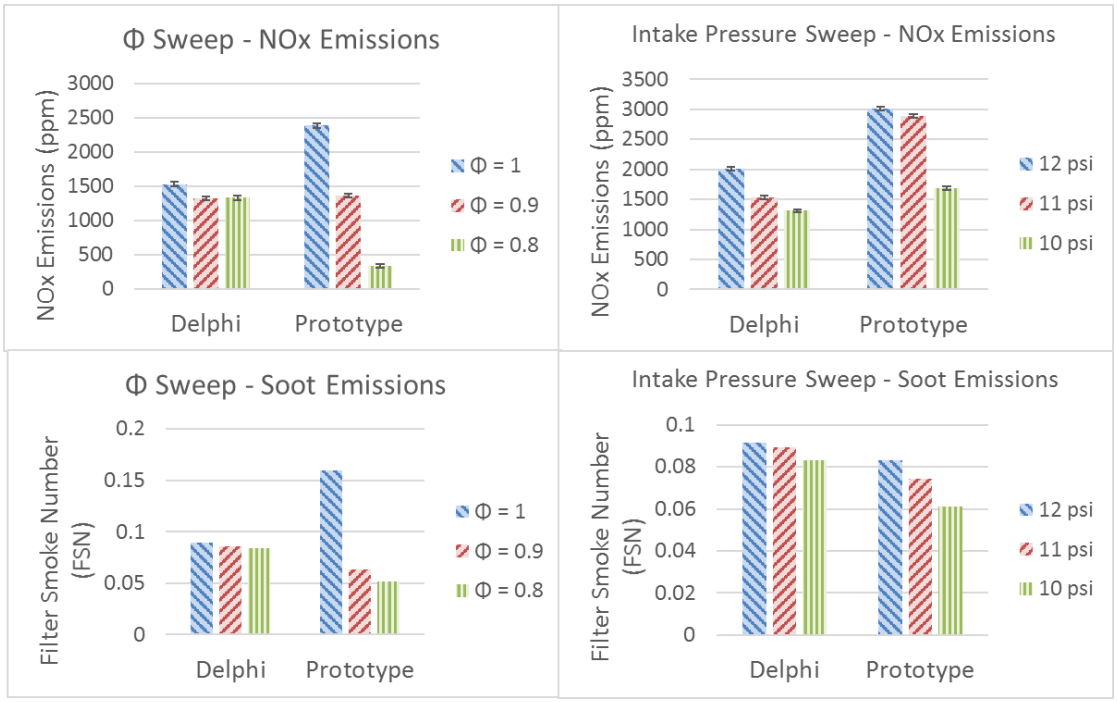

Figure 6.51 Injector comparison - NO_x, Soot emissions

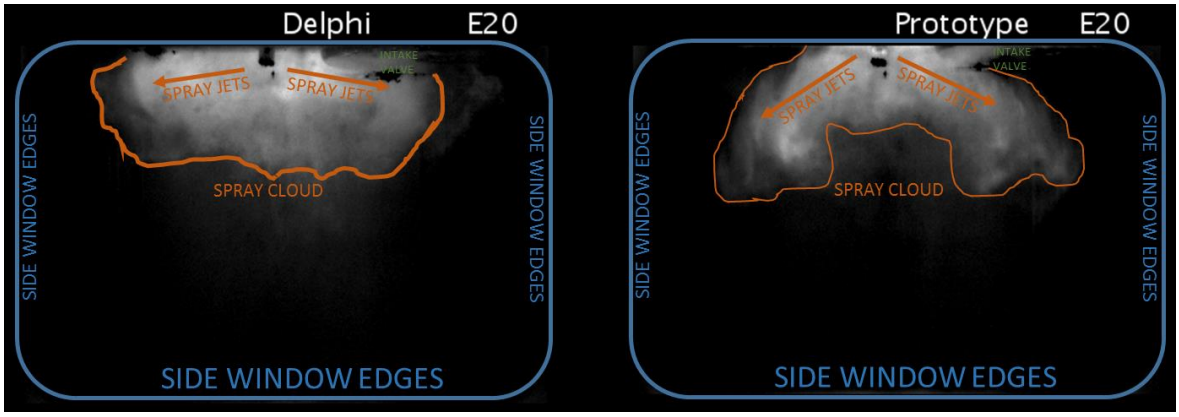

Figure 6.52 Injector comparison – Background-corrected Mie-scattering image examples

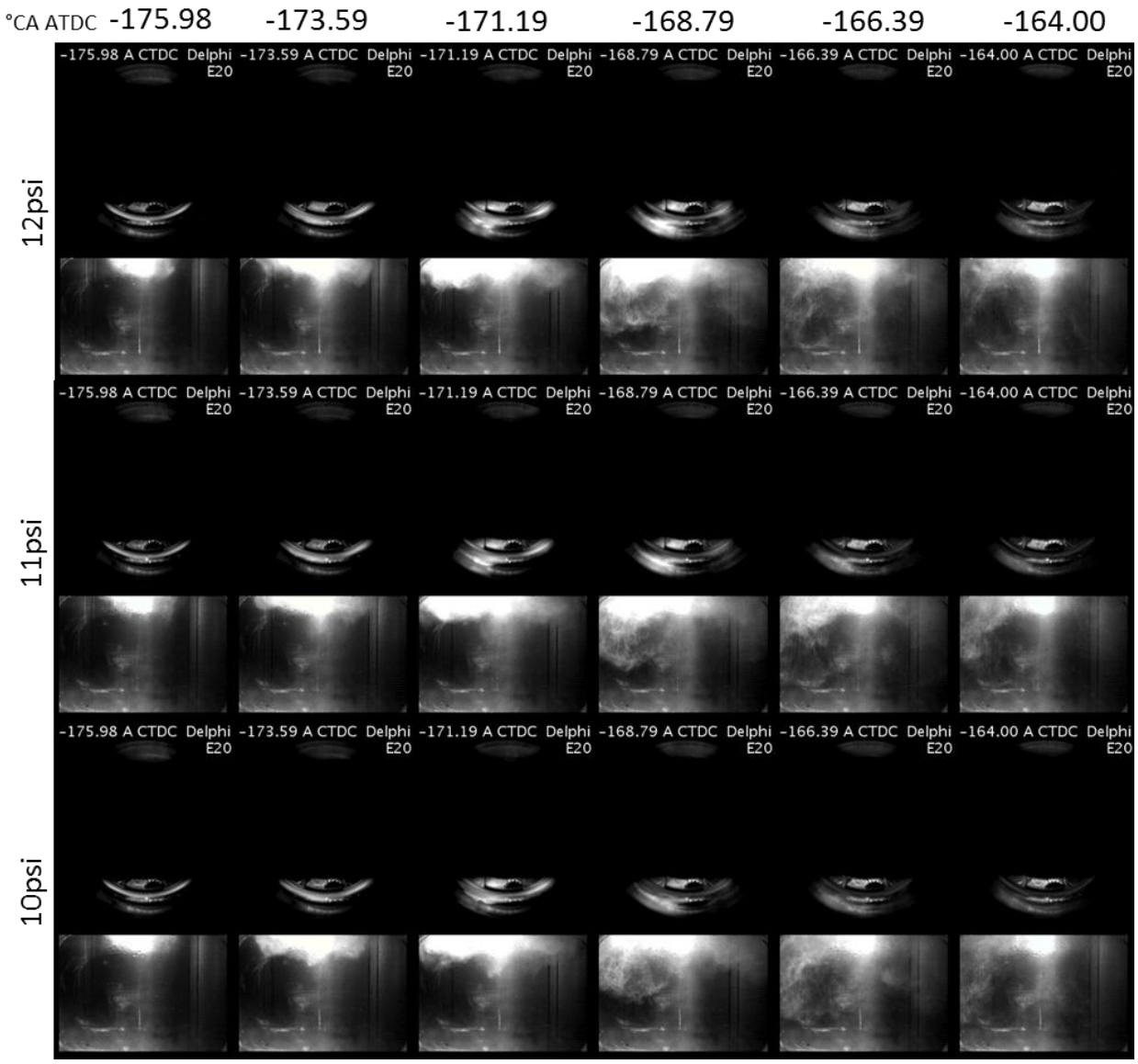

Figure 6.53 Spray imaging of Delphi injector – 1st inj. at various intake pressures (Φ =1)

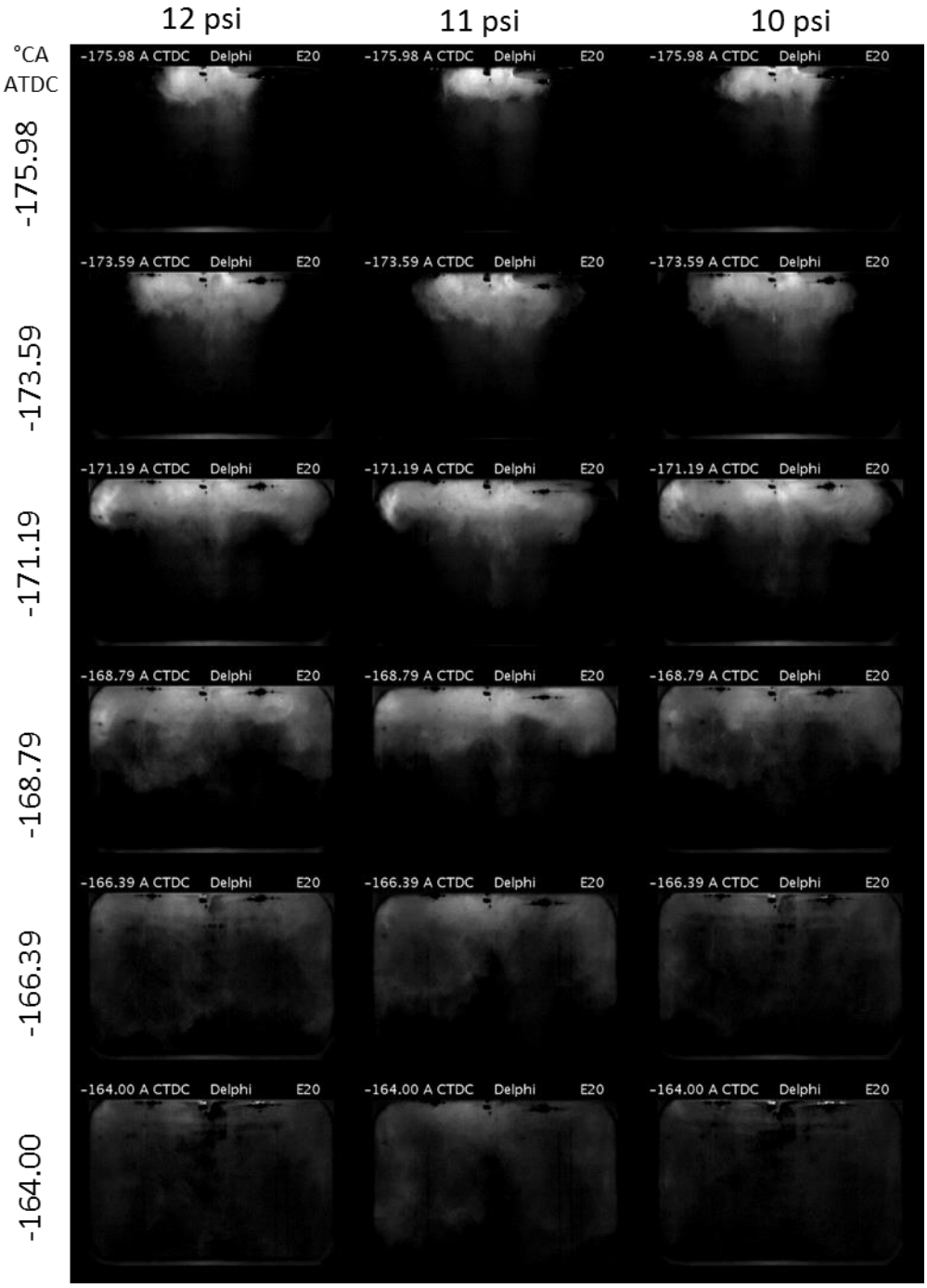

Figure 6.54 Background-corrected Spray imaging of Delphi injector – 1st inj. at various intake pressures (Φ =1)

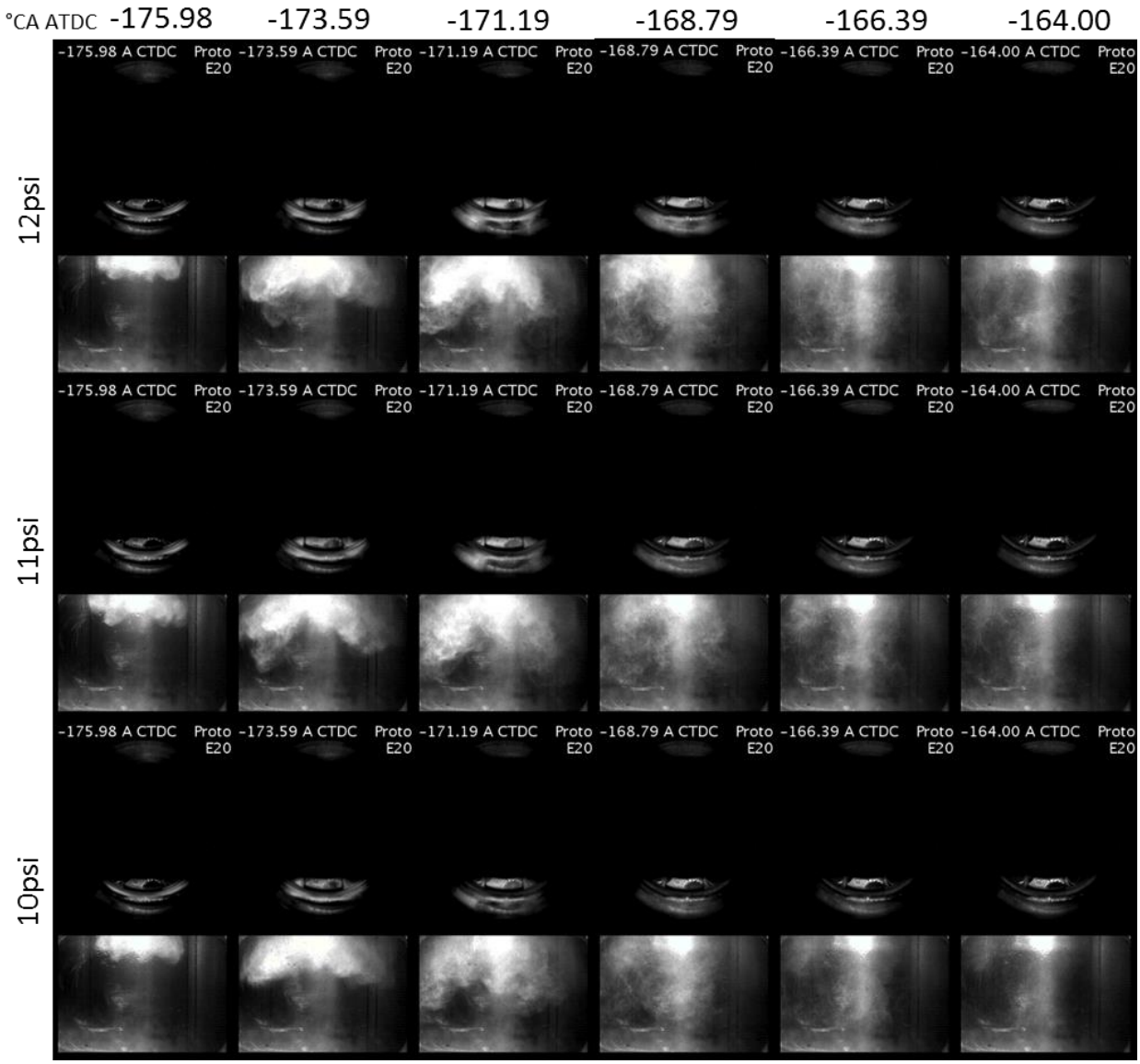

Figure 6.55 Spray imaging of Prototype injector – 1st inj. at various intake pressures (Φ =1)

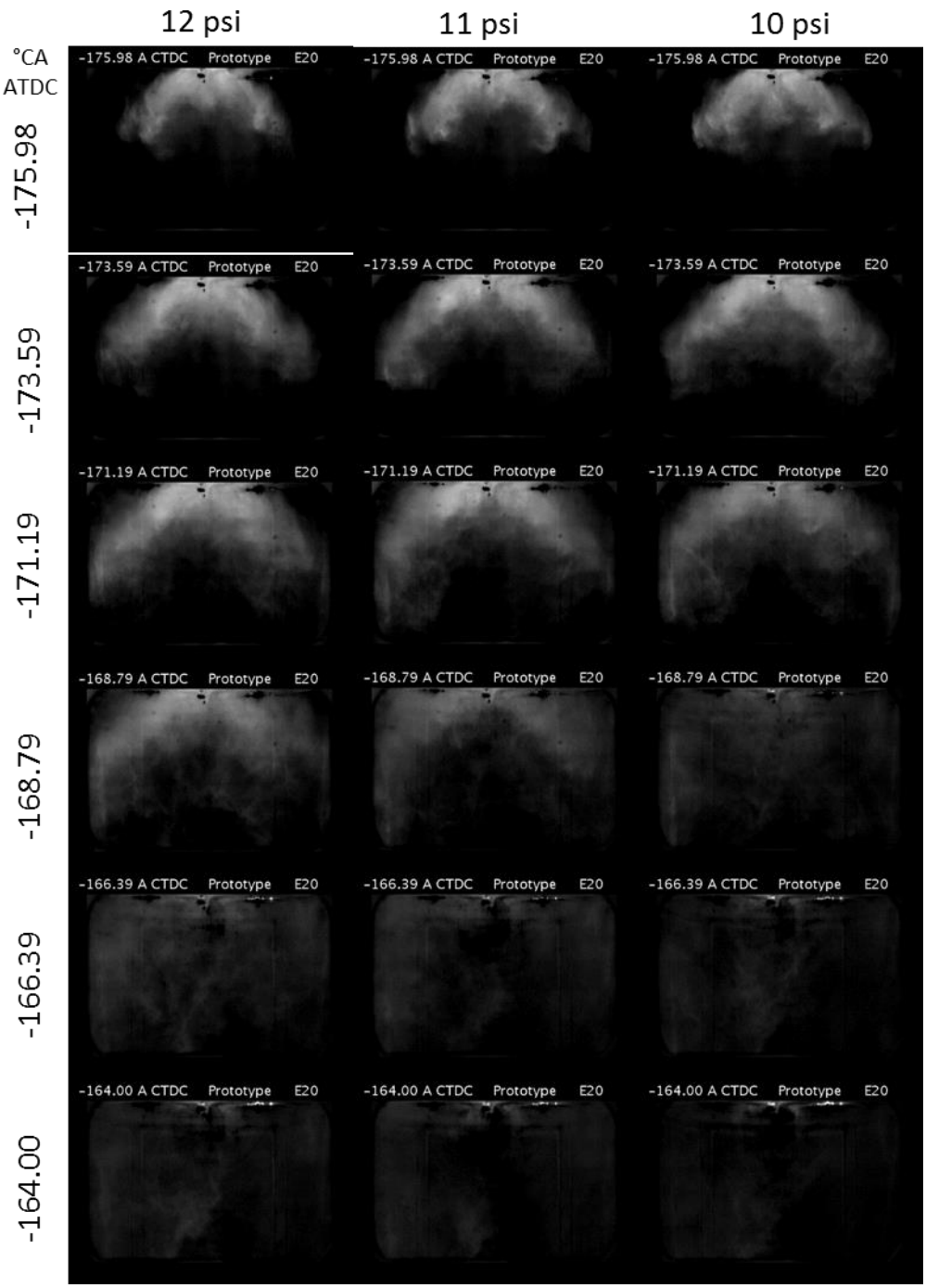

Figure 6.56 Background-corrected spray imaging of Prototype injector – 1st inj. at various intake pressures (Φ =1)

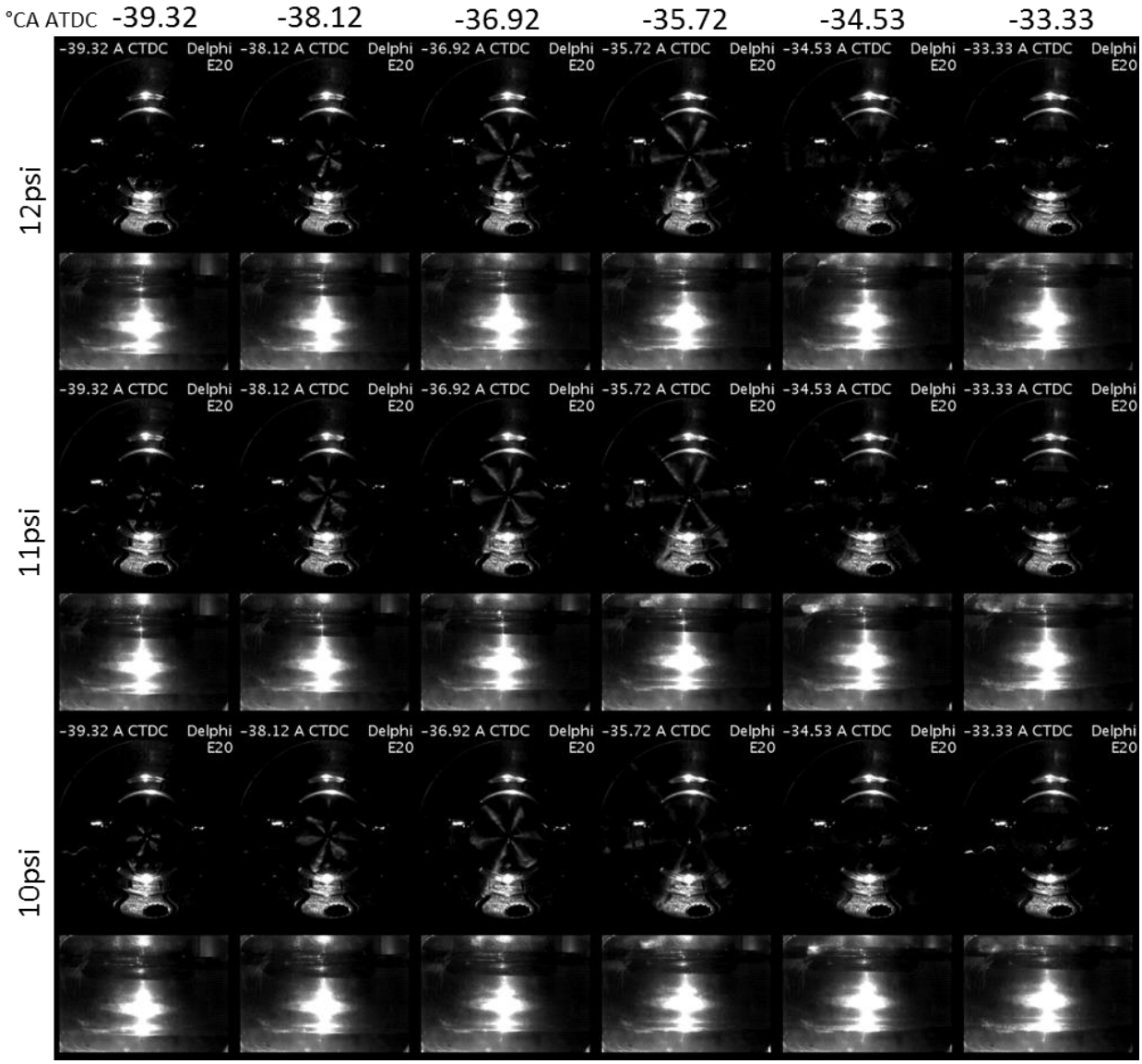

Figure 6.57 Spray imaging of Delphi injector – 2nd inj. at various intake pressures (Φ =1)

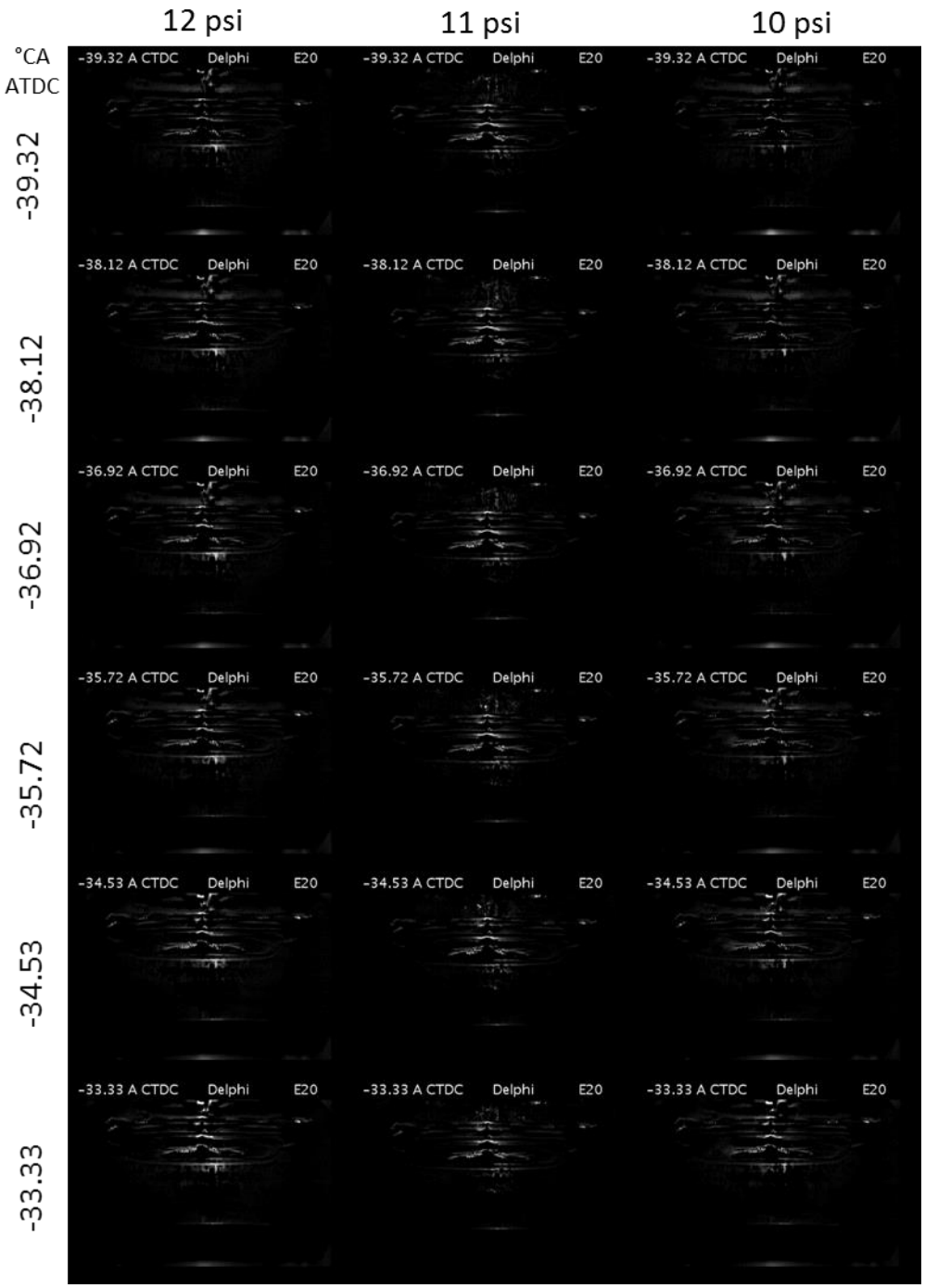

Figure 6.58 Background-corrected spray imaging of Delphi injector – 2nd inj. at various intake pressures (Φ =1)

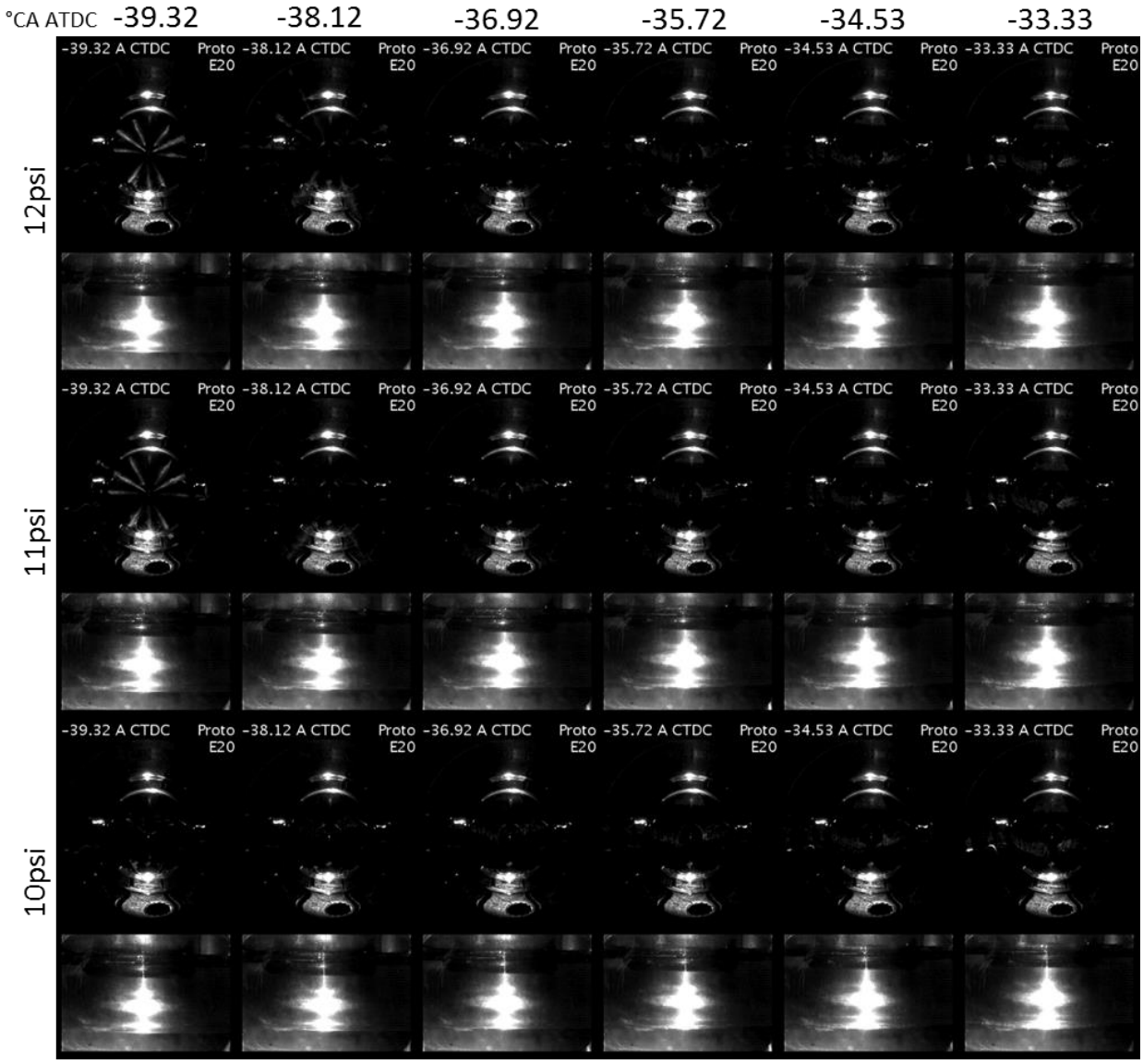

Figure 6.59 Spray imaging of Prototype injector – 2nd inj. at various intake pressures (Φ =1)

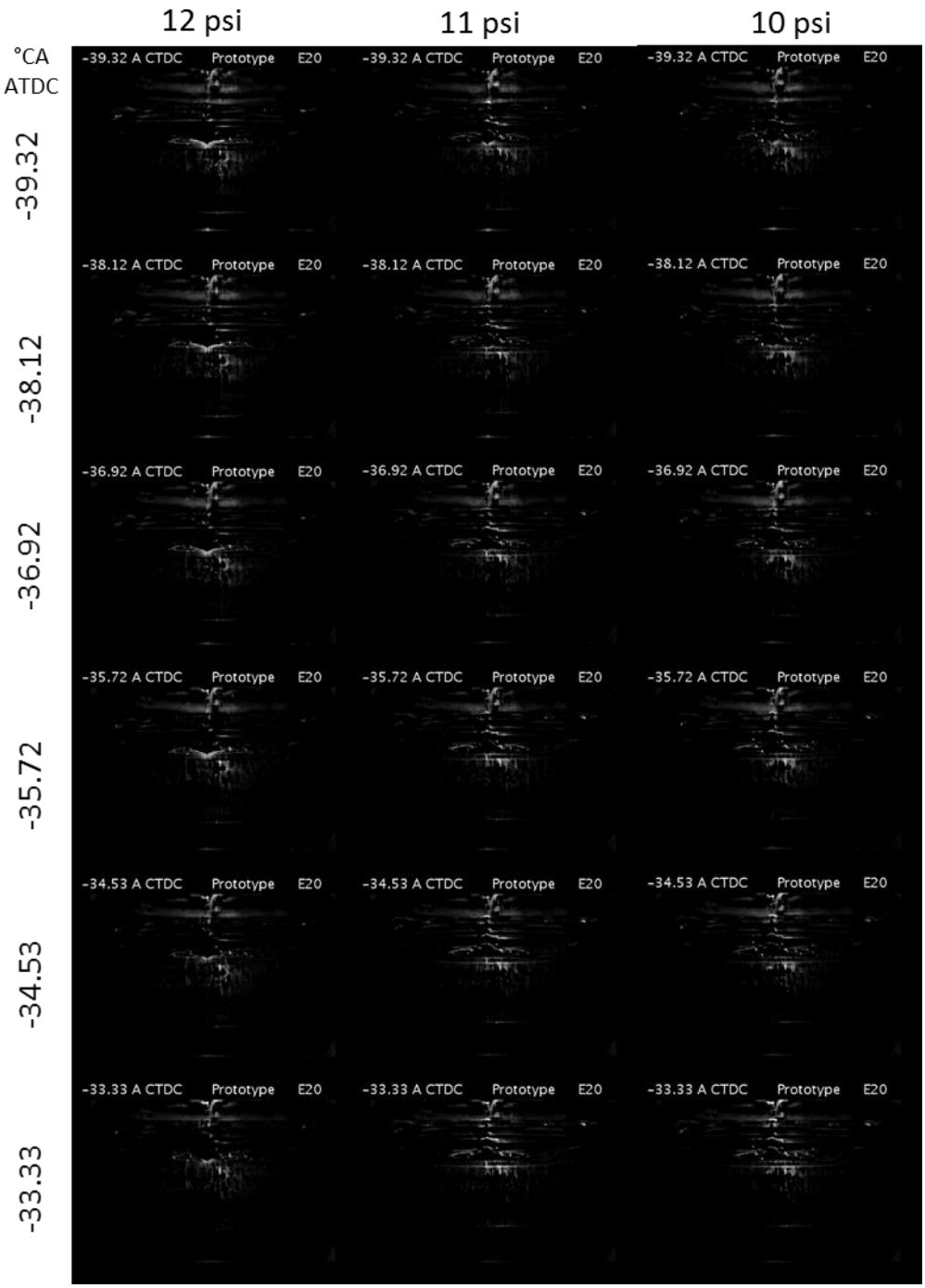

Figure 6.60 Background-corrected spray imaging of Prototype injector – 2nd inj. at various intake pressures (Φ =1)

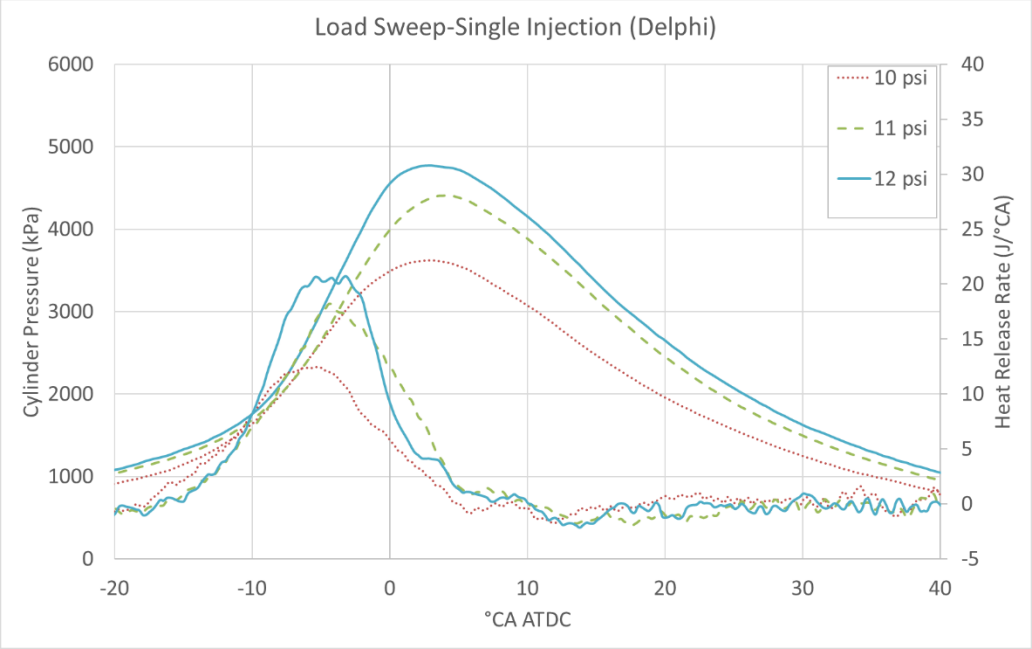

Figure 6.61 Pressure and HRR curves – Delphi – Intake pressure sweep (single inj.)

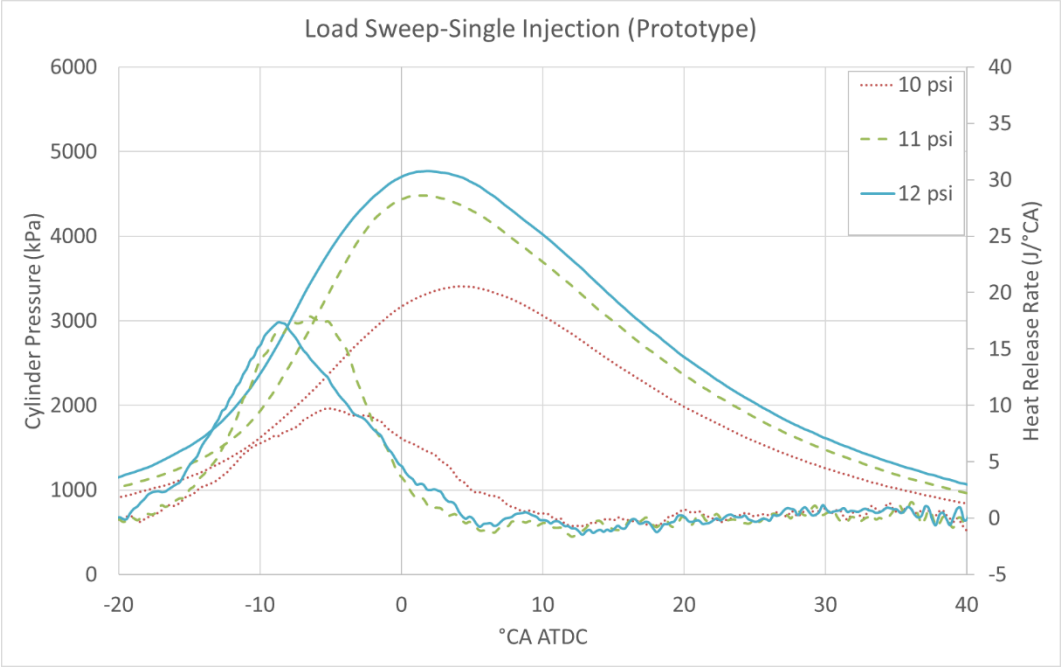

Figure 6.62 Pressure and HRR curves – Prototype – Intake pressure sweep (single inj.)

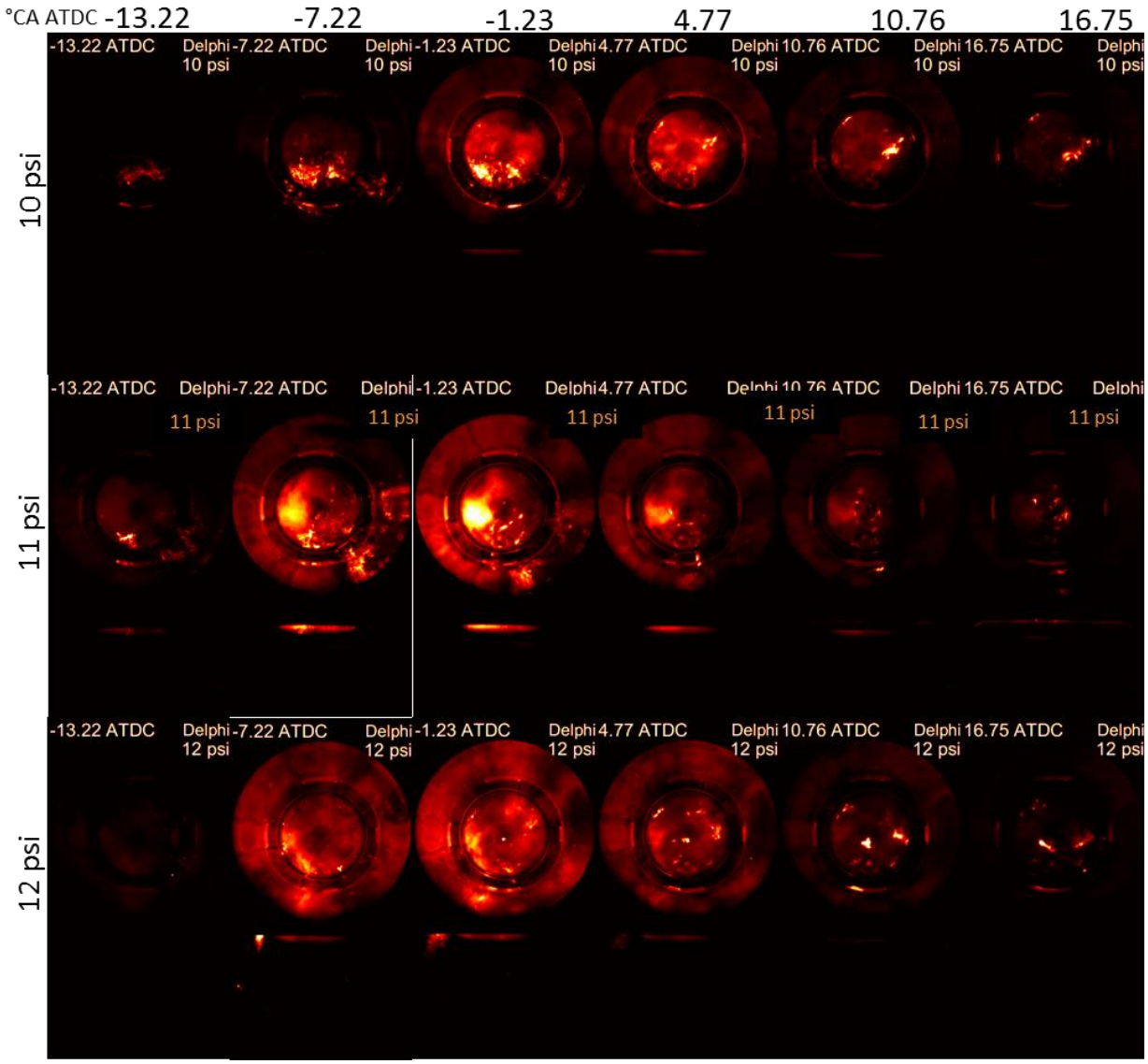

Figure 6.63 Combustion images – Delphi - various intake pressures (single inj.) – 30 µs

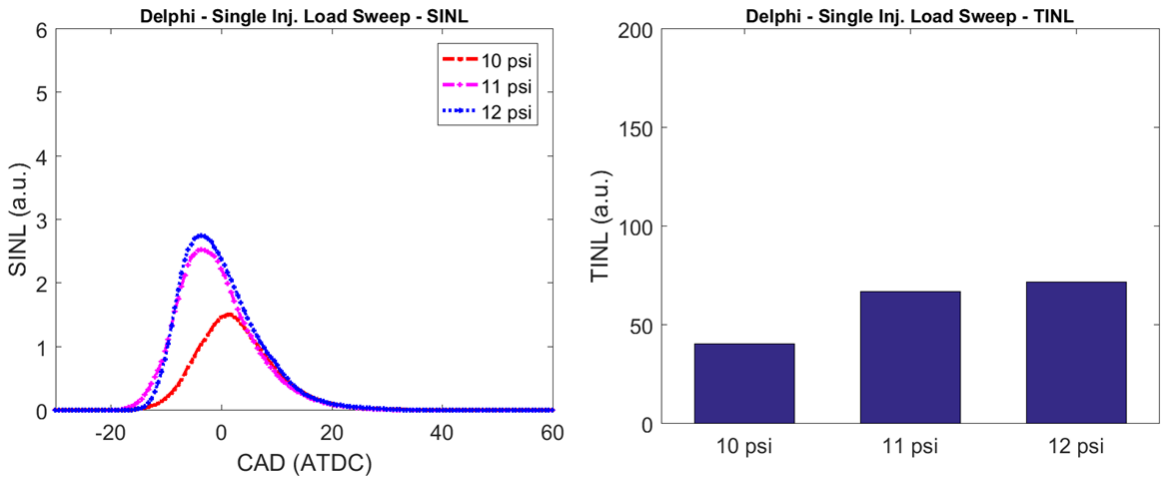

Figure 6.64 SINL and TINL – Delphi - various intake pressures (single inj.) – 30 µs

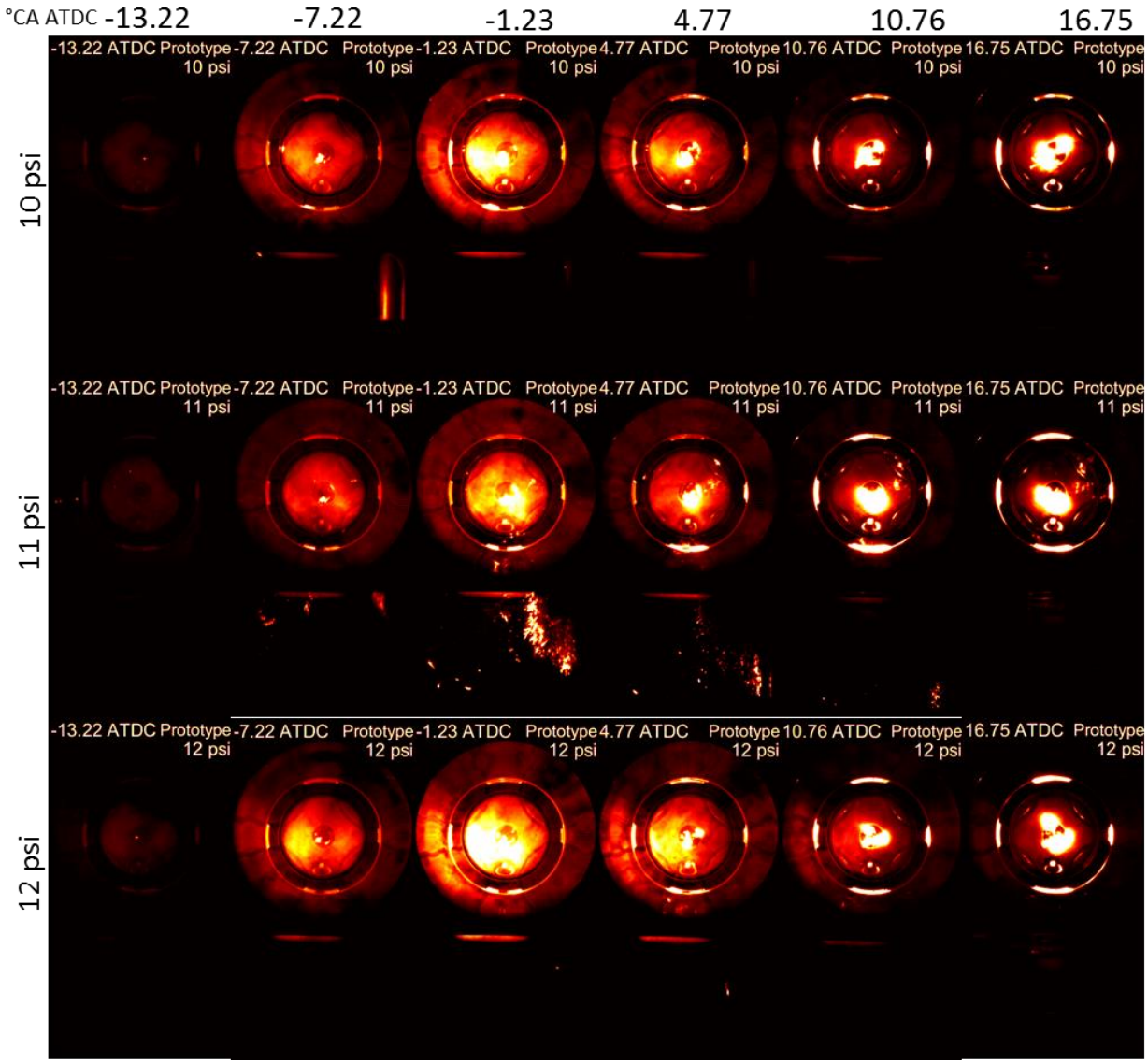

Figure 6.65 Combustion images – Prototype - various intake pressures (single inj.) – 30 µs

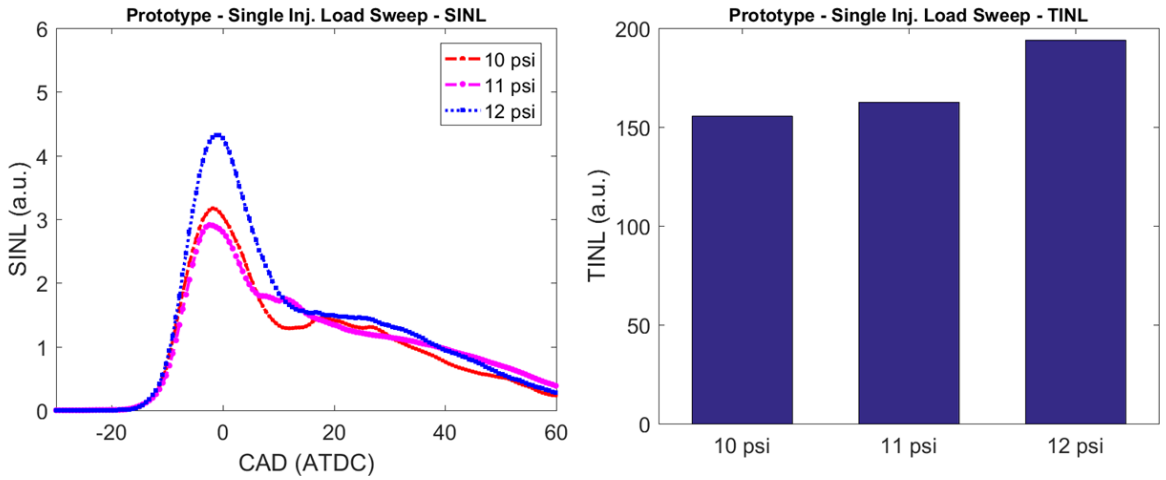

Figure 6.66 SINL and TINL – Prototype - various intake pressures (single inj.) – 30 µs

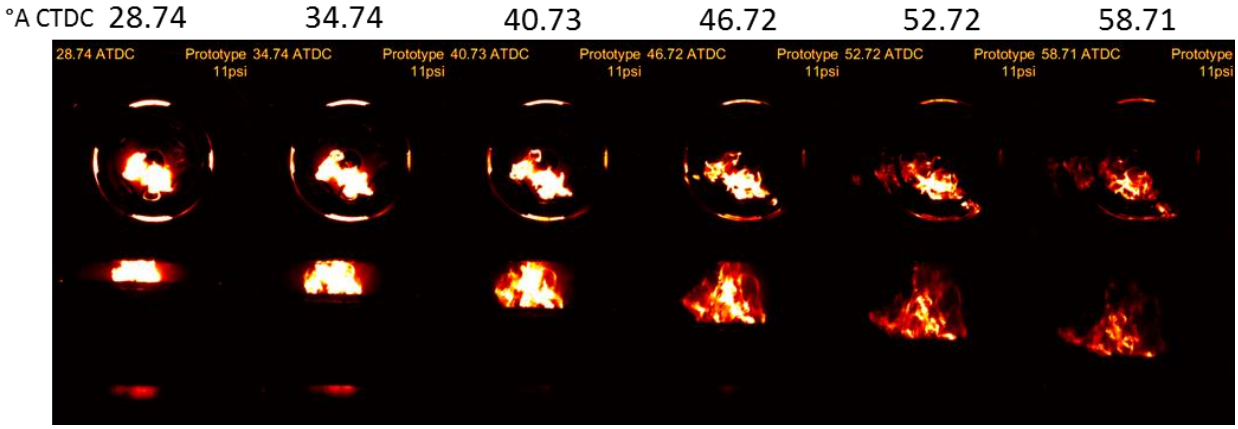

Figure 6.67 Late-cycle combustion images – Prototype – 11 psi (single inj.) – 30 µs

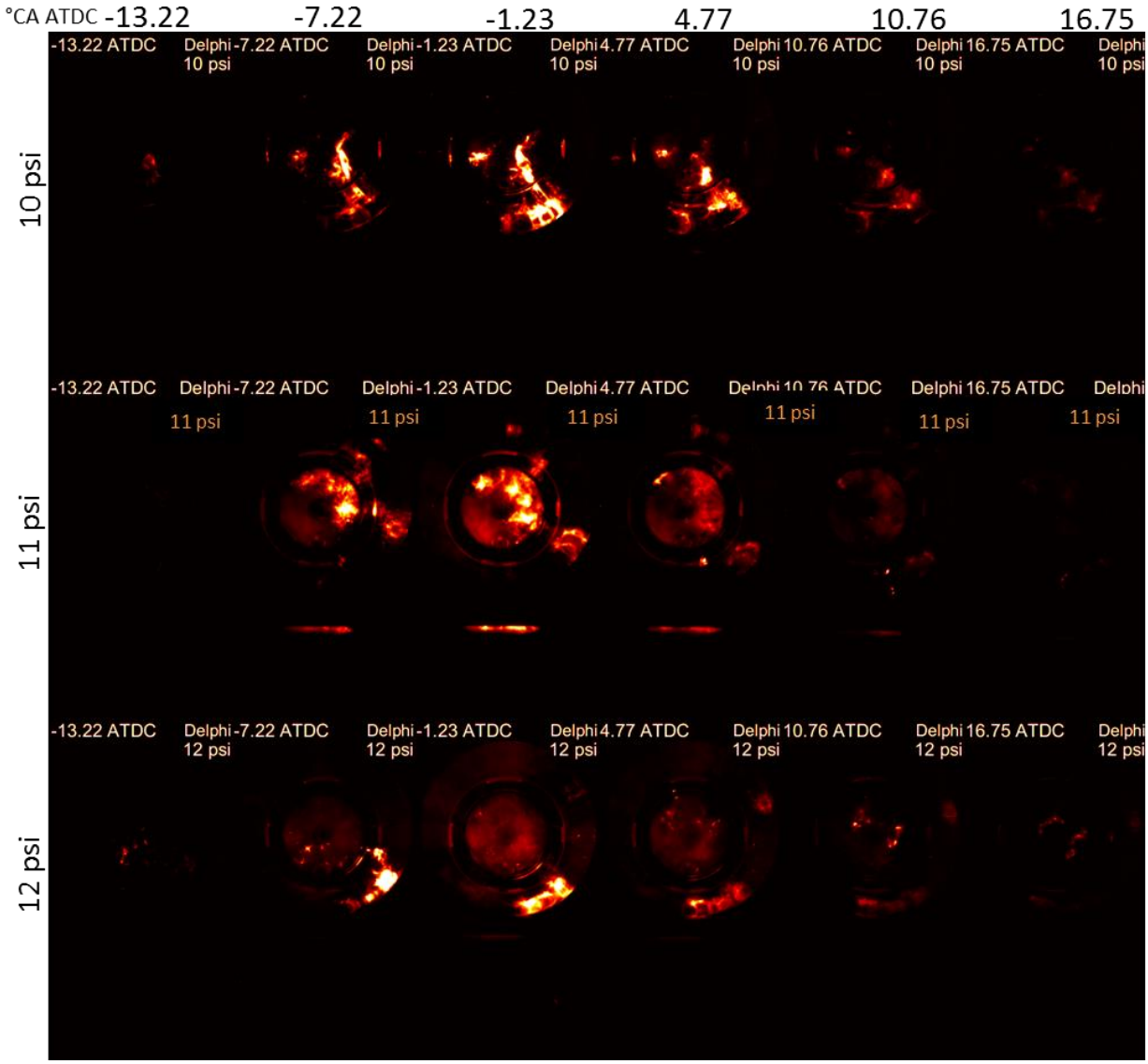

Figure 6.68 Combustion images – Delphi - various intake pressures (single inj.) – 10 µs

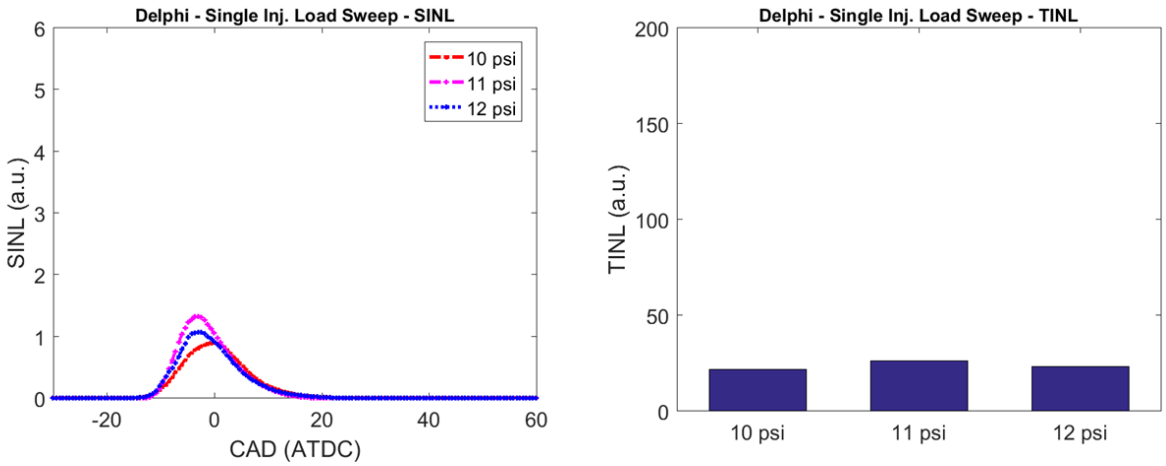

Figure 6.69 SINL and TINL – Delphi - various intake pressures (single inj.) – 10 µs

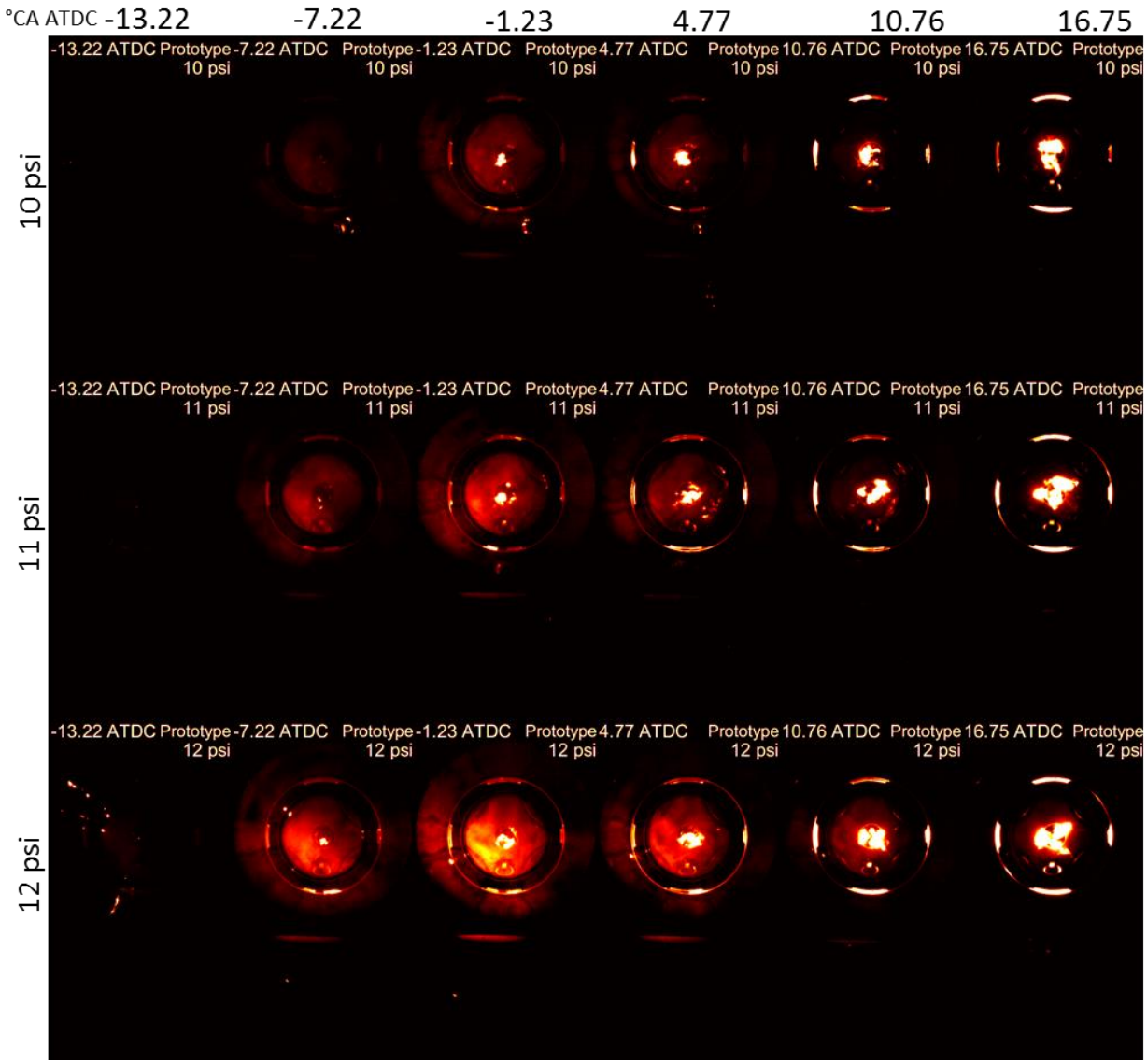

Figure 6.70 Combustion images – Prototype - various intake pressures (single inj.) – 10 µs

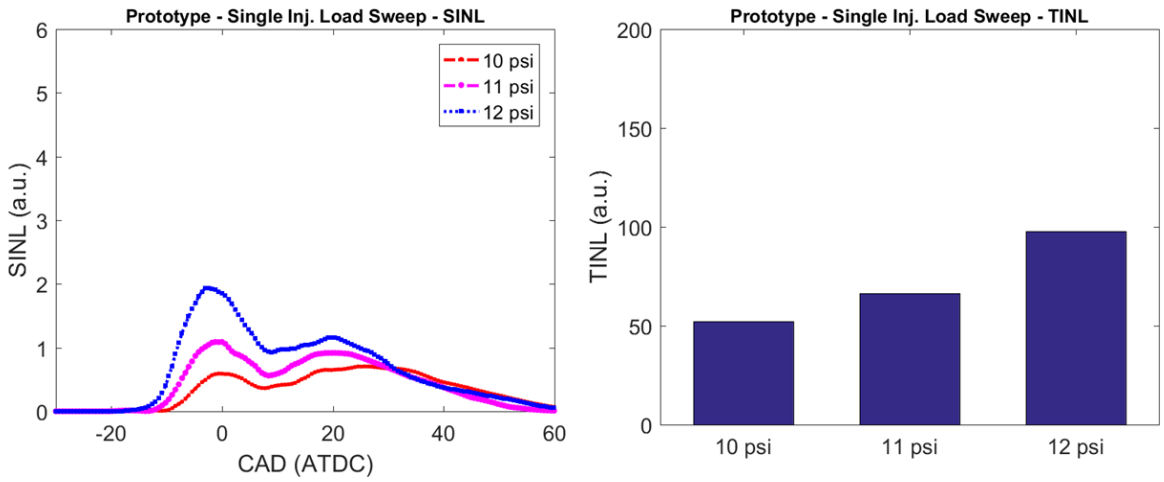

Figure 6.71 SINL and TINL – Prototype - various intake pressures (single inj.) – 10 µs

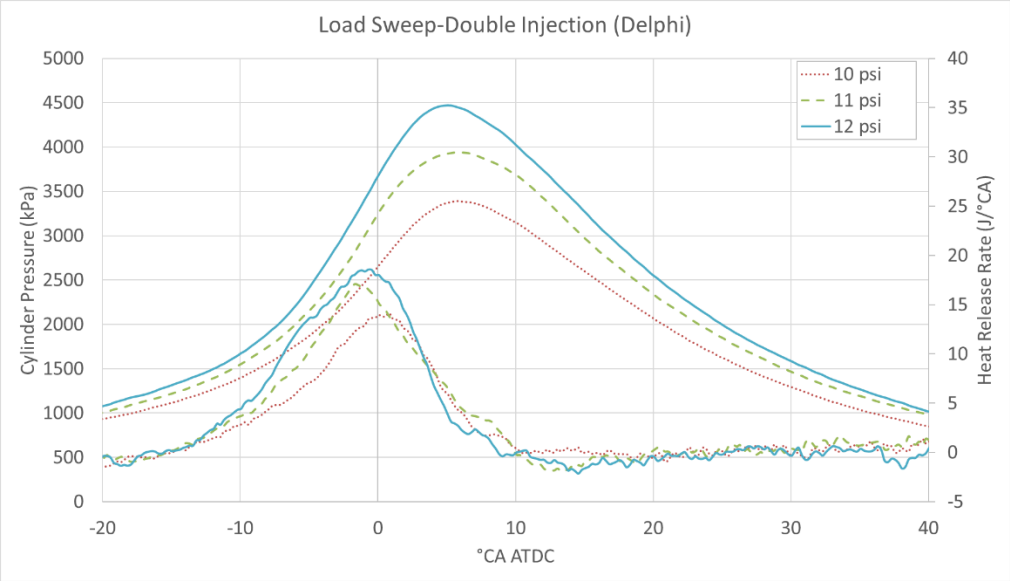

Figure 6.72 Pressure and HRR curves – Delphi – Intake pressure sweep (double inj.)

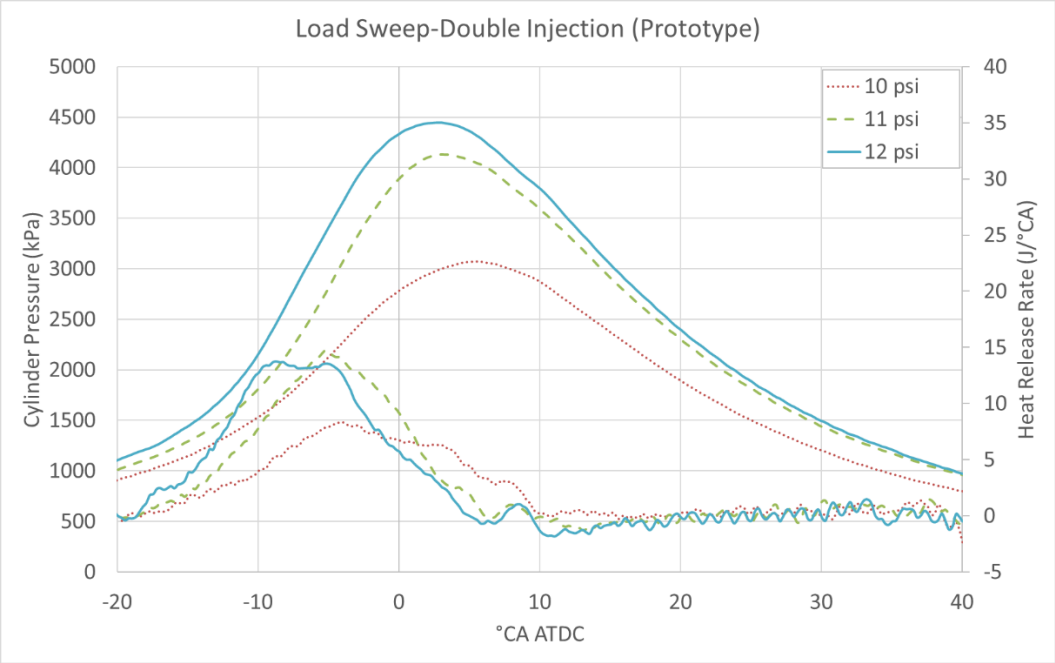

Figure 6.73 Pressure and HRR curves – Prototype – Intake pressure sweep (double inj.)

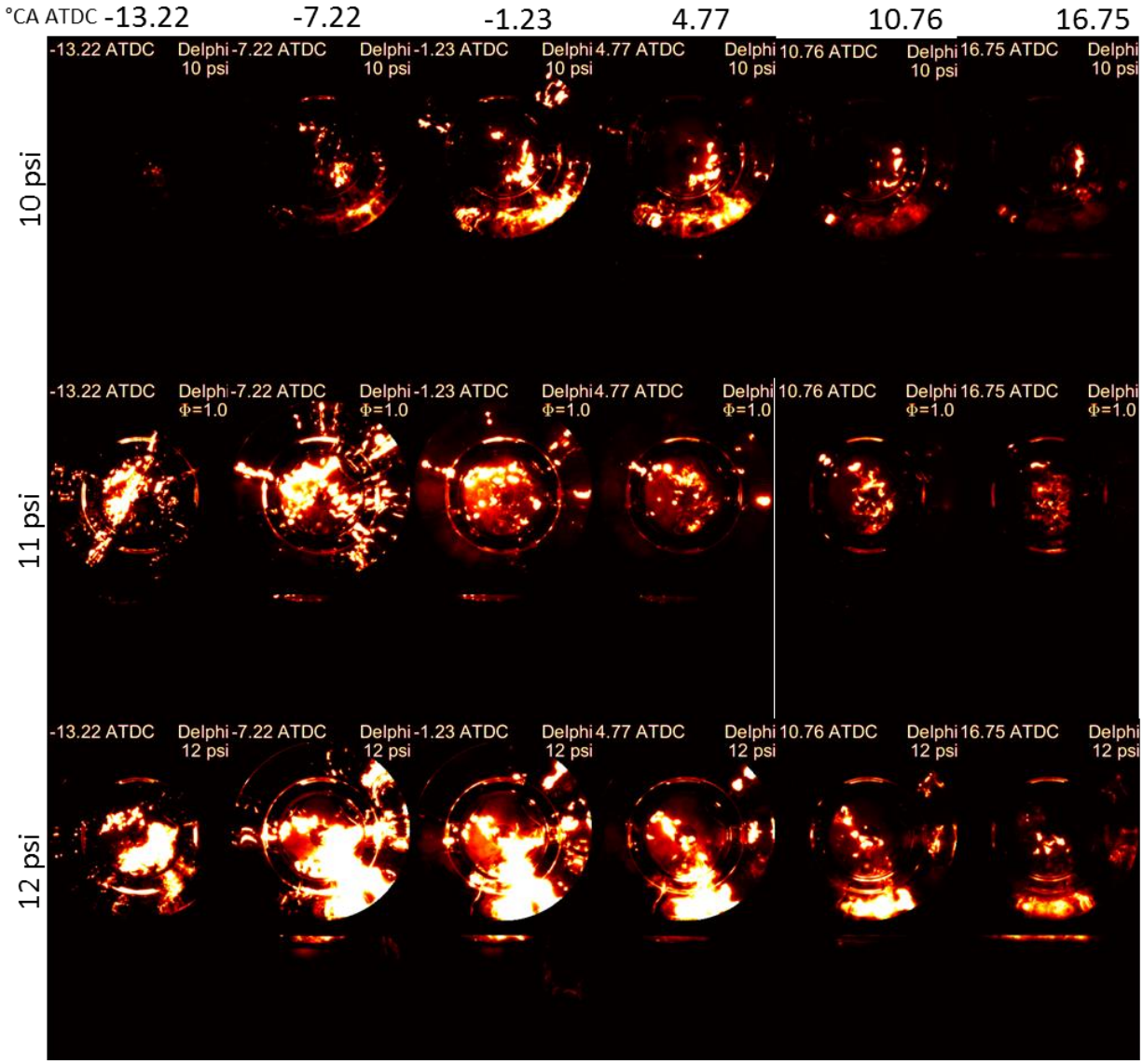

Figure 6.74 Combustion images – Delphi injector - various intake pressures (double inj.)

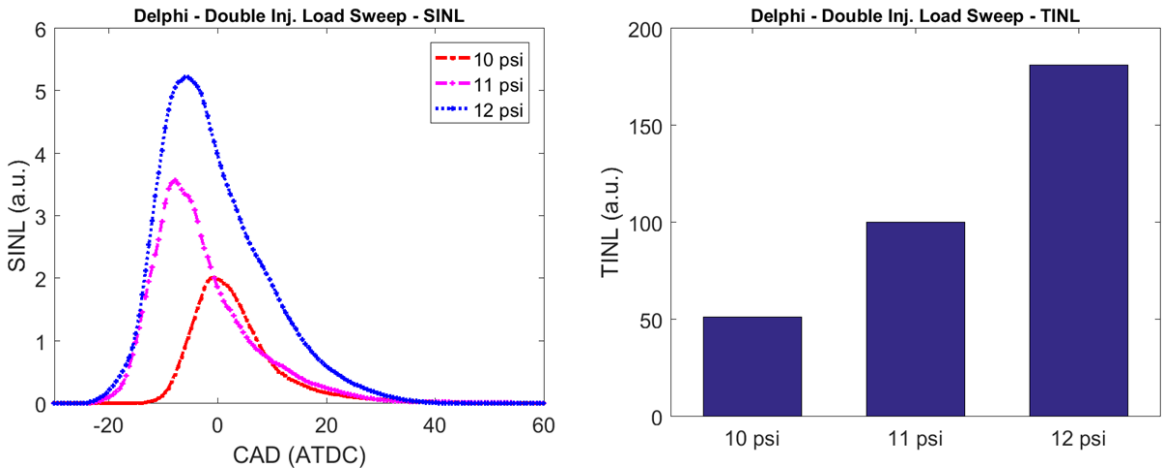

Figure 6.75 SINL and TINL – Delphi injector - various intake pressures (double inj.)

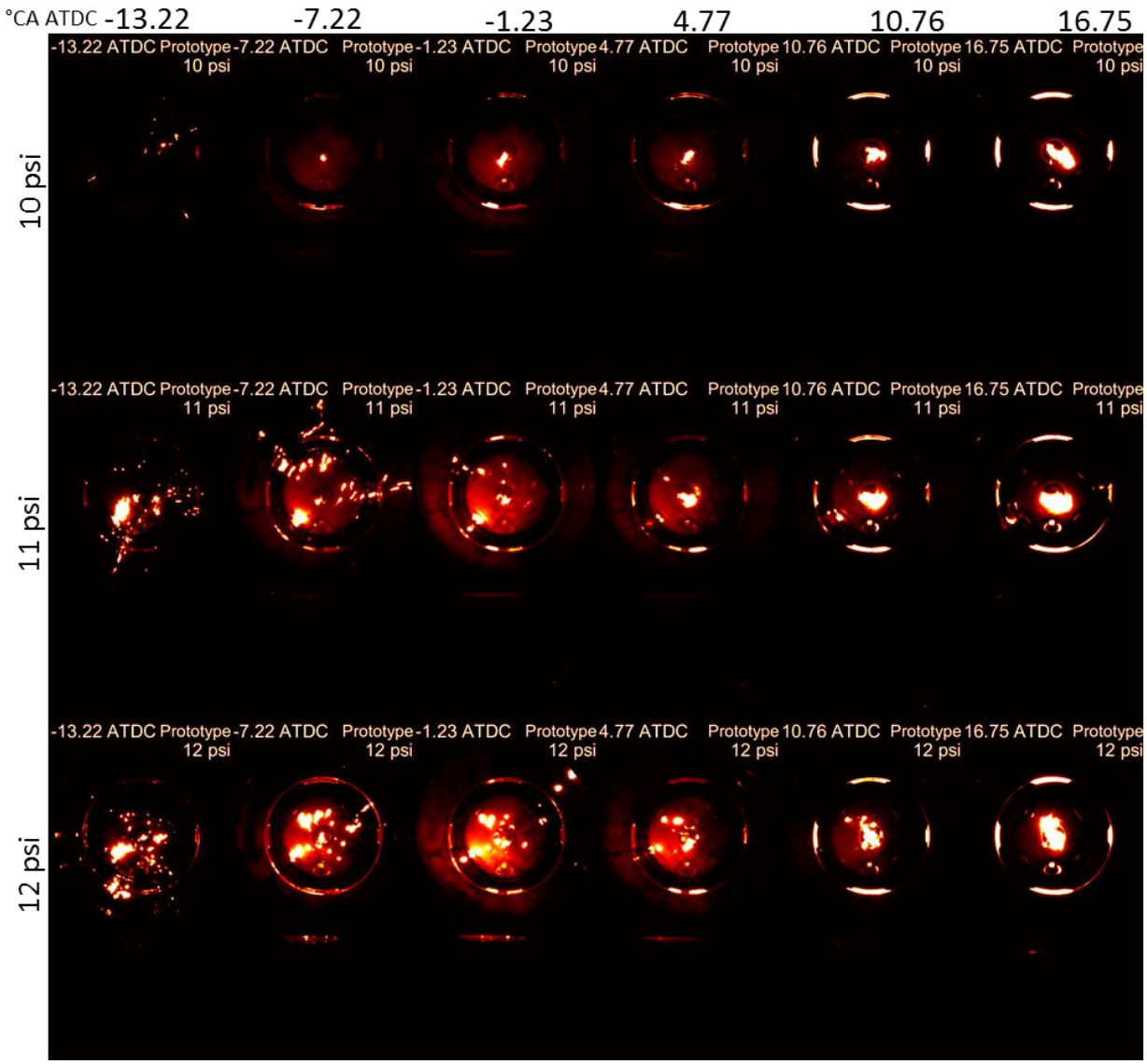

Figure 6.76 Combustion images – Prototype injector - various intake pressures (double inj.)

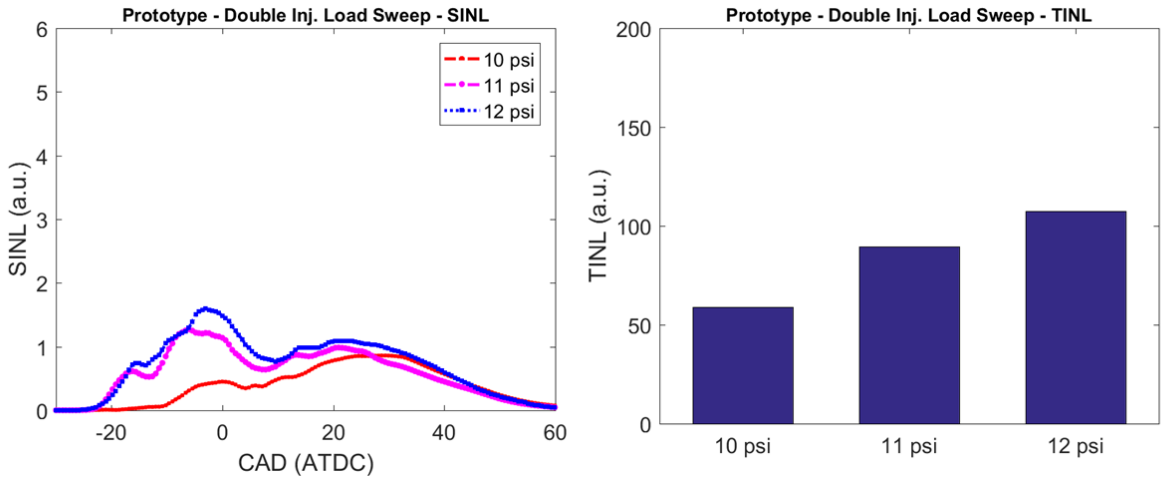

Figure 6.77 SINL and TINL – Prototype injector - various intake pressures (double inj.)

Chapter 7 Conclusions and Future Work

Conclusions of several parts of this study were offered at the end of the respective chapter. Here, some of the material is summarized and repeated for the convenience of the reader.

In Chapter 2, blends of pure ethanol-free gasoline and ABE (3:6:1 vol. % ratio), as well as neat ABE blends with varying A,B,E content were combusted in a PFI SI engine in addition to pure ethanol-free gasoline as a baseline for comparison, and the combustion performance and emission behavior were analyzed. The fuels were combusted at 1200 RPM, and 3 bar and 5 bar BMEP and measurements such as brake torque and emissions were made along with in-cylinder pressure data. Each fuel was tested across a range of equivalence ratios, from lean to rich.

- In-cylinder pressure data showed that the peak pressure of all the blends was slightly lower than that of gasoline, except for ABE80, which showed a slightly higher and advanced peak relative to gasoline. Blends with lower ABE content featured a slightly longer ignition delay and retarded 50% MFB location, which is attributed to the reduction in laminar flame speed due to ABE's charge cooling effect. Regarding the neat ABE tests, under gasoline MBT, the peak pressure of the ABE blends was slightly higher than that of gasoline, while ABE(3:6:1) also showed an advanced peak relative to gasoline. Under their MBTs, ABE(3:6:1), ABE(5:14:1) and n-butanol showed similar phasing, whereas ABE(6:3:1) and gasoline behaved similarly. Increasing n-butanol showed advanced combustion phasing (CA50) which is attributed to the increase in laminar flame speed due to butanol's higher flame speed.
- The BSFC increased steadily with increasing ABE fraction, due to the lower energy content of the blends and thus more fuel was required to match the power output of gasoline. However, ABE20's BSFC was within 5% of that of ABE0's. When using neat ABE blends,

the BTE of ABE(6:3:1) was higher than that of ABE0, whereas other fuels showed similar or slightly higher efficiency relative to ABE0.

- Emission data showed that CO decreased and UHC initially increased then decreased for all the blends, showing slightly enhanced air/fuel mixing and more fuel being partly oxidized, due to better spray collapse and mixing due to the presence of acetone (low boiling point). With respect to NO_x, no major changes were observed between gasoline and ABE, which was supported by the minor variations in exhaust gas temperature. With neat ABE blends, increasing n-butanol showed increased HC emissions and increased CO emissions, due to incomplete combustion. On the other hand, ABE(6:3:1) showed reduced HC emissions. CO for ABE(6:3:1) was roughly the same as that of ABE0. With respect to NO_x, no major changes were observed between gasoline and ABE(6:3:1), ABE(3:6:1), which was supported by the minor variations in exhaust gas temperature. However, further increase in butanol content steadily decreased NO_x emissions.

Based on these tests, a small amount of ABE(3:6:1) addition (<40%) can enhance thermal efficiency and reduce emissions. In the neat form, however, acetone addition could improve combustion quality significantly. This study affirms the potential of ABE to be used as an alternative fuel in SI engines.

In Chapter 3, pure diesel combustion and Diesel-CNG dual-fuel combustion were tested in a single-cylinder diesel research engine under different operating conditions.

- Based on the CNG substitution rate sweep, it was found that at 1200 RPM, and a 20 mg/cycle diesel equivalent load, 70 % CNG substitution provided the optimum combustion, with the

highest indicated thermal efficiency. Increasing the CNG % further deteriorated combustion quality.

- Based on the main injection timing sweep for 70% CNG at 1200 RPM and a 20 mg/cycle diesel equivalent load, 4^0 BTDC provided the highest indicated thermal efficiency. This is due to optimum combustion phasing. It appears that diesel-CNG dual-fuel combustion has an MBT diesel injection timing for different conditions that provides the highest torque.
- The pilot timing sweep for 70% CNG at 1200 RPM and a 20 mg/cycle diesel equivalent load shows that a 33% pilot split improved combustion, relative to a single diesel injection. This is because a higher spray area for CNG entrainment with a pilot fuel injection. Secondly, it was found that a pilot timing of 12^0 BTDC and main timing of 4^0 BTDC provided the highest dual-fuel combustion efficiency. The conditions that favor pure diesel combustion, also favor dual-fuel combustion because better diesel combustion provides better ignition and combustion for the CNG-air mixture.
- Based on multiple injection comparison, for 70% CNG dual-fuel combustion, the double diesel injection and triple diesel injection showed similar efficiencies – this is because the triple diesel injection reduces the main injection quantity, which reduces the spray area for proper CNG entrainment, and affects combustion phasing.
- For higher speeds and diesel equivalent loads, the injection timings must be advanced appropriately to maintain optimum combustion phasing.

Based on the experiments conducted, diesel-CNG dual-fuel combustion is able to achieve similar efficiency relative to pure diesel combustion. As such, CNG can be effectively used to substitute for diesel fuel in CI engines.

In Chapter 4, physicochemical characterization of soot from diesel/CNG dual-fuel combustion was performed using TGA, elemental analysis and HRTEM. Based on the observations, the following conclusions can be made:

- Soot oxidation reactivity increased significantly with increasing CNG content. Both the onset and the T50% temperatures were considerably lower for CNG soot.
- Elemental analysis showed that CNG soot was less "aged" relative to diesel soot.
- TEM results showed that number of particles in an aggregate decreases, as well as aggregate size, with increasing CNG due to less collisional aggregation. CNG soot has a larger distribution of particle sizes and the distribution shifts towards larger particle size with increasing CNG due to higher surface growth rate.
- HRTEM images showed that CNG70 soot appears to be immature due to shorter residence times (in spite of higher combustion temperature).
- Raman spectra showed no differences between the soot samples, indicating that initial nanostructure and orderliness of graphene layers does not affect reactivity. Therefore, Raman spectroscopy might not be a reliable method to assess reactivity for the cases tested.
- DRIFTS showed that CNG soot had markedly higher concentration of aliphatic groups and oxygen functional groups, which explains the high oxidation reactivity.
- When comparing particle sizes among different fuels, residence time alone does not provide enough information. It is essential to include reactivity in the discussion as well.

This is the first study of its kind for diesel/CNG soot characterization. With increase in CNG consumption as well as dual-fuel engines, it is necessary to understand how CNG soot differs from conventional diesel soot. Under the tested condition, it can be concluded that the use of CNG

affects the morphology, structure, chemical composition, and hence the reactivity of soot, which is relevant for design and operation of after-treatment devices.

In Chapter 5, diesel dual-fuel combustion was investigated in an optically accessible single-cylinder light duty diesel engine using a Phantom v7.3 color camera, in order to obtain high-speed combustion images, as well as soot temperature and soot volume fraction (KL factor) information using the two-color method. Pressure and HRR curves were also obtained simultaneously to study the combustion characteristics. Various CNG substitution ratios, loads and diesel injection strategies were investigated. The following observations were made from the study:

- From the NL images, it was observed that the premixed, entrained CNG mixture ignites first at multiple zones near the wall and these zones propagate towards the center. From the CNG substitution (premixed CNG/air Φ), the transition from diesel spray/diffusion combustion to a mechanism with a flame front was clearly observed. At Φ~0.38 and 0.47, no merging of reaction zones and wave-like flame propagation was observed. However, with increasing Φ~0.6, reaction zones were observed to merge and evidence of flame propagation was observed (previously only observed at Φ~0.9), wherein two waves approached each other from opposite sides. It is suspected that the early pilot injection of diesel enhances overall equivalence ratio distribution in the chamber, which leads to this behavior at relatively lower equivalence ratios. At CNG85, a single reaction zone was observed which developed into a flame front that began near the top of the frame and then spread out and propagated throughout the rest of the combustion chamber.
- From the images obtained using the 2-color method, it was found that the addition of a smaller amount of CNG (CNG30), enhanced the premixed combustion period (T > 2200 K)

and the diffusion combustion period is shortened. As the CNG substitution is increased further, the early high-temperature zone is reduced and relatively low-temperature diffusion combustion dominates the combustion process. At higher substitution ratios (CNG 70, CNG85), there are no high-temperature zones observed and the combustion is diffusion-dominant, predominantly showing a temperature T <2000 K, and the high soot concentration regions are negligible; the soot centration throughout the combustion chamber is 1.5<KL<2.5.

- It was found that using two diesel injections could enhance propagation of reaction zones towards the center, even at low equivalence ratios (Φ~0.4-0.6) and could thus, partly alleviate the unburned methane emissions issue at low loads. Compared to a single main diesel injection, when a pilot injection is added, combustion shifts considerably towards being more premixed, with a higher HRR peak and a shorter combustion duration. The first pilot injection affects the overall equivalence ratio distribution within the combustion chamber and thus enhances the rate of the initial premixed combustion period, which consists of auto-ignition of the premixed diesel fuel as well as the entrained CNG mixture. Compared to single diesel injection, more ignition zones all over the periphery of the chamber, including localized rich luminous zones within the lean premixed reaction zone were observed.
- Based on tests using different diesel injection strategies, it was observed that the main injection timing must be sufficiently separated from the pilot injection timing such that there is enough time for the diesel jets to be entrained by the CNG/air mixture and sufficiently advanced such that the increasing cylinder volume in the expansion stroke does not slow down the combustion process. Based on the soot temperature and KL factor results, it was found that the main injection timing had the most pronounced impact on the combustion

phasing and the soot temperature and KL factor distributions, while minor changes were observed with pilot injection timing variations and pilot/main injection mass variations.

In summary, this study shows through combustion visualization that multiple diesel injections could enhance overall fuel conversion in diesel dual-fuel combustion by enhancing the overall equivalence ratio distribution and thus the propagation of the reaction zones from the walls towards the center. This study also showed soot temperature and volume fraction results for the first time for CNG/diesel dual-fuel combustion.

In Chapter 6, a single-cylinder research optical diesel engine was modified into a spark ignition engine in order to investigate the Micro-Jet Enhanced Ignition (MJEI) – Embedded Micro-chamber (EMC) concept for high efficiency lean-burn combustion to address the efficiency and sooting concerns of lean-burn GDI combustion.

Combustion performance and emissions measurements along with optical investigation of the spray and combustion processes of various ethanol-gasoline blends (E20, E40, E60, E85) were performed. The observations can be summarized as follows:

- Addition of ethanol advances combustion phasing due to ethanol's higher flame speed. As a result, the peak combustion pressure is also higher. E60 shows the most advanced combustion phasing.
- E60 shows the highest IMEP under stoichiometric conditions. The indicated efficiency was also highest for E60 across the equivalence ratio range tested.
- The UHC emissions generally decrease with increasing ethanol content – under stoichiometric conditions As far as the CO emissions are concerned, they increase with

ethanol content, under stoichiometric conditions. This is likely due to the higher fuel-borne oxygen content as ethanol content is increased.

- NO_x emissions decrease initially with E40 but increase with increasing ethanol content, with E60 and E85 showing values greater than both E20 and E40. Generally, NO_x trends agree with the peak pressure trends. Soot emissions decrease steadily with decreasing equivalence ratio and with increasing ethanol content. The higher fuel-borne oxygen content significantly enhances soot oxidation and reduces tailpipe soot emissions.
- From the spray imaging, it was found that the spray jets become finer as ethanol content increases. The spray jets show a clearer, more defined spray boundary. This is likely related to the higher viscosity and surface tension of ethanol, which both resist 'break-up'.
- The overall flame luminosity decreases with increasing ethanol content. From the SINL data, it can be observed that peak luminosity (soot formation) decreases with increasing ethanol content; and from the TINL data, it can be concluded that with ethanol content of 40% vol. or higher, significant reduction of soot can be achieved.
- When a double injection strategy is used, the combustion duration is extended due to the slower combustion rate of the diffusion-like combustion of the second injection as well as the combustion rate being slowed down by expansion cooling in the early power stroke. This extended combustion duration provides more time for soot oxidation as seen by the slow rate of soot oxidation in the SINL curves.
- These tests demonstrate that using ethanol-gasoline blends with the two-zone piston has the potential to enable low-sooting, stable, and efficient combustion at equivalence ratios up to 0.6.

Combustion performance and emissions measurements along with optical investigation of the spray and combustion process comparing the commercial and prototype injectors were also performed. The following observations were made:

- The Prototype injector has two sets of holes, one set with six jets spaced 60° apart radially (narrow-angle group), and a second set spaced 120° apart (wide-angle group). Based on the SMD shown, it can be observed that the Delphi injector shows superior atomization.
- For the same intake pressure and injected fuel mass, the prototype injector shows a lower IMEP and thus, a lower indicated efficiency, with the efficiency being lower by almost 2 percentage points, across the load and equivalence ratio range tested.
- Similar or slightly better stability relative to the Delphi injector at stoichiometric conditions, however, at leaner conditions ($\Phi = 0.8$), the stability is drastically reduced to unacceptable levels.
- The wide-angle group shows impingement on the side window and significant wall-wetting. This forms a rather thick fuel film on the combustion chamber walls; the narrow-angle spray causes significant impingement and wall-wetting on the piston surface, which causes a large amount of UHC emissions. Due to a large portion of the fuel being lost as UHC emissions, the available combustible mixture gets leaned out, causing low CO, high NO_x and low soot emissions, relative to the Delphi injector.
- It was found that there is a remarkable difference between the combustion process using the two injectors. In the prototype cases, after an initial combustion period observed as a uniform distribution of luminance throughout the combustion chamber, combustion of the film formed in the bowl region due to wetting from the narrow-angle group of orifices is observed. This is reflected by the second stage of soot formation and oxidation reflected in the SINL

curves. As a result, the TINL values for the prototype cases are significantly higher (more than twice) than those observed for the corresponding Delphi cases.

- Compared to the single injection case, the second peak on the SINL curve is much more pronounced for the double injection case due to the second injection, which further exacerbates the wetting issue.
- In the future, it is expected that combustion performance and emissions characteristics could be significantly improved by tuning the prototype injector to have better atomization and shorter jet penetration.

Future Work

Planar measurement in the DIATA optical engine

The DIATA optical engine has two additional side windows, which can be used for planar measurements. Currently, these windows are sealed with metal blocks. Once they are replaced with quartz side windows (there are spares in the lab), a laser sheet can be introduced through and planar measurement will be possible. One can either use the current copper vapor laser or the Nd:YAG laser (once it is fully operational) to produce the laser sheet. By using the former one, a set of specific sheet optics provided by Oxford laser can be used to transform the scatter beam from the laser fibers into a collimated beam so that the flexibility of the laser fiber (to deliver the laser beam to a place far away from the laser source) will be maintained. Several types of planar measurement can be conducted including MIE, PIV, CH- and OH-PLIF. The planar MIE measurement will eliminate the background noise caused by the illumination of the side of the optical piston thus providing more accurate quantitative analysis on the liquid penetration and spray cone angle. PIV measurement will reveal the flow field in the optical engine, providing

valuable data for simulation validation. OH-PLIF will be another interesting study as OH radical is a good indicator of the combustion start and actual flame structure. Combining OH-PLIF and 2D soot imaging may shed more insight on the soot formation and oxidation mechanism. The current high-speed imaging could be much improved by acquiring much more powerful color high-speed cameras with temporal resolution up to ~ 100,000 fps while maintaining a reasonable spatial resolution.

Physico-chemical characterization of PM from alternative fuel combustion

This dissertation has demonstrated the value of using multiple materials research techniques such as HRTEM, TGA, Raman, DRIFTS, and CHN analysis to study particulate matter from engine exhaust. The same can be applied to study exhaust from several alternative fuels that have been gaining a lot of interest recently such as ABE, and from alternative combustion strategies/regimes such as lean-stratified GDI, gasoline compression ignition (GCI) etc. The sampling system developed and used in this dissertation can be easily fitted on the exhaust pipe of any of the engines in the lab. The Frederick Seitz MRL on the UIUC campus has the equipment to apply the techniques used in this thesis, as well as many others such as X-ray Diffraction (XRD) spectroscopy, Auger Electron spectroscopy (AES) etc., which have been used by other researchers to study PM.

References

1. Annual Energy Review 2011, Energy Information Administration U.S. Department of Energy. www.eia.gov/totalenergy/data/annual/pdf/aer.pdf
2. EPA, Light-Duty Automotive Technology, Carbon Dioxide Emissions, and Fuel Economy Trends: 1975 through 2012, March 2013
3. Annual Energy Outlook 2012, Energy Information Administration U.S. Department of Energy. www.eia.gov/forecasts/aeo/pdf/0383(2012).pdf
4. www.deere.com/wps/dcom/en_US/services_and_support/emissions_information/understanding_emission_regulations/regulations.page
5. Polonowski, C. J., Mueller, C. J., Gehrke, C. R., Bazyn, T., et al., "An Experimental Investigation of Low-Soot and Soot-Free Combustion Strategies in a Heavy-Duty, Single-Cylinder, Direct-Injection," Optical Diesel Engine, SAE 2011-01-1812, 2011
6. Johnson, T., V., "Review of Diesel Emissions and Control," SAE 2010-01-0301, 2010
7. Dollmeyer, T. A., Vittorio, D. A., Grana, T. A., Katzenmeyer, J. R., et al., "Meeting the US 2007 Heavy-Duty Diesel Emission Standards - Designing for the Customer," SAE 2007-01-4170, 2007.
8. He, B-Q., Liu, M-B., Yuan, J., and Zhao H., "Combustion and emission's characteristics of a HCCI engine fuelled with n-butanol–gasoline blends," Fuel 2013; 108:668–74. http://dx.doi.org/10.1016/j.fuel.2013.02.026.
9. Ranjan, A., and Moholkar, V. S., "Biobutanol: science, engineering, and economics," Int. J. Energy Res. 2012; 36:277–323 DOI: 10.1002/er

10. Boretti, A., Lappas, P., Zhang, B., and Mazlan, S. K., "CNG Fueling Strategies for Commercial Vehicles Engines-A Literature Review," SAE Technical Paper 2013-01-2812, doi:10.4271/2013-01-2812

11. Seagrave, J., McDonald, J. D., Bedrick, E., Edgerton, E. S., et al., "Lung toxicity of ambient particulate matter from southeastern US sites with different contributing sources: relationships between composition and effects," Environ. Health Perspect. (2006) 1387–1393.

12. Wang, C., Xu, H., Herreros, J. M., Wang, J., et al., "Impact of fuel and injection system on particle emissions from a GDI engine," Applied Energy 2014; 132:178-191, http://dx.doi.org/10.1016/j.apenergy.2014.06.012

13. Abdi, H. K., Alanazi, K. F., Rohani, A. S., Mehrani, P. and Thibault, J., "Economic comparison of a continuous ABE fermentation with and without the integration of an in situ vacuum separation unit," Can. J. Chem. Eng. 2016, 94: 833–843. doi:10.1002/cjce.22461

14. Kumar, M., Goyal, Y., Sarkar, A., Gayen, K., "Comparative economic assessment of ABE fermentation based on cellulosic and non-cellulosic feedstocks," Applied Energy, Volume 93, May 2012, Pages 193-204, ISSN 0306-2619, http://dx.doi.org/10.1016/j.apenergy.2011.12.079.

15. Lee, S. Y., Park, J. H., Jang, S. H., Nielsen, L. K., Kim, J. and Jung, K. S. (2008), "Fermentative butanol production by clostridia," Biotechnol. Bioeng., 101: 209–228. doi:10.1002/bit.22003

16. Adhami, L., Griggs, B., Himerbrook, P., Taconi, K., “Liquid-liquid extraction of butanol from dilute aqueous solutions using soybean-derived biodiesel,” J Am Oil Chem Soc 2009;86:1123e8.

17. Ishizaki, A., Michiwaki, S., Crabbe, E., Kobayashi, G., Sonomoto, K., Yoshino, S., “Extractive acetone–butanol–ethanol fermentation using methylated crude palm oil as extractant in batch culture of Clostridium saccharoperbutylacetonicum N1–4 (ATCC 13564),” J Biosci Bioeng 2009 87:352–356.

18. Crabbe, E., Nolasco-Hipolito, C., Kobayashi, G., Sonomoto, K., Ishizaki, A., “Biodiesel production from crude palm oil and evaluation of butanol extraction and fuel properties,” Process Biochem 2001 37:65–71.

19. Grobben, N. G., Eggink, G., Cuperus, F. P., Huizing, H., J., “Production of acetone, butanol, and ethanol (ABE) from potato wastes: fermentation with integrated membrane extraction,” Appl Microbiol Biotechnol 1993 39:494–498.

20. Abdehagh, N., Tezel, F. H., Thibault, J., “Separation techniques in butanol production: Challenges and developments,” Biomass and Bioenergy, Volume 60, January 2014, Pages 222-246, ISSN 0961-9534, http://dx.doi.org/10.1016/j.biombioe.2013.10.003.

21. Ranjan, A., and Moholkar, V. S., “Biobutanol: science, engineering, and economics,” Int. J. Energy Res. 2012; 36:277–323 DOI: 10.1002/er

22. Yen, H-W., Wang, Y-C., “The enhancement of butanol production by in situ butanol removal using biodiesel extraction in the fermentation of ABE (acetone–butanol–ethanol),” Bioresource Technology, Volume 145, October 2013, Pages 224-228, ISSN 0960-8524, http://dx.doi.org/10.1016/j.biortech.2012.11.039.

23. Tashiro, Y., Yoshida, T., Noguchi, T., Sonomoto, K., “Recent advances and future prospects for increased butanol production by acetone-butanol-ethanol fermentation,” Eng. Life Sci. 2013, 13, 432–445, DOI**:** 10.1002/elsc.201200128

24. Kurkijärvi, A. J., and Lehtonen, J., “Dual Extraction Process for the Utilization of an Acetone−Butanol−Ethanol Mixture in Gasoline,” dx.doi.org/10.1021/ie500131x | Ind. Eng. Chem. Res. 2014, 53, 12379−12386

25. Kujawska, A., J. Kujawski, M. Bryjak, W. Kujawski, “ABE fermentation products recovery methods—A review,” Renewable and Sustainable Energy Reviews 48(2015) 648–661, http://dx.doi.org/10.1016/j.rser.2015.04.028.

26. Chotwichien, A., Luengnaruemitchai, A., Jai-In, S., “Utilization of palm oil alkyl esters as an additive in ethanol–diesel and butanol–diesel blends,” Fuel 2009, 88:1618–1624.

27. Li, Q., Cai, H., Hao, B., Zhang, C., Yu, Z., Zhou, S., Chenjuan, L., “Enhancing clostridial acetone–butanol–ethanol (ABE) production and improving fuel properties of ABE-enriched biodiesel by extractive fermentation with biodiesel” Applied Biochemistry and Biotechnology 2010, 162, 2381–2386.

28. Zheng, Z., Li, C., Liu, H., Zhang, Y., et al., “Experimental study on diesel conventional and low temperature combustion by fueling four isomers of butanol,” Fuel 2015;141:109–19. http://dx.doi.org/10.1016/j.fuel.2014.10.053

29. Zheng, Z., Yue, L., Liu, H., Zhu, Y., et al., “Effect of two-stage injection on combustion and emissions under high EGR rate on a diesel engine by fueling blends of diesel/gasoline, diesel/n-butanol, diesel/gasoline/n-butanol and pure diesel,” Energy Convers Manage 2015;90:1–11. http://dx.doi.org/10.1016/j.enconman.2014.11.011

30. Liu, H., Wang, X., Zheng, Z., Gu, J., et al., “Experimental and simulation investigation of the combustion characteristics and emissions using n-butanol/biodiesel dual-fuel injection on a diesel engine,” Energy 2014;74:741–52. http://dx.doi.org/10.1016/j.energy.2014.07.041

31. Liu, H., Huo, M., Liu, Y., Wang, X., et al., “Time-resolved spray, flame, soot quantitative measurement fueling n-butanol and soybean biodiesel in a constant volume chamber under various ambient temperatures,” Fuel 2014;133:317–25. http://dx.doi.org/10.1016/j.fuel.2014.05.038

32. Liu, H., Li, S., Zheng, Z., Xu, J., et al., “Effects of n-butanol, 2-butanol, and methyl octynoate addition to diesel fuel on combustion and emissions over a wide range of exhaust gas recirculation (EGR) rates,” Appl. Energy 2013;112:246–56. http://dx.doi.org/10.1016/j.apenergy.2013.06.023

33. Masum, B. M., Kalam, M. A., Masjuki, H. H., Palash, S. M., et al., “Performance and emission analysis of a multicylinder gasoline engine operating at different alcohol-gasoline blends,” RSC Adv 2014;4:27898. http://dx.doi.org/10.1039/c4ra04580g

34. Costagliola, M. A., De Simio. L., Iannaccone, S., Prati, M. V., “Combustion efficiency and engine out emissions of a SI engine fueled with alcohol/gasoline blends,” Appl Energy 2013;111:1162–71. http://dx.doi.org/10.1016/j.apenergy.2012.09.042

35. Alasfour, F.N., “Butanol – a single-cylinder engine study: availability analysis,” Appl Therm Eng 17(6):537–49, 1997, doi:10.1016/S1359-4311(96)00069-5.

36. Alasfour, F.N., “Effect of using 30% iso-butanol–gasoline blend on hydrocarbon emissions from a spark-ignition engine,” Energy Sources 21(5):379–94, 1999, doi: 10.1080/00908319950014704.

37. Williams, J., Goodfellow, C., Lance, D., Ota, A., et al., "Impact of butanol and other biocomponents on the thermal efficiency of prototype and conventional engines," SAE technical paper 2009-01-1908; 2009. http://dx.doi.org/10.4271/2009-01-1908

38. Dernotte, J., Mounaim-Rousselle, C., Halter, F., Seers, P., "Evaluation of butanol–gasoline blends in a port fuel-injection, spark-ignition engine," Oil Gas Sci Technol – Rev IFP 2010; 65(2):345–51. http://dx.doi.org/10.2516/ogst/2009034

39. Wigg, B., Coverdill, R., Lee, C. F., Kyritsis, D., "Emissions characteristics of neat butanol fuel using a port fuel-injected, spark-ignition engine," SAE technical paper 2011-01-0902; 2011. http://dx.doi.org/10.4271/2011-01-0902

40. Venugopal, T., Ramesh, A., "Performance, combustion and emission characteristics of a spark-ignition engine with simultaneous injection of n-butanol and gasoline in comparison to blended butanol and gasoline," Int J Energy Res 2014;38:1060–74. http://dx.doi.org/10.1002/er.3113

41. Gu, X., Huang, Z., Cai, J., Gong, J., et al., "Emission characteristics of a spark-ignition engine fuelled with gasoline-n-butanol blends in combination with EGR," Fuel 2012;93:611–7. http://dx.doi.org/10.1016/j.fuel.2011.11.040

42. Yacoub. Y., Bara, R., Gautam, M., "The performance and emission characteristics of C1–C5 alcohol–gasoline blends with matched oxygen content in a single cylinder spark ignition engine," Proc Inst Mech Eng, Part A: J Power Energy 1998;212(5):363–79. http://dx.doi.org/10.1243/0957650981536934

43. Szwaja, S., Naber, J, D., "Combustion of n-butanol in a spark-ignition IC engine," Fuel 2010;89:1573–82. http://dx.doi.org/10.1016/j.fuel.2009.08.043

44. Wallner, T., Miers, S. A., McConnell, S., “A comparison of ethanol and butanol as oxygenates using a direct-injection, spark-ignition engine,” J Eng Gas Turbines Power 2009;131(3). http://dx.doi.org/10.1115/1.3043810 .

45. Wallner, T., Frazee, R., “Study of regulated and non-regulated emissions from combustion of gasoline, alcohol fuels and their blends in a DI-SI engine” SAE technical paper 2010-01-1571; 2010. http://dx.doi.org/10.4271/2010-01-1571.

46. Chang, Y-C., Lee, W-J., Lin, S-L., Wang, L-C., “Green energy: water containing acetone–butanol–ethanol diesel blends fueled in diesel engines,” Appl Energy 2013;109:182–91. http://dx.doi.org/10.1016/j.apenergy.2013.03.086.

47. Van Geem, K. M., Cuoci, A., Frassoldati, A., Pyl, S. P., et al., “An experimental and kinetic modeling study of pyrolysis and combustion of acetone–butanol–ethanol (ABE) mixtures,” Combust Sci Technol 2012;184:942–55, http://dx.doi.org/10.1080/00102202.2012.663987.

48. Wu, H., Nithyanandan, K., Li, B., Huo, M., Zhou, N., Lee, C., Zhang, C., “Investigation on spray and soot lift-off length of ABE–diesel blend in a constant volume chamber with diesel engine conditions,” Proc. ASME. 46162; volume 1: large bore engines; fuels; advanced combustion; emissions control systems, V001T02A011; October 19, 2014, ICEF2014-5645. http://dx.doi.org/10.1115/ICEF2014-5645

49. Wu, H., Nithyanandan, K., Lee, T. H., Lee, C. F., Zhang, C., “Spray and combustion characteristics of neat acetone–butanol–ethanol, n-butanol, and diesel in a constant volume chamber,” Energy Fuels 2014;28(10):6380–91. http://dx.doi.org/10.1021/ef5013819

50. Wu, H., Nithyanandan, K., Zhou, N., Lee, T. H., Lee, C. F., Zhang, C., “Impacts of acetone on the spray combustion of acetone–butanol–ethanol (ABE)–diesel blends under low

ambient temperature" Fuel 2015;142:109–16. http://dx.doi.org/10.1016/j.fuel.2014.10.009 .ISSN 0016-2361.

51. Zhou, N., Huo, M., Wu, H., Nithyanandan, K., Lee, C. F., Wang, Q., et al., "Low temperature spray combustion of acetone–butanol–ethanol (ABE) and diesel blends," Appl Energy 2014;117:104–15. http://dx.doi.org/10.1016/j.apenergy.2013.11.035. ISSN 0306-2619

52. Wu, H., Huo, M., Zhou, N., Nithyanandan, K., et al., "An experimental investigation of the combustion characteristics of acetone–butanol–ethanol-diesel blends with different ABE component ratios in a constant volume chamber," SAE technical paper 2014-01-1452; 2014. http://dx.doi.org/10.4271/2014-01-1452

53. Lin, Y., Wu, H., Nithyanandan, K., Lee, T. H., Lee, C. F., Zhang, C., "Investigation of high percentage acetone–butanol–ethanol (ABE) blended with diesel in a constant volume chamber," Proc. ASME. 46162; volume 1: large bore engines; fuels; advanced combustion; emissions control systems, V001T02A012; October 19, 2014, ICEF2014-5649. http://dx.doi.org/10.1115/ICEF2014-5649.

54. Liu, F., Liu, L., Feng, X., "Separation of acetone–butanol–ethanol (ABE) from dilute aqueous solutions by pervaporation," Sep Purif Technol 2005;42(3):273–82. http://dx.doi.org/10.1016/j.seppur.2004.08.005

55. García, V., Päkkilä, J., Ojamo, H., Muurinen, E., et al., "Challenges in bio-butanol production: how to improve efficiency," Renew Sustain Energy Rev 2011;15 (2):964–80. http://dx.doi.org/10.1016/j.rser.2010.11.008

56. Dirrenberger, P., Glaude, P. A., Bounaceur, R., Gall, H., et al., “Laminar burning velocity of gasolines with addition of ethanol,” Fuel 2014;115:162–9. http://dx.doi.org/10.1016/j.fuel.2013.07.015

57. van Lipzig, J. P. J., Nilsson, E. J. K., de Goey, L. P. H., Konnov, A. A., “Laminar burning velocities of n-heptane, iso-octane, ethanol and their binary and tertiary mixtures,” Fuel 2011;90:2773–81. http://dx.doi.org/10.1016/j.fuel.2011.04.029

58. Aleiferis, P. G., Serras-Pereira, J., Richardson, D., “Characterization of flame development with ethanol, butanol, iso-octane, gasoline and methane in a direct-injection spark-ignition engine,” Fuel 2011;109:256–78. http://dx.doi.org/10.1016/j.fuel.2012.12.088

59. Aleiferis, P., Malcolm, J., Todd, A., Cairns, A., et al., “An optical study of spray development and combustion of ethanol, iso-octane and gasoline blends in a DISI engine,” SAE technical paper 2008-01-0073; 2008. http://dx.doi.org/104271/2008-01-0073

60. Andrae, J.C.G., “Development of a detailed kinetic model for gasoline surrogate fuels,” Fuel 87:2013-2022, 2008, doi:10.1016/j.fuel.2007.09.010.

61. Kalghatgi, G. T., Hildingsson, L., Harrison, A. J., Johansson, B., “Autoignition quality of gasoline fuels in partially premixed combustion in diesel engines,” Proceedings of the Combustion Institute 33:3015–3021, 2011, doi: http://dx.doi.org/10.1016/j.proci.2010.07.007 .

62. Demirbas, A. “Methane gas Hydrate”, Springer Science and Business Media, (2010).

63. Lijiang, W., Peng, G., “A review on natural gas/diesel dual fuel combustion, emissions and performance,” Fuel Processing Technology, Volume 142, February 2016, Pages 264-278, ISSN 0378-3820, http://dx.doi.org/10.1016/j.fuproc.2015.09.018 .

64. Semin, R. A. B., “A Technical Review of Compressed Natural Gas as an Alternative Fuel for Internal Combustion Engines,” American J. of Engineering and Applied Sciences, 1 (4): 302-311, 2008 ISSN 1941-7020.

65. Poulton, M.L., 1994. “Alternative Fuels for Road Vehicles”, Comp. Mechanics Publications, UK.

66. Korakianitis, T., Namasivayam, A. M., Crookes, J., “Natural-gas fueled spark-ignition (SI) and compression-ignition (CI) engine performance and emissions,” Progress in Energy and Combustion Science, Volume 37, Issue 1, February 2011, Pages 89-112, ISSN 0360-1285, http://dx.doi.org/10.1016/j.pecs.2010.04.002 .

67. McTaggart-Cowan, G., Rogak, S., Hill, P., Munshi, S., Bushe, W., “The effects of fuel dilution in a natural-gas direct-injection engine,” Proc. Inst. Mech. Eng. D J. Automob. Eng., 222 (3) (2008), pp. 441–453.

68. McTaggart-Cowan, G. P., Jones, H. L., Rogak, S. N., Bushe, W. K., Hill, P. G., and Munshi, S. R., "The effects of high-pressure injection on a compression–ignition, direct injection of natural gas engine." Journal of engineering for gas turbines and power 129, no. 2 (2007): 579-588.

69. Olsen, J., Crookes, R. J. and Bob-Manuel, K. D. H., “Experiments in dual fuelling a compression ignition engine by injecting di-methyl ether as a pilot fuel to ignite varying quantities of natural gas” SAE Technical Paper 2007-01-3624.

70. McTaggart-Cowan, G. P., Reynolds, C. C. O., and Bushe, W. K. "Natural gas fuelling for heavy-duty on-road use: current trends and future direction." International journal of environmental studies 63, no. 4 (2006): 421-440.

71. Papagiannakis, R. G., and Hountalas, D. T., "Combustion and exhaust emission characteristics of a dual fuel compression ignition engine operated with pilot diesel fuel and natural gas." Energy conversion and management 45, no. 18 (2004): 2971-2987.

72. Papagiannakis, R. G., Kotsiopoulos, P. N., Zannis, T. C., Yfantis, E. A., Hountalas, D. T., and Rakopoulos, C. D., "Theoretical study of the effects of engine parameters on performance and emissions of a pilot ignited natural gas diesel engine." Energy 35, no. 2 (2010): 1129-1138.

73. Papagiannakis, R. G., Rakopoulos, C. D., Hountalas, D. T., and Rakopoulos, D. C., "Emission characteristics of high speed, dual fuel, compression ignition engine operating in a wide range of natural gas/diesel fuel proportions." Fuel 89, no. 7 (2010): 1397-1406.

74. Kusaka, J., Okamoto, T., Daisho, T., Kihara, R., and Saito, T., "Combustion and exhaust gas emission characteristics of a diesel engine dual-fueled with natural gas." JSAE review 21, no. 4 (2000): 489-496.

75. Karavalakis, G., Durbin, T. D., Villela, M., and Miller, J. W., "Air pollutant emissions of light-duty vehicles operating on various natural gas compositions." Journal of Natural Gas Science and Engineering 4 (2012): 8-16.

76. Namasivayam, A. M., Korakianitis, T., Crookes, R. J., Bob-Manuel, K. D. H., and Olsen, J., "Biodiesel, emulsified biodiesel and dimethyl ether as pilot fuels for natural gas fuelled engines." Applied Energy 87, no. 3 (2010): 769-778.

77. Korakianitis, T., Namasivayam, A. M. and Crookes, R. J., "Diesel and rapeseed methyl ester (RME) pilot fuels for hydrogen and natural gas dual-fuel combustion in compression–ignition engines." Fuel 90, no. 7 (2011): 2384-2395.

78. Yoon, S. H., and Lee, C. S., "Experimental investigation on the combustion and exhaust emission characteristics of biogas–biodiesel dual-fuel combustion in a CI engine." Fuel processing technology 92, no. 5 (2011): 992-1000.

79. Yang, B., Chengxun X., Xing W., Ke Z., and Ming-Chia L., "Parametric investigation of natural gas port injection and diesel pilot injection on the combustion and emissions of a turbocharged common rail dual-fuel engine at low load." Applied Energy 143 (2015): 130-137.

80. Yang, B., Xing W., Chengxun X., Yifu L., Ke Z., and Ming-Chia L., "Experimental study of the effects of natural gas injection timing on the combustion performance and emissions of a turbocharged common rail dual-fuel engine." Energy Conversion and Management 87 (2014): 297-304.

81. Papagiannakis, R. G., Hountalas, D. T., Rakopoulos, C. D., and Rakopoulos, C. D., "Combustion and performance characteristics of a DI diesel engine operating from low to high natural gas supplement ratios at various operating conditions" SAE Technical Paper 2008-01-1392.

82. Liu, J., Fuyuan Y., Hewu W., Minggao O., Shougang H., "Effects of pilot fuel quantity on the emissions characteristics of a CNG/diesel dual fuel engine with optimized pilot injection timing." Applied Energy 110 (2013): 201-206.

83. Cheenkachorn, K., Chedthawut, P., and Choi, G. H., "Performance and emissions of a heavy-duty diesel engine fuelled with diesel and LNG (liquid natural gas)." Energy 53 (2013): 52-57.

84. Imran, S., D. R. Emberson, A. Diez, D. S. Wen, R. J. Crookes, and T. Korakianitis. "Natural gas fueled compression ignition engine performance and emissions maps with diesel and RME pilot fuels." Applied Energy 124 (2014): 354-365.

85. Yoshimoto, Y., “Combustion Characteristics of a Dual Fuel Diesel Engine with Natural Gas (Study with Fatty Acid Methyl Esters Used as Ignition Fuels)”, SAE Technical paper 2010-32-0050.

86. Yoshimoto, Y., Kinoshita, E., Luge, S. and Ohmura, T., "Combustion Characteristics of a Dual Fuel Diesel Engine with Natural Gas (Lower limit of Cetane Number for Ignition of the Fuel)," SAE Int. J. Fuels Lubr. 5(3):2012, doi:10.4271/2012-01-1690.

87. Yoshimoto, Y., Kinoshita, E., "Influence of Intake Air Dilution with N2 or CO2 Gases on the Combustion Characteristics of a Dual Fuel Diesel Engine with Natural Gas," SAE Technical Paper 2013-01-2691, doi: 10.4271/2013-01-2691.

88. Leick, M., “Optimizing conventional combustion and implementing low temperature combustion of biodiesel in a common-rail high-speed direct-injection engine”, MS Thesis, Department of Mechanical Science and Engineering. Urbana, IL, University of Illinois at Urbana-Champaign, 2010.

89. Song-Charng, K., “A study of natural gas/DME combustion in HCCI engines using CFD with detailed chemical kinetics,” Fuel 2007;86:1483–9.

90. Karavalakis, G., Durbin, T. D., Villela, M., Miller, J. W., “Air pollutant emissions of light-duty vehicles operating on various natural gas compositions,” Journal of Natural Gas Science and Engineering, Volume 4, January 2012, Pages 8-16, ISSN 1875-5100, http://dx.doi.org/10.1016/j.jngse.2011.08.005 .

91. Jones, H. L., McTaggart-Cowan, G. P., Rogak, S. N., Bushe, W. K., Munshi, S. R., Buchholz, B. A., "Source apportionment of particulate matter from a direct injection pilot-ignited natural gas fuelled heavy duty DI engine," SAE Technical Paper 2005-01-2149; 2005.

92. Zhu, J., Lee, K. O., Yozgatligil, A., Choi, M. Y., "Effects of engine operating conditions on morphology, microstructure, and fractal geometry of light-duty diesel engine particulates," Proceedings of the Combustion Institute 30 (2005) 2781–2789, doi:10.1016/j.proci.2004.08.232.

93. Lapuerta, M., Rodriguez-Fernandez, J., Sanchez-Valdepenas, J., Salgado, M. S., "Multi-Technique Analysis of Soot Reactivity from Conventional and Paraffinic Diesel Fuels," Flow Turbulence Combust., DOI 10.1007/s10494-015-9644-y.

94. Lu, T., Cheung, C. S., and Huang, Z., "Investigation on Particulate Oxidation from a DI Diesel Engine Fueled with Three Fuels," Aerosol. Sci. Technol., 46:1349–1358.

95. Song, J., Alam, M., Boehman, A. L., and Kim, U., "Examination of the Oxidation Behavior of Biodiesel Soot," Combust. Flame, 146:589–604.

96. Salamanca, M., Mondragon, F., Agudelo, J. R., and Santamaria, A., "Influence of Palm Oil Biodiesel on the Chemical and Morphological Characteristics of Particulate Matter Emitted by a Diesel Engine," Atmos. Environ., 62:220–227.

97. Salamanca, M., Mondragon, F., Agudelo, J. R., Benjumea, P., and Santamarıa, A., "Variations in the Chemical Composition and Morphology of Soot Induced by the Unsaturation Degree of Biodiesel and a Biodiesel Blend," Combust. Flame, 2012a;159:1100–1108.

98. Lapuerta, M., Oliva, F., Agudelo, J. R., and Boehman, A. L., “Effect of Fuel on the Soot Nanostructure and Consequences on Loading and Regeneration of Diesel Particulate Filters” Combust. Flame, 2012:159:844–853.

99. Yehliu, K., Vander Wal, R. L., Armas, O., and Boehman, A. L., “Impact of Fuel Formulation on the Nanostructure and Reactivity of Diesel Soot” Combust. Flame, 2012:159:3597–3606.

100. Agudelo, J. R., Álvarez, A., Armas, O., “Impact of crude vegetable oils on the oxidation reactivity and nanostructure of diesel particulate matter,” Combustion and Flame, Volume 161, Issue 11, November 2014, Pages 2904-2915, ISSN 0010-2180, http://dx.doi.org/10.1016/j.combustflame.2014.05.013.

101. Man, X. J., Cheung, C. S., Ning, Z., Yung, K. F., “Effect of Waste Cooking Oil Biodiesel on the Properties of Particulate from a DI Diesel Engine,” Aerosol Science and Technology, 2015:49:4, 199-209, DOI: 10.1080/02786826.2015.1016214

102. Lee, K., Cole, R., Sekar, R., Choi, M. Y., Kang, J. S., Bae, C. S., Shin, H. D., “Morphological investigation of the microstructure, dimensions, and fractal geometry of diesel particulates. Proceedings of the Combustion Institute, 2002;29(1), 647-653.

103. Neer, A., and Koylu, U. O., “Effect of operating conditions on the size, morphology, and concentration of submicrometer particulates emitted from a diesel engine,” Combustion and Flame, 2006:146(1), 142-154.

104. Al-Qurashi, K., and Boehman, A. L., “Impact of exhaust gas recirculation (EGR) on the oxidative reactivity of diesel engine soot,” Combustion and Flame, 2008:155(4), 675-695..

105. Chien, Y. C., Lu, M., Chai, M., and Boreo, F. J., “Characterization of biodiesel and biodiesel particulate matter by TG, TG− MS, and FTIR,” Energy and Fuels, 2008:23(1), 202-206.

106. Li, Z., Song, C., Song, J., Lv, G., Dong, S., and Zhao, Z., “Evolution of the nanostructure, fractal dimension and size of in-cylinder soot during diesel combustion process,” Combustion and Flame, 2011:158(8), 1624-1630.

107. Wang, L., Song, C., Song, J., Lv, G., Pang, H., and Zhang, W., “Aliphatic C–H and oxygenated surface functional groups of diesel in-cylinder soot: Characterizations and impact on soot oxidation behavior,” Proceedings of the Combustion Institute, 2013:34(2), 3099-3106.

108. Yehliu, K., Armas, O., Vander Wal, R. L., and Boehman, A. L., “Impact of engine operating modes and combustion phasing on the reactivity of diesel soot,” Combustion and Flame, 2013:160(3), 682-691.

109. Jung, Y., Bae, C., “Immaturity of soot particles in exhaust gas for low temperature diesel combustion in a direct injection compression ignition engine,” Fuel, Volume 161, 1 December 2015, Pages 312-322, ISSN 0016-2361, http://dx.doi.org/10.1016/j.fuel.2015.08.068.

110. Gaddam, C. K., and VanderWal, R. L., “Physical and Chemical Characterization of SIDI Engine Particulates,” Combust. Flame, 2013:160(11):2517–2528.

111. Kuribayashi, M., Ishizuka, Y., and Aizawa, T., “Sizing of Soot Particles in Diesel Spray Flame -A Qualitative Comparison Between TEM Analysis and LII/Scattering Laser Measurements,” SAE Int. J. Fuels Lubr., 2013:6: 641–650.

112. Seong, H., Choi, S., and Lee, K., Examination of Nanoparticles from Gasoline Direct-Injection (GDI) Engines using Transmission Electron Microscopy (TEM), Int J Automot Techn., 2014:15(2):175–181.

113. Zheng Li, Chonglin Song, Jinou Song, Gang Lv, Surong Dong, Zhuang Zhao, "Evolution of the nanostructure, fractal dimension and size of in-cylinder soot during diesel combustion process," Combustion and Flame 158 (2011) 1624–1630, doi:10.1016/j.combustflame.2010.12.006.

114. Lapuerta, M., Martos, F. J., Herreros, J. M., "Effect of engine operating conditions on the size of primary particles composing diesel soot agglomerates," Journal of Aerosol Science, Volume 38, Issue 4, April 2007, Pages 455-466, ISSN 0021-8502, http://dx.doi.org/10.1016/j.jaerosci.2007.02.001.

115. Li, X., Guan, C., Luo, Y., Huang, J., "Effect of multiple-injection strategies on diesel engine exhaust particle size and nanostructure," Journal of Aerosol Science, Volume 89, November 2015, Pages 69-76, ISSN 0021-8502, http://dx.doi.org/10.1016/j.jaerosci.2015.07.008.

116. Alfè, M., Apicella, B., Rouzaud, J. N., Tregrossi, A., Ciajolo, A., "The effect of temperature on soot properties in premixed methane flames," Combustion and Flame, Volume 157, Issue 10, October 2010, Pages 1959-1965, ISSN 0010-2180, http://dx.doi.org/10.1016/j.combustflame.2010.02.007.

117. Nithyanandan, K., Zhang, J., Li, Y., et al., "Diesel-like Efficiency using CNG/Diesel Dual-fuel Combustion," ASME. J. Energy Resour. Technol. 2016;():. doi:10.1115/1.4032621.

118. Nejar, N., Makkee, M., Illián-Gómez, M. J., "Catalytic removal of NO_x and soot from diesel exhaust: Oxidation behaviour of carbon materials used as model soot," Applied

Catalysis B: Environmental, Volume 75, Issues 1–2, 29 August 2007, Pages 11-16, ISSN 0926-3373, http://dx.doi.org/10.1016/j.apcatb.2007.03.009.

119. Appel, J., Bockhorn, H., and Frenklach, M., "Kinetic modeling of soot formation with detailed chemistry and physics: laminar premixed flames of C2 hydrocarbons," Combustion and Flame, Volume 121, Issues 1–2, April 2000, Pages 122-136, ISSN 0010-2180, http://dx.doi.org/10.1016/S0010-2180(99)00135-2.
120. Constantine, M., Richard, A. D., "Comparison of Soot Growth and Oxidation in Smoking and Non–Smoking Ethylene Diffusion Flames," Combustion Science and Technology, Volume 66, Issue 1-3, 1989, pp 1-16. DOI:10.1080/00102208908947136.
121. Wang, L., Song, C., Song, J., Lv, G., Pang, H., Zhang, W., "Aliphatic C–H and oxygenated surface functional groups of diesel in-cylinder soot: Characterizations and impact on soot oxidation behavior," Proceedings of the Combustion Institute, Volume 34, Issue 2, 2013, Pages 3099-3106, ISSN 1540-7489, http://dx.doi.org/10.1016/j.proci.2012.07.052.
122. Frenklach, M., Clary, D., Gardiner, W., and Stein, S., "Detailed kinetic modeling of soot formation in shock-tube pyrolysis of acetylene," In Symposium (International) on Combustion, vol. 20, no. 1, pp. 887-901. Elsevier, 1985, http://dx.doi.org/10.1016/S0082-0784(85)80578-6.
123. Frenklach, M., "Reaction mechanism of soot formation in flames," Physical Chemistry Chemical Physics, 4(11), pp.2028-2037, 2002, http://dx.doi.org/10.1039/B110045A.
124. Harris, S.J., and Weiner, A.M., "Surface growth of soot particles in premixed ethylene/air flames," Combustion Science and Technology, 31(3-4), pp.155-167, 1983, http://dx.doi.org/10.1080/00102208308923637.

125. Singh, J., Balthasar, M., Kraft, M. and Wagner, W., “Stochastic modeling of soot particle size and age distributions in laminar premixed flames,” Proceedings of the Combustion Institute, 30(1), pp.1457-1465, 2005, http://dx.doi.org/ 10.1016/j.proci.2004.08.120.

126. Khosousi, A., and Dworkin, S.B., “Soot surface reactivity during surface growth and oxidation in laminar diffusion flames,” Combustion and Flame, 162(12), pp.4523-4532, 2015, http://dx.doi.org/ 10.1016/j.combustflame.2015.09.005

127. Carlucci, A., et al., 2010, "Study of Combustion Development in Methane-Diesel Dual Fuel Engines, Based on the Analysis of In-Cylinder Luminance", SAE, 2010-01-1297.

128. Schlatter, S., et al., 2012, "Experimental Study of Ignition and Combustion Characteristics of a Diesel Pilot Spray in a Lean Premixed Methane/Air Charge using a Rapid Compression Machine", SAE, 2012-01-0825.

129. Dronniou, N., et al., 2014, "Optical Investigation of Dual-fuel CNG/Diesel Combustion Strategies to Reduce CO2 Emissions", SAE, 2014-01-1313.

130. Khosravi, M., Rochussen, J., Yeo, J., Kirchen, P., “Effect of fuelling control parameters on combustion characteristics of diesel-ignited natural gas dual-fuel combustion in an optical engine,” ICEF2016-9399, Proceedings of the ASME 2016 Internal Combustion Engine Fall Technical Conference ICEF2016, Greenville, SC, USA.

131. Zeng, W., He, X., Jin, S., Liu, H., Li, X., Liu, F., “Analysis of the Influence of Pilot Injection Timing on Diesel Combustion in an Optical Engine by the Two-Color Method,” ASME. Internal Combustion Engine Division Fall Technical Conference, Volume 1: Large Bore Engines; Advanced Combustion; Emissions Control Systems; Instrumentation, Controls, and Hybrids ():V001T03A015. doi:10.1115/ICEF2013-19104.

132. Hottel, H. C., 1932, "Determination of True Temperature and Total Radiation from Luminous Gas Flames," Industrial and Engineering Chemistry Analytical Edition, 4(2), pp. 166-175.

133. Zhao, H., Ladommatos, N., 1998, “Optical Diagnostics for Soot and Temperature Measurement in Diesel Engines,” Progress in Energy and Combustion Science, 24, pp. 221-255.

134. Payri F., Pastor, J. V., Garcai, J. M., and Pastor, J. M., “Contribution to the application of two-colour imaging to diesel combustion,” Meas. Sci. Technol. 2007; 18(8).

135. Zhang, J., Jing, W., Roberts, W.L., and Fang, T.G., “Soot temperature and KL factor for biodiesel and diesel spray combustion in a constant volume combustion chamber,” Applied Energy, 107 (2013) 52-65.

136. Rochussen, J., et al., 2016, "Effect of Fuelling Control Parameters on Combustion and Emissions Characteristics of Diesel-Ignited Natural Gas Dual-Fuel Combustion", SAE, 2016-01-0791.

137. Taschek, M., Koch, P., Egermann, J., and Leipertz, A., “Simultaneous Optical Diagnostics of HSDI Diesel Combustion Processes,” SAE Technical Paper 2005-01-3845, 2005, doi:10.4271/2005-01-3845.

138. Ekoto, I., Colban, W., Miles, P., Park, S. et al., “Sources of UHC Emissions from a Light-Duty Diesel Engine Operating in a Partially Premixed Combustion Regime,” SAE Int. J. Engines 2(1):1265-1289, 2009, doi:10.4271/2009-01-1446.

139. Espey, C. and Dec, J., “Diesel Engine Combustion Studies in a Newly Designed Optical-Access Engine Using High-Speed Visualization and 2-D Laser Imaging,” SAE Technical Paper 930971, 1993, doi:10.4271/930971.

140. Dong, Y., Vagelopoulos, C. M., Spedding, G. R., and Egolfpoulos,F. N., “Measurement of Laminar Flame speeds through Digital Particle Velocimetry: Mixtures of Methane and Ethane with Hydrogen, Oxygen, Nitrogen and Helium,” Proceedings of the Combustion Institute (29)1419:1426, 2002, DOI:10.1016/S1540-7489(02)80174.

141. Alexandrov, A. T., "Extending the lean limit of methane-air mixtures by oxygen, nitrogen and carbon dioxide injection in the gap of the spark plug’s electrodes." Master's Thesis, University of Tennessee, 2015.

142. Alkidas, A. C., “Combustion advancements in gasoline engines,” Energy Conversion and Management, 2007;48(11), 2751-2761. doi:101016/jenconman200707027.

143. Drake, M. C., Haworth, D. C., “Advanced gasoline engine development using optical diagnostics and numerical modeling,” Proceedings of the Combustion Institute, Volume 31, Issue 1, January 2007, Pages 99-124, ISSN 1540-7489, http://dx.doi.org/10.1016/j.proci.2006.08.120.

144. Çelik, M. B., and Ozdalyan, B., “Gasoline Direct Injection, Fuel Injection,” Daniela Siano (Ed.), 2010; ISBN: 978-953-307-116-9, InTech, Available from: http://www.intechopen.com/books/fuelinjection/gasoline-direct-injection

145. Zhao, F., Lai, M. C., Harrington, D. L., “Automotive spark-ignited direct-injection gasoline engines,” Progress in Energy and Combustion Science 25 (1999) 437–562.

146. Dale, J. D., Checkel, M. D. and Smy, P. R., “Application of High Energy Ignition Systems to Engines”, Progress in Energy and Combustion Science, 1997. 23 (5-6), 379-398.

147. Lake, T., Sapsford, S., Stokes, J., and Jackson, N., "Simulation and Development Experience of a Stratified Charge Gasoline Direct Injection Engine," SAE Technical Paper 962014, 1996, doi:10.4271/962014.

148. Serras-Pereira, J., Aleiferis, P., Richardson, D., and Wallace, S., "Spray Development, Flow Interactions and Wall Impingement in a Direct-Injection Spark-Ignition Engine," SAE Technical Paper 2007-01-2712, 2007, doi:10.4271/2007-01-2712.

149. Serras-Pereira, J., Aleiferis, P., Richardson, D., and Wallace, S., "Mixture Preparation and Combustion Variability in a Spray-Guided DISI Engine," SAE Technical Paper 2007-01-4033, 2007, doi:10.4271/2007-01-4033.

150. P.G. Aleiferis et al., P. G., Taylor, A. M. K. P., Ishii, K., Urata, Y., The nature of early flame development in a lean-burn stratified-charge spark-ignition engine," Combustion and Flame 136 (2004) 283–302

151. Drake, M. C., Fansler, T. D., and Lippert, A. M., "Stratified-charge combustion: modeling and imaging of a spray-guided direct-injection spark-ignition engine," Proceedings of the Combustion Institute, 2005;30(2), 2683-2691..

152. Li, T., et al. "Effect of split injection on stratified charge formation of direct injection spark ignition engines." International Journal of Engine Research 8.2 (2007): 205-219.

153. Costa, M., Sorge, U., and Allocca, L., "Increasing energy efficiency of a gasoline direct injection engine through optimal synchronization of single or double injection strategies," Energy Conversion and Management, 2012;60, 77-86.

154. Hemdal, Stina, et al. "In-cylinder soot imaging and emissions of stratified combustion in a spark-ignited spray-guided direct-injection gasoline engine." International Journal of engine research 12.6 (2011): 549-563.

155. Park, C., Kim, S., Kim, H., and Moriyoshi, Y., "Stratified lean combustion characteristics of a spray-guided combustion system in a gasoline direct injection engine," Energy, 41(1), 401-407.

156. Oh, H., Bae, C., “Effects of the injection timing on spray and combustion characteristics in a spray-guided DISI engine under lean-stratified operation,” Fuel, Volume 107, May 2013, Pages 225-235, ISSN 0016-2361, http://dx.doi.org/10.1016/j.fuel.2013.01.019.

157. Smith, J, D, Sick, V., “The prospects ofusing alcohol-based fuels instratified-charge spark-ignition engines,” SAE paper 2007-01-4034.

158. Fatouraie, M., Wooldridge, M. and Wooldridge, S., "In-Cylinder Particulate Matter and Spray Imaging of Ethanol/Gasoline Blends in a Direct Injection Spark Ignition Engine," SAE Int. J. Fuels Lubr. 6(1):2013, doi:10.4271/2013-01-0259.

159. Maricq, M. M., Szente, J. J., Jahr, K., “The impact of ethanol fuel blends on PM emissions from a light-duty GDI vehicle,” Aerosol Sci Technol 2012;46(5):576–83.

160. Karavalakis, G., Short, D., Vu, D., Villela, M., Asa-Awuku, A., Durbin, T. D., “Evaluating the regulated emissions, air toxics, ultrafine particles, and black carbon from SI-PFI and SI-DI vehicles operating on different ethanol and iso-butanol blends” Fuel 2014;128:410–21.

161. Lee, K., Seong, H., Sakai, S., Hageman, M., Rothamer, D. A., “Detailed morphological properties of nanoparticles from gasoline direct injection engine combustion of ethanol blends,” SAE Technical Paper 2013-24-0185.

162. Daniel, R., Xu, H., Wang, C., Richardson, D., Shuai, S., “Gaseous and particulate matter emissions of biofuel blends in dual-injection compared to direct-injection and port injection,” Appl Energ 2013;105:252–61.

163. Chen, L., Stone, R., “Measurement of enthalpies of vaporization of isooctane and ethanol blends and their effects on PM emissions from a GDI engine,” Energ Fuel 2011;25(3):1254–9.

164. Matthews, W. S., “Mixing and combustion studies in an optically-accessible small-bore high-speed direct-injection diesel engine”, Ph.D. thesis, Mechanical and Industrial Engineering Department, University of Illinois, Urbana, 2004

165. Fang, T., “Low-temperature combustion in a small-bore high-speed direct injection optically accessible diesel engine”, Ph.D. thesis, Mechanical and Industrial Engineering Department, University of Illinois, Urbana, 2007

166. Donahue, R., MS Thesis, Mechanical and Industrial Engineering Department, University of Illinois, Urbana, 2017

167. Catapano, F., Sementa, P., Vaglieco, B. M., “Air-fuel mixing and combustion behavior of gasoline-ethanol blends in a GDI wall-guided turbocharged multi-cylinder optical engine,” Renewable Energy, Volume 96, Part A, October 2016, Pages 319-332, ISSN 0960-1481, http://dx.doi.org/10.1016/j.renene.2016.04.087.

168. Chen, R., Nishida, K., “Spray evaporation of ethanol–gasoline-like blend and combustion of ethanol–gasoline blend injected by hole-type nozzle for direct-injection spark ignition engines,” Fuel, Volume 134, 15 October 2014, Pages 263-273, ISSN 0016-2361, http://dx.doi.org/10.1016/j.fuel.2014.05.082.

169. Aleiferis, P. G., van Romunde, Z. R., “An analysis of spray development with iso-octane, n-pentane, gasoline, ethanol and n-butanol from a multi-hole injector under hot fuel conditions,” Fuel, Volume 105, March 2013, Pages 143-168, ISSN 0016-2361, http://dx.doi.org/10.1016/j.fuel.2012.07.044.

170. Park, S. H., Kim, H. J., Suh, H. K., Lee, C. S. “Atomization and spray characteristics of bioethanol and bioethanol blended gasoline fuel injected through a direct injection gasoline injector,” International Journal of Heat and Fluid Flow, Volume 30, Issue 6, December

2009, Pages 1183-1192, ISSN 0142-727X, http://dx.doi.org/10.1016/j.ijheatfluidflow.2009.07.002.

171. Li, Q., Jin, W., Huang, Z., “Laminar Flame Characteristics of C1–C5 Primary Alcohol-Isooctane Blends at Elevated Temperature,” Energies 2016, 9, 511.

172. O’Connor, J., Musculus, M., “Optical Investigation of Multiple Injections for Unburned Hydrocarbon Emissions Reduction with Low-Temperature Combustion in a Heavy-Duty Diesel Engine,” Paper # 0701IC-0033, 8th U. S. National Combustion Meeting, Utah, May 19-22, 2013.

173. Storch, M., Hinrichsen, F., Wensing, M., Will, S., Zigan, L., “The effect of ethanol blending on mixture formation, combustion and soot emission studied in an optical DISI engine,” Applied Energy, Volume 156, 15 October 2015, Pages 783-792, ISSN 0306-2619, http://dx.doi.org/10.1016/j.apenergy.2015.06.030.

174. Sementa, P., Vaglieco, B. M., Catapano, F., "Thermodynamic and optical characterizations of a high performance GDI engine operating in homogeneous and stratified charge mixture conditions fueled with gasoline and bio-ethanol," Fuel 96 (2012): 204-219.

175. de Francqueville, L., "Effects of Ethanol Addition in RON 95 Gasoline on GDI Stratified Combustion," SAE Technical Paper 2011-24-0055, 2011, doi:10.4271/2011-24-0055.

176. Stein, R., Anderson, J., Wallington, T., "An Overview of the Effects of Ethanol-Gasoline Blends on SI Engine Performance, Fuel Efficiency, and Emissions," SAE Int. J. Engines 6(1):470-487, 2013, doi:10.4271/2013-01-1635.

177. Stone, R., Chen, L., Hinton, N., Leach, F., Xu, F., “GDI engine operation with ethanol/gasoline blends and aqueous ethanol,” J Automotive Safety and Energy, 2012, 3(3), 257-264.

178. Turner, D., Xu, H., Cracknell, R. F., Natarajan, V., Chen, X., “Combustion performance of bio-ethanol at various blend ratios in a gasoline direct injection engine,” Fuel, 2011, 90(5), 1999-2006.